

MEASUREMENT OF ELECTROWEAK PRODUCTION OF SAME-SIGN W BOSON PAIRS WITH ATLAS

William Kennedy DiClemente

A DISSERTATION

in

Physics and Astronomy

Presented to the Faculties of The University of Pennsylvania
in Partial Fulfillment of the Requirements for the Degree of Doctor of Philosophy
2019

I. Joseph Kroll, Professor, Physics
Supervisor of Dissertation

Joshua Klein, Edmund J. and Louise W. Kahn Professor, Physics
Graduate Group Chairperson

Dissertation Committee

Elliot Lipeles, Associate Professor, Physics
Christopher Mauger, Associate Professor, Physics
Burt Ovrut, Professor, Physics
Justin Khoury, Professor, Physics
I. Joseph Kroll, Professor, Physics

MEASUREMENT OF ELECTROWEAK PRODUCTION OF
SAME-SIGN W BOSON PAIRS WITH ATLAS

COPYRIGHT
2019
William Kennedy DiClemente

All rights reserved.

Acknowledgements

It would be impossible to properly thank everyone who has helped me along this journey; nevertheless I will attempt to be as thorough as possible.

First and foremost, I would like to thank my family. My parents, Gwynne Kennedy and John DiClemente, for always believing in me and enjoying my attempts to explain what it is I am working on. My many feline friends past and present—Stella, Lucky, Julia, Elise, Lucille, Tweedie, Ruby, and Sylvie—for keeping me warm during the winter holidays back home. My girlfriend Amber Wright, for tolerating me these past few months and doing her best to keep me relatively sane.

Thanks to my advisor Joe Kroll for guiding me through the past six years at Penn; your advice both in physics and in life has been invaluable to my growth as a physicist and a person. Additional thanks to the rest of the ATLAS faculty at Penn: Elliot Lipeles, Evelyn Thomson, and Brig Williams. The amount of open collaboration between students and faculty irrespective of who works for whom has helped me learn so much.

I would also like to extend thanks to two important figures from before my time at Penn. First, to Gardner Friedlander, my high school physics teacher who first got me interested in the subject. You were the first to show me how I could use a pen and paper to predict events in real life—a fascination of mine that has continued into my work here, just with much harder math and on a more fundamental scale. Second, my undergraduate research advisor, Al Goshaw, at Duke University. You gave a college freshman who thought particle physics was “pretty neat” the opportunity to do meaningful research with one of the leading collaborations in the field. Without either of you, I likely would not be in this position today.

Thanks to the members of the Inner Detector Alignment group, including but not limited to Anthony Morley for his guidance on my qualification task, and to Shih-Chieh Hsu, Pierfrancesco Butti, Matthias Danninger, Salvador Marti, and Steffen Henkelmann for numerous collaborative

alignment efforts.

The entire $W^\pm W^\pm jj$ 13 TeV analysis group, and those with whom I worked most closely: Philip Sommer, Emily Duffield, Rustem Ospanov, Stefanie Todt, and Liqing Zhang. Special thanks to Rustem for pushing me to find my voice in the analysis. Thanks to my $W^\pm W^\pm jj$ HL-LHC prospects collaborators Claire Lee and Karolos Potamiamos.

Lastly, thanks to my fellow Penn ATLAS graduate students, Bijan Haney, Joey Reichert, Khilesh Mistry, Leigh Schaefer, Bill Balunas, Christian Herwig, Elodie Ressegue, and many more, for listening to my ramblings, answering my many questions, and for countless entertaining lunchtime discussions.

ABSTRACT

MEASUREMENT OF ELECTROWEAK PRODUCTION OF SAME-SIGN W BOSON PAIRS WITH ATLAS

William Kennedy DiClemente

J. Kroll

This thesis presents two studies of electroweak same-sign $W^\pm W^\pm jj$ scattering performed with the ATLAS experiment at the CERN Large Hadron Collider (LHC). The first is a measurement of the fiducial cross section at $\sqrt{s} = 13$ TeV using 36.1 fb^{-1} of data recorded in 2015 and 2016. Particular emphasis is placed on the determination of the non-prompt lepton background. The electroweak production is observed with a signal significance of 6.9σ , and the fiducial cross section is measured to be $\sigma_{\text{meas}}^{\text{fid}} = 2.91^{+0.51}_{-0.47}(\text{stat})^{+0.28}_{-0.29}(\text{sys}) \text{ fb}$. The second is a study on the future prospects for the $W^\pm W^\pm jj$ process at the planned High-Luminosity LHC with a projected $\sqrt{s} = 14$ TeV and 3000 fb^{-1} of data, with a focus on the optimization of the signal event selection. The expected electroweak production cross section is determined with a total uncertainty of 6%, and the purely longitudinal scattering component is extracted with an expected significance of 1.8σ . This thesis also describes work performed on the alignment of the ATLAS Inner Detector, which is used to reconstruct the trajectories of charged particles and to determine their momenta. A precise alignment is essential for the majority of physics results from the ATLAS experiment. The main topics presented are the alignment campaign performed at the beginning of the 2015 data taking period and the monitoring of momentum biases in the Inner Detector.

Contents

Acknowledgements	iii
Abstract	v
Contents	vi
List of Tables	x
List of Figures	xiii
Preface	xx
1 Introduction	1
2 Theoretical Framework	3
2.1 Introduction to the Standard Model	3
2.2 Electroweak symmetry breaking and the Higgs boson	6
2.3 Electroweak vector boson scattering	9
3 LHC and the ATLAS Detector	13
3.1 The Large Hadron Collider	13
3.2 The ATLAS Detector	16
3.2.1 The Inner Detector	17
3.2.1.1 Pixel Detector	18
3.2.1.2 Semiconductor Tracker	19
3.2.1.3 Transition Radiation Tracker	19

3.2.2	The Calorimeters	20
3.2.2.1	Liquid Argon Calorimeter	21
3.2.2.2	Tile Calorimeter	22
3.2.3	The Muon Spectrometer	23
3.3	Particle reconstruction	23
3.3.1	Track reconstruction	24
3.3.2	Electron reconstruction	25
3.3.3	Muon reconstruction	28
4	Alignment of the ATLAS Inner Detector	32
4.1	The alignment method	33
4.1.1	Alignment levels	37
4.1.2	Alignment coordinate systems	38
4.2	Early 2015 alignment of the ATLAS detector	40
4.2.1	June alignment procedure	40
4.2.2	Alignment results	42
4.2.2.1	Residual distributions from collisions	43
4.2.2.2	Track parameter resolution from cosmic rays	47
4.2.3	Error scaling	48
4.3	Level 2 alignment of the TRT	50
4.4	Momentum bias from sagitta deformations	51
4.4.1	Sagitta bias monitoring with electron E/p	52
4.4.1.1	Measuring $\langle E/p \rangle$	53
4.4.1.2	Results in 13 TeV data	55
5	Measurement of same-sign WW production at $\sqrt{s} = 13$ TeV with ATLAS	58
5.0.1	Experimental overview of vector boson scattering	58
5.0.2	Same-sign $W^\pm W^\pm$ scattering	59
5.0.3	Overview of backgrounds	61
5.1	Data and Monte Carlo samples	63
5.1.1	Monte Carlo samples	64
5.2	Object and event selection	66
5.2.1	Object selection	66

5.2.1.1	Muon candidate selection	66
5.2.1.2	Electron candidate selection	67
5.2.1.3	Jet candidate selection	69
5.2.1.4	Treatment of overlapping objects	69
5.2.2	Signal event selection	70
5.3	Background estimations	71
5.3.1	Estimation of the WZ background	72
5.3.2	Estimation of the $V\gamma$ background	73
5.3.3	Estimation of backgrounds from charge misidentification	75
5.3.3.1	Validation of the charge misidentification estimate	77
5.3.4	Estimation of non-prompt backgrounds with the fake-factor method	78
5.3.4.1	Overview of the default fake-factor method	79
5.3.4.2	The fake-factor with p_T^{cone}	81
5.3.4.3	Application of the fake-factor	82
5.3.4.4	Systematic uncertainties	86
5.3.4.5	Results of the fake-factor	87
5.3.4.6	Validation of the fake-factor	90
5.3.5	Reduction of WZ background using custom overlap removal	90
5.4	Cross section measurement	95
5.4.1	Maximum likelihood fit	95
5.4.2	Definition of the fiducial volume	97
5.4.3	Cross section extraction	98
5.5	Summary of uncertainties	99
5.5.1	Experimental uncertainties	99
5.5.2	Theoretical uncertainties	100
5.5.2.1	Uncertainties from EWK-QCD interference	102
5.6	Results	103
5.7	Beyond the Standard Model extensions of $W^\pm W^\pm jj$	105
5.7.1	Doubly charged Higgs bosons	106
5.7.2	Anomalous quartic couplings	108
6	Prospects for same-sign WW at the High Luminosity LHC	111
6.0.3	Analysis Overview	112

6.1	Theoretical motivation	113
6.1.1	Experimental sensitivity to longitudinal polarization	113
6.2	Monte Carlo samples	114
6.3	Background estimations	115
6.3.1	Truth-based isolation	116
6.4	Object and event selection	117
6.4.1	Object selection	117
6.4.2	Event selection	117
6.5	Selection optimization	118
6.5.1	Random grid search algorithm	119
6.5.2	Inputs to the optimization	120
6.5.3	Results of the optimization	121
6.6	Results	122
6.6.1	Event yields	122
6.6.2	Uncertainties	126
6.6.3	Cross section measurement	127
6.6.4	Longitudinal scattering significance	127
7	Conclusion	130
A	Additional material on $W^\pm W^\pm jj$ measurement at $\sqrt{s} = 13\text{TeV}$	131
A.1	Impact of experimental uncertainty on MC background estimations	131
A.2	Pre-fit event yields	133
B	Additional material on $W^\pm W^\pm jj$ prospects at the HL-LHC	134
B.1	Truth isolation	134
B.1.1	TRUTH1++ derivations	135
B.1.2	Check of truth-based isolation	136
B.1.3	Loose isolation working point	136
B.2	Plots of other optimization variables	139
Bibliography		141

List of Tables

4.1	The four alignment levels for each of the detector subsystems and their components (first introduced in Section 3.2). The total number of alignable structures and degrees of freedom (DoF) to be aligned are given for each level.	39
4.2	Summary of the highest level of alignment applied to each ID subsystem when deriving the June alignment.	42
4.3	Estimated value of the error scaling term b for each subdetector component with the June alignment.	49
5.1	Predicted cross sections for EWK and QCD production of diboson processes relevant to VBS at $\sqrt{s} = 13\text{TeV}$ using the SHERPA MC generator. The numbers for the $W^\pm W^\pm jj$ process are in bold. Leptons are required to have $p_T \geq 25\text{ GeV}$ and lie within $ \eta \leq 2.5$ with $m_{ll} > 20\text{ GeV}$, and at least two jets are required with $p_T \geq 30\text{ GeV}$ and $ \eta < 4.5$. The VBS contributions are enhanced by requiring the dijet invariant mass $m_{jj} > 500\text{ GeV}$ and dijet separation $\Delta y_{jj} > 2.4$	61
5.2	Summary of MC samples used in the analysis.	65
5.3	Muon selection criteria. All muons are required to pass the preselection (top), and then either the signal (middle) or loose (bottom) criteria is applied to the preselected electrons.	67
5.4	Electron selection criteria. All electrons are required to pass the preselection (top), and then either the signal (middle) or loose (bottom) criteria is applied to the preselected electrons.	68
5.5	Jet selection criteria. All jets are required to pass the above selection in order to be used in the analysis.	69
5.6	Summary of the overlap removal procedure used in the analysis. If the criteria in the “check” column is met, in the “result” column, the object on the left of the arrow is removed in favor of the object on the right.	70
5.7	Summary of trigger requirements for electrons and muons for $\sqrt{s} = 13\text{TeV}$ data collected in 2015 and 2016. At least one of the triggers must be satisfied.	71
5.8	The signal event selection.	72
5.9	Event yields in the WZ control region before normalization. All lepton flavor channels are combined.	73
5.10	Selection criteria for the $V\gamma$ control region.	74

5.11	Event yields in the $V\gamma$ control region. The $V\gamma$ scale factor of 1.77 is calculated by scaling up the $Z\gamma$ and Z +jets backgrounds to account for the difference between the data and predicted total background.	75
5.12	Selection criteria for the same-sign inclusive validation region.	78
5.13	Event selection for the dijet region used for calculating the fake-factor. The selected lepton can pass either the nominal (signal) or loose selections. In the case of the nominal leptons, the $p_T > 27$ GeV requirement is replaced with $p_T > 15$ GeV.	84
5.14	Values of the fake-factor in each p_T bin and for each individual systematic source.	89
5.15	Estimated yields for the fake lepton background. The estimated yield is shown in the first column together with the statistical uncertainty followed by the systematic uncertainties from variations of the the fake-factors within their statistical (stat.) and systematic (syst.) uncertainties. The labels f_e and f_μ indicate the fake-factors for electrons and muons, respectively.	89
5.16	Selection criteria for the same-sign top fakes validation region.	90
5.17	Custom OR definition. Leptons must pass this selection in order to be counted for the trilepton veto.	94
5.18	Definition of the fiducial volume.	97
5.19	Impact of various systematic effects on the fiducial cross section measurement. The impact of a given source of uncertainty is computed by performing the fit with the corresponding nuisance parameter varied up or down by one standard deviation from its nominal value.	100
5.20	List of sources of experimental uncertainties on the reconstruction of physics objects.	101
5.21	Impact of experimental uncertainties for the $W^\pm W^\pm jj$ EWK processes in all channels.	101
5.22	Impact of experimental uncertainties for the WZ process in all channels.	101
5.23	The set of generator level cuts used for generating the interference samples with MadGraph	102
5.24	Cross sections for each different $W^\pm W^\pm jj$ production mode (inclusive, EWK only, QCD only, and interference only) generated using MadGraph . The cross sections are calculated using a minimal set of generator level cuts from events where the W decays to a muon.	103
5.25	Table of the data and prediction event yields in the signal region after the fit. Numbers are shown for the six lepton flavor and charge channels and for all channels combined. The background estimations from the fake-factor are included in the “Non-prompt” category, and backgrounds from $V\gamma$ production and electron charge misidentification are combined in the “ e/γ conversions” category. Finally, ZZ , VVV , and $t\bar{t}V$ backgrounds are combined in the “Other prompt” category.	104
5.26	Observed 95% confidence limits set by CMS at $\sqrt{s} = 13$ TeV on the nine dimension-eight operators that modify the $WWWW$ QGC listed in Equation 5.33.	110
6.1	Summary of MC samples used in the analysis.	115
6.2	Truth-based isolation requirements for electrons and muons.	116
6.3	Summary of the signal event selection.	118
6.4	Updates to the $W^\pm W^\pm jj$ event selection criteria after optimization. Cuts not listed remain unchanged from the default selection in Table 6.3.	122
6.5	Signal and background event yields using the default event selection for an integrated luminosity of $\mathcal{L} = 3000 \text{ fb}^{-1}$. Events containing a fake or charge-flipped electron are removed from their respective sources and combined into a single entry each.	123
6.6	Signal and background event yields using the optimized event selection for an integrated luminosity of $\mathcal{L} = 3000 \text{ fb}^{-1}$. Events containing a fake or charge-flipped electron are removed from their respective sources and combined into a single entry each.	124
6.7	Summary of estimated experimental and rate uncertainties.	126

A.1	Impact of experimental uncertainties for the $W^\pm W^\pm jj$ QCD processes in all channels	131
A.2	Impact of experimental uncertainties for triboson process in all channels.	132
A.3	Impact of experimental uncertainties for $t\bar{t}V$ processes in all channels.	132
A.4	Impact of experimental uncertainties for the $W\gamma$ process in all channels.	132
A.5	Impact of experimental uncertainties for the $Z\gamma$ process in all channels.	132
A.6	Impact of experimental uncertainties for the ZZ process in all channels.	133
A.7	Table of the data and prediction event yields in the signal region before the fit. Numbers are shown for the six lepton flavor and charge channels and for all channels combined. Here the WZ background yields are normalized to the data in the WZ control region. The background estimations from the fake-factor are included in the “Non-prompt” category, and backgrounds from $V\gamma$ production and electron charge misidentification are combined in the “ e/γ conversions” category. Finally, ZZ , VVV , and $t\bar{t} + V$ backgrounds are combined in the “Other prompt” category.	133
B.1	Event yields prior to applying any form of truth-based isolation criteria.	134
B.2	Event yields after applying a test version of the truth-based isolation.	135
B.3	Electron and muon isolation requirements for the loose working point.	136
B.4	Event yields broken down by sample and by background type using the loose isolation working point. Events containing a fake or charge-flipped electron are removed from their respective sample and added to the “fakes” and “charge flip” rows, respectively. Errors include statistical uncertainty and estimated systematic rate uncertainty based on the background process.	137
B.5	Event yields broken down by background type using the tight isolation working point. Events containing a fake or charge-flipped electron are removed from their respective sample and added to the “fakes” and “charge flip” rows, respectively. Errors include sta- tistical uncertainty and estimated systematic rate uncertainty based on the background process.	138

List of Figures

2.1	Summary of several Standard Model total and fiducial production cross section measurements compared to the corresponding theoretical predictions calculated at NLO or higher. The dark colored error bar represents the statistical uncertainty, and the light colored error bar represents the full uncertainty (including systematic and luminosity uncertainties). The data/theory ratio, luminosity used and reference for each measurement are also shown.	4
2.2	An illustration of the potential term $V(\phi)$ in Equation 2.6 for the cases where $\mu^2 > 0$ (left) and $\mu^2 < 0$ (right). The right-hand plot shows the Higgs potential, or “Mexican hat potential”, with the minimum at $ \phi = \sqrt{-\frac{\mu^2}{\lambda}}$ rather than at $ \phi = 0$ as in the left-hand plot.	7
2.3	A graphical representation of the EWSB mechanism involving the $SU(2) \times U(1)$ bosons and the Higgs field. The W^\pm and Z bosons each obtain mass by eating a degree of freedom (dof) from the Higgs field, and in the process gain a longitudinal polarization mode, while the photon stays massless (with two dof) and the SM Higgs boson h remains.	9
2.4	Feynman diagram of a generic VBS process. The gray circle represents any interaction with two incoming and two outgoing vector bosons, including any of the diagrams shown in Figures 2.5 and 2.6.	10
2.5	Leading order $VV \rightarrow VV$ Feynman diagrams involving EWK bosons. From left to right: s -channel, t -channel, u -channel, and the quartic gauge coupling.	10
2.6	Leading order $VV \rightarrow VV$ Feynman diagrams involving the exchange of a Higgs boson. From left to right: s -channel, t -channel, and u -channel.	10
2.7	Cross sections in nanobarns for five different longitudinally polarized VBS processes as a function of center of mass energy \sqrt{s} . Without a Higgs boson (left), the cross sections grow unbounded with \sqrt{s} . With a 120 GeV Higgs boson (right), the cross sections no longer diverge.	12
3.1	The CERN accelerator complex. For LHC collisions, protons are accelerated by the Linac 2 (purple), the PSB (light purple), the PS (magenta), and the SPS (light blue) before entering the LHC ring (dark blue).	14
3.2	Peak instantaneous luminosity delivered to ATLAS during 13TeV pp data taking as a function of time.	15
3.3	Integrated luminosity collected by ATLAS as a function of time at 13TeV from 2015-2018.	15

3.4	Distribution of the mean number of interactions per bunch crossing for the 2015 and 2016 pp collision data at 13TeV.	16
3.5	Cut-away view of the ATLAS detector.	17
3.6	The barrel layers of the Pixel, SCT, and TRT detectors making up the Inner Detector.	18
3.7	Cut-away view of the ATLAS calorimeter systems.	20
3.8	Diagram of the cells within the LAr barrel. The accordion structure can be seen in the cut-away view.	22
3.9	Measured LH electron ID efficiencies in $Z \rightarrow ee$ events for the LooseLH (blue), MediumLH (red), and TightLH (black) working points as a function of electron E_T . The bottom panel shows data-to-simulation ratios.	26
3.10	Measured isolation efficiencies for the LooseTrackOnly (black), Loose (red), GradientLoose (blue), and Gradient (yellow) working points as a function of electron E_T . The bottom panel shows data-to-simulation ratios.	28
3.11	Muon reconstruction efficiencies in $Z \rightarrow \mu\mu$ events for the Loose (yellow), Medium (red), and Tight (blue) ID working points as a function of muon η . The drop in efficiency for Medium and Tight muons in the range $ \eta < 0.1$ is due to the exclusion of CT and ME muons, which are used to recover acceptance in this region. Collision data (solid points) is compared to simulation (open points) and the ratio is in the lower panel.	30
3.12	Muon isolation efficiencies in $Z \rightarrow \mu\mu$ events for the Loose (left) and GradientLoose (right) working points as a function of muon p_T . Collision data (black) is compared to simulation (red) and the ratio is in the lower panel.	31
4.1	Graphical representation of the effect of a misaligned detector element. The reconstructed particle track (dashed arrow) differs from the actual trajectory of the particle (solid arrow) due to a shift in the third detector element. The cyan lines represent the track-to-hit residuals.	33
4.2	Graphical representation of a track-hit residual in the local x direction according to Equation 4.2. The sensor in this example measures a particle hit in the local x and y directions, with each having its own residual.	34
4.3	Flow chart depicting the ID alignment chain.	36
4.4	A schematic representation of the Inner Detector in the longitudinal plane with the global coordinate system overlaid on top. The Pixel detector and IBL are shown in blue, the SCT in green, and the TRT in red. The local coordinates for each subdetector module are inset on the right.	39
4.5	The d_0 distributions with respect to the reconstructed primary vertex using 13TeV collision data sample reconstructed using the June (black) and March (green) alignments. The data is compared to a MC simulation using a perfect detector geometry (red). The distributions are normalized to the same number of entries.	43
4.6	Local x (left) and local y (right) residual distributions of the IBL planar sensors using 13TeV collision data sample reconstructed using the June (black) and March (green) alignments. The data is compared to a MC simulation using a perfect detector geometry (red). The distributions are normalized to the same number of entries.	44
4.7	The mean of the local x (left) and local y (right) residual distributions as a function of the global z position of each IBL module using 13TeV collision data sample reconstructed using the June (black) and March (green) alignments. The data is compared to a MC simulation using a perfect detector geometry (red).	45

4.8 Local x (left) and local y (right) residual distributions for the Pixel barrel (excluding the IBL) using 13TeV collision data sample reconstructed using the June (black) and March (green) alignments. The data is compared to a MC simulation using a perfect detector geometry (red). The distributions are normalized to the same number of entries.	45
4.9 Local x (left) and local y (right) residual distributions for the Pixel endcaps using 13TeV collision data sample reconstructed using the June (black) and March (green) alignments. The data is compared to a MC simulation using a perfect detector geometry (red). The distributions are normalized to the same number of entries.	46
4.10 Local x residual distributions for the SCT barrel (left) and end-caps (right) using 13TeV collision data sample reconstructed using the June (black) and March (green) alignments. The data is compared to a MC simulation using a perfect detector geometry (red). The distributions are normalized to the same number of entries.	46
4.11 Residual distributions for the TRT barrel (left) and end-caps (right) using 13TeV collision data sample reconstructed using the June (black) and March (green) alignments. The data is compared to a MC simulation using a perfect detector geometry (red). The distributions are normalized to the same number of entries.	47
4.12 Representation of splitting a single cosmic ray track passing through the entire detector (left) into two separate tracks (right).	48
4.13 Distribution of the difference in the impact parameter Δd_0 (left) and charge over transverse momentum $\Delta q/p_T$ (right) between the two cosmic ray split tracks. The June (black) and March (green) alignments are compared. The distributions are normalized to the same number of entries.	48
4.14 Pull distributions in local x (left) and y (right) for the IBL using 13TeV collision data sample after applying the error scaling.	49
4.15 Residual means by straw layer in two TRT ϕ -sectors affected by a tilt misalignment. The tilts in each of the three modules are clearly visible in the red points representing the reconstructed data prior to alignment. After four iterations of L2 alignment, the residual means in the gray points are flat.	50
4.16 Two dimensional map of residuals in the first layer of the TRT barrel vs z and ϕ . Each bin represents the mean of a Gaussian fit to the TRT residuals in that bin. The map on the left is after the L3 (wire-by-wire) alignment of the TRT performed in 2010, and the map on the right is after the L2 alignment at the end of 2015. The z -axis for both plots use the same scale.	51
4.17 Representation of a curl distortion in the detector. The image represents a cutaway view of the transverse plane of the barrel region. The deformation is represented by the red arrows, and the impact on the reconstructed positive (blue) and negative (green) tracks are shown. The dashed lines represent the true particle trajectories, and the solid lines represent the reconstructed trajectories.	52
4.18 Geometric definition of the sagitta s in relation to the length of the chord l and the radius R of a circular arc.	53
4.19 E/p distributions of electrons and positrons in two different $\eta\phi$ bins of the detector. The left hand plot is taken from a region with no momentum bias where $\langle E/p \rangle^+ = \langle E/p \rangle^-$, while the right hand plot shows an 8% disagreement in $\langle E/p \rangle$ between electrons and positrons.	54
4.20 Sagitta bias in the $\sqrt{s} = 13\text{TeV}$ data collected by ATLAS in 2016 as a function of η and ϕ for the prompt (left) and reprocessed (right) alignments using the E/p method.	56
4.21 Sagitta bias in the $\sqrt{s} = 13\text{TeV}$ data collected by ATLAS in 2016 projected along η for the prompt (gray) and reprocessed (blue) alignments using the E/p method.	56

4.22 Sagitta bias in the $\sqrt{s} = 13\text{TeV}$ data collected by ATLAS in 2017 as a function of η and ϕ in reconstructed electrons (left) and after two iterations of momentum corrections (right) from the E/p method.	56
4.23 Sagitta bias in the $\sqrt{s} = 13\text{TeV}$ data collected by ATLAS in 2017 projected along η in reconstructed electrons (gray) and after one (red) and two (blue) iterations of momentum corrections from the E/p method.	57
5.1 Tree-level Feynman diagrams for VBS EWK $VVjj$ production including triple gauge couplings involving W and/or Z bosons (top left and top middle), quartic gauge coupling (top right), or the exchange of a Higgs boson (s -channel bottom left and t -channel bottom right). The labels are quarks (q), fermions (f), and gauge bosons ($V = W, Z$).	60
5.2 Tree-level Feynman diagrams for non-VBS EWK $VVjj$ production. The labels are quarks (q), fermions (f), and gauge bosons ($V = W, Z$).	60
5.3 Tree-level Feynman diagrams for QCD $VVjj$ production. The labels are quarks (q), fermions (f), and gauge bosons ($V = W, Z$).	60
5.4 Leading order Feynman diagrams for VBS EWK production of $W^\pm W^\pm jj$ events. The leftmost diagram contains a quartic gauge coupling vertex, and the rightmost diagram contains an exchange of a Higgs boson.	62
5.5 $W^\pm W^\pm jj$ VBS event topology containing two leptons (1 and 2) with the same electric charge, two neutrinos, and two forward tagging jets (3 and 4) with large rapidity separation Δy	62
5.6 Generator level comparisons at $\sqrt{s} = 7\text{TeV}$ of dijet invariant mass (m_{jj} , left) and dijet rapidity (Δy_{jj} , right) in EWK (red) and QCD (blue) $W^\pm W^\pm jj$ events with no selection cuts applied.	63
5.7 ATLAS event display of a $pp \rightarrow W^+W^+ \rightarrow \mu^+\nu_\mu\mu^+\nu_\mu jj$ event. The muons are represented by the red lines travelling from the ID through the MS, and the forward jets are represented by the blue cones with yellow energy deposits in the calorimeters. The direction of the E_T^{miss} in the transverse plane is indicated by the gray dashed line in the inset image.	64
5.8 Leading lepton p_T (left) and η (right) distributions in the WZ control region before normalization. All lepton channels are combined.	73
5.9 Trilepton invariant mass m_{lll} distribution in the WZ control region before normalization. All lepton channels are combined.	74
5.10 Charge misidentification rates for electrons as a function of $ \eta $ and p_T . Rates are calculated from $Z \rightarrow e^+e^-$ MC after applying scale factors to approximate the charge mis-ID rates in data.	76
5.11 Dilepton invariant mass distribution m_{ll} for the ee channel in the same-sign inclusive VR.	78
5.12 p_T distributions for the leading (left) and subleading (right) electron for the ee channel in the same-sign inclusive VR. In these plots, the cut requiring m_{ee} to fall within the Z mass window has been inverted in order to test the modelling away from the Z peak.	79
5.13 Graphical representation of how the fake factor method is used to estimate the fake background in a given NN region.	80
5.14 Δp_T distributions for nominal (blue) and loose (red) muons in simulated $t\bar{t}$ events. Each muon has been matched to a truth-level jet. Both distributions are normalized to unit area.	82
5.15 Δp_T distributions for muons (top) and electrons (bottom) in simulated $t\bar{t}$ events. Each lepton has been matched to a truth-level jet, and that truth jet has had its p_T corrected to include all truth muons within a cone of $\Delta R < 0.4$. The nominal leptons are in black. Δp_T is calculated for the loose leptons using p_T (red) and $p_T + p_T^{\text{cone}}$ (blue).	83

5.16 Distributions of p_T^{cone}/p_T for nominal (black) and loose (red) muons in simulated $t\bar{t}$ events.	84
5.17 The measured fake-factor as a function of muon $p_T + p_T^{\text{cone}}$. The error bars represent the statistical uncertainty only.	85
5.18 The measured fake-factor as a function of electron $p_T + p_T^{\text{cone}}$ in the central ($ \eta < 1.37$, blue) and forward ($ \eta > 1.37$, red) regions of the detector. The error bars represent the statistical uncertainty only.	86
5.19 Systematic variations in the fake-factor as a function of muon $p_T + p_T^{\text{cone}}$. The individual fake-factors obtained for each systematic variation are displayed with their statistical uncertainties.	87
5.20 Systematic variations in the fake-factor as a function of electron $p_T + p_T^{\text{cone}}$ in the central ($ \eta < 1.37$, top) and forward ($ \eta > 1.37$, bottom) regions of the detector. The individual fake-factors obtained for each systematic variation are displayed with their statistical uncertainties.	88
5.21 Distributions of the subleading lepton p_T in the same-sign top fakes VR for $\mu^\pm\mu^\pm$ events (top right), $e^\pm e^\pm$ events (top left), $\mu^\pm e^\pm$ events (bottom left), and all events combined (bottom right). All errors are statistical only.	91
5.22 Pseudorapidity (η) distributions of truth muons (top) and electrons (bottom) for Sherpa $W^\pm W^\pm jj$ and WZ MC samples. The blue vertical lines represent the allowed η range for each lepton flavor. The numbers correspond to the number of raw MC events that fall within and outside of the allowed η range for each MC sample.	92
5.23 Distributions of $p_{T,\text{ratio}}(\mu, j)$ for EWK and QCD $W^\pm W^\pm jj$ signal (black) and WZ background (teal) for truth-matched third muons in events that pass the trilepton veto. Both distributions are normalized to unit area. The associated efficiency curves are on the right where efficiency is defined as the percentage of total events that would pass a cut on $p_{T,\text{ratio}}(\mu, j)$ at a given value on the x -axis.	92
5.24 Distributions of $\Delta R(\mu, j)$ for EWK and QCD $W^\pm W^\pm jj$ signal (black) and WZ background (teal) for truth-matched third muons in events that pass the trilepton veto. Both distributions are normalized to unit area. The associated efficiency curves are on the right where efficiency is defined as the percentage of total events that would pass a cut on $\Delta R(\mu, j)$ at a given value on the x -axis.	93
5.25 Distributions of $p_{T,\text{ratio}}(e, j)$ for EWK and QCD $W^\pm W^\pm jj$ signal (black) and WZ background (teal) for truth-matched third electrons in events that pass the trilepton veto. Both distributions are normalized to unit area. The associated efficiency curves are on the right where efficiency is defined as the percentage of total events that would pass a cut on $p_{T,\text{ratio}}(e, j)$ at a given value on the x -axis.	93
5.26 Two-dimensional plots of $p_{T,\text{ratio}}(\mu, j)$ vs $\Delta R(\mu, j)$ for truth-matched third muons in events that pass the trilepton veto for EWK and QCD $W^\pm W^\pm jj$ signal (left) and WZ background (right). The blue overlay indicates the area in which the third leptons will pass the custom OR and result in the event failing the trilepton veto.	94
5.27 Visual representation of the different kinematic regions relevant to the cross section measurement. The acceptance factor \mathcal{A} converts from the truth level total phase space to the truth level fiducial region, and the efficiency correction \mathcal{C} translates the fiducial region in to the reconstruction level signal region.	98

5.28 The dijet invariant mass m_{jj} distributions for data and predicted signal and background in the signal region after the fit. The shaded band represents the statistical and systematic uncertainties added in quadrature. Note that the bins have been scaled such that they represent the number of events per 100 GeV in m_{jj} . The background estimations from the fake-factor are included in the “Non-prompt” category, and backgrounds from $V\gamma$ production and electron charge misidentification are combined in the “ e/γ conversions” category. Finally, ZZ , VVV , and $t\bar{t}+V$ backgrounds are combined in the “Other prompt” category.	104
5.29 The event yields for data and predicted signal and background in the WZ and low- m_{jj} control regions after the fit. The shaded band represents the statistical and systematic uncertainties added in quadrature. The background estimations from the fake-factor are included in the “Non-prompt” category, and backgrounds from $V\gamma$ production and electron charge misidentification are combined in the “ e/γ conversions” category. Finally, ZZ , VVV , and $t\bar{t}V$ backgrounds are combined in the “Other prompt” category.	105
5.30 Comparison of the measured $W^\pm W^\pm jj$ EWK fiducial cross section with theoretical calculations from SHERPA v2.2.2 and POWHEG-BOX v2 . The light orange band represents the total experimental uncertainty on the measured value, and the dark orange hashed band is the statistical uncertainty. For the simulations, the light blue band represents the total theoretical uncertainty, and the dark blue hashed band are the scale uncertainties. The theory predictions do not include the interference between the EWK and QCD production.	106
5.31 CMS observed and expected upper limits for the $H^{\pm\pm} \rightarrow W^\pm W^\pm$ cross section at 95% CL at $\sqrt{s} = 13\text{TeV}$ as a function of $H^{\pm\pm}$ mass. The region above the observed limit is excluded by the measurement.	107
5.32 ATLAS observed and expected upper limits for the $H^{\pm\pm} H^{\mp\mp} \rightarrow W^\pm W^\pm W^\mp W^\mp$ cross section at 95% CL at $\sqrt{s} = 13\text{TeV}$ as a function of $H^{\pm\pm}$ mass. The region above the observed limit is excluded by the measurement.	108
5.33 Invariant mass distributions of the $2l2\nu$ system in $pp \rightarrow e^+\nu_e\mu^+\nu_\mu jj$ events at LO and NLO with the VBFNLO MC generator. SM predictions are compared to those with the anomalous coupling $\frac{f_{T,1}}{\Lambda^4} = 200\text{TeV}^{-4}$. The left plot shows the differential cross section for each prediction, and the right plot shows the K -factors for the SM and anomalous coupling predictions as well as the cross section ratio between the anomalous coupling and SM predictions at LO and NLO.	110
6.1 Comparison of the leading (left) and subleading (right) lepton p_T distributions for purely longitudinal (LL, black) and mixed polarization (LT+TT, cyan) $W^\pm W^\pm jj$ events.	113
6.2 Comparison of the azimuthal dijet separation ($ \Delta\phi_{jj} $) for purely longitudinal (LL, black) and mixed polarization (LT+TT, cyan) $W^\pm W^\pm jj$ events.	114
6.3 A visual representation of a two-dimensional rectangular grid (left) and a random grid (right) in variables x and y . The signal events are the black circles, and the red squares are the background events. Each intersection of gray dashed lines represents a cut point to be evaluated by the optimization.	120
6.4 Leading (top) and subleading (bottom) jet p_T distributions. The default and optimized cuts are represented by the red and green dashed lines, respectively. The $W^\pm W^\pm jj$ EWK signal (black points) is normalized to the same area as the sum of the backgrounds (colored histogram).	123
6.5 Lepton-jet centrality distribution. The default and optimized cuts are represented by the red and green dashed lines, respectively. The $W^\pm W^\pm jj$ EWK signal (black points) is normalized to the same area as the sum of the backgrounds (colored histogram).	124

6.6	p_T distributions for the leading jet using the default (left) and optimized (right) event selections for all channels combined.	125
6.7	p_T distributions for the subleading jet using the default (left) and optimized (right) event selections for all channels combined.	125
6.8	p_T distributions for lepton-jet centrality ζ using the default (left) and optimized (right) event selections for all channels combined.	126
6.9	Projections of the statistical (black), theoretical (blue), systematic (yellow), and total (red) uncertainties on the measured cross section as a function of integrated luminosity using the optimized event selection.	128
6.10	Dijet azimuthal separation ($ \Delta\phi_{jj} $) for the low m_{jj} region ($520 < m_{jj} < 1100$ GeV, top) and the high m_{jj} region ($m_{jj} > 1100$ GeV, bottom). The purely longitudinal (LL, gray) is plotted separately from the mixed and transverse (LT+TT, cyan) polarizations.	129
6.11	Projections of the expected longitudinal scattering significance as a function of integrated luminosity when considering all sources of uncertainties (black) or only statistical uncertainties (red).	129
B.1	Number of truth particles within $\Delta R < 0.4$ of a selected muon or electron using the ATLAS standard TRUTH1 (left) and the custom TRUTH1++ (right) derivations in $t\bar{t}$ simulation. The complete truth record is stored in the TRUTH1++ derivation, and this is best seen in the first bin, where the lepton has no nearby truth particles.	135
B.2	Leading lepton p_T distribution. The default and optimized cuts are represented by the red and green dashed lines, respectively. The $W^\pm W^\pm jj$ EWK signal (black points) is normalized to the same area as the sum of the backgrounds (colored histogram).	139
B.3	Dilepton invariant mass distribution. The default and optimized cuts are represented by the red and green dashed lines, respectively. The $W^\pm W^\pm jj$ EWK signal (black points) is normalized to the same area as the sum of the backgrounds (colored histogram).	139
B.4	Dijet invariant mass distribution. The default and optimized cuts are represented by the red and green dashed lines, respectively. The $W^\pm W^\pm jj$ EWK signal (black points) is normalized to the same area as the sum of the backgrounds (colored histogram).	140

Preface

This thesis presents the major highlights of my work with the ATLAS experiment as a graduate student at the University of Pennsylvania from Fall of 2013 until early Spring of 2019.

The first step of working on the experiment is to complete a *qualification task* in order to be included on the author list of ATLAS publications. These tasks are an opportunity to contribute to the experiment as a whole, such as maintaining detector hardware or monitoring physics performance. For my qualification task, I worked with the Inner Detector Alignment group which works to make sure we have accurate knowledge of the locations of each and every sensor in the tracking detector. My qualification task involved investigating a possible momentum bias in the Monte Carlo (MC) simulated data. The MC is supposed to be reconstructed with a perfect detector geometry and should in principle be free of any momentum biases. Ultimately I determined that the size of the biases were small enough to be negligible compared to what is seen in the real data, and that they could be corrected for if necessary.

My work with the alignment group would continue for the duration of my time here at Penn. In early 2015, at the start of the LHC’s second data-taking run (Run 2), I assisted with the validation of the first set of alignment constants using $\sqrt{s} = 13$ TeV proton-proton collision data. At this point I took over the responsibility of alignment of the TRT subdetector. The TRT was aligned to high accuracy in Run 1, and over the course of my time working on alignment, the TRT never required a straw-by-straw alignment; however it did require a module-level alignment at the end of 2015. My final responsibility in the alignment group was monitoring momentum biases using the energy-momentum ratio (E/p) of electrons. For the large data reprocessing, the E/p method served as a cross check to a similar method using Z boson events for monitoring and aligning out momentum biases in the detector. The results from both methods were also used in the uncertainties for the tracking measurements.

On the analysis side, I had previous experience in Standard Model (SM) electroweak physics from my time as an undergraduate at Duke University, and it remained a point of interest for me in graduate school. As such, I was happy to work with fellow Penn students on the cross section measurement of SM WZ diboson production with the early $\sqrt{s} = 13$ TeV ATLAS data. My contribution to the analysis was primarily on the software side, as I maintained and updated the analysis framework. While the WZ measurement is not covered by this thesis, it provided me with invaluable analysis experience in electroweak physics, as well as a detailed understanding of a major background to many diboson processes. The results for this analysis can be found published in Physics Letters B in 2016 [1].

The final two analyses I worked on involved the scattering of same-sign W bosons, and they make up the majority of this thesis. The first analysis is a measurement of the $W^\pm W^\pm jj$ cross section at $\sqrt{s} = 13$ TeV. This measurement along with that of the CMS collaboration represent the first observation of the $W^\pm W^\pm jj$ scattering process. My primary contribution to the analysis was in the estimation of the fake lepton background, where we implemented a brand new version of the fake-factor method using particle isolation variables. I also did a preliminary study of the interference between electroweak and strong production of $W^\pm W^\pm jj$ events, assisted in the production of data samples for use with the analysis framework, and used my familiarity with the WZ process to optimize the rejection of this background. Ultimately the results of this optimization were not included in the final result; however, it is still covered in the thesis in the hopes that it will be useful for similar analyses in the future. The measurement was presented at the XXXIX International Conference on High Energy Physics (ICHEP 2018) in Seoul, Korea [2], and a final publication is expected to be submitted soon.

The second $W^\pm W^\pm jj$ analysis is a study on the prospects for a measurement of the process at the upgraded High-Luminosity LHC, scheduled to begin operation in 2026. Here my main contribution was an optimization of the event selection using a Random Grid Search algorithm. Through the optimization we expect to take advantage of the higher center of mass energy and greater volume of data and tighten certain selection cuts to increase the strength of the $W^\pm W^\pm jj$ signal. In addition, I once again maintained and updated the analysis framework and produced the group's data samples, and I also developed a truth-based particle isolation criteria in order to reduce contributions from backgrounds involving the top quark. The results of this prospects study are published as a part of the annual Yellow Report for the High-Luminosity LHC [3].

Will K. DiClemente

Philadelphia, April 2019

CHAPTER 1

Introduction

The Large Hadron Collider (LHC) at CERN is the most powerful collider experiment in the world. At the time of its construction, the largest unanswered question in the Standard Model (SM) was the mechanism behind electroweak symmetry breaking (EWSB). As a result, one of the primary goals of the experiment is to learn as much as possible about this mechanism. Thus far, the LHC has succeeded in discovering a particle consistent with the long-awaited Higgs boson. In addition, measurements of many SM processes have been performed for the first time, or at better precision than before, thanks to the high collision energy and large volume of data collected by the LHC.

Processes involving the scattering of two massive electroweak (EWK) gauge bosons are of particular interest at the LHC for two main reasons. Firstly, they allow for tests of the self-interactions predicted by the EWK gauge theory through triple and quartic gauge couplings. While the triple couplings have been studied by previous experiments as well as at the LHC, the quartic couplings of the massive gauge bosons have not been accessible previously. Thus, processes involving these couplings can be measured and compared to the SM predictions for the first time. Secondly, the scattering of two massive gauge bosons is sensitive to the underlying EWSB mechanism. The W^\pm and Z bosons are given non-zero masses—and consequently a longitudinal polarization mode—through the Higgs mechanism, and thus their interactions serve as a direct probe of the symmetry breaking sector.

This thesis presents two separate analyses dealing with the scattering of two same-sign¹ W bosons with the LHC’s ATLAS experiment. The $W^\pm W^\pm jj$ process is a particularly interesting one: it has access to the $WWWW$ quartic gauge coupling, production modes that involve the exchange of a Higgs boson, and relatively low backgrounds. Evidence of EWK $W^\pm W^\pm jj$ production was first seen

¹*Same-sign* refers to both bosons having the same electric charge.

by the ATLAS and CMS experiments at $\sqrt{s} = 8$ TeV; however, the data set was too small to claim observation of the process. The first analysis covered here is the follow up to the above ATLAS measurement, measuring the EWK fiducial cross section at $\sqrt{s} = 13$ TeV with a larger data sample. The second analysis explores the prospects for future measurements of the $W^\pm W^\pm jj$ process at the planned High-Luminosity LHC (HL-LHC). The prospects for a measurement of the production cross section as well as sensitivity to the purely longitudinal component of the $W^\pm W^\pm$ scattering is presented.

In addition to the SM measurements, a part of this thesis is devoted to alignment of the detector components making up ATLAS’s Inner Detector (ID). Precise knowledge of the locations of detector elements is essential for accurate particle track reconstruction, which in turn results in improved resolutions for physics measurements. The ATLAS alignment algorithm determines the positions of each ID sensor through minimizing the distance between reconstructed particle tracks and the true hit position within the sensor. Special emphasis is given to the monitoring of momentum biases that may exist in the ID even after alignment.

The first few chapters of this thesis are intended to provide context for the main topics. Chapter 2 gives a brief introduction to the Standard Model with a focus on the EWSB mechanism and vector boson scattering. The experimental apparatus—the LHC and the ATLAS detector—are detailed in Chapter 3. The next three chapters present the main body of work. Chapter 4 covers the alignment of the ATLAS Inner Detector. Chapters 5 and 6 detail the ATLAS $\sqrt{s} = 13$ TeV $W^\pm W^\pm jj$ cross section measurement and the $\sqrt{s} = 14$ TeV HL-LHC $W^\pm W^\pm jj$ prospects study, respectively.

CHAPTER 2

Theoretical Framework

This chapter outlines the theoretical groundwork for the rest of the thesis. An overview of the Standard Model of particle physics (SM) is given in Section 2.1, followed by the electroweak symmetry breaking mechanism involving the Higgs boson in Section 2.2. Finally, Section 2.3 will go into detail on the interests of electroweak vector boson scattering (VBS).

2.1 Introduction to the Standard Model

The Standard Model of particle physics serves as a mathematical description of the fundamental particles of the universe and their interactions. It has been developed over the course of the past century, incorporating both predictions from theory and results from experiments. All in all, the SM has proven to be very accurate in describing the particle interactions seen in experiments, as can be seen in the summary plot in Figure 2.1 comparing ATLAS measurements to their SM predictions.

The SM is a quantum field theory (QFT) [5, 6] in which the fundamental particles are represented as excited states of their corresponding fields. The spin- $\frac{1}{2}$ fermionic fields give rise to the quarks and leptons comprising ordinary matter, the spin-1 fields correspond to the electroweak bosons and the gluon which mediate the electroweak and strong forces, respectively, and finally the scalar Higgs field is responsible for electroweak symmetry breaking. The excitations and interactions of the fields are governed by the SM Lagrangian, which is invariant under local transformations of the group $SU(3) \times SU(2) \times U(1)$.

The first quantum field theory to be developed was quantum electrodynamics (QED) [7], which describes the electromagnetic interaction. The theory predicts the existence of a $U(1)$ gauge field that interacts with the electrically charged fermions. This field corresponds to the photon. A key

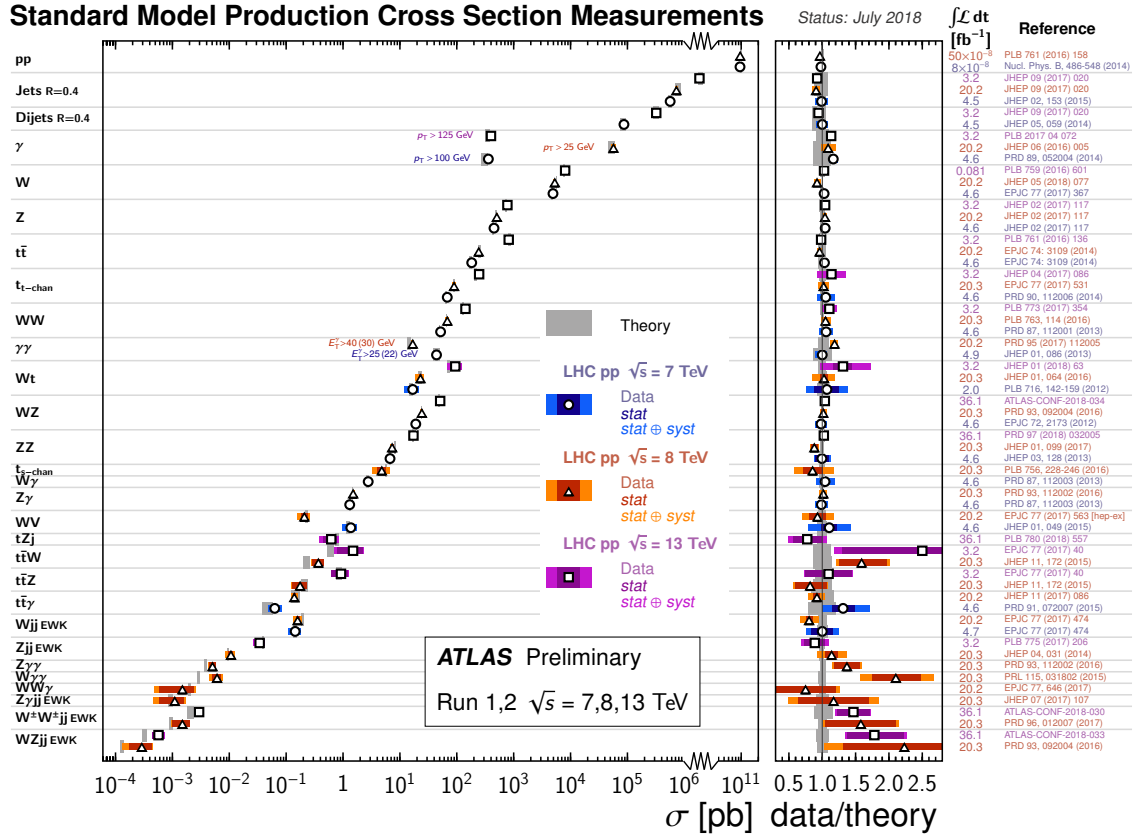


Figure 2.1: Summary of several Standard Model total and fiducial production cross section measurements compared to the corresponding theoretical predictions calculated at NLO or higher. The dark colored error bar represents the statistical uncertainty, and the light colored error bar represents the full uncertainty (including systematic and luminosity uncertainties). The data/theory ratio, luminosity used and reference for each measurement are also shown [4].

aspect of QED is that it is perturbative: the coupling constant $\alpha = e^2/4\pi$ is small, where e is electrical charge of the field, allowing for the use of perturbation theory in calculations. In this case, calculations can be written as a power series in α , where successive higher order terms contribute less to the final result. The accuracy of perturbative calculations is an essential tool for being able to make predictions from the SM.

The strong interaction—the theory of quarks and gluons—has also been described using QFT as quantum chromodynamics (QCD). The symmetry group for QCD is SU(3), and its eight generators correspond to the eight differently charged, massless gluons [8]. Unlike in QED, which has the familiar positive and negative electric charges, the strong force has three “colors”. Color charge

combined with the non-Abelian nature of $SU(3)$, which allows the gluons to interact with each other, result in the most well-known property of QCD: color confinement. In order to increase the separation between two color-charged quarks, the amount of energy required increases until it becomes energetically favorable to pair-produce a new quark-antiquark pair, which then bind to the original quarks. The end result of this is that only color-neutral objects exist in isolation. What this means for the strong coupling constant α_s is that its value at the low energies where confinement occurs is large, on the order of $\alpha_s \sim 1$. The consequence of this is that perturbation theory cannot be used to approximate these interactions. While this appears at first to be a critical problem for prediction, fortunately it turns out that α_s “runs”, or decreases in magnitude at higher energy [9, 10]. This so-called “asymptotic freedom” allows QCD to be calculated perturbatively [11] at energies accessible by collider experiments including the LHC.

The last gauge field corresponds to the weak interaction. Ultimately, the weak $SU(2)$ and the electromagnetic $U(1)$ mix to form the $SU(2) \times U(1)$ *electroweak* (EWK) interaction [12, 13]. A more detailed description of the mixing will be discussed in conjunction with electroweak symmetry breaking (EWSB) in Section 2.2; however, a summary of the resulting EWK interaction is presented here, at the risk of some repeated information to follow. There are three weak isospin bosons arising from the $SU(2)$ group (W_μ^1 , W_μ^2 , and W_μ^3) and one weak hypercharge boson from the $U(1)$ group (B_μ). The W_3 and B bosons mix according to the weak mixing angle θ_W to form the Z boson and the photon according to

$$\begin{pmatrix} \gamma \\ Z \end{pmatrix} = \begin{pmatrix} \cos \theta_W & \sin \theta_W \\ -\sin \theta_W & \cos \theta_W \end{pmatrix} \begin{pmatrix} B_\mu \\ W_\mu^3 \end{pmatrix}. \quad (2.1)$$

The value of θ_W is not predicted by the SM; it is one example of an experimental input to the theory, measured to be $\sin^2 \theta_W = 0.23153 \pm 0.00016$ [14]. The charged W^\pm bosons are a mixture of the remaining W_μ^1 and W_μ^2 bosons:

$$W^\pm = \frac{1}{\sqrt{2}}(W_\mu^1 \mp iW_\mu^2). \quad (2.2)$$

Unlike the photon (and the gluon of QCD), the W^\pm and Z bosons are massive. This means that even though $SU(2)$ is non-Abelian, the range of interaction is short and confinement does not occur. Lastly, the EWK interaction is chiral, only coupling to the left-handed component of the fermion fields.

One final field remains within the SM: the scalar Higgs field. It was originally proposed in the 1960’s to explain the masses of the W^\pm and Z bosons [15, 16, 17] and is the mechanism for the

EWSB process. The particle associated with the field is a massive scalar boson, the Higgs boson, which was recently discovered by ATLAS and CMS in 2012 [18, 19] with a mass of 125 GeV.

2.2 Electroweak symmetry breaking and the Higgs boson

The results of electroweak mixing and the implications of the Higgs field have been introduced in the previous section. If the EWK theory were an unbroken symmetry, the associated W^\pm and Z bosons would be massless; however, when first observed experimentally [20, 21], they were found to be quite heavy; currently, their masses are known to be approximately 80 GeV and 91 GeV, respectively [22]. The following presents the Higgs mechanism, including how it “spontaneously breaks” the EWK symmetry, resulting in the massive W^\pm and Z bosons and the massless photon.

Beginning by writing the Higgs field as a complex scalar doublet

$$\phi = \begin{pmatrix} \phi^+ \\ \phi^0 \end{pmatrix} = \sqrt{\frac{1}{2}} \begin{pmatrix} \phi_1 + i\phi_2 \\ \phi_3 + i\phi_4 \end{pmatrix}, \quad (2.3)$$

a simple Lagrangian \mathcal{L} can be written as

$$\mathcal{L} = (\mathcal{D}_\mu \phi)^\dagger (\mathcal{D}^\mu \phi) - \mu^2 \phi^\dagger \phi - \lambda(\phi^\dagger \phi)^2, \quad (2.4)$$

where $\lambda > 0$ and μ^2 are constants (the sign of μ^2 will be addressed shortly). \mathcal{D}_μ is the covariant derivative defined such that \mathcal{L} is invariant under a local $SU(2) \times U(1)$ gauge transformation:

$$\mathcal{D}_\mu \phi = \left(\partial_\mu + \frac{ig}{2} \tau_a W_\mu^a + \frac{ig'}{2} B_\mu \right) \phi. \quad (2.5)$$

Here, W_μ^a ($a = 1, 2, 3$) are the $SU(2)$ fields with generators τ_a and coupling constant g , and B_μ is the $U(1)$ field with coupling constant g' .

Isolating the Lagrangian’s potential term,

$$V(\phi) = \mu^2 \phi^\dagger \phi + \lambda(\phi^\dagger \phi)^2, \quad (2.6)$$

a choice must be made on the sign of μ^2 . The case of interest is when $\mu^2 < 0$, which results in the so-called “Mexican hat potential” shown in Figure 2.2. The potential is minimized along the collection of points

$$\phi^\dagger \phi = \frac{1}{2} (\phi_1^2 + \phi_2^2 + \phi_3^2 + \phi_4^2) = -\frac{\mu^2}{2\lambda}. \quad (2.7)$$

This means that the minimum of the potential is not at $\phi = 0$ (as it would be in the case where $\mu^2 > 0$), but rather at a value

$$v \equiv \sqrt{-\frac{\mu^2}{\lambda}}. \quad (2.8)$$

With no loss of generality due to the SU(2) symmetry, $\phi_1 = \phi_2 = \phi_4 = 0$ can be imposed on Equation 2.7, leaving $\phi_3^2 = v^2$. Finally, the *vacuum expectation value* (VEV) of the field can be written:

$$\langle \phi \rangle = \sqrt{\frac{1}{2}} \begin{pmatrix} 0 \\ v \end{pmatrix}. \quad (2.9)$$

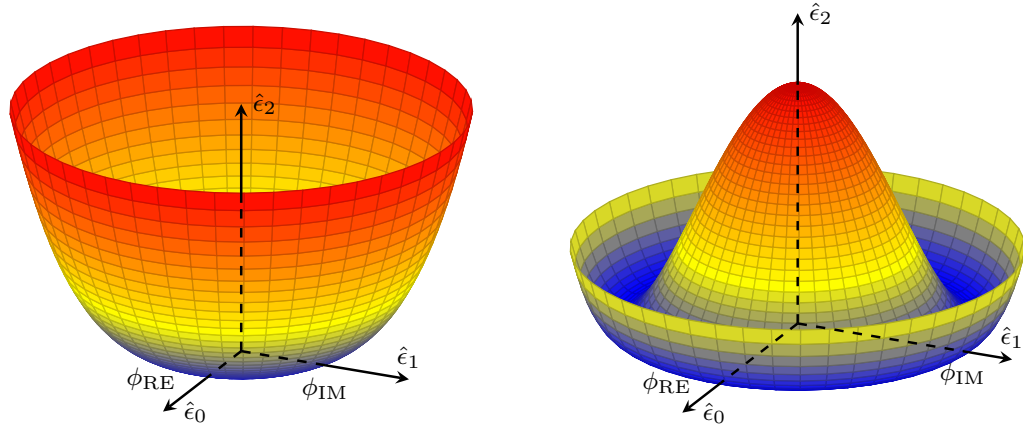


Figure 2.2: An illustration of the potential term $V(\phi)$ in Equation 2.6 for the cases where $\mu^2 > 0$ (left) and $\mu^2 < 0$ (right). The right-hand plot shows the Higgs potential, or ‘‘Mexican hat potential’’, with the minimum at $|\phi| = \sqrt{-\frac{\mu^2}{\lambda}}$ rather than at $|\phi| = 0$ as in the left-hand plot.

The VEV can be substituted back into the original Lagrangian of Equation 2.4, and, following quite a bit of math [23], a collection of mass terms can be identified:

$$\mathcal{L} \subset \mathcal{L}_M \equiv \frac{1}{8}v^2g^2 \left[(W_\mu^1)^2 + (W_\mu^2)^2 \right] + \frac{1}{8}v^2 \left[g^2(W_\mu^3)^2 - 2gg'W_\mu^3B^\mu + g'^2(B_\mu)^2 \right]. \quad (2.10)$$

Focusing on the first term for the moment, if Equation 2.2 for the physical W^\pm bosons is substituted in, the mass term becomes

$$M_W^2 W^+ W^- = \left(\frac{1}{2}vg \right)^2 W^+ W^-, \quad (2.11)$$

which then simplifies to

$$M_W = \frac{1}{2}vg. \quad (2.12)$$

With a bit of clever forward-thinking, the second term of Equation 2.10 can be rewritten as

$$\frac{1}{8}v^2 \left[gW_\mu^3 - g'B_\mu \right]^2 + 0 \left[g'W_\mu^3 - gB_\mu \right]^2 = \frac{1}{2}M_Z^2 Z_\mu^2 + \frac{1}{2}M_A^2 A_\mu^2, \quad (2.13)$$

where Z_μ^2 and A_μ^2 represent the physical Z boson and photon, respectively:

$$Z_\mu = \frac{gW_\mu^3 - g'B_\mu}{\sqrt{g^2 + g'^2}} \quad (2.14)$$

$$A_\mu = \frac{g'W_\mu^3 - gB_\mu}{\sqrt{g^2 + g'^2}}. \quad (2.15)$$

From this, it can be seen that the photon is massless ($M_A = 0$ in Equation 2.13), and the mass of the Z boson is identified as

$$M_Z = \frac{1}{2}v\sqrt{g^2 + g'^2}. \quad (2.16)$$

Lastly, the Higgs field can couple directly to the fermions. Taking the electron as an example, an additional Lagrangian term can be written:

$$\mathcal{L}_e = -G_e[\bar{e}_L\phi e_R + \bar{e}_R\phi^\dagger e_L], \quad (2.17)$$

where e_L and e_R are the left-handed doublet and right-handed singlet, respectively, and ϕ is as in Equation 2.3. The symmetry can be spontaneously broken by a perturbation about the VEV of the form

$$\phi = \sqrt{\frac{1}{2}} \begin{pmatrix} 0 \\ v + h(x) \end{pmatrix}. \quad (2.18)$$

\mathcal{L}_e then becomes

$$\begin{aligned} \mathcal{L}_e &= -\frac{G_e}{\sqrt{2}}v(\bar{e}_L e_R + \bar{e}_R e_L) - \frac{G_e}{\sqrt{2}}(\bar{e}_L e_R + \bar{e}_R e_L)h \\ &= -m_e \bar{e}e - \frac{m_e}{v} \bar{e}eh, \end{aligned} \quad (2.19)$$

which gives a value for the electron mass of $m_e = \frac{G_e v}{\sqrt{2}}$. From the second term above, it can be seen that the strength of the Higgs coupling to the electron is proportional to the mass of the electron. The rest of the fermion couplings follow from this example.

What is accomplished here is quite remarkable. The weak and electromagnetic interactions have been unified into a single $SU(2) \times U(1)$ interaction, and the physical bosons observed in nature arise as mixtures of the four gauge fields. Three of the four degrees of freedom in the scalar field ϕ of Equation 2.3, are absorbed (or “eaten”) by the W^\pm and Z bosons, giving them a longitudinal polarization mode corresponding to a massive particle, and the fourth generates the Higgs boson. This process is summarized in Figure 2.3. Additionally, it is shown that the Higgs couples to fermions in proportion to their mass. From experimental measurements, the value of the VEV has been determined to be $v \approx 246$ GeV [22]. However, it should be noted that the theory does not predict the mass of the Higgs boson or of the fermions; these must all be determined from experiment.

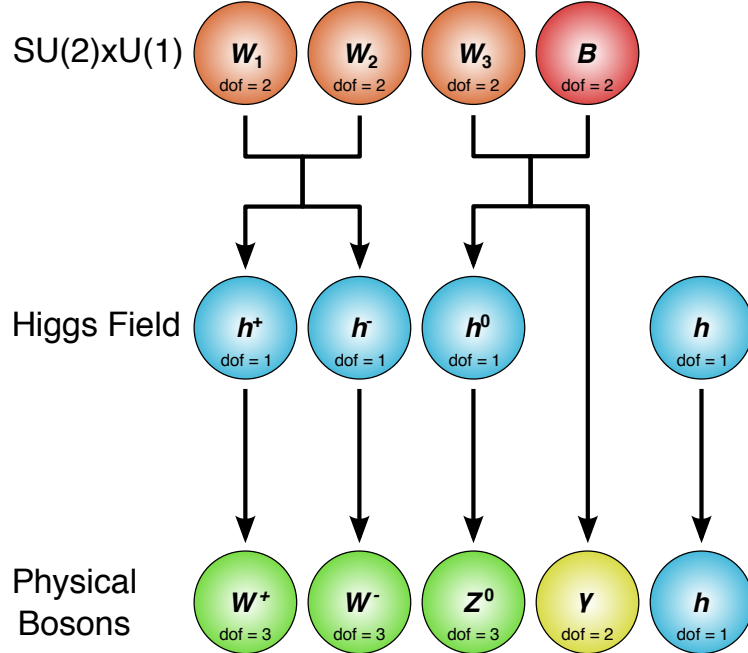


Figure 2.3: A graphical representation of the EWSB mechanism involving the $SU(2) \times U(1)$ bosons. The W^\pm and Z bosons each obtain mass by eating a degree of freedom (dof) from the Higgs field, and in the process gain a longitudinal polarization mode, while the photon stays massless (with two dof) and the SM Higgs boson h remains.

2.3 Electroweak vector boson scattering

Due to the non-Abelian nature of the EWK interaction, the associated gauge bosons are allowed to self-interact. This results in triple and quartic couplings of gauge bosons (TGCs and QGCs, respectively). The SM allowed TGCs are the $WW\gamma$ and WWZ vertices, which can be measured experimentally via diboson production or through vector boson fusion (VBF). The QGCs predicted by the SM are $WWZ\gamma$, $WW\gamma\gamma$, $WWZZ$, and $WWWW$, and these vertices are accessible via triboson production or vector boson scattering (VBS)² [24]. VBS processes are defined by a $VV \rightarrow VV$ signature, where V represents one of the EWK gauge bosons (W^\pm , Z , or γ), as shown in Figure 2.4. The actual interaction between the incoming and outgoing vector bosons can be mediated by the exchange of a virtual V , directly via a QGC (both are shown in Figure 2.5), or by the exchange of a Higgs boson (as in Figure 2.6).

As detailed in the previous section, the Higgs mechanism produces three Goldstone bosons and a

²Vector boson fusion and scattering typically refer to the s -channel and t -channel exchanges of a vector boson, respectively; however, often both are used interchangeably to describe the $VV \rightarrow VV$ process. Therefore, for the remainder of this thesis, *vector boson scattering* will refer to both the VBF and VBS production mechanisms.

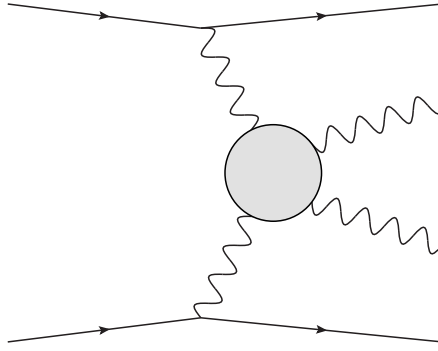


Figure 2.4: Feynman diagram of a generic VBS process. The gray circle represents any interaction with two incoming and two outgoing vector bosons, including any of the diagrams shown in Figures 2.5 and 2.6.

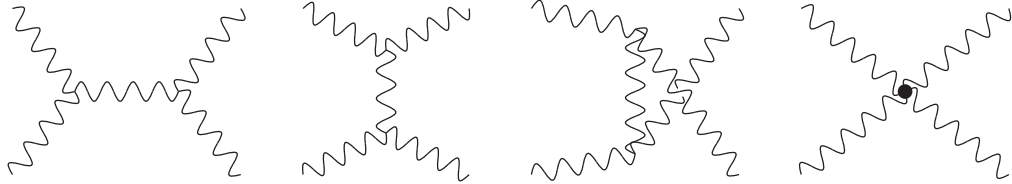


Figure 2.5: Leading order $VV \rightarrow VV$ Feynman diagrams involving EWK bosons. From left to right: s -channel, t -channel, u -channel, and the quartic gauge coupling.

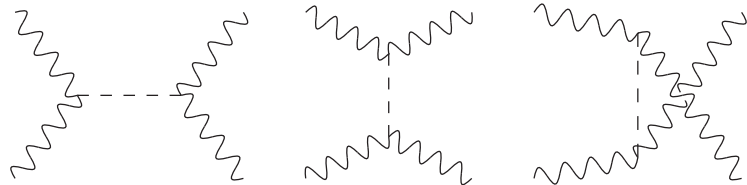


Figure 2.6: Leading order $VV \rightarrow VV$ Feynman diagrams involving the exchange of a Higgs boson. From left to right: s -channel, t -channel, and u -channel.

Higgs boson. The Goldstone bosons are then “eaten” by the physical gauge bosons, giving them mass and consequently a longitudinal polarization³. In fact, according to the Electroweak Equivalence Theorem, the high-energy interactions of longitudinal gauge bosons can be accurately described by the Goldstone bosons of the EWSB mechanism [25]. Thus, the scattering of the massive gauge bosons is inextricably linked to EWSB.

It turns out that without a light SM Higgs boson, the scattering amplitude of longitudinally

³A massless spin-1 boson can have one of two transverse polarization states, while a massive spin-1 boson can also be longitudinally polarized. As a result, only the massive W^\pm and Z bosons, and not the massless photon, are sensitive to EWSB.

polarized vector bosons grows with center-of-mass energy and ultimately violates unitarity above $\sqrt{s} \approx 1.2$ TeV [26, 27]. The equations for the two transverse (ϵ_{\pm}^{μ}) and longitudinal (ϵ_L^{μ}) polarization vectors of a gauge boson of mass M_V can be written as

$$\epsilon_{\pm}^{\mu} = \frac{1}{\sqrt{2}}(0, 0, \pm i, 0) \quad (2.20)$$

and

$$\begin{aligned} \epsilon_L^{\mu} &= \frac{1}{M_V}(|\vec{p}|, 0, 0, E) \\ &= \frac{p^{\mu}}{M_V} + v^{\mu}, \end{aligned} \quad (2.21)$$

where v^{μ} is of the order M_V/E and becomes small in the high energy limit [28]. From this, it can be seen that ϵ_L^{μ} grows with the momentum of the boson p^{μ} . Thus, the dominant contribution to the VBS process at high energy comes from the longitudinally polarized gauge bosons [29].

The high-energy behavior of longitudinally polarized vector boson scattering can be explored in the case of opposite-sign $W^+W^- \rightarrow W^+W^-$ scattering. In the high-energy limit ($s \gg M_W^2, M_H^2$), the amplitude of W^+W^- scattering without considering the Higgs contributions (the appropriate diagrams from Figure 2.5) can be written as

$$\mathcal{M}_{\text{gauge}} = -\frac{g^2}{4M_W^2}u + \mathcal{O}\left(\left[\frac{E}{M_W}\right]^0\right), \quad (2.22)$$

where g is the EWK coupling and u is one of the Mandelstam variables [27]. The $\mathcal{O}(E^4)$ terms cancel out between the TGC and QGC diagrams [29]. What is left is an amplitude proportional to E^2 that diverges as $E/M_W \rightarrow \infty$. However, the amplitude from the diagrams involving the Higgs boson (the relevant diagrams from Figure 2.6) is

$$\mathcal{M}_{\text{Higgs}} = -\frac{g^2}{4M_W^2} \left[\frac{(s - M_W^2)^2}{s - m_H^2} + \frac{(t - M_W^2)^2}{t - M_H^2} \right], \quad (2.23)$$

which reduces to

$$\mathcal{M}_{\text{Higgs}} = \frac{g^2}{4M_W^2}u + \mathcal{O}\left(\left[\frac{E}{M_W}\right]^0\right) \quad (2.24)$$

in the high-energy limit. Adding the two equations together cancels out the E^2 term and leaves only terms constant in energy. Therefore, with a SM Higgs, the scattering amplitude for longitudinally polarized W bosons no longer diverges. Plots of the cross section of several $VV \rightarrow VV$ scattering processes are shown in Figure 2.7 with and without a SM Higgs boson.

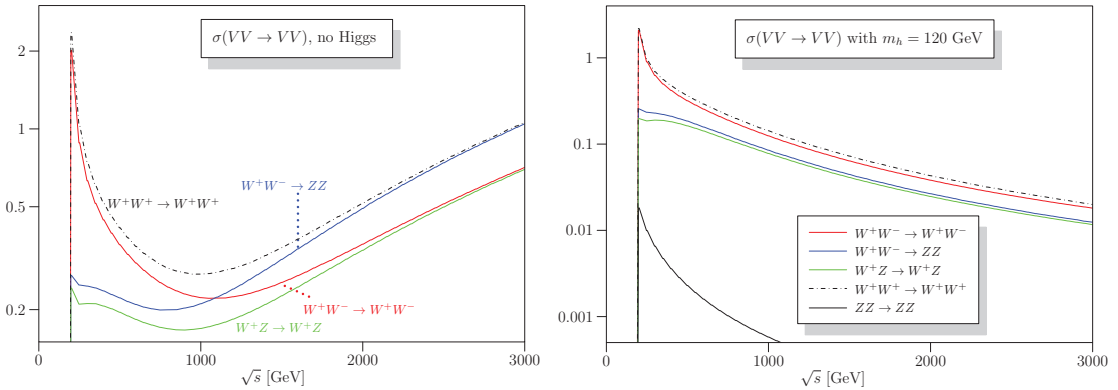


Figure 2.7: Cross sections in nanobarns for five different longitudinally polarized VBS processes as a function of center of mass energy \sqrt{s} . Without a Higgs boson (left), the cross sections grow unbounded with \sqrt{s} . With a 120 GeV Higgs boson (right), the cross sections no longer diverge. Plots taken from [30].

CHAPTER 3

LHC and the ATLAS Detector

This chapter covers the experimental apparatus relevant to this thesis: the Large Hadron Collider (LHC) and the ATLAS detector in Sections 3.1 and 3.2, respectively. Some time is taken in Section 3.3 to overview the methods used to identify and measure various particle types within ATLAS.

3.1 The Large Hadron Collider

The Large Hadron Collider (LHC) [31] is the most powerful particle accelerator in the world, colliding two beams of protons at a center of mass energy of $\sqrt{s} = 13$ TeV. It is operated by the European Organization for Nuclear Research (CERN) and consists of a 27 km ring located beneath the France–Switzerland border. A chain of smaller accelerators incrementally boost the protons⁴ up to higher and higher energies before they reach the final collision energy within the main LHC ring. Collisions occur at each of four detector experiments situated around the ring: ATLAS [32], ALICE [33], CMS [34], and LHCb [35].

Protons are obtained from hydrogen atoms stripped of their electrons by an electric field. A beam of protons is first accelerated up to 50 MeV in the Linac 2 accelerator, then to 1.4 GeV in the Proton Synchrotron Booster (PSB), 25 GeV in the Proton Synchrotron (PS), and finally to 450 GeV in the Super Proton Synchrotron (SPS). Two beams are then injected into the LHC ring in running in opposite directions where they accelerate up to the collision energy of 6.5 TeV. Each consists of bunches containing on the order of 10^{11} protons separated by 25 ns [36]. A schematic of the CERN accelerator complex, including the chain of accelerators mentioned above, is shown in Figure 3.1.

⁴The LHC can also collide beams of heavy ions; however, this thesis focuses exclusively on the proton-proton collisions.

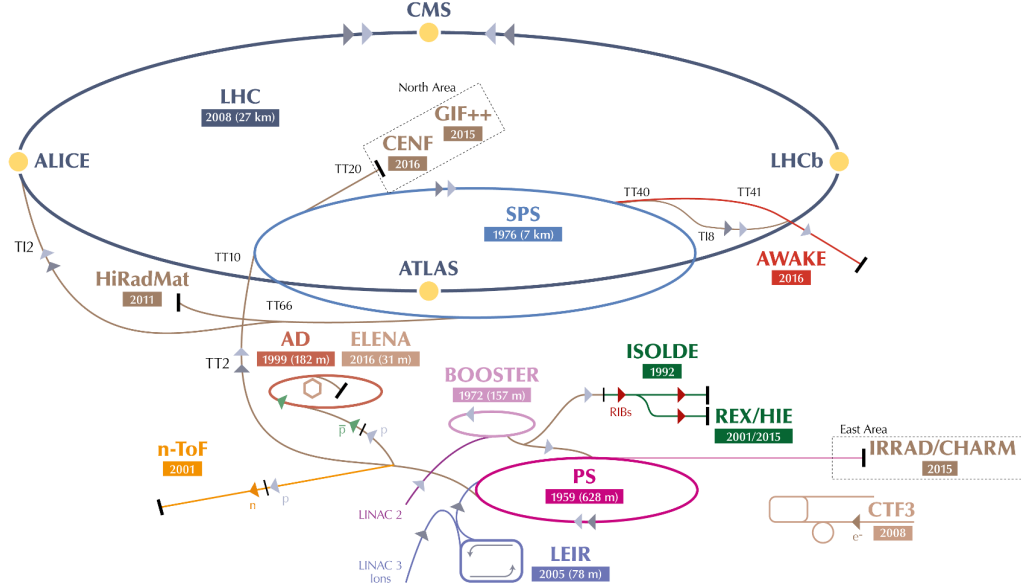


Figure 3.1: The CERN accelerator complex. For LHC collisions, protons are accelerated by the Linac 2 (purple), the PSB (light purple), the PS (magenta), and the SPS (light blue) before entering the LHC ring (dark blue) [37].

In addition to a high center of mass energy, the LHC must also deliver enough data to measure rare processes. The amount of data collected is measured in terms of *luminosity*. The instantaneous luminosity \mathcal{L} is defined in terms of the number of events per second $\frac{dR}{dt}$ and the production cross section σ_p :

$$\mathcal{L} = \frac{1}{\sigma_p} \frac{dR}{dt}. \quad (3.1)$$

The calculation itself can be quite tricky, as it depends on a number of factors including the number of particles per bunch, the spread of the beam, and the crossing angle of the beams [38].

The LHC was originally designed to operate at an instantaneous luminosity of $1.0 \times 10^{34} \text{ cm}^{-2}\text{s}^{-1}$; however, this number was exceeded by the end of the 2016 data taking period, with a peak luminosity of $1.38 \times 10^{34} \text{ cm}^{-2}\text{s}^{-1}$. By the end of Run 2 in December 2018, the LHC was running at more than twice the design luminosity [39]. The instantaneous luminosity of proton-proton collisions as a function of time in 2015 and 2016 are shown in Figure 3.2.

The total amount of data collected is reported in terms of *integrated* luminosity, which is simply the time integral of the instantaneous luminosity. By the end of Run 2 (2015-2018), approximately 140 fb^{-1} of 13 TeV data collected by the ATLAS detector is available for physics, as shown in Figure 3.3. The 36.1 fb^{-1} collected during the first two years (2015 and 2016) is used for the

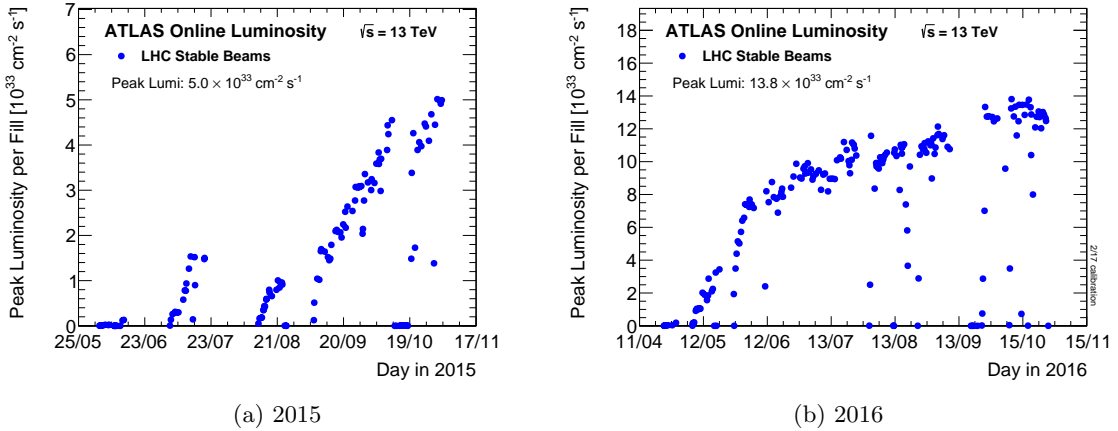


Figure 3.2: Peak instantaneous luminosity delivered to ATLAS during 13 TeV pp data taking as a function of time [39].

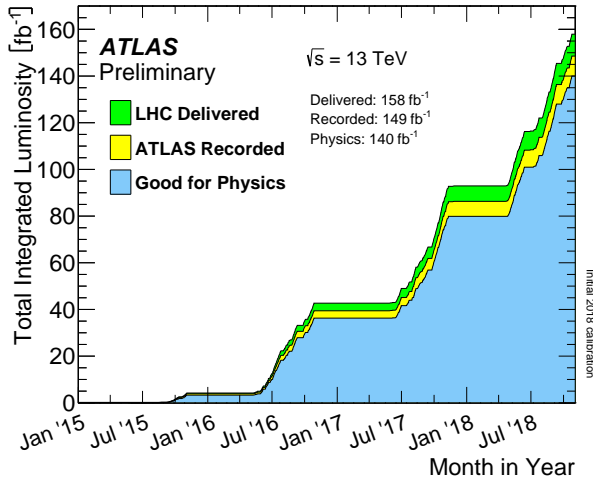


Figure 3.3: Integrated luminosity collected by ATLAS as a function of time at 13 TeV from 2015-2018 [39].

analysis later in this thesis.

Due to the high instantaneous luminosity, more than one pp interaction occurs in a single bunch crossing, referred to as *pileup*. During the 2016 data taking campaign, the average number of interactions per bunch crossing $\langle\mu\rangle$ was approximately 24 but has increased to upwards of 37 in 2017 and 2018 [39]. Figure 3.4 contains the average μ for the 2015-2016 data set used for analysis in this thesis. The high pileup is a challenge for accurately reconstructing an individual collision.

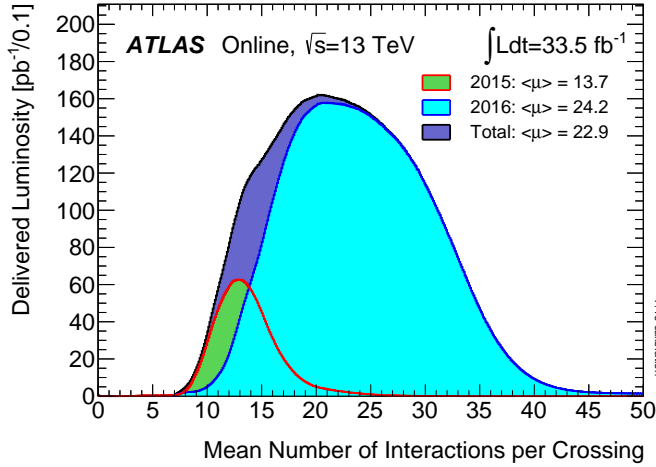


Figure 3.4: Distribution of the mean number of interactions per bunch crossing for the 2015 and 2016 pp collision data at 13 TeV [39].

3.2 The ATLAS Detector

ATLAS (A Toroidal LHC ApparatuS) is a general-purpose particle detector. It contains several sub-detector systems designed to measure different types of particles. Starting from the beam line and working outwards, the Pixel Detector (PIX), Semiconductor Tracker (SCT), and Transition Radiation Tracker (TRT) make up the Inner Detector (ID) and are responsible for measuring the trajectories and momenta of charged particles. Next are two calorimeters, the Liquid Argon Calorimeter (LAr) and the Tile Calorimeter (TileCal), which stop electromagnetic and hadronic objects and measure their energies. Finally, the outermost Muon Spectrometer (MS) measures muon tracks as they leave the detector, as they are too heavy to be stopped by the calorimeters. The ATLAS detector and its subsystems are shown in Figure 3.5.

ATLAS uses a global, right-handed coordinate system with the origin at the center of the detector (the nominal interaction point). The x -axis points from the origin inwards to the center of the LHC ring, the y -axis points upwards, and the z -axis points along the beam line. Due to the azimuthal symmetry of the detector, it is useful to use cylindrical coordinates (r, ϕ) in the plane transverse to the z -axis, where ϕ is the azimuthal angle. Instead of using the polar angle θ to describe particle trajectories, pseudorapidity is used instead:

$$\eta = -\ln(\tan(\theta/2)). \quad (3.2)$$

Pseudorapidity has the useful property that differences in η are invariant under Lorentz boosts along

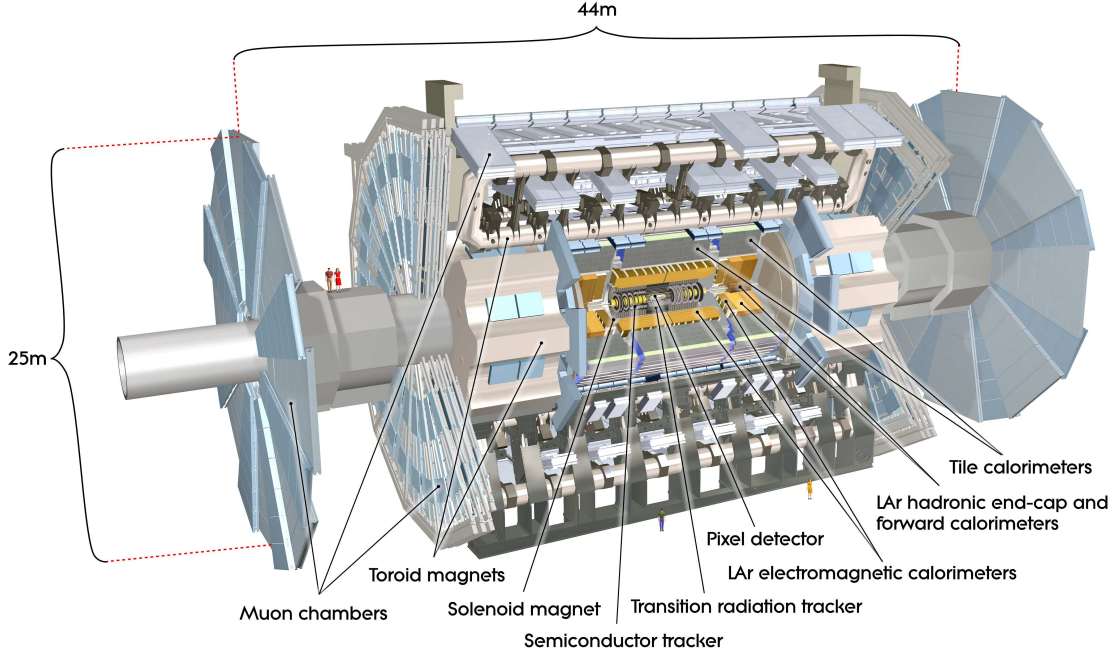


Figure 3.5: Cut-away view of the ATLAS detector [32].

the z -axis. The angular separation between two particles p_i and p_j is often expressed in terms of the quantity ΔR , defined as

$$\Delta R(p_i, p_j) = \sqrt{\Delta\eta_{i,j}^2 + \Delta\phi_{i,j}^2}, \quad (3.3)$$

where $\Delta\phi_{i,j} \in [-\pi, \pi]$ since ϕ is periodic in 2π and “wraps around” the detector in the azimuthal direction.

3.2.1 The Inner Detector

The ID [40, 41] is a tracking system that reconstructs the trajectories of charged particles. It spans just over a meter in radius, with the innermost layer of sensors at a radius of 33.25 cm from the beam line. Charged particles traveling through the ID leave *hits* in each sensor they pass through, and a *track* representing the path of the particle is fit to the hits according to the procedure outlined in Section 3.3.1. The ID’s pseudorapidity coverage extends out to $|\eta| < 2.5$. A solenoid magnet outside the ID produces a 2 T magnetic field that bends the particles, allowing for their momenta in the direction transverse to the field to be measured according to

$$p_T = q \cdot B \cdot r, \quad (3.4)$$

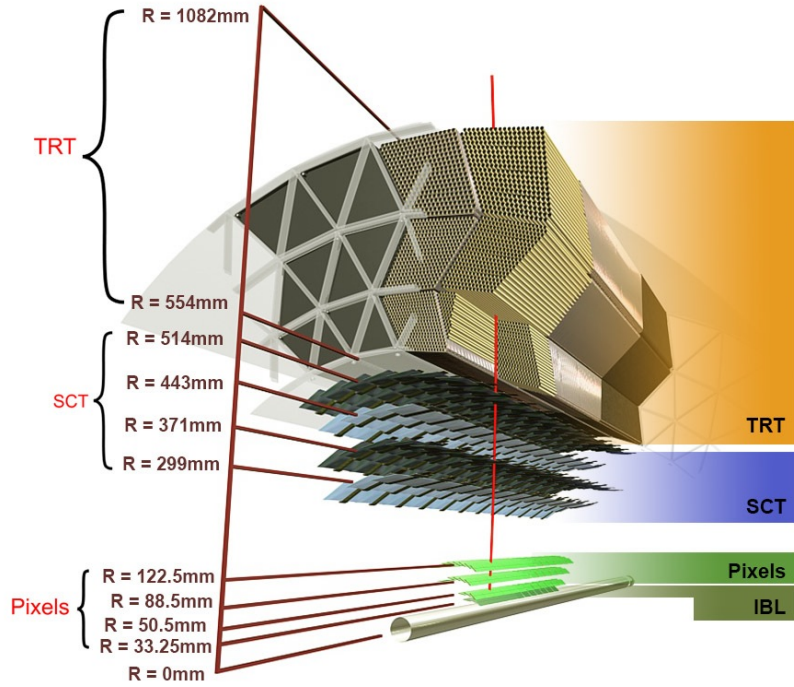


Figure 3.6: The barrel layers of the Pixel, SCT, and TRT detectors making up the Inner Detector. Figure taken from [42].

where q is the charge of the particle (± 1), B is the strength of the magnetic field, and r is the radius of the track's curvature. A cut-away view of the barrel region of the ID is shown in Figure 3.6.

3.2.1.1 Pixel Detector

The Pixel Detector consists of four cylindrical barrel layers⁵ and three endcap disks on either side. It is the innermost subdetector of the ID with coverage up to $|\eta| < 2.5$. The individual sensors measure $50 \mu\text{m} \times 400 \mu\text{m}$ and are installed on silicon wafers that make up the layers. All in all, there are 1744 wafers with 80 million readout channels. The sensors themselves are silicon semiconducting diodes that provide a signal when a charged particle passes through. The Pixel Detector has the finest resolution of all the ID subdetectors, at $10 \mu\text{m}$ in the $r\phi$ plane and $40 \mu\text{m}$ in the z direction.

During the upgrade period between Run 1 and Run 2, a new innermost layer was added to the Pixel detector barrel: the Insertable B-Layer (IBL) [43]. The IBL lies closest to the interaction point, at a radius of 33.25 cm from the beam line, and it is relied upon to provide high-precision

⁵For now, the outer three barrel layers will be covered in conjunction with the endcaps; the innermost layer will be described separately.

measurements close to the interaction point. Its addition allows better precision in detecting displaced vertices from b -jets, for example. The IBL consists of 280 silicon pixel modules arranged on 14 staves that run parallel to the beam line. Each stave consists of 12 two-chip planar modules in the middle ($|\eta| < 2.7$) with four 3D sensors [44] on either side ($2.7 < |\eta| < 3.0$). The IBL’s pixel sensors are $50 \mu\text{m} \times 250 \mu\text{m}$ in size and have a resolution of $10 \mu\text{m}$ in $r\text{-}\phi$ and $75 \mu\text{m}$ in z [45].

3.2.1.2 Semiconductor Tracker

The next subdetector of the ID is the SCT, which has four barrel layers and nine endcap disks per side which provide coverage up to $|\eta| < 2.5$. The SCT operates on the same principle as the Pixel Detector, but the sensitive elements are larger silicon “strips” placed on the wafers. This shape change assists in covering the larger surface area required by the increasing detector radius. Each detector layer is actually made up of two layers of wafers, placed back-to-back with an angle of 40 mrad between them. The resolution in the $r\text{-}\phi$ plane is very fine at $17 \mu\text{m}$, but, due to the strip shape, the resolution along z is rather poor at $580 \mu\text{m}$.

3.2.1.3 Transition Radiation Tracker

The outermost component of the ID is the TRT [46, 47, 48], which uses a completely different technology from the Pixel and SCT to identify particle hits. The TRT is unique in that it combines a drift tube tracker with transition radiation detection to assist with electron identification. The TRT’s sensitive elements are drift tubes (referred to as “straws”) that are 4 mm in diameter and consist of a cylindrical cathode with an anode wire running through the center. Each straw is filled with a gas mixture including xenon or argon which provides ionizing radiation when high energy particles pass through them. The resulting electrons drift to the anode and register a voltage, indicating a hit in the detector element.

Between the straws are polyethylene fibers in the barrel and polypropylene foil in the endcaps in order to encourage particles to emit transition radiation photons. These photons also ionize the gas within the straws, leading to a higher signal. The TRT takes advantage of the fact that lighter particles are more likely to emit transition radiation by using a ternary output: zero, low-threshold, and high-threshold. High-threshold hits are generally caused by electrons due to their low mass, and this can help in identifying electron tracks from backgrounds.

There are over 100,000 straws in the barrel of the TRT, and nearly 250,000 in the endcaps. The TRT provides pseudorapidity coverage up to $|\eta| < 2.0$ with a resolution in the $r\text{-}\phi$ plane of $130 \mu\text{m}$.

Since the drift tubes are insensitive along the direction of the wire, the TRT does not provide a measurement along the z direction.

3.2.2 The Calorimeters

ATLAS utilizes two different calorimeters, the Liquid Argon and Tile Calorimeters [49, 50], in order to measure electromagnetic and hadronic objects. The general principle behind both calorimeters is the same: an incoming particle showers as it passes through, eventually coming to a stop, and the resulting energy deposits are read out. Both are sampling calorimeters, which consist of alternating layers of a dense material to induce the showering (called the *absorber*) and a second material which measures the energy (called the *active material*). An advantage to this type of calorimeter is that a very dense absorber can be used in order to produce a shower in a limited space, even if it is unsuitable for measuring the energy from the shower. However, as a result, some of the energy is deposited in the absorbers, and the total shower energy must be estimated. ATLAS's calorimeter systems are shown in Figure 3.7.

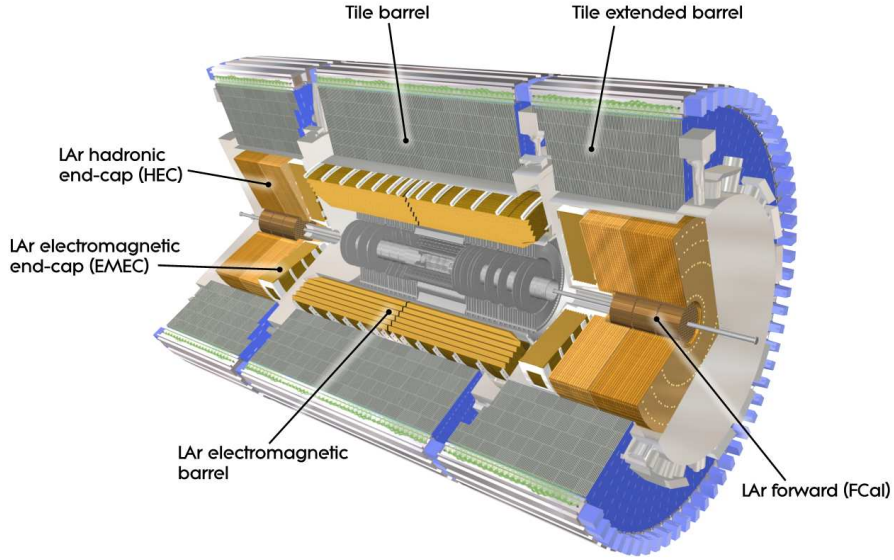


Figure 3.7: Cut-away view of the ATLAS calorimeter systems [51].

Electromagnetic objects, such as electrons and photons, shower via cascades of bremsstrahlung photons and e^+e^- pairs. The radiation length X_0 is defined as the mean distance over which an electron's energy is reduced to $1/e$ of its original value, or $E(x) = E_0 e^{-x/X_0}$. The majority of the

shower energy is deposited in the first few radiation lengths. The longitudinal shower depth scales logarithmically with particle energy, and the transverse shower width is described by the Molière radius⁶ of the material.

Hadronic showers (referred to as *jets*) are the result of quarks or gluons which hadronize and shower primarily via the strong interaction. Hadronic showers are generally wider than the electromagnetic showers described above. The longitudinal depth of the hadronic shower scales with the nuclear interaction length of the material λ , defined as the mean distance for the number of particles in a hadronic jet to be reduced to $1/e$ of the initial number. In addition, about 1/3 of the shower products are neutral pions π^0 which decay electromagnetically via the process described above.

3.2.2.1 Liquid Argon Calorimeter

The LAr Calorimeter contains four individual calorimeters: the electromagnetic barrel (EMB) and endcaps (EMEC), and the hadronic endcap (HEC) and forward calorimeter (FCal). The entire calorimeter is surrounded by a cryostat held at a temperature around 90 K.

Focusing on the electromagnetic components first, the EMB covers $|\eta| < 1.475$ and the two EMECs cover $1.375 < |\eta| < 3.2$. They consist of alternating layers of lead absorber and liquid argon. The exact thickness of the lead depends on the location within the detector, ranging from 1.1-2.2 mm. The absorbers are folded into an accordion shape, where the folding angles are varied in order to keep the thickness of the liquid argon gap constant across the barrel (about 2.1 mm). The electromagnetic calorimeter is thick enough that the minimum number of radiation lengths a particle travels through is 24 X_0 , including the material from other subdetectors.

There are four layers within the EMB and EMEC, including an innermost pre-sampler that helps correct for energy lost before the shower reaches the calorimeter. The next three layers consist of differently shaped cells successively reducing in granularity. The first layer consists of narrow strips for fine-grained η resolution, while the majority of the shower energy is deposited in the second layer; the third layer captures most of the energy that escapes the previous two. The accordion shape as well as the sizes of the cells in the EMB are shown in Figure 3.8.

The HEC is located directly behind the EMEC and covers $1.5 < |\eta| < 3.2$. It uses thick copper plates as the absorber (25 mm in the front wheels and 50 mm in the rear wheels) separated by 8.5 mm gaps filled with liquid argon. Rather than the accordion shape, the HEC cells are rectangular.

⁶A cone with a radius equal to the Molière radius (M_R) will contain approximately 90% of the shower energy. At a radius of $2M_R$, 95% of the energy will be contained.

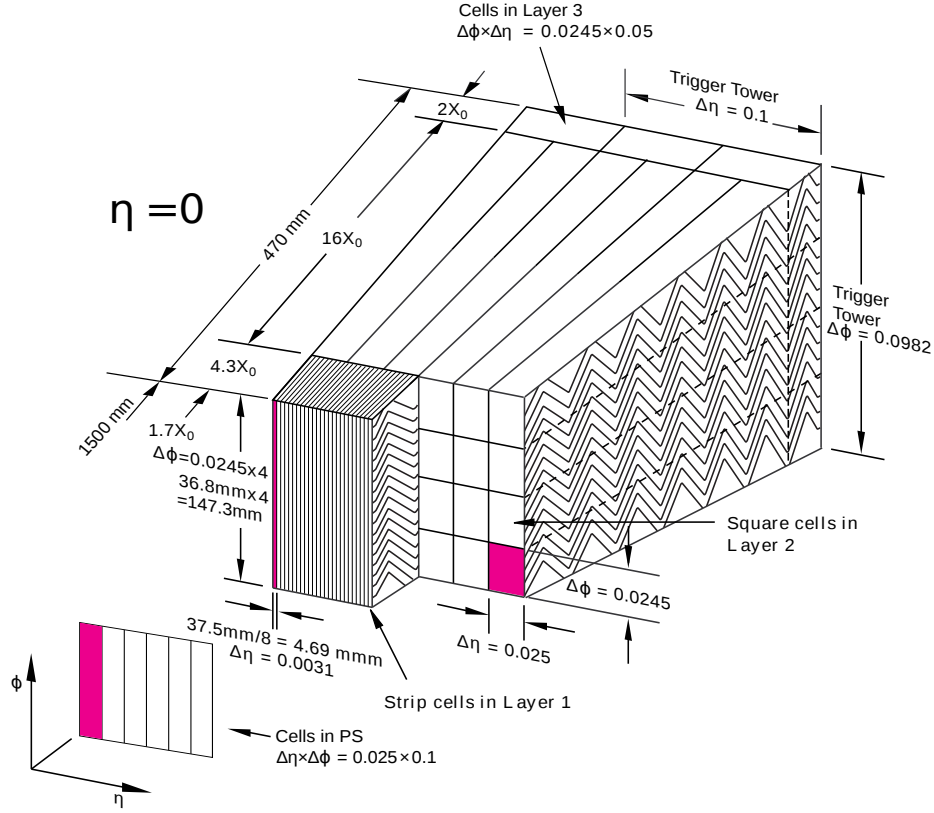


Figure 3.8: Diagram of the cells within the LAr barrel. The accordion structure can be seen in the cut-away view [49].

The FCal provides coverage for hadronic jets over the range $3.2 < |\eta| < 4.9$. Each FCal endcap consists of three layers. The first is an electromagnetic calorimeter with a copper absorber, while the other two hadronic layers use a tungsten absorber. Due to the high particle flux entering the FCal, the liquid argon gaps are very narrow, and electrodes are embedded into the absorbers parallel to the beam line.

3.2.2.2 Tile Calorimeter

The TileCal consists of a barrel and two “extended barrel” sections which cover the range $|\eta| < 1.7$. It consists of alternating layers of steel plates and polystyrene scintillator tiles as the absorbers and active material, respectively. The total thickness of the TileCal is approximately 9λ . As the shower passes through the scintillators, photons are emitted that are picked up by wavelength shifting fibers and passed to photomultiplier tubes.

3.2.3 The Muon Spectrometer

The outermost subdetector in ATLAS is the Muon Spectrometer [52]. Due to the high mass of muons compared to electrons, they pass through the calorimeters, necessitating their own detector. The MS is a high-resolution spectrometer which provides tracking for muon reconstruction within $|\eta| < 2.7$. A set of toroid magnets generate an azimuthal magnetic field that bends the muons for momentum measurements, much like in the ID. Four different technologies are used in the MS:

- Monitored Drift Tubes (MDT) are used across the entire η range for precision measurements of the tracks with a per-hit resolution in the range of 60-80 μm . These consist of an aluminum tube filled with a gas mixture containing argon and an anode wire running through the middle of the tube. When a muon passes through, the gas is ionized, and the electrons are collected on the wire.
- Cathode Strip Chambers (CSC) are used for the forward regions of the endcaps (above $|\eta| > 2.0$). They operate on a similar principle to the MDTs, with strips containing a mesh of anode wires running in parallel instead of tubes with a single wire each.
- Resistive Plate Chambers (RPC) in the barrel are primarily used to provide input for the muon trigger system. They consist of pairs of plastic resistive plates with a 2 mm gap between them filled with a gas mixture. Electrodes are attached to the plates to create a potential between them, and muons passing through ionize the gas and lead to electric discharges which in turn reduce the potential.
- Thin Gap Chambers (TGC) are used for triggering in the endcaps. The TGCs are arranged on circular disks consisting of two rings, and are similar in function to the CSCs but with a different gas mixture.

3.3 Particle reconstruction

In order to convert the raw detector readouts to information about a given particle, various sets of reconstruction algorithms are run. This includes building particle trajectories in the ID, as well as identifying and measuring electrons and muons. A brief overview of these reconstruction methods follow in order to provide context for when these objects are used later in the thesis.

3.3.1 Track reconstruction

Track reconstruction is the process by which a particle’s trajectory is reconstructed from the raw measurements recorded in the ID. The ATLAS track reconstruction algorithm [53] follows three main steps: clusterization, track finding, and ambiguity solving.

The first step, clusterization, uses hits from the Pixel and SCT detectors. Neighboring pixels or silicon strips that registered a hit in a sensor are grouped together into clusters using a connected component analysis. Each cluster represents a *space-point*, or a three-dimensional measurement corresponding to the point where the particle intersected the sensor. Since the SCT sensors consist of two strip layers on top of each other (as described in Section 3.2.1.2), clusters from each layer combine to form a single space-point. It is possible to have overlapping clusters from multiple particles in a single sensor, and care is taken that these *merged clusters* are identified and handled accordingly.

Next, track seeds are formed using sets of three space-points. This number allows for a first momentum estimate to be made while still allowing for the as large a number of track combinations as possible. The impact parameters of a track seed—the distance of closest approach to the collision—are estimated by assuming a perfect helical trajectory in a uniform magnetic field. In order to ensure the quality of a track seed, criteria on the momentum and impact parameters are imposed as well as a requirement that at least one additional space-point lies along the preliminary trajectory. Finally, a combinatorial Kalman filter [54] builds track candidates from the track seeds by incorporating additional space-points lying along the preliminary trajectory. The filter allows for multiple track candidates to be fit to the same track seed if more than one set of space-points is compatible.

The final step of the reconstruction process is the ambiguity solving. Each collected track candidate is processed individually before being sorted by its *track score*, a metric for quantifying the likelihood that a given track candidate correctly represents the particle’s trajectory. The track score is determined from a number of factors. Each cluster along the track candidate increases the score by a weighted amount that incorporates the intrinsic resolution of the relevant detector’s sensors in addition to other factors. Conversely, if a track candidate passes through a sensor but there is no associated cluster (called a *hole*), the score is reduced. The χ^2 of the track fit contributes as well in order to promote tracks with high quality fits. Finally, the logarithm of the momentum adds to the score to suppress tracks with incorrectly assigned clusters, as these tracks typically have low momenta. A track candidate is rejected by the ambiguity solver if its score is too low, or if it fails to meet a basic set of quality criteria. If a cluster would be shared by more than one track, at

most two tracks are allowed to pass through it. In this case, preference is given to tracks already passing through the ambiguity solver, which by construction results in the two highest scoring tracks using the shared cluster being kept.

Following this procedure, TRT hits can be incorporated into the track fit through *TRT track extension* [55]. Compatible sets of TRT measurements are found for tracks found in the silicon detectors surviving the ambiguity solving. The algorithm requires that the original silicon-only track not be modified by the inclusion of the TRT hits; it is simply an extension of the existing track.

What is described above is the *inside-out* reconstruction algorithm; there is also an *outside-in* reconstruction that begins in the TRT. This algorithm is not covered in detail here, as much of the process is similar to the above. The general workflow begins with finding track segments in the TRT, constructing the track candidates including the silicon hits, and finally ambiguity solving.

3.3.2 Electron reconstruction

Electron reconstruction [56] uses information from both the ID and the electromagnetic calorimeters. The characteristic signature of an electron in ATLAS is a charged particle track in the ID that is matched in $\eta\phi$ to localized clusters of energy deposited in the calorimeter.

Calorimeter cluster candidates are seeded from localized energy deposits according to a sliding-window algorithm [57]. The clusters are a 3×5 rectangle of calorimeter towers in $\eta \times \phi$ with a total transverse energy greater than 2.5 GeV. In the event that two clusters overlap, if the E_T of the clusters vary by more than 10%, the highest E_T cluster is kept, otherwise the candidate with the highest E_T in the central tower is kept. The ID tracks are those generated using the algorithm detailed above in Section 3.3.1, and tracks with a nearby calorimeter cluster are re-fit using a Gaussian-sum filter designed to take into account bremsstrahlung effects [58].

To reconstruct the final electron candidate, the refit track and the cluster are subject to the final matching criteria:

$$|\eta_{\text{cluster}} - \eta_{\text{track}}| < 0.05 \quad \text{and} \quad (3.5)$$

$$-0.10 < q \times \Delta\phi_{\text{cluster, track}} < 0.05 \quad \text{or} \quad -0.10 < q \times \Delta\phi_{\text{res}} < 0.05,$$

where q is the charge of the track and $\Delta\phi_{\text{res}}$ is the azimuthal separation between the cluster position and the track after rescaling its momentum to the energy of the cluster. If multiple tracks satisfy the above criteria, the primary track is selected by an algorithm that takes into account the center of

each cluster relative to the parameters of the candidate track. Finally, the clusters are reconstructed about the seed cluster using a larger window size, 3×7 in the barrel and 5×5 in the endcaps, and the energy is calibrated to the original electron energy using techniques described in [59, 60].

Electron identification To determine whether an electron candidate is a signal electron or background object, an identification criteria (ID) is implemented, covered in more detail in [56, 61]. Electron ID is performed using a multivariate likelihood technique (LH) that simultaneously evaluates a list of measurements of an electron candidate, including both tracking and calorimeter clustering information. To cover the different requirements of various physics and performance studies, four different likelihood working points are constructed corresponding to increasing thresholds for the LH discriminant: `VeryLooseLH`, `LooseLH`, `MediumLH`, and `TightLH`. Each successive working point is a subset of its predecessors. The efficiencies of the `LooseLH`, `MediumLH`, and `TightLH` working points as a function of electron E_T are shown in Figure 3.9.

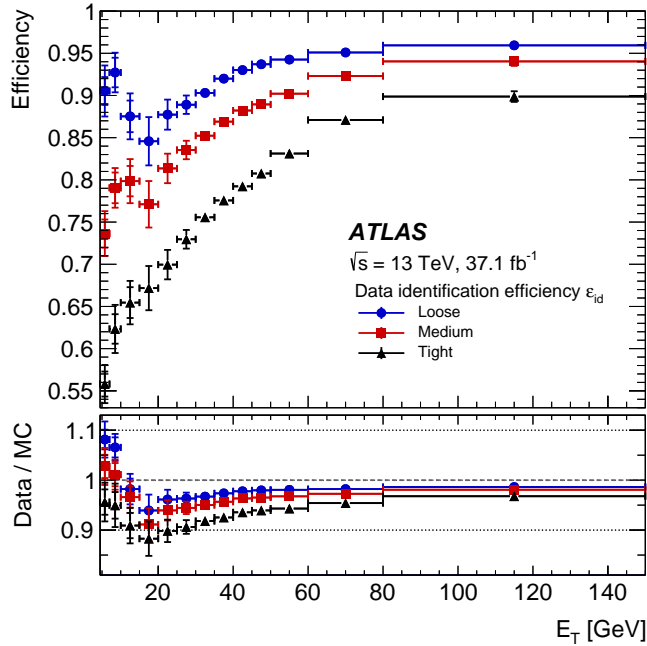


Figure 3.9: Measured LH electron ID efficiencies in $Z \rightarrow ee$ events for the `LooseLH` (blue), `MediumLH` (red), and `TightLH` (black) working points as a function of electron E_T . The bottom plot shows data-to-simulation ratios. Plot taken from [56].

Electron isolation Signal electrons, such as those from the decay of a W boson, tend to have little detector activity nearby in both the ID and the calorimeters. Background electrons, such as those from photon conversions or jets, are often produced in association with other particles. To take advantage of this, variables are constructed to quantify the amount of activity within a cone of a specified radius in ΔR about an electron in both the tracking systems and the calorimeters.

The track-based isolation consists of the sum of the transverse momentum of tracks within a cone of a specified radius about an electron (not including the electron itself). The tracks are required to have $p_T > 1$ GeV, satisfy basic quality requirements, and be associated with the vertex from which the electron originated. Additionally, particles from bremsstrahlung radiation are considered part of the original electron and are subtracted from the isolation cone. A variable cone radius dependent on the p_T of the electron is used in order to compensate for busy detector environments:

$$\Delta R = \min\left(\frac{10 \text{ GeV}}{p_T}, R_{\max}\right), \quad (3.6)$$

where R_{\max} is the largest allowed cone size, typically set at 0.2 for electrons.

Calorimeter isolation is a bit more difficult due to the size of the energy deposits relative to the cone size, as parts of an energy cluster can lie outside of the cone. As such, topological clusters [62] (topo clusters) are seeded by calorimeter cells with deposited energy greater than four times the expected noise-level of that cell. The cluster is then expanded to incorporate electromagnetic and hadronic cells recording an energy greater than two times their expected noise-levels until no adjacent clusters remain satisfying the requirement. The isolation cone is then the sum of the E_T of all positive-energy topo clusters whose barycenters fall within a cone of radius $\Delta R < 0.2$. The electron's energy is subtracted by removing the cells within a rectangle around the electron.

When applying the isolation selection, *relative isolation* is used, defined as the ratio of the track- or calorimeter-based isolation variable divided by the electron p_T . Four isolation working points are defined targeting specific values of efficiency. `Loose` and `LooseTrackOnly` target a fixed efficiency value across the p_T and η spectrum of the electrons, with the latter not applying a cut on calorimeter isolation. `Gradient` and `GradientLoose` target a p_T -dependent fixed efficiency that is uniform in η . The efficiencies for these working points as a function of electron E_T are shown in Figure 3.10. Additional working points are also provided that instead use fixed values for the relative track and calorimeter isolation cuts.

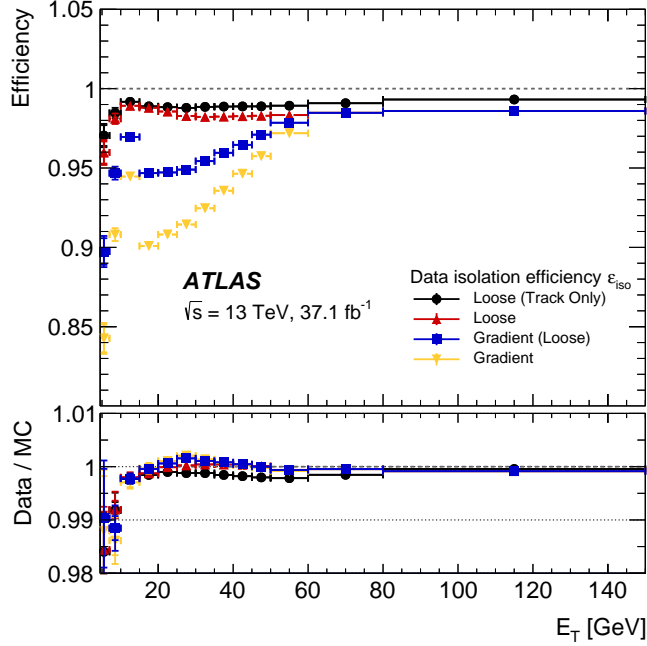


Figure 3.10: Measured isolation efficiencies for the `LooseTrackOnly` (black), `Loose` (red), `GradientLoose` (blue), and `Gradient` (yellow) working points as a function of electron E_T . The bottom panel shows data-to-simulation ratios. Plot taken from [56].

3.3.3 Muon reconstruction

Muon reconstruction [63, 64] first occurs independently in the ID and the MS, and then the information from both is combined to form the final muon tracks used in analysis. Muons in the ID are reconstructed as a charged particle track following the standard procedure detailed in Section 3.3.1.

In the MS, hits within each muon chamber are collected into segments, with separate algorithms for each of the four different detector components described in Section 3.2.3. Muon track candidates are then built by fitting together segments using a combinatorial search seeded by segments in the middle layers first, and then expanding to the outer and inner layers. A track must contain at least two matching segments, except in the transition region between the barrel and endcap where a single segment can be used. In the event that a segment is shared by multiple tracks, an overlap removal algorithm decides which track should keep the segment, or if it should remain shared. Finally, the hits within each track candidate are fit using a global χ^2 , and the track is accepted if the χ^2 satisfies a set of selection criteria.

The ID and MS tracks are then combined according to several different reconstruction criteria

determined by the available information from the ID, MS, and calorimeters. This results in four different muon “types”:

- Combined (CB): Independent tracks in the ID and MS are combined with a global track refit using both sets of hits. MS hits may be added or removed if it improves the quality of the track fit. Muons are typically reconstructed outside-in, matching a MS track to one in the ID; however, an inside-out matching is also used as a complementary approach.
- Segment-tagged (ST): An ID track is classified as a muon if it can be extrapolated to at least one track segment in the MDT or CSC chambers. These are used when a muon only crosses one layer of the MS, either due to low p_T or falling in a region of reduced acceptance.
- Calorimeter-tagged (CT): An ID track is classified as a muon if it can be matched to a calorimeter energy deposit compatible with a minimum ionizing particle. These muons are generally lower in purity than the other types, but they are useful for recovering acceptance in the region $|\eta| < 0.1$ where the MS is only partially instrumented.
- Extrapolated (ME): The muon is reconstructed using a MS track that is loosely compatible with having originated from the interaction point. The MS track must transverse at least two layers of the MS in the central region and three in the forward region. These muons are generally used to extend the acceptance of muon reconstruction in the forward regions not covered by the ID ($2.5 < |\eta| < 2.7$).

Muon identification Muon identification serves to select signal muons with a high quality momentum measurement from backgrounds (mainly from pions and kaons). For CB muons, three variables are used:

- q/p significance: The absolute value of the difference in q/p of the muons (where q is the muon’s charge) as measured by the ID and the MS divided by the corresponding uncertainties added in quadrature.
- ρ' : The absolute value of the difference between the p_T measurements in the ID and the MS divided by the p_T of the combined track.
- The normalized χ^2 of the combined track fit.

Additional requirements are imposed on the number of hits within the ID to ensure the tracks’ momenta are well measured.

There are three primary muon identification working points⁷ of increasing background rejection: **Loose**, **Medium**, and **Tight**. **Loose** muons include all four types listed above, but CT and ST muons are restricted to the region $|\eta| < 0.1$. The default recommendation for analysis are **Medium** muons, which only include CB and ME tracks. Finally, **Tight** muons are made up of CB muons with hits in at least two components of the MS and that pass the **Medium** requirements. Each successive working point is a subset of the previous one, and the cuts on the three variables listed above are tightened in each step. The muon reconstruction efficiency for each of these three working points in $Z \rightarrow \mu\mu$ events is shown in Figure 3.11.

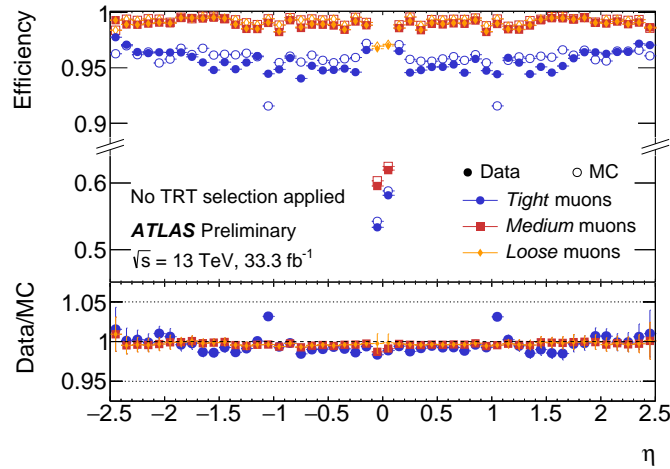


Figure 3.11: Muon reconstruction efficiencies in $Z \rightarrow \mu\mu$ events for the **Loose** (yellow), **Medium** (red), and **Tight** (blue) ID working points as a function of muon η . The drop in efficiency for **Medium** and **Tight** muons in the range $|\eta| < 0.1$ is due to the exclusion of CT and ME muons, which are used to recover acceptance in this region. Collision data (solid points) is compared to simulation (open points) and the ratio is in the lower panel. Plot taken from [65].

Muon isolation Isolation for muons is handled in much the same way as for electrons (see Section 3.3.2). A track-based variable is computed by summing the transverse momenta of tracks with $p_T > 1 \text{ GeV}$ within a cone of variable radius as in Equation 3.6 with $R_{\max} = 0.3$. The calorimeter-based isolation again uses topo clusters of radius $\Delta R < 0.2$ with the energy deposit corresponding to the muon removed. Similar isolation working points are constructed using the same criteria as for electrons, and the efficiency of the **Loose** and **GradientLoose** working points as a function of muon p_T are shown in Figure 3.12.

⁷A fourth working point, **Highpt**, is optimized for high mass searches, such as W' and Z' resonances, and is not covered here.

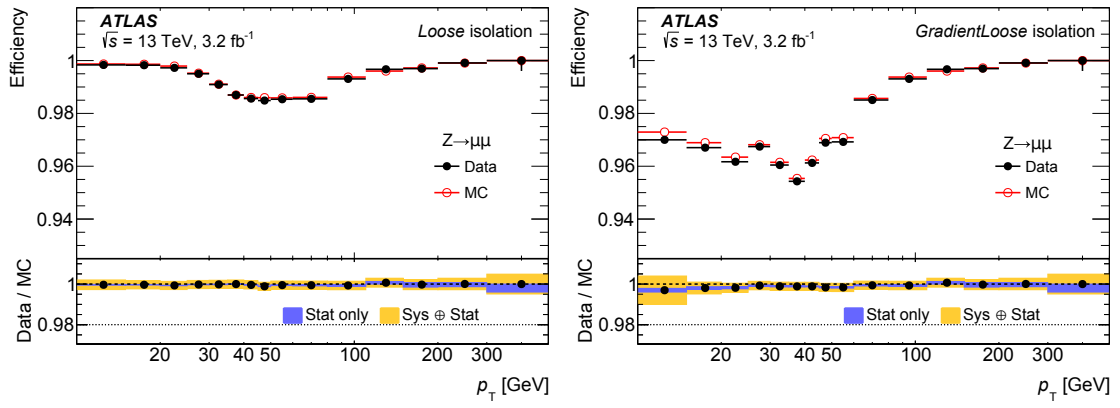


Figure 3.12: Muon isolation efficiencies in $Z \rightarrow \mu\mu$ events for the Loose (left) and GradientLoose (right) working points as a function of muon p_T . Collision data (black) is compared to simulation (red) and the ratio is in the lower panel. Plots taken from [64].

CHAPTER 4

Alignment of the ATLAS Inner Detector

As a charged particle passes through the ATLAS ID, it leaves *hits* in the sensors along its path in the form of ionization. The particle’s trajectory, or *track*, can be reconstructed from a fit to these hits via the procedure described in Section 3.3.1. In order to reconstruct an accurate particle track, it is necessary to know where in space each hit occurred as precisely as possible, which in turn requires knowledge of the physical location of the sensor that registered the hit. If one of the sensors is displaced relative to its expected position in the known detector geometry, or *misaligned*, the assumed location of the corresponding hit will not match its actual location, resulting in inaccurate track parameters and a poor track fit. The first misalignments were a result of not knowing the exact positions of each sensor after the initial installation of the detector. Subsequent misalignments occur when sensors shift due to mechanical stress and strain, which can be the result of cycles in ATLAS’s magnetic field, changes in operating temperatures, or when components are removed and replaced during maintenance. A visualization of how a misaligned detector element can affect the track reconstruction is shown in Figure 4.1.

In order to correct the misalignments, the ID alignment procedure is applied to accurately determine the physical position and orientation of each detector element. The baseline accuracy of the alignment is required to be such that the track parameter resolutions are not degraded by more than 20% with respect to those derived from a perfect detector geometry⁸ [40]. This corresponds to a precision of better than $10 \mu\text{m}$ in the positioning of the elements of the silicon detectors [66].

This chapter covers the ID alignment algorithm and procedure, its implementation during the 2015 data taking period, and the steps taken to measure momentum biases that may exist after

⁸The so-called *perfect geometry* refers to the description of the ATLAS detector in which every sensor precisely matches its design specifications. The perfect geometry contains no misalignments, and the position of each sensor is known exactly.

alignment.

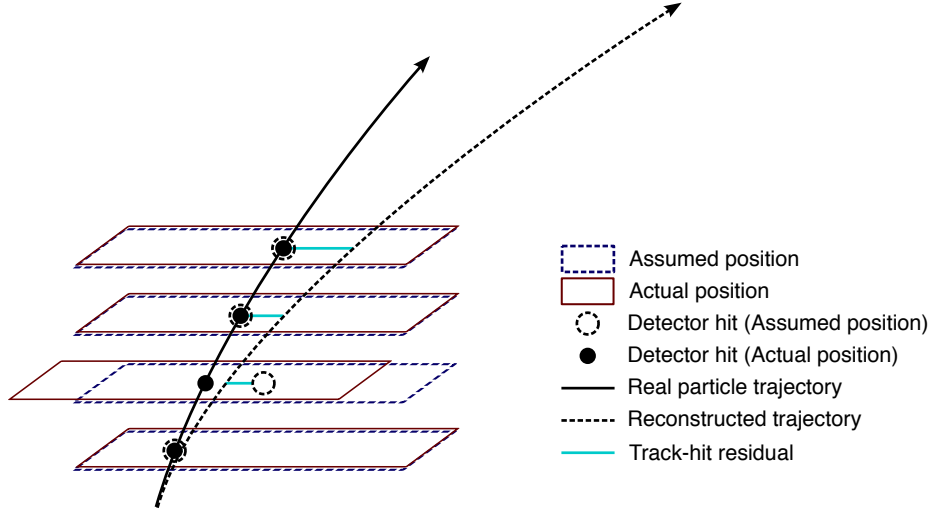


Figure 4.1: Graphical representation of the effect of a misaligned detector element. The reconstructed particle track (dashed arrow) differs from the actual trajectory of the particle (solid arrow) due to a shift in the third detector element. The cyan lines represent the track-to-hit residuals.

4.1 The alignment method

The alignment procedure uses a track-based algorithm that updates the locations of detector elements in order to minimize the set of track-hit *residuals*. These residuals are defined as the distance between the where fitted track intersects a given detector element and the position of the actual hit recorded by the same element, shown by the cyan lines in Figure 4.1.

Tracks in ATLAS are parameterized as five-dimensional vectors [67]:

$$\vec{\tau} = (d_0, z_0, \phi_0, \theta, q/p), \quad (4.1)$$

where d_0 and z_0 are the transverse and longitudinal impact parameters with respect to the origin, ϕ_0 is the azimuthal angle of the track at the point of closest approach to the origin, θ is the polar angle, and q/p is the charge of the track divided by its momentum. The residual for the i^{th} hit of a given track can then be written in terms of the track parameters $\vec{\tau}$ and a set of alignment parameters \vec{a} that describe the hit location [68]:

$$r_i(\vec{\tau}, \vec{a}) = (\vec{m}_i - \vec{e}_i(\vec{\tau}, \vec{a})) \cdot \hat{k}, \quad (4.2)$$

where \vec{e}_i is the intersection point of the extrapolated track with the sensor, and \vec{m}_i is the position of the associated hit within the sensor. \hat{k} is a unit vector corresponding to the direction of the

measurement within the sensor, as shown in Figure 4.2. \vec{r} then is the vector of residuals for the track.

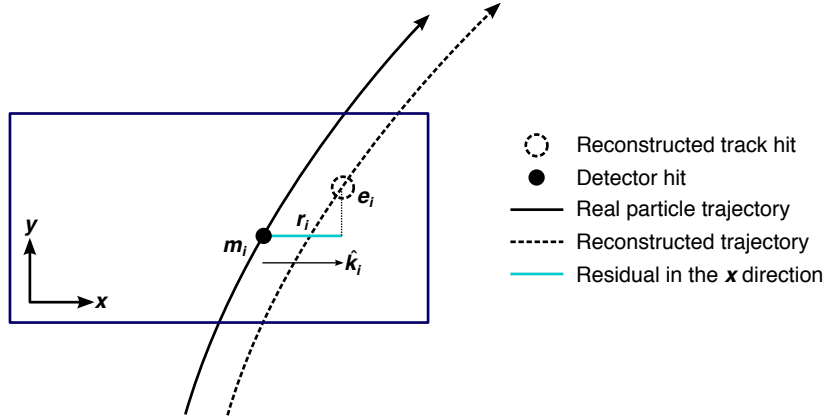


Figure 4.2: Graphical representation of a track-hit residual in the local x direction according to Equation 4.2. The sensor in this example measures a particle hit in the local x and y directions, with each having its own residual.

A χ^2 function can be built from the residuals of all collected tracks:

$$\chi^2 = \sum_{\text{tracks}} \vec{r}^T V^{-1} \vec{r}, \quad (4.3)$$

where V is the covariance matrix of the hit measurements. The χ^2 function is then minimized with respect to the alignment parameters \vec{a} , which contain all degrees of freedom being aligned. The minimization condition with respect to \vec{a} is

$$\frac{d\chi^2}{d\vec{a}} = 0 \rightarrow 2 \sum_{\text{tracks}} \left(\frac{d\vec{r}}{d\vec{a}} \right)^T V^{-1} \vec{r} = 0. \quad (4.4)$$

This equation can be difficult to solve exactly, so the residual is rewritten as a first order Taylor expansion:

$$\vec{r} = \vec{r}_0 + \frac{d\vec{r}}{d\vec{a}} \delta \vec{a}, \quad (4.5)$$

where \vec{r}_0 is dependent on an initial set of track and alignment parameters \vec{r}_0 and \vec{a}_0 , respectively; the dependence of \vec{r} on the track parameters is included when evaluating the total derivative $\frac{d\vec{r}}{d\vec{a}}$. Equation 4.5 can then be inserted into the minimization condition from Equation 4.4 to give

$$\left[\sum_{\text{tracks}} \left(\frac{d\vec{r}}{d\vec{a}} \right)^T V^{-1} \left(\frac{d\vec{r}}{d\vec{a}} \right) \right] \delta \vec{a} + \sum_{\text{tracks}} \left(\frac{d\vec{r}}{d\vec{a}} \right)^T V^{-1} \vec{r}_0 = 0. \quad (4.6)$$

From this equation, the alignment matrix \mathcal{M}_a and alignment vector $\vec{\nu}_a$ can be defined:

$$\mathcal{M}_a = \sum_{\text{tracks}} \left(\frac{d\vec{r}}{d\vec{a}} \right)^T V^{-1} \left(\frac{d\vec{r}}{d\vec{a}} \right) \quad (4.7)$$

$$\vec{\nu}_a = \sum_{\text{tracks}} \left(\frac{d\vec{r}}{d\vec{a}} \right)^T V^{-1} \vec{r}_0. \quad (4.8)$$

Finally, the alignment corrections $\delta\vec{a}$ can be solved for by inverting the alignment matrix:

$$\delta\vec{a} = -\mathcal{M}_a^{-1} \vec{\nu}_a, \quad (4.9)$$

which results in a system of linear equations of a size equal to the number of alignment degrees of freedom [66].

Inverting the full matrix and solving the resulting system of equations is referred to as *Global χ^2* alignment [68]. This can be useful, as \mathcal{M}_a contains all the correlations between the structures that are being aligned, or *alignable structures*. However, inverting the matrix is difficult when the number of degrees of freedom becomes large—as the number of alignable structures increases, so too does the size of the matrix \mathcal{M}_a . Eventually, inverting the matrix becomes too computationally intensive to be practical.

This problem is solved by the *Local χ^2* algorithm [69]. In this case, the alignment matrix is constructed to be block-diagonal, allowing for it to be easily inverted even for large numbers of degrees of freedom. This is achieved by replacing the full derivative in Equation 4.6 with the partial derivative $\frac{\partial\vec{r}}{\partial\vec{a}}$. The new alignment matrix \mathcal{M}'_a and alignment vector $\vec{\nu}'_a$ become

$$\mathcal{M}'_a = \sum_{\text{tracks}} \left(\frac{\partial\vec{r}}{\partial\vec{a}} \right)^T V^{-1} \left(\frac{\partial\vec{r}}{\partial\vec{a}} \right) \quad (4.10)$$

$$\vec{\nu}'_a = \sum_{\text{tracks}} \left(\frac{\partial\vec{r}}{\partial\vec{a}} \right)^T V^{-1} \vec{r}_0. \quad (4.11)$$

Inverting \mathcal{M}'_a is considerably faster and requires less computing memory compared to \mathcal{M}_a , even for large numbers of degrees of freedom; however, the correlations between the alignable structures is lost. Due to the Taylor expansion used in Equation 4.6, several iterations of the alignment algorithm may be necessary to converge on a final set of alignment constants. The Local χ^2 alignment typically requires more iterations due to the loss of the correlation information [70].

In practice, the ATLAS reconstruction is run over a set of events, and the resulting tracks are fed to the alignment algorithm. The residuals are calculated, the alignment matrix is built and inverted, and a new set of alignment constants is obtained. The convergence is checked in two ways:

1. Measuring change in the χ^2 with respect to the previous iteration. If it is near zero, then the χ^2 is approaching its minimum.
2. Looking at the residual distributions for different alignable structures. A well aligned detector will have a residual distribution that is approximately Gaussian, with a mean of zero with a width approximating the intrinsic resolution of the detector.

If the above checks are satisfied, the process is finished, and the final set of alignment constants are obtained; if not, another iteration is performed. A visual representation of the alignment chain is shown in Figure 4.3.

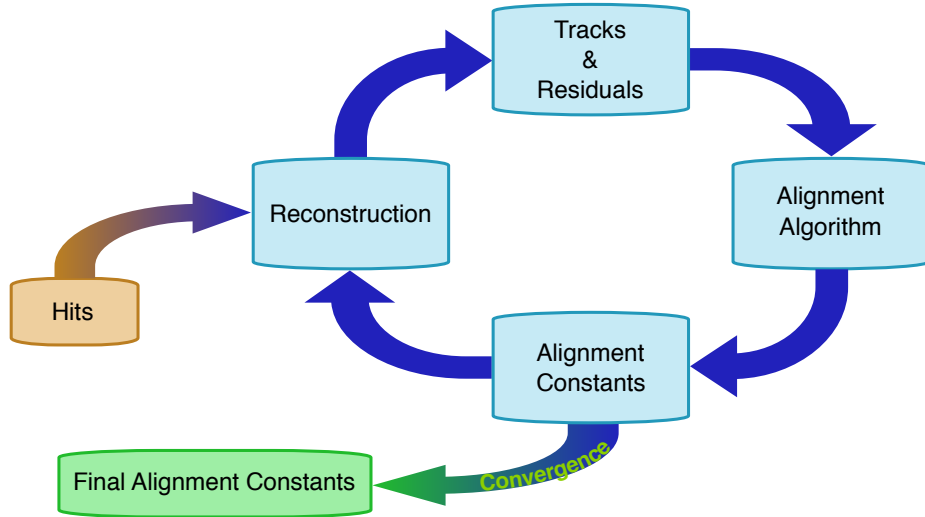


Figure 4.3: Flow chart depicting the ID alignment chain.

Since a χ^2 minimization is used to align the detector, if there is a systematic misalignment in the detector that does not adversely affect the χ^2 , the algorithm will be insensitive to it. These misalignments are referred to as *weak modes*, and special care is taken to remove them [71]. One potential impact of weak modes is a bias in the track momentum of reconstructed particles. This particular effect is the subject of Section 4.4.

The detector is aligned both in “real-time” as data is collected and during dedicated offline alignment campaigns. The real-time alignment is performed in ATLAS’s *calibration loop*, which comprises the first stage in the preparation of data for physics analysis. The calibration loop requires the alignment—as well as various other detector calibrations—to be available within 48 hours for

initial data processing. A fast, coarse-grained alignment⁹ is run on a subset of the available data containing full tracking information, and the results are propagated to the reconstruction of that particular dataset [72]. Due to the time constraints imposed on the calibration loop, a full sensor-by-sensor alignment is not possible.

The more thorough and finely tuned alignments are reserved for dedicated alignment campaigns, typically near the beginning and at the end of data taking campaigns. The former generally occurs once a sufficient amount of data is collected after a detector shutdown, in order to obtain a good baseline alignment for use in the remainder of the data taking period. One such alignment campaign, the initial offline alignment of the ATLAS detector at the beginning of Run 2, is the subject of Section 4.2. Once data taking is complete, a new set of alignment constants is derived for the full set of available data, and it is typically divided into several “blocks” to account for potential run-by-run shifts in the alignment constants. The data is then reprocessed using the newly derived detector geometry.

4.1.1 Alignment levels

The alignment of the detector is performed at several levels of increasing granularity. This adds flexibility in being able to align only as finely as needed, and it also allows for global, detector-level misalignments to be corrected first before dealing with finer adjustments. The main alignment levels are as follows:

- Level 1 (L1) alignment involves moving entire subdetector components as a single unit. The entire Pixel detector (barrel and endcaps) is treated as a single structure, while the SCT and TRT barrel and endcaps are individually aligned. These often have the largest misalignments, but they are easily corrected and do not require large volumes of data to do so.
- Level 2 (L2) alignment treats individual layers in the silicon detectors (modules in the TRT) and end cap disks as individual alignable objects.
- Level 2.7 (L27) alignment was introduced with the addition of the IBL to the ID in Run 2. It involves the stave-by-stave alignment of the IBL and Pixel barrel¹⁰.

⁹The calibration loop runs up to a Level 2 alignment in the silicon detectors, which involves treating each layer of sensors as a single object. The alignment levels are defined in greater detail in Table 4.1.

¹⁰Even though the IBL is considered a part of the Pixel Detector, for the purposes of this Chapter, “Pixel” will refer to the original three layers of the Pixel barrel and its endcaps, and the IBL will be referenced separately.

- Level 3 (L3) alignment treats each module in the silicon detectors and each straw in the TRT as an individual alignable object. It is the finest grained alignment available but also the most computationally intensive due to the large number of degrees of freedom. Due to the large number of individual detector elements being aligned, high statistics are required.

The different alignment levels are listed in more detail in Table 4.1, including the number of alignable structures and associated degrees of freedom for each detector component.

The implementation of the alignment algorithm in the software is flexible enough to allow each subsystem to be aligned individually at a specified level. Each alignable structure has six degrees of freedom: 3 translations (T_x, T_y, T_z) and 3 rotations (R_x, R_y, R_z)¹¹; however individual degrees of freedom may be turned on and off as required. In a typical alignment job, L1 and L2 contain few enough degrees of freedom that the Global χ^2 algorithm can be used, but L3 alignments (which can contain over 36,000 degrees of freedom in the silicon detectors alone) require the Local χ^2 algorithm.

4.1.2 Alignment coordinate systems

The global coordinate system (x, y, z) used by the ID alignment matches that of the ATLAS detector in general. The positions and orientations of individual detector modules of the ID are defined by a right-handed local coordinate system (x', y', z') where the origin is defined as the geometrical center of the module. The x' -axis for each silicon module is defined to point along the most sensitive direction of the module, the y' -axis is oriented along the long side of the module, and the z' -axis is orthogonal to the (x', y') plane. For the TRT straws, the x' -axis is perpendicular to both the wire and the radial direction, defined from the origin of the global frame to the straw center, the y' -axis points along the straw, and once again the z' -axis is orthogonal to the (x', y') plane. A depiction of the global and local coordinate systems for the ID is shown in Figure 4.4.

When considering the alignment degrees of freedom listed earlier in Section 4.1.1, grouped collections of modules, layers, or entire subdetectors use the global coordinate system; individual modules use their respective local coordinate systems. The translations T_i are with respect to the origin of the given reference frame, and the rotations R_i are taken about the Cartesian axes.

¹¹The TRT is an exception, as the subdetector does not have any resolution along the length of the straw. Therefore, for the barrel, T_z is omitted. Similarly for the straws themselves, only two parameters are defined: translation with respect to the radial direction (T_ϕ) and rotation with respect to the radial axis (R_r for the barrel and R_z for the end-caps) [73].

Level	Description of alignable structure	Structures	DoF	
1	IBL detector	1	6	
	Whole Pixel detector	1	6	
	SCT barrel and 2 end-caps	3	18	
	TRT barrel and 2 end-caps (T_z fixed)	3	17	
Total:		8	47	
2	IBL detector	1	6	
	Pixel barrel layers	3	18	
	Pixel end-cap disks	2×3	36	
	SCT barrel layers	4	24	
	SCT end-cap disks	2×9	108	
	TRT barrel 32 modules (T_z fixed)	3×32	480	
	TRT end-cap wheels	2×40	480	
Total:		208	792	
2.7	IBL staves	14	84	
	Pixel barrel staves	$22+38+52$	672	
	Pixel end-cap disks	2×3	18	
	Total:		132	1,878
3	IBL modules	280	1,680	
	Pixel modules	1,744	10,464	
	SCT modules	4,088	24,528	
	TRT barrel wires (T_ϕ, R_r only)	105,088	210,176	
	TRT end-cap wires (T_ϕ, R_Z only)	245,760	491,520	
	Total silicon sensors:		6,112	36,672
	Total TRT wires:		350,848	701,696

Table 4.1: The four alignment levels for each of the detector subsystems and their components (first introduced in Section 3.2). The total number of alignable structures and degrees of freedom (DoF) to be aligned are given for each level.

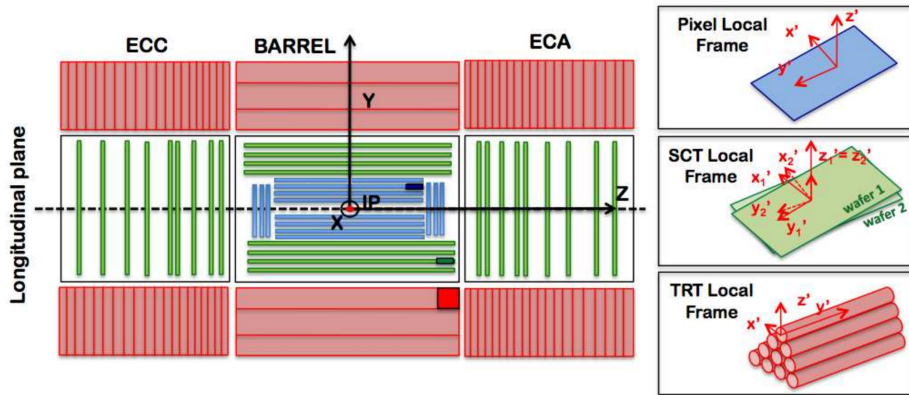


Figure 4.4: A schematic representation of the Inner Detector in the longitudinal plane with the global coordinate system overlaid on top. The Pixel detector and IBL are shown in blue, the SCT in green, and the TRT in red. The local coordinates for each subdetector module are inset on the right. Image taken from [74].

4.2 Early 2015 alignment of the ATLAS detector

At the end of Run 1, the LHC was shut down for upgrades and maintenance. During this time, a number of upgrades were performed on the ATLAS detector, including the installation of the Insertable B-Layer (IBL), mounted on a new beam pipe. These changes to the ID required some detector components to be removed temporarily, and many elements shifted relative to each other over the course of the maintenance process. In order to correct for these large detector movements prior to 13 TeV data taking, an alignment was performed using cosmic ray data collected in early 2015 [74]. This alignment was able to correct for the majority of the large detector-wide misalignments as well as determine the global position of the IBL at the micron level.

In June of 2015, shortly after the data taking period began, the first track-based alignment of the refurbished ID was performed using the initial 7.9 pb^{-1} of $\sqrt{s} = 13 \text{ TeV}$ proton-proton collision data [75]. Starting from the geometry determined by the cosmic ray alignment, referred to hereafter as the *March alignment*, an improved set of alignment constants (the *June alignment*) was derived from a data set of approximately 1.4 million selected tracks. A sample of Monte Carlo (MC) events containing approximately 2.7 million tracks from dijet events simulated using a perfect detector geometry is used as a comparison to the data; the MC events are reweighted to match the η and p_T distributions found in the data. Additional validation of the alignment results uses a set of cosmic ray data collected by the detector during the LHC collisions.

4.2.1 June alignment procedure

The data set used as the input for the alignment is made up of a subset of physics events used for prompt reconstruction recorded at a rate of 10 Hz. To ensure that only high quality tracks are used for the alignment, each track is required to have transverse momentum $p_T > 3 \text{ GeV}$, contain at least one hit in the Pixel detector, at least seven hits in the combined silicon detectors (IBL, Pixel, and SCT), and at least 25 hits in the TRT.

A full L3 alignment of the IBL was included in the March alignment; however, a realignment was still necessary. Since cosmic rays pass through the detector top-down, the staves on the sides of the IBL recorded fewer hits and thus could not be aligned as precisely as those on the top and bottom. Additionally, the IBL was operating at a temperature of -20°C during the cosmic data taking, and it was set to -10°C for collision data taking. This proved to be significant, as it was observed that the IBL staves experience a temperature-dependent, parabolic bowing in the local x -direction of approximately $-10\mu\text{m}/\text{K}$ [76]. As a result, a full L3 alignment of the IBL was essential in order to

correct for the bowing. Due to it being a brand new element of the detector as well as its importance in vertexing and b -jet tagging, aligning the IBL sensors with a high degree of precision was one of the main goals of the June alignment.

The June alignment was performed in two stages, with the first pass focusing on relative movements of the big structures and correcting for the bowing of the IBL. The March alignment corrected for these larger movements as well; however, it was observed during Run 1 that these sort of misalignments are introduced by changing conditions in the detector [71], such as adjustments in the cooling system settings or magnet power cycling, which may have occurred between the early cosmic data taking and the first $\sqrt{s} = 13$ TeV collisions. The silicon detectors were aligned at several different levels and the IBL was aligned at the module level; the TRT detector was kept fixed to act as a global reference frame. The full alignment chain for the first pass consisted of the following steps:

1. The IBL, Pixel, and SCT detectors were aligned at L1. The SCT barrel was not aligned in T_z in order to constrain global displacements along the z -axis, as the TRT is not sensitive to that degree of freedom.
2. The IBL, and Pixel barrel and end-caps, and SCT barrel were aligned at L2. The SCT end-caps were aligned at L1.
3. The IBL and pixel barrel were aligned at L27, using all six degrees of freedom. The Pixel end-cap disks were only aligned in the plane (T_x , T_y , and R_z). The SCT was treated the same as in the previous step.
4. The IBL was aligned at L3 using all six degrees of freedom for each module.

The primary goal for the second pass was to remove a bias in the transverse impact parameter d_0 found in the March alignment. In addition to the bias, the resolution of d_0 was also observed to be poorer than expected. In order to correct for this, an additional constraint was passed to the alignment which added the impact parameter with respect to the beam spot as a pseudo-measurement [77]. With this setup, when the alignment algorithm minimizes the χ^2 , it will take care of the impact parameter minimization as well. Only the IBL and Pixel detectors were aligned in the second pass. The different alignment stages are listed below, with the beam spot constraint being used in each:

1. The IBL and Pixel detectors were aligned at L2 with the SCT fixed.

2. The IBL was aligned at L27
3. The IBL and Pixel barrel and end-caps were aligned at L3.

The set of alignment constants obtained at the end of the second pass represents the June alignment. The highest level of alignment each subdetector received over the course of the two passes is listed in Table 4.2.

Detector	Highest level of alignment
IBL	L3
Pixel	Barrel
	End-caps
SCT	Barrel
	End-caps
TRT	None

Table 4.2: Summary of the highest level of alignment applied to each ID subsystem when deriving the June alignment.

4.2.2 Alignment results

Alignment quality is primarily assessed by looking at the track-hit residual distributions. If the detector is well aligned, the residuals will be Gaussian-distributed with a mean of zero and a width approximating the detector’s resolution. The residual distributions are constructed from the same selection of tracks that were used to perform the alignment, and are the focus of Section 4.2.2.1. A second check on the alignment involves observables sensitive to the track parameter resolution. In this case, cosmic rays are used, making use of a “split track” technique that takes advantage of the top-to-bottom cosmic ray trajectory (compared to the center-out trajectory of collision tracks). This method and the corresponding tests of the alignment are detailed in Section 4.2.2.2

Additionally, the effect of the beam spot constrained alignment on the impact parameter d_0 needed to be checked. The d_0 distributions for both the March and June alignments are compared to the MC simulation using a perfect geometry in Figure 4.5. In the March alignment, there is a clear bias of $18 \mu\text{m}$ in the mean of the distribution and the width is nearly twice that of the perfect geometry. After the second pass of the June alignment, the mean has shifted to $1 \mu\text{m}$ and the distribution has narrowed considerably. From this, it appears that the constrained alignment successfully removed the d_0 bias.

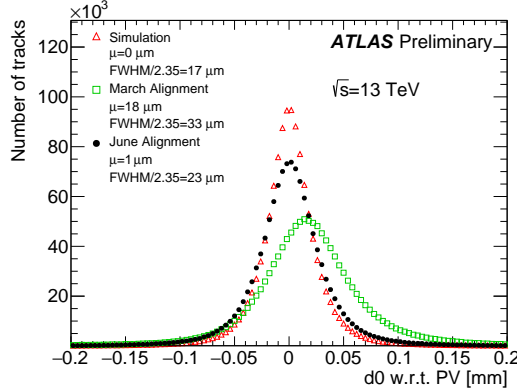


Figure 4.5: The d_0 distributions with respect to the reconstructed primary vertex using 13 TeV collision data sample reconstructed using the June (black) and March (green) alignments. The data is compared to a MC simulation using a perfect detector geometry (red). The distributions are normalized to the same number of entries.

4.2.2.1 Residual distributions from collisions

As mentioned previously, the primary focus of the June alignment campaign was on the IBL and the Pixel detectors. These subdetectors are the closest to the beam line and have the finest resolutions within the ID. The residual distributions in local x and y of the IBL planar sensors¹² are shown in Figure 4.6. These and subsequent figures in this section compare the June and March alignments to the perfectly-aligned MC simulation. Noticeable improvement in the distribution widths can be seen in both the local x - and y -directions, nearly matching the simulation in local x , the most sensitive direction.

Due to the temperature-dependent bowing of the IBL, it is also interesting to look at the means of the residual distributions for each ring of IBL sensors along the beam line, as shown in Figure 4.7. A deformation is clearly visible in the March alignment in both measurement directions, and the shape in the local x -direction is consistent with an average stave bowing due to the different operating temperature of the IBL during the March alignment and the 13 TeV collisions. This feature was nearly eliminated in both directions through the L3 alignment of the IBL sensors.

The local x and y residual distributions for the Pixel detector barrel and end-caps are shown in Figures 4.8 and 4.9. Even though the IBL is not included in the plots of the barrel, some of the noticeable improvement in the more sensitive local x -direction is an effect of the improved IBL alignment. Similarly, the relatively broad local y residual distribution in the barrel likely indicates

¹²The IBL contains 12 planar sensors in the center of a stave, with four 3D sensors on either end. Only the planar sensors are shown here due to low statistics in the 3D sensors as well as poor MC modeling of these sensors.

that further refinement of the IBL alignment was needed along that direction. Even so, the June alignment outperforms the March alignment and rivals the simulation in most of the plots.

Similar distributions for the SCT and TRT barrel and end-caps are shown in Figures 4.10 and 4.11, respectively. Much like with the Pixel residuals, there is a reduction in the width of the TRT residuals between the March and June alignments due to the alignment of the other subdetectors improving the quality of the track fit. Even though neither subdetector was aligned at module-level, the residuals indicate that the previous L3 alignment performed in Run 1 did not degrade significantly during the upgrade and maintenance period.

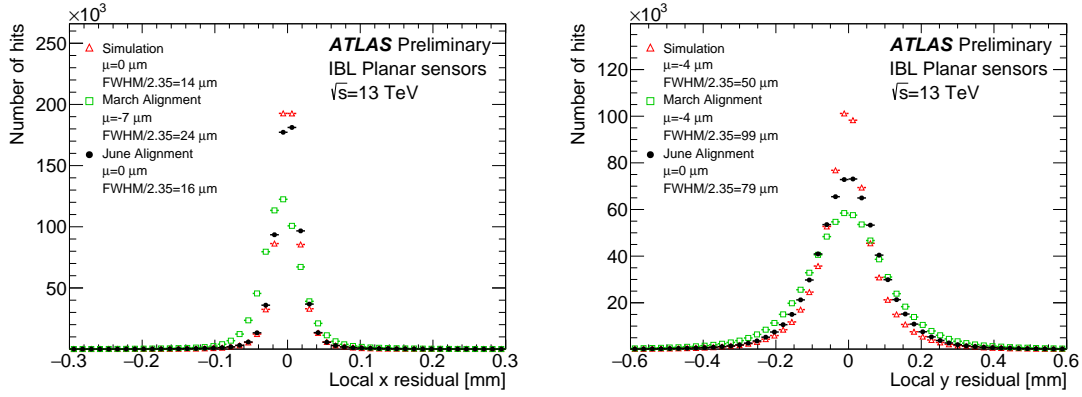


Figure 4.6: Local x (left) and local y (right) residual distributions of the IBL planar sensors using 13 TeV collision data sample reconstructed using the June (black) and March (green) alignments. The data is compared to a MC simulation using a perfect detector geometry (red). The distributions are normalized to the same number of entries.

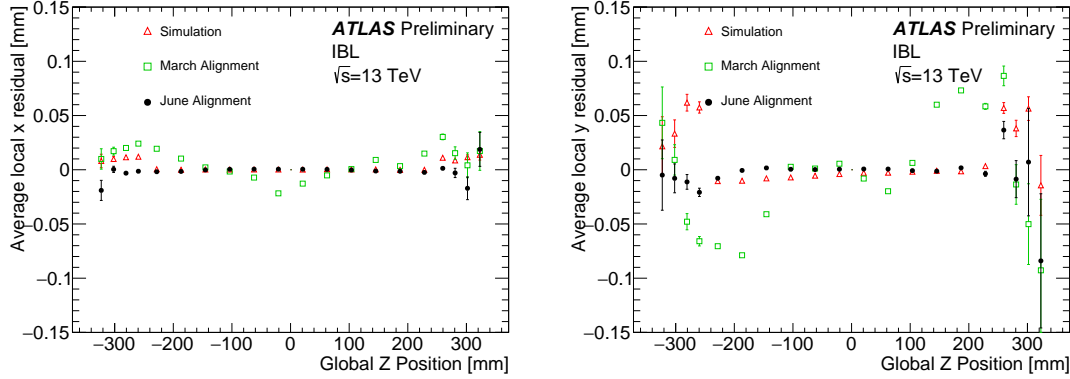


Figure 4.7: The mean of the local x (left) and local y (right) residual distributions as a function of the global z position of each IBL module using 13 TeV collision data sample reconstructed using the June (black) and March (green) alignments. The data is compared to a MC simulation using a perfect detector geometry (red).

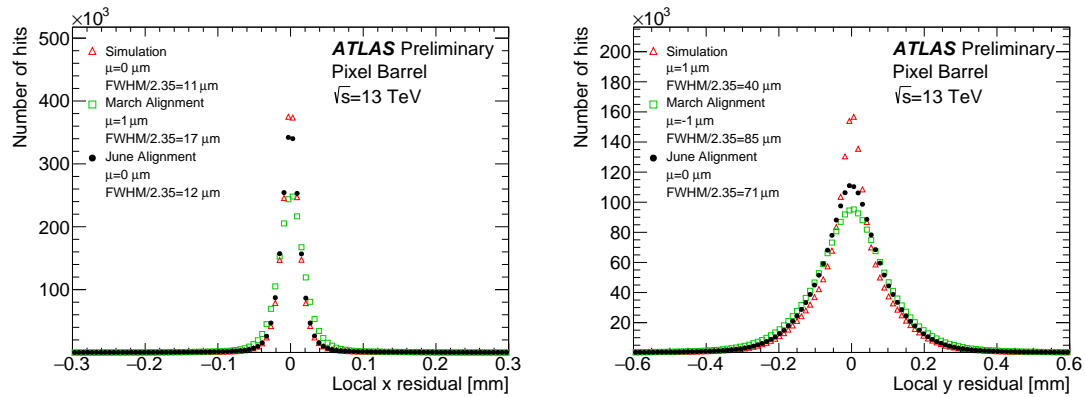


Figure 4.8: Local x (left) and local y (right) residual distributions for the Pixel barrel (excluding the IBL) using 13 TeV collision data sample reconstructed using the June (black) and March (green) alignments. The data is compared to a MC simulation using a perfect detector geometry (red). The distributions are normalized to the same number of entries.

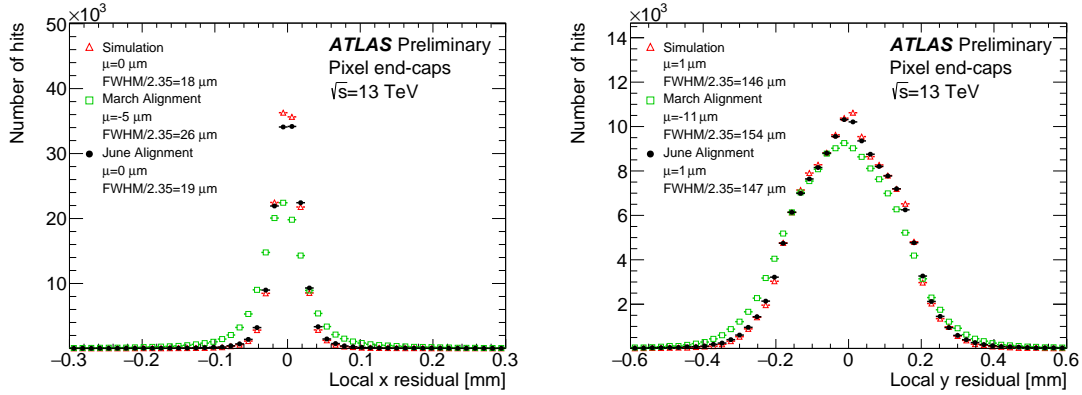


Figure 4.9: Local x (left) and local y (right) residual distributions for the Pixel end-caps using 13 TeV collision data sample reconstructed using the June (black) and March (green) alignments. The data is compared to a MC simulation using a perfect detector geometry (red). The distributions are normalized to the same number of entries.

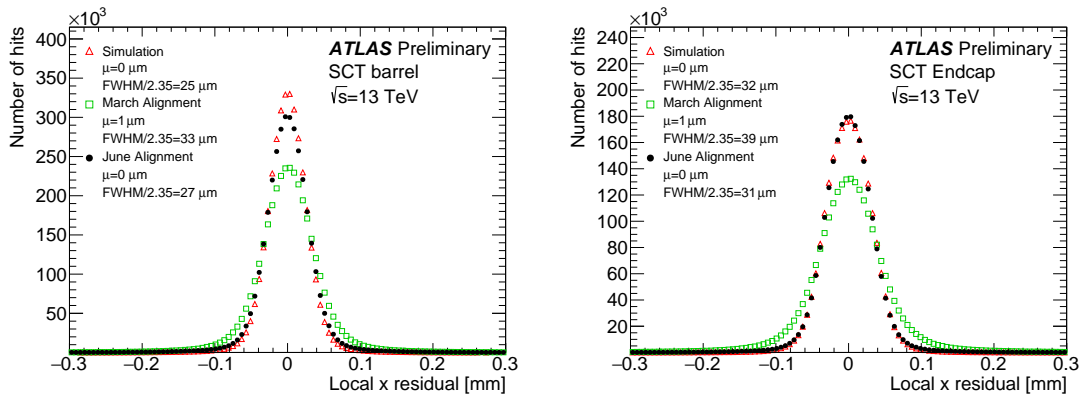


Figure 4.10: Local x residual distributions for the SCT barrel (left) and end-caps (right) using 13 TeV collision data sample reconstructed using the June (black) and March (green) alignments. The data is compared to a MC simulation using a perfect detector geometry (red). The distributions are normalized to the same number of entries.

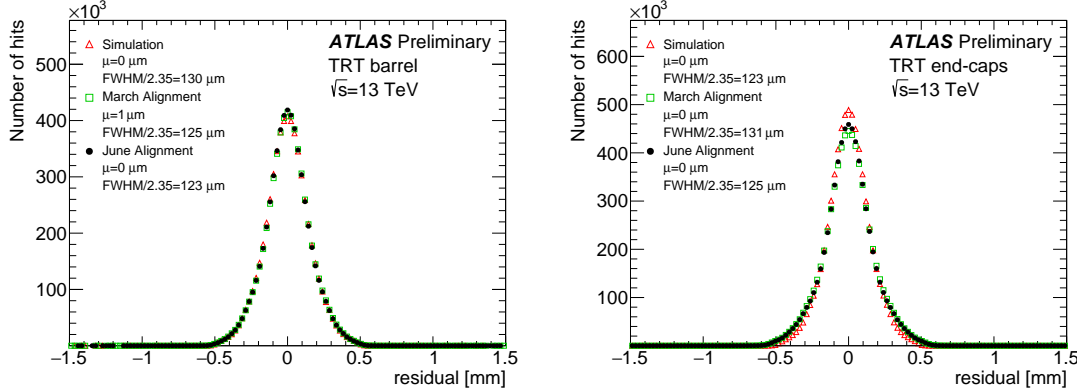


Figure 4.11: Residual distributions for the TRT barrel (left) and end-caps (right) using 13 TeV collision data sample reconstructed using the June (black) and March (green) alignments. The data is compared to a MC simulation using a perfect detector geometry (red). The distributions are normalized to the same number of entries.

4.2.2.2 Track parameter resolution from cosmic rays

Cosmic ray data is very useful as an independent check on the alignment in the barrel of the detector. While tracks from proton-proton collisions originate within the detector and travel outwards, a cosmic ray that passes through the center of the detector leaves a track in both halves of the detector. If the cosmic ray is split in half, as in Figure 4.12, then it can be treated as two separate tracks each with nearly identical track parameters (some differences arise due to energy loss as the particle passes through the detector). The distribution of the difference in a given track parameter $\Delta\tau$ is approximately Gaussian with a variance $\sigma^2(\Delta\tau)$. Since both tracks come from the same particle, each track individually has a variance equal to $\sigma^2(\Delta\tau)/2$. The resolution of the track parameter is then given by the root mean square of the distribution divided by $\sqrt{2}$.

Cosmic rays whose split tracks each have transverse momentum $p_T > 2$ GeV and at least one, eight, and 25 hits in the barrels of the Pixel, SCT, and TRT detectors, respectively, were selected to measure a collection of track parameters. Figure 4.13 shows the difference in the impact parameter Δd_0 and the charge divided by the transverse momentum $\Delta q/p_T$ of the selected split-track cosmic rays for both the March and June alignments. Both distributions show a reduction in width in the June alignment, corresponding to an improvement in the resolution of each track parameter. The Δd_0 plot in particular shows significant improvement with the June alignment, further validating the removal of the bias in the impact parameter.

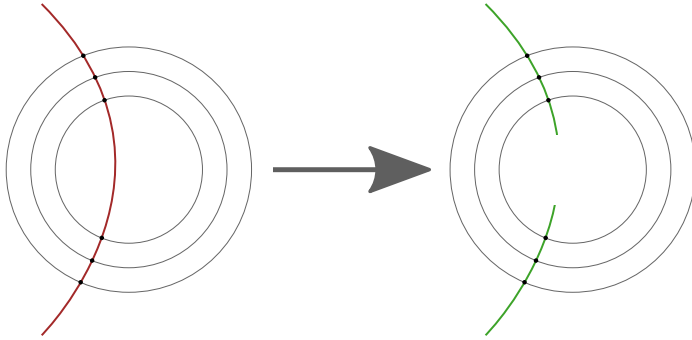


Figure 4.12: Representation of splitting a single cosmic ray track passing through the entire detector (left) into two separate tracks (right).

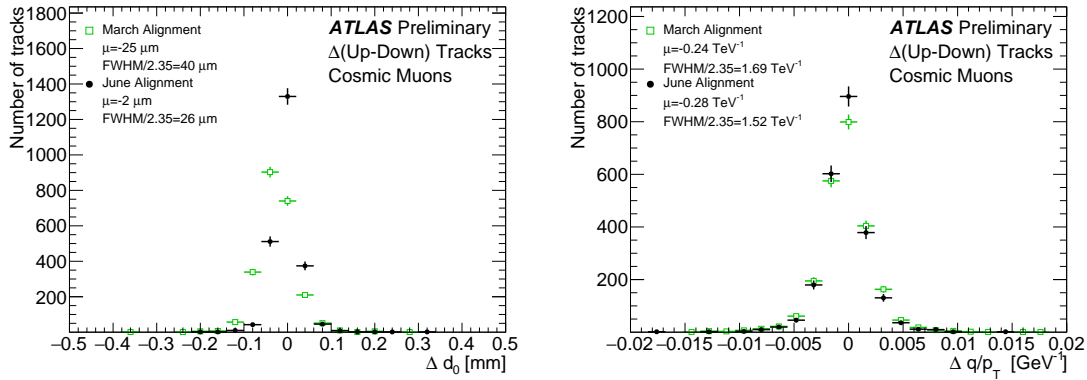


Figure 4.13: Distribution of the difference in the impact parameter Δd_0 (left) and charge over transverse momentum $\Delta q/p_T$ (right) between the two cosmic ray split tracks. The June (black) and March (green) alignments are compared. The distributions are normalized to the same number of entries.

4.2.3 Error scaling

The final step in preparing the new set of June alignment constants deals with the adjustment of the hit errors, or *error scaling*. Knowledge of the exact position of a hit measurement on a track is limited by the accuracy with which the sensors' positions are known. Let σ represent the hit uncertainty used in track fitting, and σ_0 be the detector's intrinsic uncertainty. If $\sigma = \sigma_0$, the pull of the track-hit residual distributions should form a Gaussian distribution centered at zero with unit width [66]. In the case of residual misalignment, the pull distributions' standard deviations will stray from unity. The hit uncertainty can be written as

$$\sigma = a \cdot \sigma_0 \oplus b, \quad (4.12)$$

where a is a scaling factor, and b is a constant term which can be interpreted as a measure of any remaining misalignment of the detector elements. In the June alignment campaign, the value of a was fixed at $a = 1$, and b was evaluated from the residual pull distributions for each subdetector in its sensitive directions.

Once the value of b is determined, pull distributions derived from the new value of σ should have unit width. The error scaling values for each subdetector are listed in Table 4.3, and the pull distributions for the IBL after error scaling are shown in Figure 4.14

Detector	Coordinate	$b(\mu\text{m})$
IBL	x	6.4
	y	43.6
Pixel	x	5.2
	y	28.6
Pixel	x	7.5
	y	0
SCT	x	10.8
	x	8.6
TRT	$r\phi$	0
	$r\phi$	0

Table 4.3: Estimated value of the error scaling term b for each subdetector component with the June alignment.

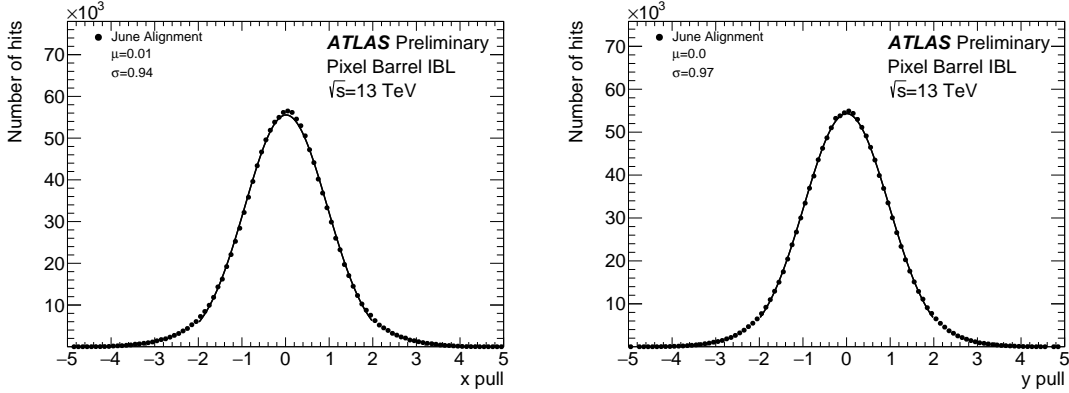


Figure 4.14: Pull distributions in local x (left) and y (right) for the IBL using 13 TeV collision data sample after applying the error scaling.

4.3 Level 2 alignment of the TRT

During validation of the final end-of-year reprocessing of the 2015 data, a misalignment was found in the barrel of the TRT detector, as several modules (triangular clusters of straws) showed rotations in the local y coordinate. The then-best available constants included a full L3 alignment of the silicon detectors and a separate L2 alignment of the TRT. However, not all degrees of freedom were enabled when the TRT was aligned. To correct for these tilts, an additional four iterations of L2 alignment was performed on the TRT enabling all available degrees of freedom (T_x , T_y , R_x , R_y , and R_z in the barrel, and T_x , T_y , and R_z for the endcaps). Plots of the residual means from TRT barrel ϕ -sectors containing modules affected by the tilt misalignment are shown in Figure 4.15 before and after the L2 alignment.

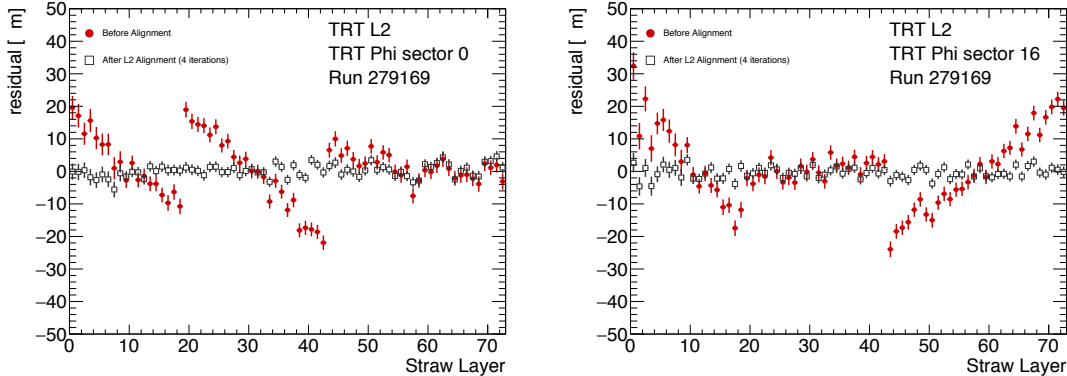


Figure 4.15: Residual means by straw layer in two TRT ϕ -sectors affected by a tilt misalignment. The tilts in each of the three modules are clearly visible in the red points representing the reconstructed data prior to alignment. After four iterations of L2 alignment, the residual means in the gray points are flat.

Following the L2 alignment, some additional time was taken to determine if a full wire-by-wire L3 alignment of the TRT was necessary. The TRT was last aligned at L3 during Run 1, but initial alignment campaigns in Run 2 did not show signs of misalignment (see, for example, the residual distributions shown earlier in Figure 4.11). In order to assess the alignment more carefully, two dimensional residual maps in ϕ and z were constructed for each layer in the TRT barrel and endcaps using the current alignment. These maps were compared to a similar set using the L3 alignment from 2010, from which it was determined that the straw-level alignment indeed hadn't degraded, and a new L3 alignment was not needed. The maps for the first layer of the TRT barrel are shown in Figure 4.16 for both sets of alignment constants.

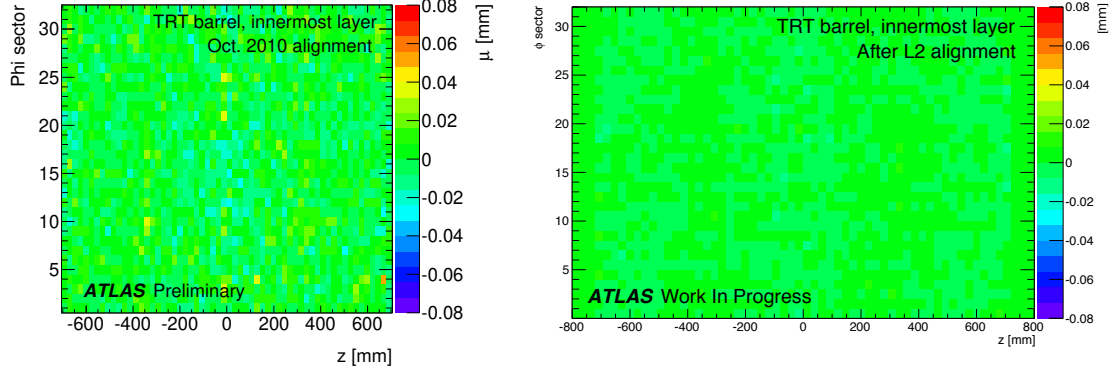


Figure 4.16: Two dimensional map of residuals in the first layer of the TRT barrel vs z and ϕ . Each bin represents the mean of a Gaussian fit to the TRT residuals in that bin. The map on the left is after the L3 (wire-by-wire) alignment of the TRT performed in 2010, and the map on the right is after the L2 alignment at the end of 2015. The z -axis for both plots use the same scale. Left figure taken from [66].

4.4 Momentum bias from sagitta deformations

A variety of weak mode deformations can exist in the detector even after alignment. As mentioned previously, these weak modes consist of misalignments which don't affect the χ^2 of the residuals and thus are not handled by the unconstrained alignment algorithm. In the presence of a weak mode, the description of the detector geometry can still provide efficient and high quality track fits, but there may also be systematic biases in one or more track parameters. Several weak modes, their impacts on the reconstruction, and the steps taken to eliminate them are detailed in [71, 78]. This section focuses specifically on *sagitta* deformations that result in a bias in the reconstructed track momentum.

These sagitta distortions consist of detector movements orthogonal to the trajectory of the outgoing particle. The effect on the reconstructed track curvature is different for positively and negatively charged particles, resulting in a charge-antisymmetric bias. An example of this is illustrated by the curl deformation in Figure 4.17.

In the plane transverse to ATLAS's magnetic field, outgoing particle tracks form circular arcs. The sagitta is defined as the distance from the center of this arc to the center of its base, as shown in Figure 4.18, and it represents the “amount of bending” in the track. In the case where the sagitta s is considerably smaller than the detector radius R_0 , which is a valid assumption when working

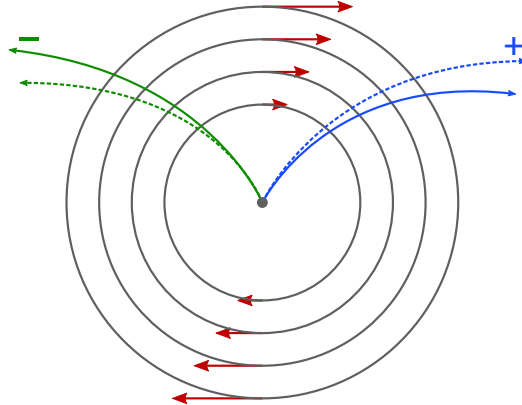


Figure 4.17: Representation of a curl distortion in the detector. The image represents a cutaway view of the transverse plane of the barrel region. The deformation is represented by the red arrows, and the impact on the reconstructed positive (blue) and negative (green) tracks are shown. The dashed lines represent the true particle trajectories, and the solid lines represent the reconstructed trajectories.

with high momentum tracks, the transverse momentum of a particle of charge q can be written as

$$p_T \propto qB \frac{R_0^2}{8s}, \quad (4.13)$$

where B is the strength of the detector's magnetic field [79]. If a sagitta bias is present, the track's transverse momentum shifts by

$$q/p_T \rightarrow q/p_T + \delta_s \quad \text{or} \quad p_T \rightarrow p_T \cdot (1 + qp_T\delta_s)^{-1}, \quad (4.14)$$

where δ_s is a universal bias parameter that uniquely defines the deformation [78]. Finally, since the reconstructed polar angle does not change under a sagitta deformation, the longitudinal component of the momentum scales along with the transverse component, and an equivalent equation can be written for the total momentum:

$$p \rightarrow p \cdot (1 + qp_T\delta_s)^{-1}. \quad (4.15)$$

4.4.1 Sagitta bias monitoring with electron E/p

Since a sagitta bias results in changes in the momenta of particle tracks as measured by the ID, they can be identified using independent measurements from other systems in the detector. One such method involves using the energy-momentum ratio of electrons (E/p). Since the electron's energy is measured in ATLAS's calorimeter systems, it is not sensitive to any sagitta bias that may exist

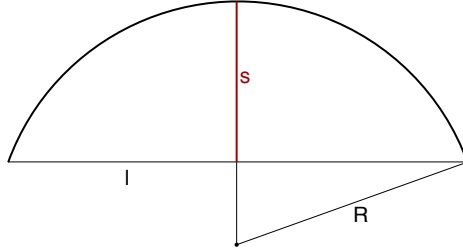


Figure 4.18: Geometric definition of the sagitta s in relation to the length of the chord l and the radius R of a circular arc.

in the ID and in the corresponding measurement of the track momentum. Under the assumption that the calorimeter response is independent of the charge of incoming particles, a charge-dependent momentum bias in the ID will manifest as a difference in the E/p ratio for electrons and positrons.

In the presence of a sagitta bias, the momentum will change according to Equation 4.15 and the average measured $\langle E/p \rangle$ can be written as

$$\langle E/p \rangle^\pm \rightarrow \langle E/p \rangle^\pm \pm \langle E_T \rangle \delta_s , \quad (4.16)$$

where the approximation $p_T \approx E_T$ is used. Assuming that $\langle E/p \rangle^+ = \langle E/p \rangle^-$ in the absence of a bias, the sagitta bias parameter can be solved for:

$$\delta_s = \frac{\langle E/p \rangle^+ - \langle E/p \rangle^-}{2\langle E_T \rangle} . \quad (4.17)$$

If the kinematic selections for electrons and positrons are identical, the energy scale of the calorimeter will not factor into the $\langle E/p \rangle$ difference; however, it will affect $\langle E_T \rangle$, which would scale the measured δ_s . This is expected to be a small effect, as the energy scale for electrons has been measured at 13 TeV with uncertainties on the per-mil level across the entire detector [80].

4.4.1.1 Measuring $\langle E/p \rangle$

The E/p ratio is measured using electrons and positrons from $Z \rightarrow ee$ events in order to obtain a high purity sample of candidate particles. They are required to pass a basic selection criteria to ensure they are well measured in both the ID and the calorimeters:

- $E_T > 25$ GeV
- $|\eta| < 2.47$, excluding the calorimeter's barrel-to-endcap transition region in $1.37 < |\eta| < 1.52$
- Pass the MediumLH identification working point detailed in Section 3.3.2

- Pass a selection of quality cuts, including a requirement that the electron be identified using cluster information in the calorimeter
- The associated track must have at least one hit in the IBL, three in the Pixel detector, and five in the SCT detector.

Events containing exactly two opposite-charge electrons passing this selection with an invariant mass within 30 GeV of the Z boson mass are then used for the E/p calculation.

Since the size of the sagitta bias δ_s is not expected to be constant across the entire detector, a two-dimensional rectangular grid is constructed binned in detector η and ϕ . From the selected events, separate distributions of E/p are made for electrons and positrons within each bin. Each distribution is fit with Crystal Ball function¹³, and the peak of the distribution is taken as the value of $\langle E/p \rangle$. If there is no bias on the track momentum in the bin, the peaks for electrons and positrons should agree. Example E/p distributions including the Crystal Ball fits are shown in Figure 4.19.

It is important to emphasize that deviations from one in the *ratio* of $\langle E/p \rangle^+$ to $\langle E/p \rangle^-$ points to a potential momentum biases. The value of $\langle E/p \rangle$ itself is not expected to equal one exactly, as the track momentum on average tends to be slightly lower than the energy measurement in the calorimeter. This is due to the fact that if the electron were to radiate a photon, its momentum would change slightly, while it is likely that both the electron and the emitted photon would leave energy deposits near each other in the calorimeter and be reconstructed into the same object.

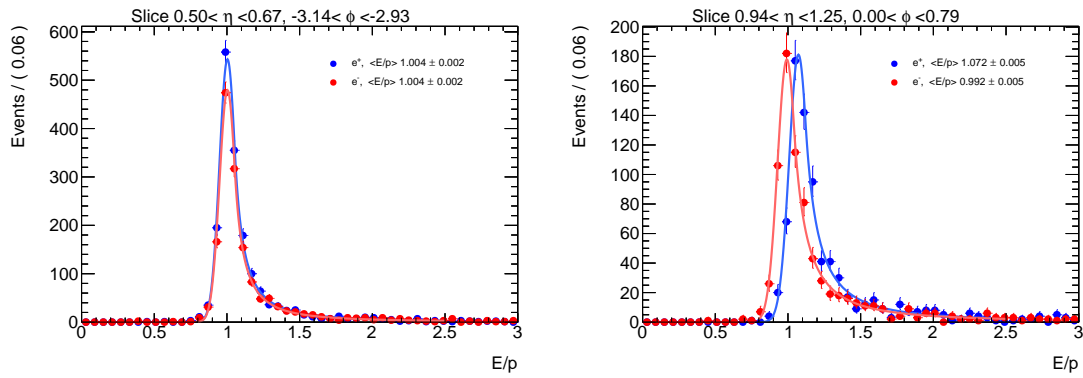


Figure 4.19: E/p distributions of electrons and positrons in two different $\eta\phi$ bins of the detector. The left hand plot is taken from a region with no momentum bias where $\langle E/p \rangle^+ = \langle E/p \rangle^-$, while the right hand plot shows an 8% disagreement in $\langle E/p \rangle$ between electrons and positrons.

¹³The Crystal Ball function is a probability density function consisting of a Gaussian core and a power-law tail.

Once the $\langle E/p \rangle^\pm$ distributions in each $\eta\text{-}\phi$ bin have been extracted from the fits, a two dimensional map of δ_s can be constructed using Equation 4.17. The map gives an overview of sagitta biases that may be present in the detector, and can be used by the alignment algorithm to reduce the bias in the next iteration. In this case, the tracks fed to the alignment have their momenta corrected according to

$$q/p_{\text{corr}} = q/p_{\text{reco}}(1 - qp_T\delta_s), \quad (4.18)$$

where p_{reco} is the reconstructed momentum of the track [78]. The corrected momentum is then constrained in the alignment.

4.4.1.2 Results in 13 TeV data

The E/p method has been used to monitor sagitta biases in the detector several times over the course of Run 2. During this time, it has primarily served as an independent cross-check to a second method using $Z \rightarrow \mu\mu$ events [78]. The $Z \rightarrow \mu\mu$ method identifies individual track momentum biases through shifts in the reconstructed Z mass, which leaves it relatively insensitive to global sagitta biases. For this reason, the sagitta bias maps produced using this technique are normalized to those from the E/p method before being used to constrain the alignment. The results of two implementations of the E/p method are presented here.

1. The first follows the end-of-year reprocessing of the entire ATLAS 2016 data set. Two sets of alignment constants are compared: the *prompt* alignment, which was derived shortly after each run was recorded, and the *reprocessed* alignment. The maps of the sagitta bias in each alignment calculated using the E/p method are shown in Figure 4.20, and the comparison of the η projection of the maps is shown in Figure 4.21.
2. The second uses the 2017 data after reprocessing, and compares the effects of multiple iterations of the E/p method. In each iteration, the momenta of the electrons and positrons are corrected according to Equation 4.15 using the value of δ_s computed in the previous iteration, and a new sagitta bias map is calculated. If the method is indeed characterizing the sagitta biases correctly, the corrections should converge quickly. The initial sagitta bias map is compared to the map after two such iterations in Figure 4.22, and the sagitta bias projected along η for each iteration is shown in Figure 4.23. Indeed, after just two iterations, δ_s is consistent with zero in nearly all bins.

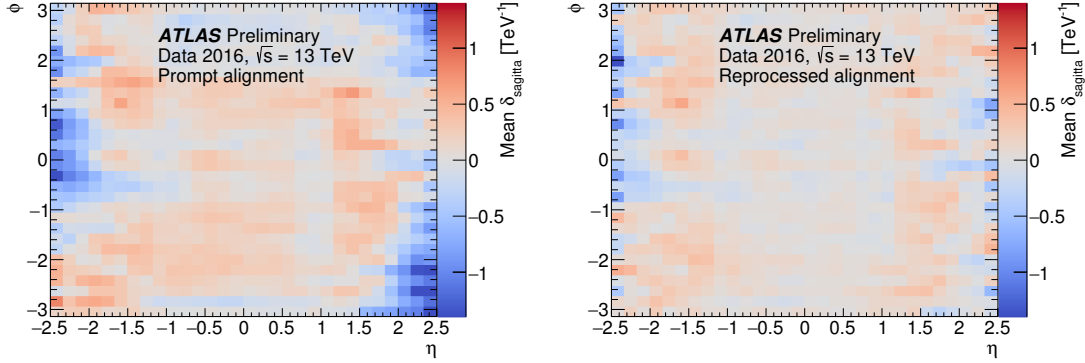


Figure 4.20: Sagitta bias in the $\sqrt{s} = 13$ TeV data collected by ATLAS in 2016 as a function of η and ϕ for the prompt (left) and reprocessed (right) alignments using the E/p method.

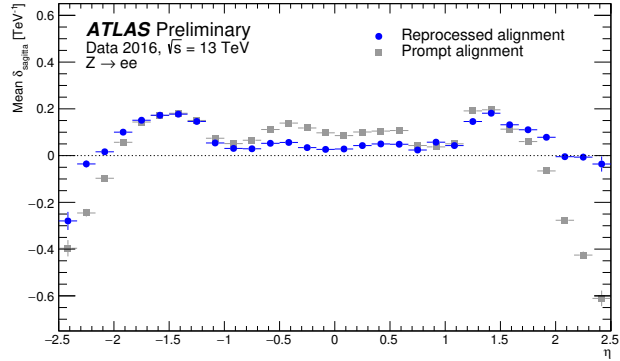


Figure 4.21: Sagitta bias in the $\sqrt{s} = 13$ TeV data collected by ATLAS in 2016 projected along η for the prompt (gray) and reprocessed (blue) alignments using the E/p method.

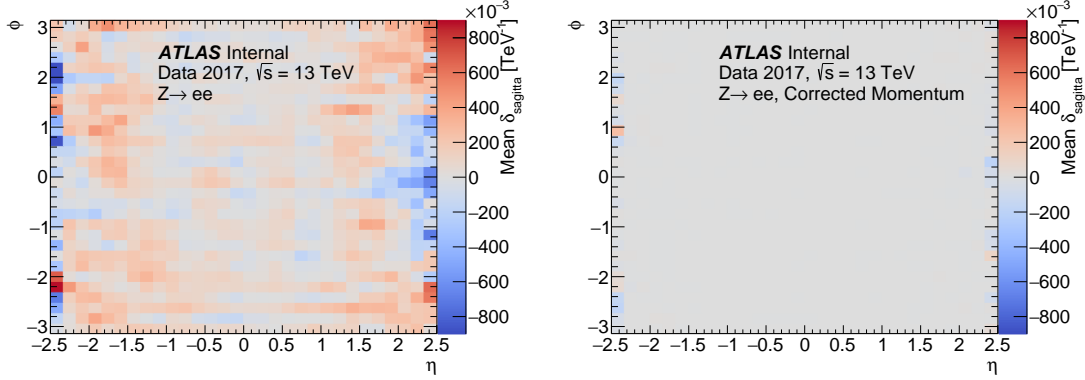


Figure 4.22: Sagitta bias in the $\sqrt{s} = 13$ TeV data collected by ATLAS in 2017 as a function of η and ϕ in reconstructed electrons (left) and after two iterations of momentum corrections (right) from the E/p method.

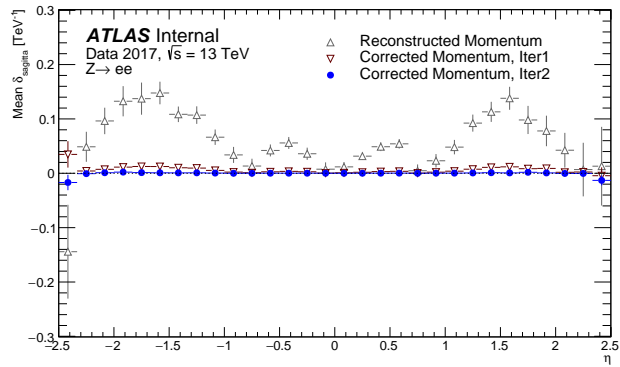


Figure 4.23: Sagitta bias in the $\sqrt{s} = 13 \text{ TeV}$ data collected by ATLAS in 2017 projected along η in reconstructed electrons (gray) and after one (red) and two (blue) iterations of momentum corrections from the E/p method.

CHAPTER 5

Measurement of same-sign WW production at $\sqrt{s} = 13$ TeV with ATLAS

Production of same-sign W boson pairs is a particularly interesting SM process. When produced via vector boson scattering (VBS), $W^\pm W^\pm jj$ is sensitive to the electroweak symmetry breaking (EWSB) mechanism as well as potential Beyond the Standard Model (BSM) physics processes. $W^\pm W^\pm jj$ events can be produced via electroweak-mediated (EWK) diagrams, of which VBS is a subset, or QCD-mediated diagrams. The biggest advantage of same-sign $W^\pm W^\pm jj$ over other VBS processes lies in its ratio of electroweak (EWK) to QCD production cross sections. Despite the opposite-sign $W^\pm W^\mp$ having a larger total cross section, its EWK-mediated diagrams are much smaller than its QCD-mediated diagrams, while for same-sign $W^\pm W^\pm$ the EWK production is considerably larger. This makes $W^\pm W^\pm jj$ one of the premier channels for studying VBS at the LHC.

The first evidence of electroweak (EWK) $W^\pm W^\pm jj$ production was seen by the ATLAS and CMS experiments at $\sqrt{s} = 8$ TeV with excesses of 3.6σ [81] and 2.0σ [82] over backgrounds, respectively. More recently, ATLAS and CMS have both observed the EWK process at $\sqrt{s} = 13$ TeV with significances of 6.9σ [2] and 5.5σ [83], respectively. The ATLAS $\sqrt{s} = 13$ TeV observation and cross section measurement of EWK-produced $W^\pm W^\pm jj$ is presented in this chapter [84, 85].

5.0.1 Experimental overview of vector boson scattering

VBS processes are very important to understand due to their sensitivity to the EWSB mechanism. As explained in Section 2.3, in the absence of a light SM Higgs boson, the scattering amplitude of longitudinally polarized vector bosons grows with center-of-mass energy. However, once the Higgs

is introduced, the divergences cancel and the cross section no longer grows unbounded.

With the discovery of the Higgs boson in 2012 [18, 19], the EWSB mechanism can now be directly studied. Due to the potential exchange of a Higgs boson in the VBS diagrams ($W^\pm W^\pm jj$ itself does not contain an s -channel Higgs exchange), VBS processes are directly sensitive to properties of the Higgs. For example, the high-mass tail in the VV scattering system allows an approximation of the effective coupling strength of the Higgs to vector bosons that is independent of any assumptions on the Higgs width [86]. Additionally, the center of mass energy dependence of the VV scattering can reveal whether the Higgs boson unitarizes the longitudinal scattering amplitude fully or only partially [87].

VBS events are characterized by two quarks from the colliding protons each radiating a vector boson which then scatter and decay in the detector. The incoming quarks carry a large amount of momentum and only deflect a small amount upon emitting the vector boson; as a result, they often enter the calorimeters very close to the beam line. Ignoring the decay products of the scattered bosons for now, these VBS events result in a final state of two vector bosons (V) and two jets (j) at high pseudorapidity (called *forward jets* or *tag jets*) from the outgoing quarks. The shorthand $VVjj$ is used to represent this final state.

$VVjj$ events can be produced via two different physical processes. The first involves purely electroweak interactions in the tree-level diagrams, of order $\mathcal{O}(\alpha_{\text{EWK}}) = 6$ in the electroweak coupling constant, and will be referred to as *EWK production*. This can be further broken down into VBS and non-VBS events. In the VBS EWK production, the scattering occurs via triple or quartic gauge couplings, as well as the exchange of a Higgs boson. The non-VBS EWK production contains the same final state of two vector bosons and two outgoing quarks, but the bosons do not scatter. Due to gauge invariance, it is not possible to separate the VBS from the non-VBS productions [88]; therefore, both are included in the signal generation and are indistinguishable from one another. The second process involves a mix of the EWK and strong interactions, of order $\mathcal{O}(\alpha_s) = 2 \otimes \mathcal{O}(\alpha_{\text{EWK}}) = 4$, and will be referred to as *QCD production*. The tree-level Feynman diagrams for VBS EWK, non-VBS EWK, and QCD $VVjj$ production are found in Figures 5.1, 5.2, and 5.3, respectively.

5.0.2 Same-sign $W^\pm W^\pm$ scattering

Same-sign $W^\pm W^\pm jj$ scattering is considered to be one of the best channels for studying VBS at the LHC due to its favorable ratio of EWK to QCD production [86]. Since the VBS diagrams are the primary interest for analysis, the QCD production is considered a background. Therefore a

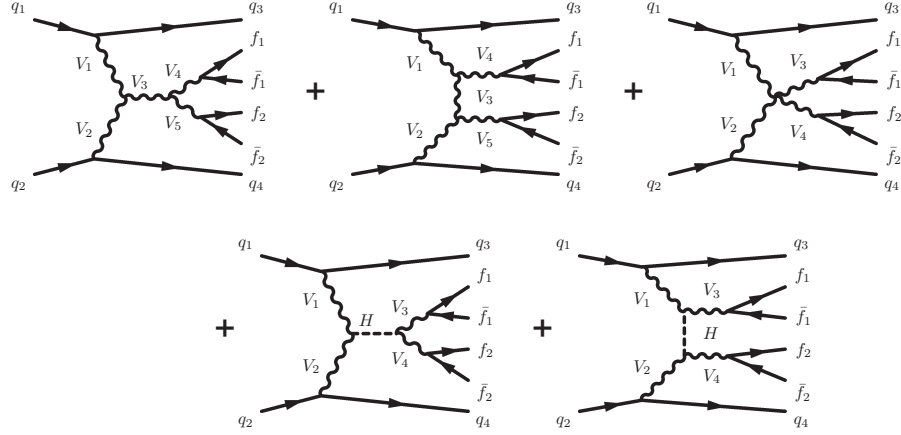


Figure 5.1: Tree-level Feynman diagrams for VBS EWK $VVjj$ production including triple gauge couplings involving W and/or Z bosons (top left and top middle), quartic gauge coupling (top right), or the exchange of a Higgs boson (s -channel bottom left and t -channel bottom right). The labels are quarks (q), fermions (f), and gauge bosons ($V = W, Z$).

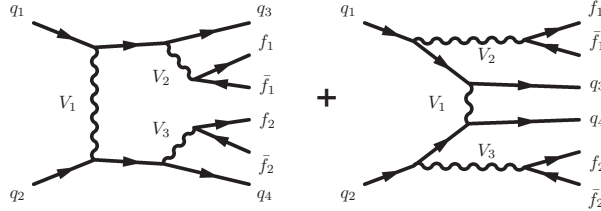


Figure 5.2: Tree-level Feynman diagrams for non-VBS EWK $VVjj$ production. The labels are quarks (q), fermions (f), and gauge bosons ($V = W, Z$).

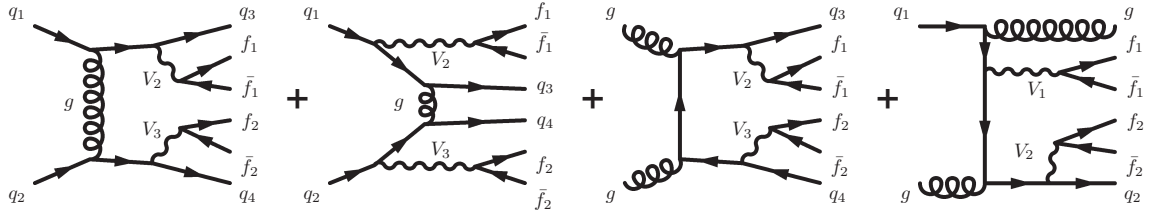


Figure 5.3: Tree-level Feynman diagrams for QCD $VVjj$ production. The labels are quarks (q), fermions (f), and gauge bosons ($V = W, Z$).

higher EWK-to-QCD ratio results in increased sensitivity to VBS. EWK and QCD cross sections at $\sqrt{s} = 13$ TeV for six leptonic $VVjj$ final states were calculated using the **SHERPA** MC generator in a VBS-enriched fiducial phase space in [89]. Despite its relatively low total cross section compared to some other $VVjj$ processes, the EWK-to-QCD ratio for $W^\pm W^\pm jj$ is 10-20 times higher than for other processes after applying VBS-enhancing selection criteria.

Final state	Process	σ_{EWK} [fb]	σ_{QCD} [fb]	$\sigma_{\text{EWK}}/\sigma_{\text{QCD}}$
$l^\pm l^\mp l^\pm l^\mp jj$	ZZ	0.098	0.100	0.98
$l^\pm l^\pm l^\mp \nu\nu jj$	$W^\pm Z$	2.34	4.38	0.53
$l^\pm l^\mp \nu\nu jj$	$W^\pm W^\mp, ZZ$	12.3	21.8	0.56
$l^\pm l^\pm \nu\nu jj$	$W^\pm W^\pm$	3.97	0.346	11.47
$l^\pm \nu\nu jj$	$W^\pm Z$	7.64	15.5	0.49
$\nu\nu\nu\nu jj$	ZZ	1.68	1.38	1.22

Table 5.1: Predicted cross sections for EWK and QCD production of diboson processes relevant to VBS at $\sqrt{s} = 13$ TeV using the **SHERPA** MC generator. The numbers for the $W^\pm W^\pm jj$ process are in bold. Leptons are required to have $p_T \geq 25$ GeV and lie within $|\eta| \leq 2.5$ with $m_{ll} > 20$ GeV, and at least two jets are required with $p_T \geq 30$ GeV and $|\eta| < 4.5$. The VBS contributions are enhanced by requiring the dijet invariant mass $m_{jj} > 500$ GeV and dijet separation $\Delta y_{jj} > 2.4$. Numbers taken from [89].

This analysis studies $W^\pm W^\pm jj$ scattering where both W bosons decay leptonically to $e\nu$ or $\mu\nu$ ¹⁴. The $W^\pm W^\pm jj$ VBS final state consists of two leptons with the same electric charge, two neutrinos, and two high energy forward jets with a large invariant mass. Tree-level Feynman diagrams of VBS $W^\pm W^\pm jj$ production can be found in Figure 5.4 and a visual representation of the VBS topology can be found in Figure 5.5.

The two tag jets in the characteristic VBS signature also serve as a powerful tool to suppress the QCD production mode. In EWK events, the two jets tend to have much higher separation and a larger combined invariant mass than the two leading jets in a QCD event. The two plots shown in Figure 5.6 highlight the differences in these dijet quantities between the two production modes. Finally, an ATLAS event display of a real $W^\pm W^\pm jj$ candidate event is shown in Figure 5.7.

5.0.3 Overview of backgrounds

In addition to QCD production of $W^\pm W^\pm jj$ events, there are several other processes with a final state of two same-sign leptons, two neutrinos, and two jets. However, due to the ± 2 final state charge,

¹⁴Throughout the rest of this chapter, unless stated otherwise, l denotes either electrons (e) or muons (μ), and ν denotes a neutrino. Additionally, e , μ , and ν with no charge or anti-particle designation refer interchangeably to either the particle or anti-particle.

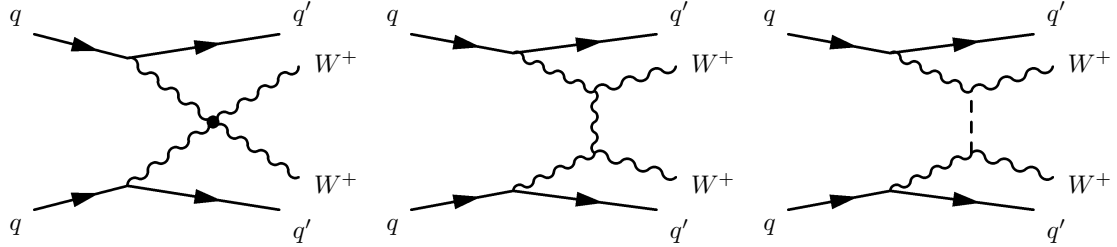


Figure 5.4: Leading order Feynman diagrams for VBS EWK production of $W^\pm W^\pm jj$ events. The leftmost diagram contains a quartic gauge coupling vertex, and the rightmost diagram contains an exchange of a Higgs boson.

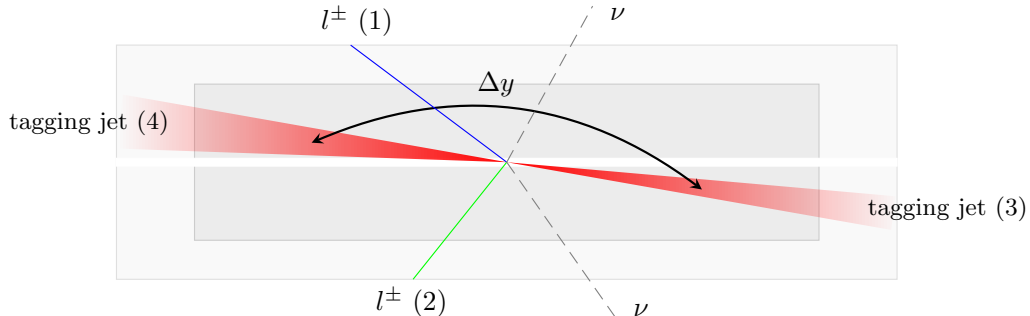


Figure 5.5: $W^\pm W^\pm jj$ VBS event topology containing two leptons (1 and 2) with the same electric charge, two neutrinos, and two forward tagging jets (3 and 4) with large rapidity separation Δy . Figure taken from [90].

there is a considerable reduction in SM backgrounds (such as Z boson events) when compared to an analysis like opposite-sign $W^\pm W^\mp jj$.

One of the largest background sources involves processes with prompt leptons¹⁵. These are events that contain two leptons with the same electric charge and one or more additional leptons that are “lost”, either by failing the selection criteria or falling outside of the detector’s acceptance. The number of processes that can contribute is limited by the requirement of same-sign leptons, and as a result this background is dominated by multi-boson processes, with the largest contribution coming from WZ events and smaller contributions from ZZ and $t\bar{t} + V$ events. Triboson events where one boson decays hadronically also contribute to this background; however, the jets are generally softer and more central than in a typical VBS event, and the cuts applied on the forward jets suppress

¹⁵Prompt leptons are those that are produced in the primary collision and are a direct decay product of the process of interest. Non-prompt leptons originate from some secondary process, such as a b -hadron decay. Jets that are mis-reconstructed as a lepton are also considered non-prompt.

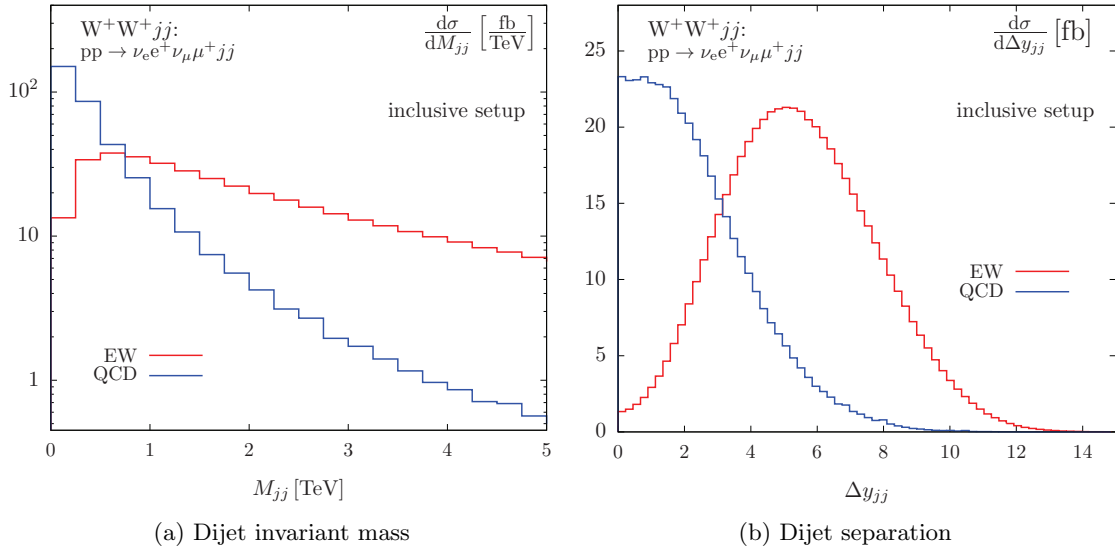


Figure 5.6: Generator level comparisons at $\sqrt{s} = 7$ TeV of dijet invariant mass (M_{jj} , left) and dijet rapidity (Δy_{jj} , right) in EWK (red) and QCD (blue) $W^\pm W^\pm jj$ events with no selection cuts applied. Plots taken from [91].

these contributions.

The other dominant background comes from non-prompt, or “fake”, leptons. Here one or more leptons originate from the decay of another particle unrelated to the signal process, such as a heavy-flavor decay or photon conversion, or come from a jet that is misidentified as a lepton. This background is mostly made up of events from $t\bar{t}$ and $W+jets$ processes, with a much smaller contribution from conversions in $V\gamma$ events.

Finally, opposite-sign lepton pairs can enter the signal region if one of the leptons is reconstructed with the wrong charge (called *charge misidentification*¹⁶). In practice, this only affects events with electrons, as the charge misidentification rate for muons is negligible [92]. This is a major background in events with two electrons, dominated by $Z \rightarrow ee$ events; it is a much smaller contribution for events with one electron and one muon, where the primary contribution comes from $t\bar{t}$ events.

5.1 Data and Monte Carlo samples

This analysis uses 36.1 fb^{-1} of $\sqrt{s} = 13$ TeV proton-proton collisions recorded by ATLAS during the 2015 and 2016 data taking periods. The uncertainty in the combined integrated luminosity is 2.1%. It is derived following a methodology similar to that detailed in [93] and using the LUCID-2

¹⁶Charge misidentification is also referred to interchangeably as *charge mis-ID* and *charge flip*.

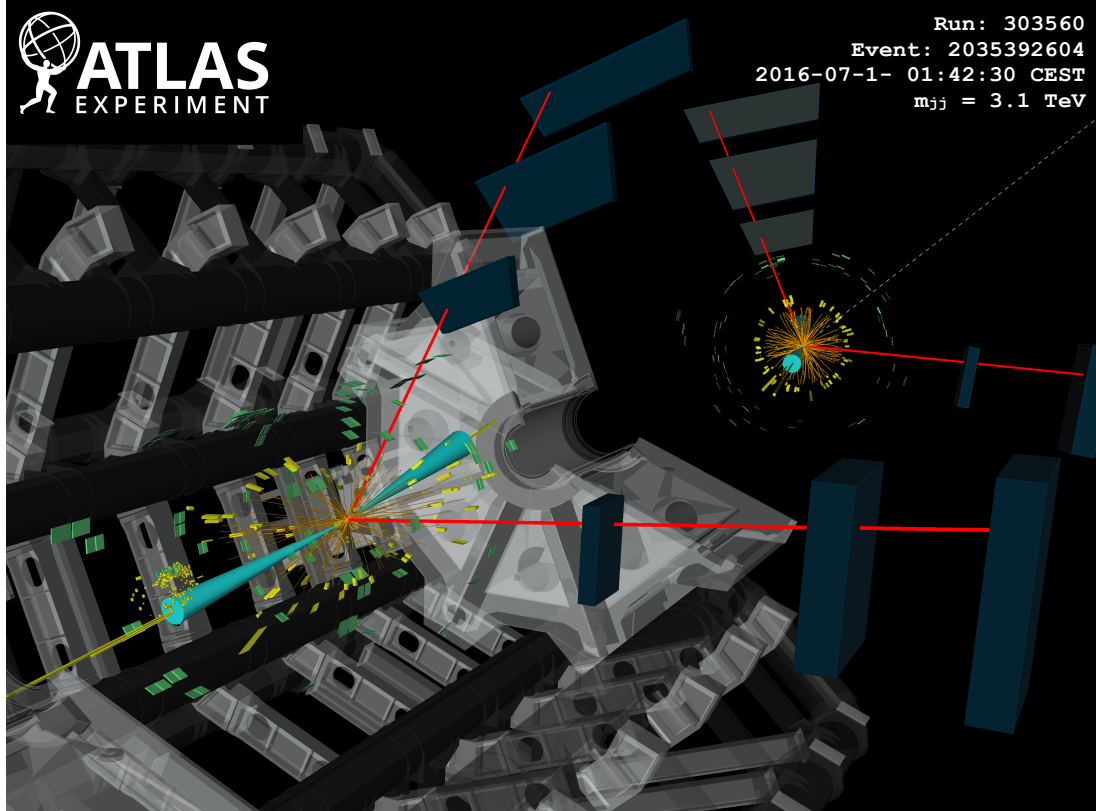


Figure 5.7: ATLAS event display of a $pp \rightarrow W^+W^+ \rightarrow \mu^+\nu_\mu\mu^+\nu_\mu jj$ event. The muons are represented by the red lines travelling from the ID through the MS, and the forward jets are represented by the blue cones with yellow energy deposits in the calorimeters. The direction of the E_T^{miss} in the transverse plane is indicated by the gray dashed line in the inset image. Event display taken from [84].

detector for the baseline luminosity measurements [94] from calibration of the luminosity scale using x - y beam-separation scans.

5.1.1 Monte Carlo samples

A number of Monte Carlo (MC) simulations are employed to model signal and background processes. In order to model the real collision data as closely as possible, each MC sample has been passed through a full simulation of the ATLAS detector in GEANT4 [95, 96], and events have been reconstructed using the same algorithms as the data. The simulation reproduces as closely as possible the momentum resolutions and calorimeter responses of the detector, and also includes the effects of pileup by including soft QCD interactions using PYTHIA v8.1 [97]. The MC samples used in this

Process	Generator	Comments
$W^\pm W^\pm jj$ (EWK)	SHERPA v2.2.2	Signal sample
$W^\pm W^\pm jj$ (EWK)	POWHEG-BOX v2	Systematics sample
$W^\pm W^\pm jj$ (QCD)	SHERPA v2.2.2	
Diboson	SHERPA v2.2.2	Both bosons decay leptonically ($llll$, $ll\nu\nu$, $l\nu\nu\nu$)
	SHERPA v2.2.1	One boson decays leptonically, the other hadronically
Triboson	SHERPA v2.1.1	
$W+jets$	SHERPA v2.2.1	
$Z+jets$	Madgraph5_aMC@NLO	
$V\gamma$	SHERPA v2.1.1	
$V\gamma jj$ (EWK)	SHERPA v2.2.4	
$t\bar{t}V$	Madgraph5_aMC@NLO	
$t\bar{t}$	POWHEG-BOX v2	
Single top	POWHEG-BOX v1	EWK t -, s -, & Wt -channels

Table 5.2: Summary of MC samples used in the analysis.

analysis are detailed in this section and summarized in Table 5.2.

The $W^\pm W^\pm jj$ samples are modeled using **SHERPA** v2.2.2 [98, 99, 100] with the NNPDF3.0 PDF set [101]. The EWK signal samples were generated by fixing the electroweak coupling constant to $\mathcal{O}(\alpha_W) = 6$, and a QCD background sample was also generated with $\mathcal{O}(\alpha_W) = 4$. **SHERPA** includes up to one parton at next-to-leading order (NLO) and up to three at leading order (LO) in the strong coupling constant α_s . A second $W^\pm W^\pm jj$ EWK sample was generated using **POWHEG-BOX** v2 [102] with the NNPDF3.0 PDF set and at NLO accuracy. This sample is only used for systematic studies, as **POWHEG-BOX** does not include resonant triboson contributions in its matrix element, which are non-negligible at NLO [103].

Diboson processes (VV where $V = W, Z$) are simulated with **SHERPA** v2.2.2 for mixed hadronic and leptonic decays and **SHERPA** v2.2.1 for fully leptonic decays of the bosons. Similarly, triboson (VVV) and $V\gamma$ processes are simulated using **SHERPA** v2.1.1 with up to one parton at NLO and up to three at LO. $W+jets$ processes are simulated with **SHERPA** v2.2.1 with up to two partons at NLO and four at LO. All the above **SHERPA** samples use the NNPDF3.0 PDF set and **SHERPA**'s own parton showering. The $Z+jets$ events are generated with **Madgraph5_aMC@NLO** [104] at LO and interfaced with **PYTHIA** v8.1 for parton showering.

$t\bar{t}$ events are generated using **POWHEG-BOX** v2 with the CT10 PDF set [105]. $t\bar{t}V$ samples are generated at NLO with **Madgraph5_aMC@NLO** and the NNPDF3.0 PDF set interfaced with **PYTHIA** v8 for parton showering. Finally, single top events are generated with **POWHEG-BOX** v1 and the CT10f4 PDF set interfaced with **PYTHIA** v6 [106] for parton showering.

5.2 Object and event selection

This section details the selection criteria for objects used in the analysis as well as the selection for signal events.

5.2.1 Object selection

Muons, electrons, and jets all must pass strict selection requirements to ensure that only high quality, well measured objects are used. For leptons, a baseline selection is defined (called the *preselection*), which all leptons must pass in order to be considered for the analysis. This preselection is an intentionally loose set of criteria designed to have high acceptance in order to reject backgrounds with additional leptons (such as $WZ \rightarrow 3l\nu jj$). Signal leptons are then required to satisfy a much tighter *signal selection* aimed at suppressing backgrounds from non-prompt or fake leptons. A third set of lepton selection criteria, the *loose selection*, defines a sample enriched in non-prompt leptons, and it is used in the fake-factor method for estimating the non-prompt background, discussed in detail in Section 5.3.4. Jets are only required to pass one set of selection criteria. These selections are outlined in the following subsections and summarized in Table 5.3 for muons, Table 5.4 for electrons, and Table 5.5 for jets.

5.2.1.1 Muon candidate selection

Cuts on muon momentum serve to reject low momentum leptons from background processes and from additional collisions occurring in pileup events. Preselected muons must have transverse momentum $p_T > 6$ GeV, and the signal muons must pass $p_T > 27$ GeV. The p_T requirement for loose muons is lower than for signal muons, at $p_T > 15$ GeV, for reasons that are discussed in Section 5.3.4.3. Muons are required to fall within the detector’s η acceptance: $|\eta| < 2.7$ for preselected muons, which is tightened to $|\eta| < 2.5$ for the signal muons.

Cuts on the transverse and longitudinal impact parameters are applied to ensure that the candidate muon originated from the primary particle interaction and not some other source. The preselection and the loose selection both have relaxed requirements on the transverse impact parameter significance (d_0/σ_{d_0}) than the signal selection; all three have the same requirement on the transverse impact parameter ($|z_0 \times \sin \theta|$).

Finally, the muon candidates are required to pass a particle identification and an isolation criteria as defined in [64]. The methods used in constructing the identification and isolation working points are described in more detail in Section 3.3.3. The muon identification serves to select prompt muons

with high efficiency and well measured momenta. This analysis uses two different working points: **Loose** for preselected muons and **Medium** for loose and signal muons, where **Medium** muons are a tighter subset of those that pass the **Loose** requirement. Muon isolation is a measurement of detector activity around the muon candidate, and it is measured with both track-based and calorimeter-based variables. The isolation working point used for the signal muons, **Gradient**, is defined such that there is 90% or better background rejection efficiency for 25 GeV muons, and 99% efficiency at 60 GeV. There is no minimum isolation requirement for preselected or loose muons. Loose muons are additionally required to fail one or both of the signal transverse impact parameter cut and signal isolation requirement.

Muon preselection	
Momentum cut	$p_T > 6$ GeV
Angular acceptance	$ \eta < 2.7$
Longitudinal impact parameter	$ z_0 \times \sin \theta < 0.5$ mm
Transverse impact parameter	$d_0/\sigma_{d_0} < 10$
Particle identification	Loose

Muon signal selection	
Momentum cut	$p_T > 27$ GeV
Angular acceptance	$ \eta < 2.5$
Longitudinal impact parameter	$ z_0 \times \sin \theta < 0.5$ mm
Transverse impact parameter	$d_0/\sigma_{d_0} < 3$
Particle identification	Medium
Particle isolation	Gradient

Muon loose selection	
Momentum cut	$p_T > 15$ GeV
Angular acceptance	$ \eta < 2.5$
Longitudinal impact parameter	$ z_0 \times \sin \theta < 0.5$ mm
Transverse impact parameter	$d_0/\sigma_{d_0} < 10$
Particle identification	Medium
Fail signal transverse impact parameter and/or isolation cuts	

Table 5.3: Muon selection criteria. All muons are required to pass the preselection (top), and then either the signal (middle) or loose (bottom) criteria is applied to the preselected electrons.

5.2.1.2 Electron candidate selection

The electron candidate selections are very similar to those for muons. The momentum cut starts at $p_T > 6$ GeV for the preselection, increases to $p_T > 20$ GeV for loose electrons, and finally to

$p_T > 27$ GeV for signal electrons. The $|\eta|$ cut for electrons requires $|\eta| < 2.47$ for all electrons, with the region $1.37 \leq |\eta| \leq 1.52$ removed from loose and signal electrons. This is where the electromagnetic calorimeter transitions from the barrel to the endcaps and is not fully instrumented. Both the transverse and longitudinal impact parameter cuts are the same for all electron selections.

The electron particle identification uses a multivariate likelihood technique (LH) detailed in Section 3.3.2. Preselected electrons must pass the `LooseLH` working point with an additional requirement that there be a reconstructed track hit in the first layer of the pixel detector (a so-called *B*-layer hit). The LH requirement for the loose and signal electrons increases in tightness using `MediumLH` and `TightLH` electrons, respectively. As for isolation, the `Gradient` working point is required for signal electrons only. The loose electrons must fail one or both of the signal identification and isolation requirements.

Electron preselection	
Momentum cut	$p_T > 6$ GeV
Angular acceptance	$ \eta < 2.47$
Longitudinal impact parameter	$ z_0 \times \sin \theta < 0.5$ mm
Transverse impact parameter	$d_0/\sigma_{d_0} < 5$
Particle identification	<code>LooseLH</code> + <i>B</i> -layer hit

Electron signal selection	
Momentum cut	$p_T > 27$ GeV
Angular acceptance	$ \eta < 2.47$, excluding $1.37 \leq \eta \leq 1.52$
Longitudinal impact parameter	$ z_0 \times \sin \theta < 0.5$ mm
Transverse impact parameter	$d_0/\sigma_{d_0} < 5$
Particle identification	<code>TightLH</code>
Particle isolation	<code>Gradient</code>

Electron loose selection	
Momentum cut	$p_T > 20$ GeV
Angular acceptance	$ \eta < 2.47$, excluding $1.37 \leq \eta \leq 1.52$
Longitudinal impact parameter	$ z_0 \times \sin \theta < 0.5$ mm
Transverse impact parameter	$d_0/\sigma_{d_0} < 5$
Particle identification	<code>MediumLH</code>
Fail signal identification and/or isolation cuts	

Table 5.4: Electron selection criteria. All electrons are required to pass the preselection (top), and then either the signal (middle) or loose (bottom) criteria is applied to the preselected electrons.

5.2.1.3 Jet candidate selection

The final objects that need to pass selection are jets. Jets are clustered using the anti- k_t algorithm [107] within a radius of $\Delta R = 0.4$. The jets are then calibrated using E_T - and η -dependent correction factors that are trained using MC simulations [108]. The calibrated jets are required to have $p_T > 30$ GeV if they lie in the forward regions of the detector ($2.4 < |\eta| < 4.5$) and $p_T > 25$ GeV in the central region ($|\eta| \leq 2.4$). In order to suppress pileup jets, the so-called jet-vertex-tagger (JVT) discriminant associates a jet with the primary interaction vertex [109]; central jets with $p_T > 60$ GeV are required to pass the **Medium** JVT working point, which corresponds to an average efficiency of over 92%. Finally, the jets are required to be separated from the selected leptons by at least $\Delta R(j, l) > 0.3$.

Jet selection	
Momentum cut	$p_T > 30$ GeV for $2.4 < \eta < 4.5$ $p_T > 60$ GeV for $ \eta < 2.4$
JVT cut	Medium
Jet-lepton separation	$\Delta R(j, l) > 0.3$

Table 5.5: Jet selection criteria. All jets are required to pass the above selection in order to be used in the analysis.

5.2.1.4 Treatment of overlapping objects

In the event that one or more objects are reconstructed very close to each other, there is the possibility for double-counting if both originated from the same object. The procedure by which this ambiguity is resolved is called *overlap removal* (OR). The standard ATLAS recommendation for OR [110, 111] is implemented in this analysis and is summarized in Table 5.6.

Since electrons leave a shower in the EM calorimeter, every electron has a jet associated with it. Therefore, any jets close to an electron (within $\Delta R(e, j) < 0.2$) are rejected due to the high probability that they are the same object. On the other hand, when jets and electrons overlap within a larger radius of $0.2 < \Delta R(e, j) < 0.4$, it is likely that the electron and jet both are part of a heavy-flavor decay, and the electron is rejected.

High energy muons can produce photons via bremsstrahlung radiation or collinear final state radiation which result in nearby energy deposits in the calorimeters. Non-prompt muons from hadronic decays produce a similar signature; however, in this case the jet has a higher track multiplicity in the ID. It is possible to address both cases simultaneously by rejecting the jet when the

ID track multiplicity is less than three, and otherwise rejecting the muon, for jets and muons within $\Delta R(\mu, j) < 0.4$.

In addition to the case above where muon bremsstrahlung results in a nearby reconstructed jet, the ID track from the muon and the calorimeter energy deposit from the photon can lead to an electron being reconstructed. In this case, if both a muon and an electron share a track in the ID, the muon is kept and the electron is rejected, unless the muon is calorimeter-tagged (see Section 3.3.3), in which case the muon is removed in favor of the electron.

Overlap	Check	Result (remove → keep)
Electron & Jet	$\Delta R(e, j) < 0.2$	Jet → Electron
	$0.2 < \Delta R(e, j) < 0.4$	Electron → Jet
Muon & Jet	$\Delta R(\mu, j) < 0.4$ and Jet N_{ID} tracks < 3	Jet → Muon
	$\Delta R(\mu, j) < 0.4$ and Jet N_{ID} tracks ≥ 3	Muon → Jet
Electron & Muon	Shared ID track	Electron → Muon
	Shared ID track & muon is calo-tagged	Muon → Electron

Table 5.6: Summary of the overlap removal procedure used in the analysis. If the criteria in the “check” column is met, in the “result” column, the object on the left of the arrow is removed in favor of the object on the right.

5.2.2 Signal event selection

After the objects have been selected, cuts are applied on a per-event level to select $W^\pm W^\pm jj$ signal events. The event selection is summarized in Table 5.8.

The initial event selection chooses events that pass one or more of the trigger requirements listed in Table 5.7. At least one signal lepton is “matched” to a passed trigger in order to ensure that it was indeed a signal lepton that fired the trigger. A collection of *event cleaning* cuts must also be passed in order to remove events collected during periods in which one or more components of the detector were not operating optimally. Finally, the events are required to contain at least one interaction vertex. An event can have multiple reconstructed vertices from additional proton-proton collisions that occurred in the same bunch crossing. In this case, the *primary vertex* is determined by choosing the vertex with the largest sum of the p_T^2 of its associated tracks.

Events are then required to contain exactly two signal leptons with the same electric charge. The dilepton pair must have a combined invariant mass of $m_{ll} \geq 20$ GeV in order to suppress low mass Drell-Yan backgrounds. Two additional selections are applied to events containing two electrons: both are required to have $|\eta| < 1.37$ with an invariant mass at least 15 GeV away from the Z -boson mass to reduce events where one electron is reconstructed with the wrong charge (this

	2015 data	2016 data
Electrons	$p_T > 24$ GeV and Medium ID	$p_T > 26$ GeV and Tight ID and Loose isolation
	$p_T > 60$ GeV and Medium ID	$p_T > 60$ GeV and Medium ID
	$p_T > 120$ GeV and Loose ID	$p_T > 140$ GeV and Loose ID
Muons	$p_T > 20$ GeV and Loose isolation $p_T > 50$ GeV	$p_T > 26$ GeV and Medium isolation $p_T > 50$ GeV

Table 5.7: Summary of trigger requirements for electrons and muons for $\sqrt{s} = 13$ TeV data collected in 2015 and 2016. At least one of the triggers must be satisfied.

background will be discussed in more detail in Section 5.3.3). To suppress backgrounds from final states with more than two leptons, such as WZ or ZZ , events with more than two leptons passing the preselection are vetoed.

Missing transverse energy (E_T^{miss}) represents any particles that escape the detector without being measured, such as neutrinos, and it is defined as the magnitude of the vector sum of transverse momenta of all reconstructed objects. It can be difficult to calculate accurately, as it involves measurements from all subsystems within the detector, and it is sensitive to any corrections that may be applied to the reconstructed physics objects [112]. These corrections, including the momentum smearing for muons, energy scale and smearing for electrons, and jet calibrations, are propagated to the E_T^{miss} calculation. Events are required to contain $E_T^{\text{miss}} > 30$ GeV in order to account for the two neutrinos from the W boson decays.

At least two jets are required. The leading and subleading jets must have $p_T > 65$ GeV and $p_T > 35$ GeV, respectively, and are referred to as the *tagging jets*. Events are vetoed if they contain one or more jets that have been tagged as a b -jet to suppress backgrounds from heavy flavor decays (especially top quark events). The b -tagging algorithm used by ATLAS is a boosted decision tree (BDT) called MV2c10, and this analysis uses a working point with 85% efficiency [113].

Finally, cuts are applied on the VBS signature outlined in Section 5.0.2. The tagging jets are required to have a dijet invariant mass $m_{jj} > 200$ GeV and be separated in rapidity by $|\Delta y_{jj}| > 2.0$. This preferentially selects the VBS EWK events over the QCD-produced $W^\pm W^\pm jj$ events.

5.3 Background estimations

The major sources of background events are summarized in Section 5.0.3, and the methods used to estimate them are detailed in this section. Prompt backgrounds from ZZ and $t\bar{t} + V$ are estimated directly from MC simulations. The shape of the WZ and $V\gamma$ backgrounds are taken from MC, and the predicted yields are normalized to the data predictions in dedicated control regions, as outlined

Event selection	
Event preselection	Pass at least one trigger with a matched lepton Pass event cleaning At least one reconstructed vertex
Lepton selection	Exactly two leptons passing signal selection Both signal leptons with the same electric charge Dilepton mass $m_{ll} > 20$ GeV $ \eta < 1.37$ and $ M_{ee} - M_Z > 15$ GeV (ee-channel only) Veto events with more than two preselected leptons
Missing transverse energy	$E_T^{\text{miss}} \geq 30$ GeV
Jet selection	At least two jets Leading jet $p_T > 65$ GeV Subleading jet $p_T > 35$ GeV $m_{jj} > 200$ GeV $N_{\text{b-jet}} = 0$ $ \Delta y_{jj} > 2.0$

Table 5.8: The signal event selection.

in Sections 5.3.1 and 5.3.2, respectively. Opposite sign events with a charge misidentified electron are estimated by a data-driven background method which is summarized in Section 5.3.3. Finally, a *fake-factor* method is used to estimate the contributions from non-prompt backgrounds and is the subject of Section 5.3.4.

5.3.1 Estimation of the WZ background

The dominant background involving prompt leptons comes from $WZ + \text{jets}$ events. The contribution is estimated from MC simulation and normalized to data in a control region enriched in WZ events. This region is defined by the same event selection as the signal region in Table 5.8, with the following changes applied to increase the purity of the WZ process:

- The third lepton veto is inverted, requiring a third lepton with $p_T > 15$ GeV
- Two of the leptons must make a same-flavor opposite-sign pair. If more than one pair exists, the one with m_{ll} closest to the Z boson mass is chosen.
- The trilepton invariant mass is required to be $m_{lll} > 106$ GeV to reduce contributions from $Z\gamma$ and $Z + \text{jets}$

Once the event yields in the control region are calculated, they are propagated to the final signal region fit, detailed in Section 5.4.1, in a single bin combining all the lepton channels. The systematic

uncertainties of the WZ background are also calculated at this time. The event yields for the WZ control region are listed in Table 5.9, and distributions of the leading lepton p_T and η as well as trilepton invariant mass m_{lll} are found in Figures 5.9 and 5.8, respectively.

Event yields in the WZ control region	
WZ	197.9 ± 1.4
ZZ	14.1 ± 0.3
Triboson	1.26 ± 0.1
top	10.8 ± 1.1
$Z\gamma$	3.1 ± 1.1
$Z+jets$	2.5 ± 1.4
Total prediction	229.7 ± 2.5
Data	201 ± 14.2

Table 5.9: Event yields in the WZ control region before normalization. All lepton flavor channels are combined.

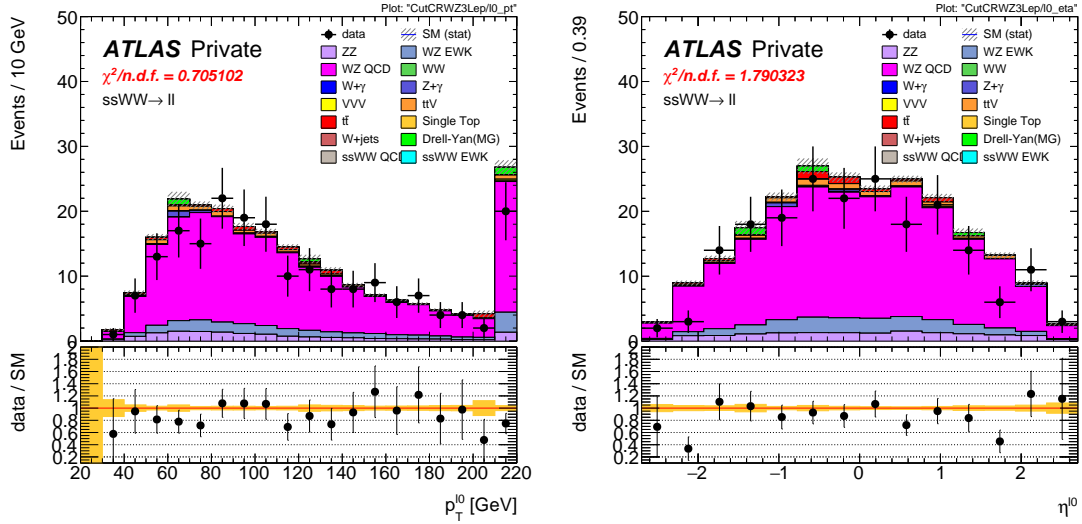


Figure 5.8: Leading lepton p_T (left) and η (right) distributions in the WZ control region before normalization. All lepton channels are combined.

5.3.2 Estimation of the $V\gamma$ background

Events from $V\gamma$ processes can pass selection if the photon converts into an e^+e^- pair and one of the electrons passes the selection criteria. The background is estimated from MC simulations which are then scaled by a normalization factor calculated from a control region enriched in $Z \rightarrow \mu\mu + \gamma$ events.

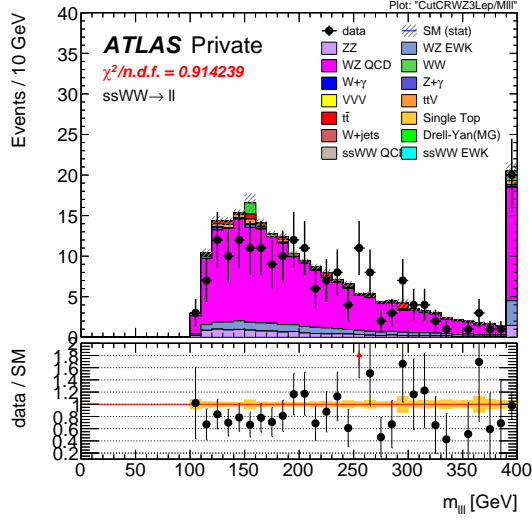


Figure 5.9: Trilepton invariant mass m_{lll} distribution in the WZ control region before normalization. All lepton channels are combined.

This control region selects two opposite-sign muons and an additional electron that is assumed to come from the photon conversion. The full event selection is detailed in Table 5.10.

$V\gamma$ control region
Exactly two muons with $p_T > 27$ GeV and $p_T > 20$ GeV
Exactly one additional electron with $p_T > 15$ GeV
Remove overlap between $Z+jets$ and $Z\gamma$
Di-muon + photon invariant mass $75 < M_{\mu\mu\gamma} < 100$ GeV
$E_T^{\text{miss}} < 30$ GeV

Table 5.10: Selection criteria for the $V\gamma$ control region.

The $Z\gamma$ MC samples available do not cover the full range of p_T^γ and $\Delta R(\gamma, l)$; thus, additional Drell-Yan samples ($Z+jets$) are used to fill out the phase space. Overlap between the two samples are removed to avoid double counting. Events with final state photons are checked at truth level¹⁷ to ensure that the photon did not originate from a hadronic decay. Cuts on $p_T^\gamma > 10$ GeV and $\Delta R(\gamma, l) > 0.1$ are then applied at generator level, and $Z\gamma$ events that fail this additional selection and $Z+jets$ events that pass it are removed.

The normalization factor is calculated directly from the event yields in the $V\gamma$ control region rather than in the signal fit, as is done for the WZ background. The event yields are listed in

¹⁷Truth particles are the particles produced directly by the MC generator before being passed through the full detector simulation, at which point they are considered *reconstruction-level* (or *reco-level*) particles.

Table 5.11, and the normalization factor is determined to be 1.77. No MC events from $Z\gamma$ processes survive the full event selection; thus, the scaling is only applied to the $W\gamma$ background in the signal region. A systematic uncertainty of 44% is assigned to the background based off of the uncertainties in the calculation of the normalization factor.

Event yields in the $V\gamma$ control region	
$Z\gamma$	24.6 ± 3.3
$Z+jets$	3.0 ± 1.5
diboson + triboson	6.7 ± 0.3
top	1.5 ± 0.5
Total prediction	35.8 ± 3.7
Data	57 ± 7.6

Table 5.11: Event yields in the $V\gamma$ control region. The $V\gamma$ scale factor of 1.77 is calculated by scaling up the $Z\gamma$ and $Z+jets$ backgrounds to account for the difference between the data and predicted total background.

5.3.3 Estimation of backgrounds from charge misidentification

If an electron's charge is mis-reconstructed, it can lead to a real opposite-sign lepton pair passing the same-sign requirement in the event selection. There are two primary reasons this can occur:

1. An electron emits a photon via bremsstrahlung which then converts into an electron-positron pair, and the conversion track with the wrong electric charge is matched to the original electron. This is the dominant process leading to charge flip, and it is highly dependent on the electron η due to the different amount of detector material the electron passes through.
2. The curvature of the electron's track is mis-measured, resulting in the wrong charge being assigned. This process is dependent on the momentum of the electron, as its track becomes more straight as the momentum of the electron increases.

In order to estimate this background, the rate at which an electron's charge is misidentified is calculated from $Z \rightarrow ee$ MC simulation. It is known that the MC does not perfectly model the material effects leading to charge flip; as a result, scale factors are applied to the MC in order for it to better reflect the real performance. These scale factors are obtained from the ratio of charge mis-ID rates in data and uncorrected MC in [85] following the method outlined in [114]. Once the scale factors are applied, the charge misidentification rate ε can be extracted by comparing the

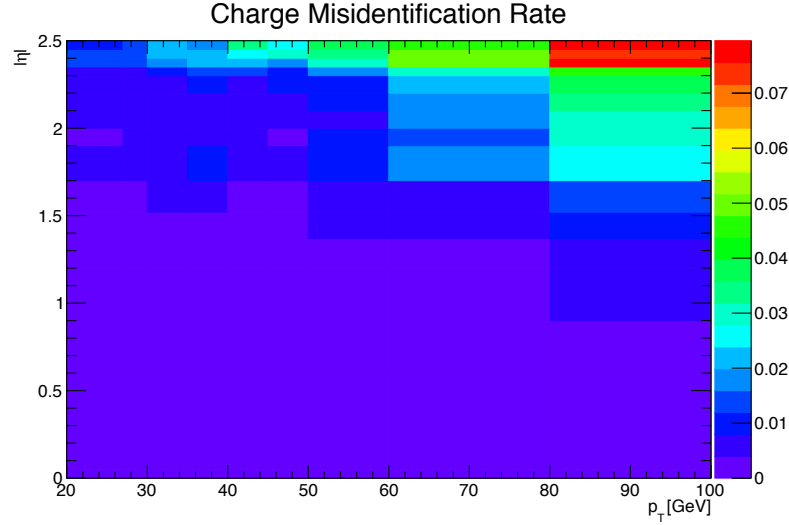


Figure 5.10: Charge misidentification rates for electrons as a function of $|\eta|$ and p_{T} . Rates are calculated from $Z \rightarrow e^+e^-$ MC after applying scale factors to approximate the charge mis-ID rates in data.

electron's reconstructed charge with the charge of its truth particle:

$$\varepsilon(\eta, p_{\text{T}}) = \frac{N_{\text{wrong charge}}}{N_{\text{prompt electrons}}} . \quad (5.1)$$

The charge mis-ID rate is calculated in bins of electron $|\eta|$ and p_{T} , and it varies from below 0.1% in the central region of the detector up to 8% in the forward regions for high p_{T} (above 80 GeV) electrons. A two-dimensional plot of ε can be found in Figure 5.10.

Given the charge flip rate $\varepsilon(\eta, p_{\text{T}})$, the rate at which an electron has its charge correctly reconstructed is $(1 - \varepsilon)$. Thus there are three possible combinations of charge identification, assuming a two-electron event:

1. Both electrons are reconstructed correctly: $(1 - \varepsilon)^2$
2. Both electrons are mis-reconstructed: ε^2
3. Only one electron is mis-reconstructed: $2\varepsilon(1 - \varepsilon)$

In order to estimate the size of the background from charge misidentification, opposite-sign events are selected using the default event selection for a given signal or control region with the same-sign requirement inverted. These events are then weighted by the probability for one of the electrons to

be reconstructed with the wrong charge:

$$\omega = \frac{\varepsilon_1(1 - \varepsilon_2) + \varepsilon_2(1 - \varepsilon_1)}{(1 - \varepsilon_1)(1 - \varepsilon_2) + \varepsilon_1\varepsilon_2}, \quad (5.2)$$

where the subscripts 1 and 2 refer to the leading and subleading electrons, respectively, and ε_i is a function of the η and p_T of the i^{th} electron. In the case of an event with one electron and one muon ($\varepsilon_\mu = 0$), Equation 5.2 simplifies to

$$\omega = \frac{\varepsilon}{1 - \varepsilon}. \quad (5.3)$$

This method assumes that there is little contamination from fake electrons in the opposite-sign sample, and this has been verified with MC simulation.

Additionally, charge-flipped electrons tend to be reconstructed with lower energy when compared to electrons with the correct charge. This is due to energy loss from the material interactions that can cause the charge to be misidentified in the first place. A correction factor is calculated from MC simulations, comparing the p_T of the truth electron to its reconstructed counterpart:

$$\alpha = \frac{\left(\frac{p_T^{\text{reco}}}{p_T^{\text{truth}}} - 1\right)_{\text{correct charge}}}{\left(\frac{p_T^{\text{reco}}}{p_T^{\text{truth}}} - 1\right)_{\text{wrong charge}}}. \quad (5.4)$$

The correction is then applied to the p_T of the charge-flipped electron via

$$p_T = p_T^0 / (1 + \alpha) + dE, \quad (5.5)$$

where p_T^0 is the uncorrected p_T of the electron and dE is a Gaussian smearing factor centered at zero with a width related to the energy resolution. Since which electron is mis-reconstructed is never determined in this method, in the case of a two-electron event, the energy correction is applied randomly to one of the two electrons based on the probabilities for them to be charge-flipped. This also determines the overall sign of the event; the charge of the electron that does not receive the correction is taken to be the charge for both.

Systematic uncertainties on the charge mis-ID rates are calculated by generating two additional sets of rates with the uncertainties on the scale factors varied up and down. The size of the estimated charge flip background without the energy correction applied is also taken as a systematic uncertainty. These systematic uncertainties are estimated to be approximately $\pm 15\%$.

5.3.3.1 Validation of the charge misidentification estimate

The performance of the charge misidentification estimation is tested in the same-sign inclusive validation region (VR), defined in Table 5.12. For ee events, the mass of the dilepton pair is required

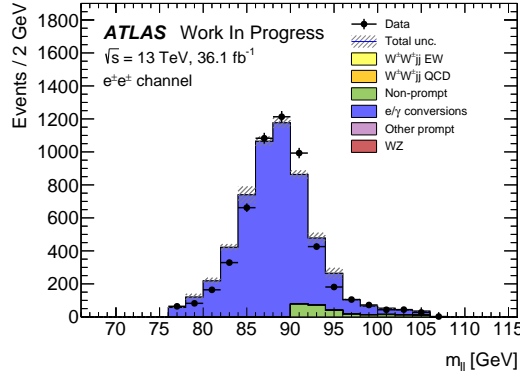


Figure 5.11: Dilepton invariant mass distribution m_{ll} for the ee channel in the same-sign inclusive VR.

to lie within 15 GeV of the Z boson mass to increase the purity of the charge flip background. $t\bar{t}$ production, which can contribute to both the charge mis-ID and fake lepton backgrounds, is suppressed by the b -jet veto. The di-electron invariant mass is shown in Figure 5.11, and distributions of the leading and subleading electron p_T in the ee -channel are shown in Figure 5.12 with the Z mass cut inverted. Agreement between data and prediction is seen within the total statistical and systematic uncertainties in the VR.

Same-sign inclusive VR
Exactly 2 same-sign signal leptons
$p_T > 27$ GeV for both leptons
$m_{ll} > 20$ GeV
$ m_{ee} - m_Z > 15$ GeV ($e^\pm e^\pm$ -channel only)
$N_{b\text{-jet}} = 0$

Table 5.12: Selection criteria for the same-sign inclusive validation region.

5.3.4 Estimation of non-prompt backgrounds with the fake-factor method

Events with one prompt lepton produced in association with hadronic jets can pass the event selection if a jet is misidentified as a charged lepton or if a non-prompt lepton from the decay of a heavy flavor particle (such as b - and c -hadrons) passes the signal lepton criteria. These misidentified jets and non-prompt leptons are collectively referred to as *fake leptons*, or simply *fakes*. The rate at which a fake lepton is misidentified is generally not modelled well enough by the MC to accurately estimate their contributions directly from simulation. Therefore, a data-driven technique called the

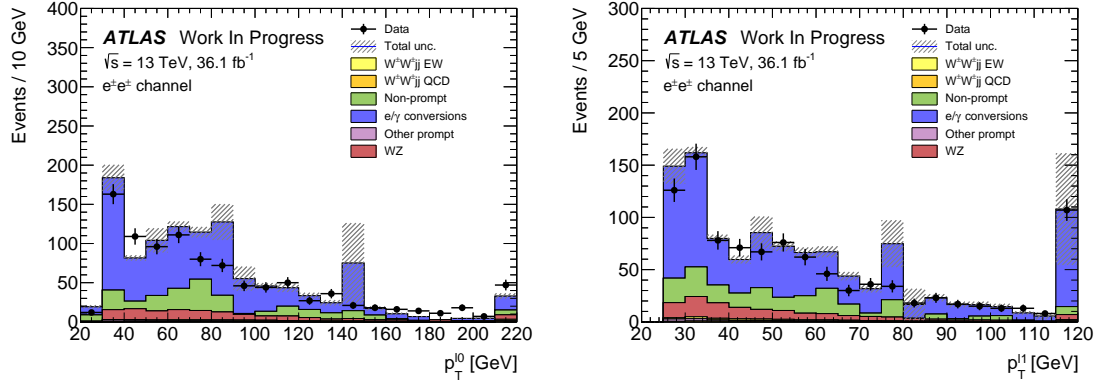


Figure 5.12: p_T distributions for the leading (left) and subleading (right) electron for the ee channel in the same-sign inclusive VR. In these plots, the cut requiring m_{ee} to fall within the Z mass window has been inverted in order to test the modelling away from the Z peak.

fake-factor is used to estimate the size and shape of background processes from fake leptons. In this analysis, a new modification to the fake-factor is used involving the particle isolation variables; the method is outlined first in the context of the *default* fake-factor in Section 5.3.4.1, and the modified fake-factor is covered in Section 5.3.4.2.

5.3.4.1 Overview of the default fake-factor method

The goal of the fake-factor method is to measure the fake rate from real collision events in a region enriched in fake leptons and use it to estimate the size of the fake lepton background in a chosen signal or control region. This is done by creating two samples using different lepton definitions:

1. The *nominal* sample is made up of leptons passing the signal selection.
2. The *loose* sample is made up of leptons that fail the signal selection while still passing a loosened set of criteria. This sample is enriched in fake leptons and is orthogonal to the set of nominal leptons.

Using the sets of nominal and loose leptons, a fake-factor f can be calculated from a region enriched in processes that are prone to producing fake leptons:

$$f = \frac{N_{\text{nominal}}}{N_{\text{loose}}} . \quad (5.6)$$

Since the fake rate is not expected to be constant over the entire phase space, the fake-factor can be divided into bins:

$$f(b) = \frac{N_{\text{nominal}}(b)}{N_{\text{loose}}(b)} , \quad (5.7)$$

where b represents the bin number. In this analysis, the fake-factor is binned in lepton p_T .

In order to estimate the fake background contribution in a given signal or control region, the fake-factor is applied to a second control region with a selection identical to the region of interest except one of the leptons required to satisfy the loose criteria. The region for which the background is estimated contains two nominal leptons and is referred to as *nominal+nominal* (NN), and the associated control region where the fake-factor is applied contains one nominal and one loose lepton and is referred to as *nominal+loose* (NL). The fake background in a NN region can then be calculated as

$$N_{NN}^{\text{fake bkg.}} = \sum_b f(b) N_{NL}(b). \quad (5.8)$$

Backgrounds containing two prompt leptons can also enter the NL region if one of the leptons passes the nominal selection and the other passes the loose selection. Since the fake-factor method estimates the fake background by scaling the amount of non-prompt events in the NL region, if these prompt contributions are not removed, they will be included in the scaling, and the background will be overpredicted. The final estimate of the fake background becomes

$$N_{NN}^{\text{fake bkg.}} = \sum_b f(b) (N_{NL}(b) - N_{NL}^{\text{prompt}}(b)). \quad (5.9)$$

A visual representation of the fake background estimation process is shown in Figure 5.13.

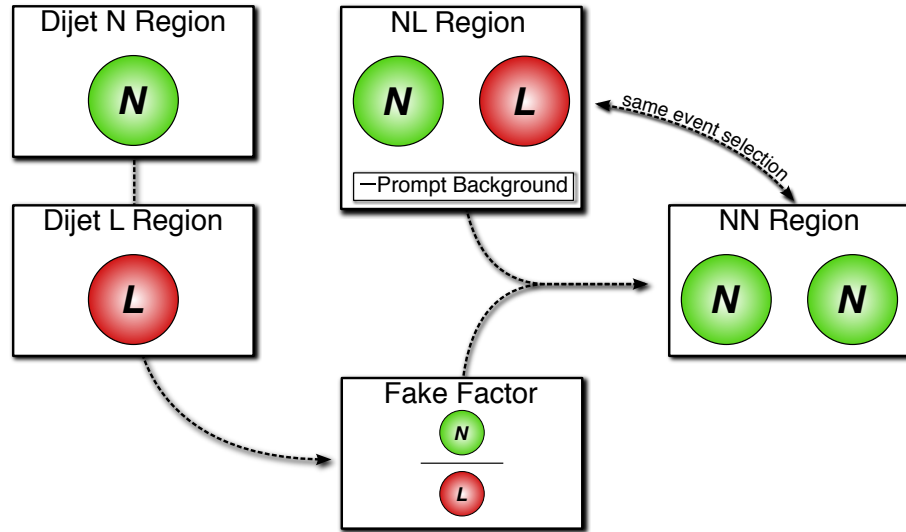


Figure 5.13: Graphical representation of how the fake factor method is used to estimate the fake background in a given NN region.

5.3.4.2 The fake-factor with p_T^{cone}

When a jet produces a non-prompt lepton, that lepton only carries a fraction of the underlying jet's total momentum. Due to the isolation cut applied to the nominal leptons, they typically carry a much larger percentage of the underlying jet momentum than the loose leptons. Since the isolation essentially sets a limit on the amount of detector activity allowed around the lepton, if other nearby particles carried a significant amount of momentum, the lepton would likely fail this cut.

This discrepancy in the underlying jet momentum fraction can cause problems in the calculation of the fake-factor f . Consider the case of two separate events with muons of identical momentum, but one passes the nominal selection, and the other passes the loose selection. The loose lepton on average will originate from a jet with higher p_T than the one corresponding to the nominal lepton despite both muons having the same momentum. This can be seen explicitly when comparing the p_T of a muon to its associated truth jet:

$$\Delta p_T(\mu, j) = \frac{p_T(j) - p_T(\mu)}{p_T(j) + p_T(\mu)}. \quad (5.10)$$

Since muons are not included in the jet reconstruction algorithm, Δp_T approximates the momentum of the muon compared to the rest of the jet. For muons that carry more than 50% of the jet's momentum, Δp_T will be negative and vice-versa. The Δp_T distributions for nominal and loose muons in $t\bar{t}$ MC events is shown Figure 5.14, where a 25 GeV nominal muon on average corresponds to a 35 GeV jet, and a 25 GeV loose muon on average corresponds to a 62 GeV jet¹⁸.

Since the default fake-factor defined in Equation 5.7 is binned in lepton p_T , the 25 GeV muons in the example above would occupy the same bin despite originating from very different jets. As a result, within a given bin, the underlying jet p_T spectrum can differ substantially between the numerator and the denominator. Additionally, these differences can vary depending on the process producing the non-prompt leptons or on the specific kinematic selections of the signal or control regions where the fake-factor is applied.

Fortunately, the majority of the jet momentum not carried by the non-prompt lepton (excluding neutrinos) can be recovered using isolation variables. A track-based isolation is chosen, referred to as p_T^{cone} , and it contains the sum of the p_T of all particle tracks with $p_T > 1$ GeV originating from the primary vertex within a cone of $\Delta R < 0.3$ around the lepton. Thus, the sample of loose leptons in the denominator of the fake-factor calculation is binned in $p_T + p_T^{\text{cone}}$ rather than simply

¹⁸To better illustrate the point, here the muon is added back into the jet p_T , and the corresponding muon p_T is obtained via $\Delta p_T(\mu, j) = \frac{(p_T(j) - p_T\mu) - p_T(\mu)}{(p_T(j) - p_T\mu) + p_T(\mu)} = \frac{p_T(j) - 2p_T(\mu)}{p_T(j)}$.

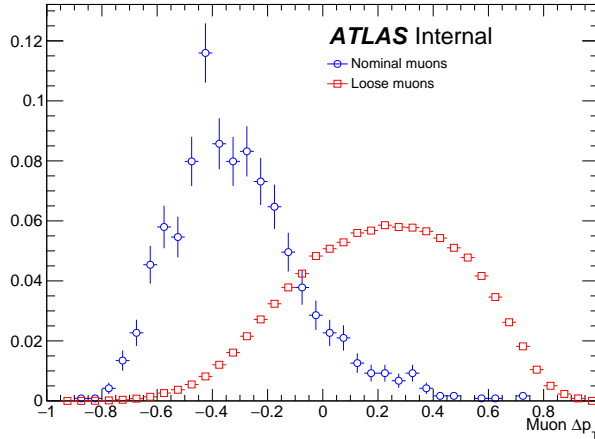


Figure 5.14: Δp_T distributions for nominal (blue) and loose (red) muons in simulated $t\bar{t}$ events. Each muon has been matched to a truth-level jet. Both distributions are normalized to unit area.

lepton p_T . Adding the isolation cone greatly reduces the difference in the fraction of the underlying jet momentum carried by the nominal and loose leptons. To check this, a new Δp_T is calculated between a lepton and its matched truth jet, where the truth jet p_T has been corrected to include all muons within a cone of $\Delta R < 0.4$:

$$p_T(j) = p_T(j_{\text{truth}}) + \sum_{\Delta R < 0.4} p_T(\mu_{\text{truth}}). \quad (5.11)$$

The Δp_T distributions comparing p_T and $p_T + p_T^{\text{cone}}$ for nominal and loose leptons using the corrected jet p_T are found in Figure 5.15, and better agreement is seen between the numerator (nominal) and denominator (loose with $p_T + p_T^{\text{cone}}$) distributions.

The numerator remains binned in lepton p_T , due to the fact that it is meant to mirror the signal region as closely as possible, and the signal lepton selection does not use $p_T + p_T^{\text{cone}}$. The impact of this is expected to be negligible due to the p_T^{cone} isolation being small for signal leptons, as shown for muons in Figure 5.16. Finally, the fake-factor f becomes

$$f(b) = \frac{N_{\text{nominal}}(b(p_T))}{N_{\text{loose}}(b(p_T + p_T^{\text{cone}}))}. \quad (5.12)$$

5.3.4.3 Application of the fake-factor

The fake-factor itself is measured from a sample of collision events passing a dijet selection that requires exactly one lepton (either passing the nominal or loose selections) and at least one jet.

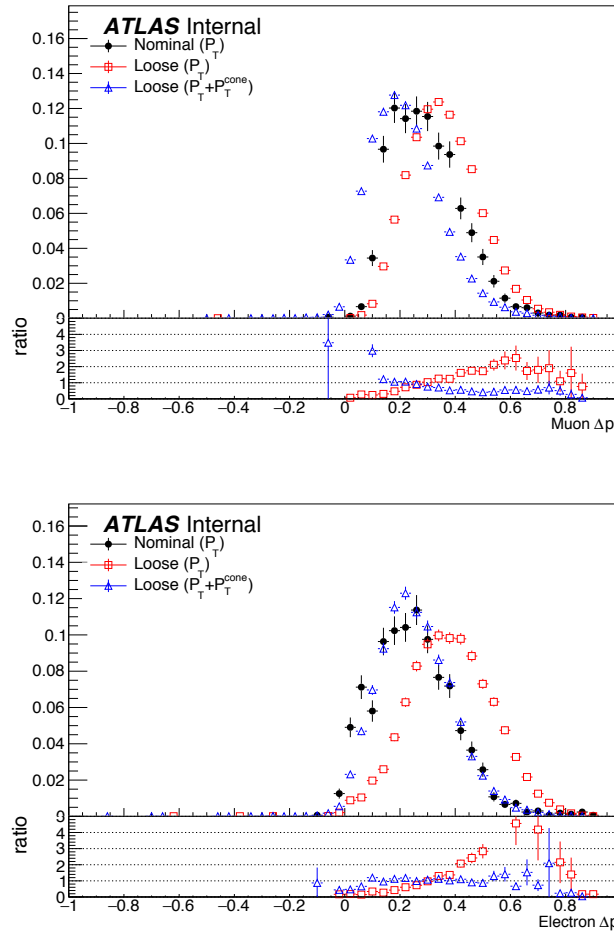


Figure 5.15: Δp_T distributions for muons (top) and electrons (bottom) in simulated $t\bar{t}$ events. Each lepton has been matched to a truth-level jet, and that truth jet has had its p_T corrected to include all truth muons within a cone of $\Delta R < 0.4$. The nominal leptons are in black. Δp_T is calculated for the loose leptons using p_T (red) and $p_T + p_T^{\text{cone}}$ (blue).

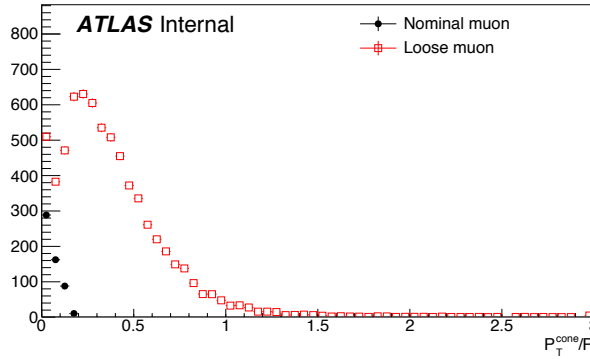


Figure 5.16: Distributions of p_T^{cone}/p_T for nominal (black) and loose (red) muons in simulated $t\bar{t}$ events.

The leading jet must also be b -tagged and approximately back-to-back with the lepton in order to enhance non-prompt lepton contributions while reducing contributions from processes involving W and Z bosons. W boson events are further suppressed by requiring the sum of the $E_{\text{T}}^{\text{miss}}$ and the transverse mass of the lepton to be less than 50 GeV. The full event selection for the dijet region is summarized in Table 5.13.

Dijet event selection
Event preselection
Exactly one lepton with $p_T > 15$ GeV
$N_{\text{jet}} > 0$
Leading jet is b -tagged
$p_T^{\text{lead. jet}} > 25$ GeV
$p_T^{\text{lead. jet}} > 30$ GeV if $ \eta_j > 2.5$
$ \Delta\phi(l, \text{lead. jet}) > 2.8$
$m_T(l, E_{\text{T}}^{\text{miss}}) + E_{\text{T}}^{\text{miss}} < 50$ GeV

Table 5.13: Event selection for the dijet region used for calculating the fake-factor. The selected lepton can pass either the nominal (signal) or loose selections. In the case of the nominal leptons, the $p_T > 27$ GeV requirement is replaced with $p_T > 15$ GeV.

The numerator sample is constructed from dijet events in which the lepton passes the nominal (signal) selection and is binned in the lepton p_T . Similarly, the denominator sample is made up of the remaining dijet events where the lepton passes the loose selection and is binned in the lepton $p_T + p_T^{\text{cone}}$. The nominal and loose leptons pass the signal selection¹⁹ and loose selection, respectively, defined earlier in Table 5.3 for muons and Table 5.4 for electrons. Backgrounds from $W + \text{jets}$, $Z + \text{jets}$,

¹⁹The $p_T > 27$ GeV cut in the signal lepton selection is dropped in favor of the $p_T > 15$ GeV requirement in the dijet selection.

$t\bar{t}$, and single top processes are estimated from MC simulations requiring one lepton to be prompt using the truth information; these contributions are subtracted from the dijet data. The fake-factor is then calculated using Equation 5.12 for muons and for central and forward electrons separately. The muon fake-factor is shown in Figure 5.17, and the two electron fake-factors (one each for central and forward electrons) are shown in Figure 5.18. The numerical values of the fake-factors, including their systematic uncertainties (which will be discussed in Section 5.3.4.4) are listed in Table 5.14.

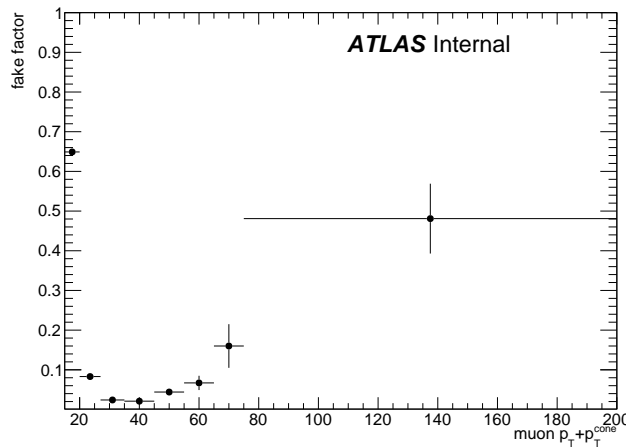


Figure 5.17: The measured fake-factor as a function of muon $p_T + p_T^{\text{cone}}$. The error bars represent the statistical uncertainty only.

In order to properly account for the denominator being binned in $p_T + p_T^{\text{cone}}$, special care needs to be taken when estimating the fake background from the NL regions. For the purposes of the fake-factor calculation, it is perhaps more intuitive to consider a loose *object* with $p_T = p_T + p_T^{\text{cone}}$ instead of simply a loose lepton, as the lepton and the underlying jet are treated as a whole with this method. When the lepton p_T cuts required by a particular signal or control region are applied to nominal and loose leptons, the cut is applied to the p_T of the nominal lepton and to the $p_T + p_T^{\text{cone}}$ of the loose object. Similarly, when looking up the fake-factor weight for a given NL event, the value is taken from the bin corresponding to the $p_T + p_T^{\text{cone}}$ of the loose object. Finally, when applying the weight to the NL event, $p_T + p_T^{\text{cone}}$ is assigned as the p_T of the loose object. This can be visualized by referring back to Figure 5.13; every time a loose lepton is used (the red circles in the Figure), $p_T + p_T^{\text{cone}}$ is used in place of p_T .

Finally, it should be noted that the addition of p_T^{cone} to the loose object may cause the loose leptons in the denominator sample to migrate into higher bins. This results in an overall decrease in

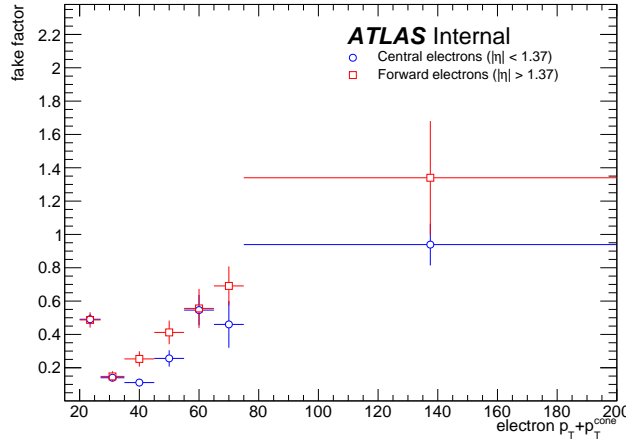


Figure 5.18: The measured fake-factor as a function of electron $p_T + p_T^{\text{cone}}$ in the central ($|\eta| < 1.37$, blue) and forward ($|\eta| > 1.37$, red) regions of the detector. The error bars represent the statistical uncertainty only.

the number of loose objects in the lower $p_T + p_T^{\text{cone}}$ bins due to there not being additional leptons at lower p_T to replace them. Since the fake-factor is a ratio of the number of events in a bin, this effect causes the first few bins of the fake-factor to increase, as can be seen clearly in Figure 5.17. However, the signal and control regions (and their corresponding NL regions) contain a $p_T > 27$ GeV cut that prevents these migrations from negatively impacting the fake estimation.

5.3.4.4 Systematic uncertainties

Four sources of systematic uncertainty are considered: the dijet event selection, prompt background subtraction, jet flavor composition, and residual dependence on the underlying jet p_T spectrum. In order to measure the impact of these systematics, new fake-factors are computed with variations in each of the systematic sources and the differences from the nominal values are taken as the uncertainty.

1. In order to estimate uncertainties due to the dijet selection, the cut on $M_T + E_T^{\text{miss}}$ is varied by ± 5 GeV, the jet-lepton separation $\Delta\phi(l, j)$ by ± 0.1 , and the jet p_T cut by ± 5 GeV.
2. To estimate the systematic uncertainty on the prompt background subtraction, the MC prediction in a $W+\text{jets}$ control region is compared to data. The discrepancy between data and MC is found to be approximately 10% [85]. Therefore, the prompt background used for the subtraction is scaled up and down by $\pm 10\%$.

3. The difference in the jet flavor composition between the dijet events and the events in the NL regions can affect the accuracy of the fake background estimation. The dijet sample is dominated by light jets, while the NL regions tend to be dominated by heavy flavor from $t\bar{t}$. To account for this, the fake-factor is computed with a b -jet veto.
4. To measure any residual dependence on the underlying jet p_T spectrum, the leading jet p_T distribution is reweighted to match the p_T spectrum of truth jets that produce fake leptons in MC simulations. This results in an increase in the number of nominal and loose leptons at high momentum [85].

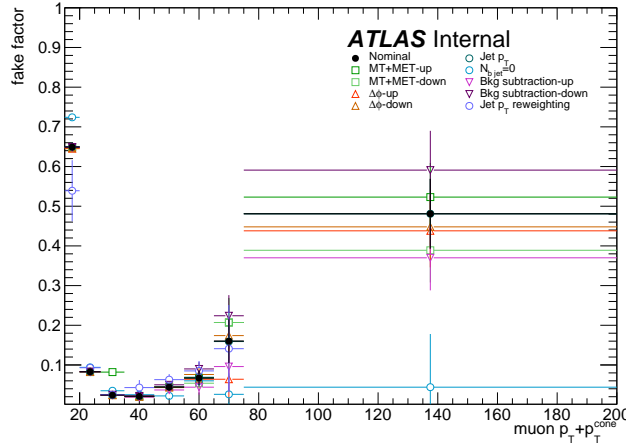


Figure 5.19: Systematic variations in the fake-factor as a function of muon $p_T + p_T^{\text{cone}}$. The individual fake-factors obtained for each systematic variation are displayed with their statistical uncertainties.

5.3.4.5 Results of the fake-factor

The fake background contribution in the signal region is estimated by applying the fake-factors to the equivalent NL region using Equation 5.9, where the fake-factor used corresponds to the flavor of the loose lepton in the event. As usual, the prompt background is subtracted from the NL events using MC simulation. Charge misidentification is handled using the same method as in Section 5.3.3, with an additional set of charge flip rates calculated for loose leptons. The fake background yields in the signal region are listed in Table 5.15. An overall uncertainty of 50% is assigned to the fake background estimation in $\mu^\pm\mu^\pm$ events, and between 40% to 90% for $e^\pm e^\pm$ and $\mu^\pm e^\pm$ events, including both statistical and systematic effects.

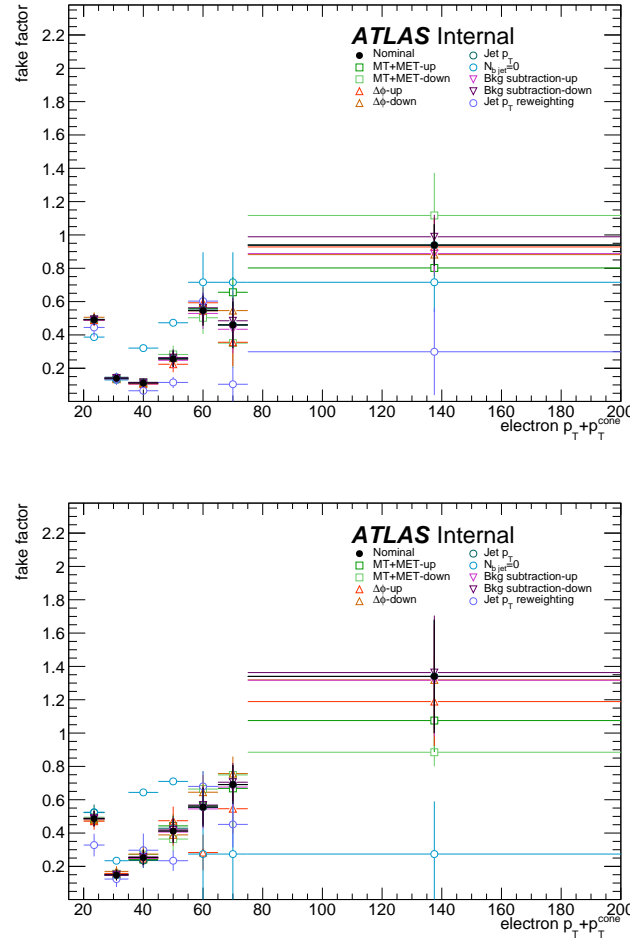


Figure 5.20: Systematic variations in the fake-factor as a function of electron $p_T + p_T^{\text{cone}}$ in the central ($|\eta| < 1.37$, top) and forward ($|\eta| > 1.37$, bottom) regions of the detector. The individual fake-factors obtained for each systematic variation are displayed with their statistical uncertainties.

fake-factor	$p_T[15, 20]$	$p_T[20, 27]$	$p_T[27, 35]$	$p_T[35, 45]$	$p_T[45, 55]$	$p_T[55, 65]$	$p_T[65, 75]$	$p_T[75, 200]$
nominal	0.649 ± 0.007	0.083 ± 0.002	0.024 ± 0.002	0.021 ± 0.003	0.044 ± 0.007	0.067 ± 0.018	0.160 ± 0.055	0.481 ± 0.088
MT+MET	0.649 ± 0.007	0.082 ± 0.002	0.082 ± 0.002	0.020 ± 0.003	0.045 ± 0.007	0.068 ± 0.018	0.207 ± 0.062	0.523 ± 0.086
$\Delta\phi(\ell, j)$	0.648 ± 0.007	0.083 ± 0.003	0.024 ± 0.002	0.022 ± 0.004	0.044 ± 0.007	0.054 ± 0.020	0.207 ± 0.060	0.389 ± 0.081
Jet p_T	0.645 ± 0.008	0.083 ± 0.003	0.024 ± 0.002	0.021 ± 0.004	0.045 ± 0.008	0.064 ± 0.021	0.064 ± 0.058	0.438 ± 0.092
$N_{b\text{-jet}} = 0$	0.646 ± 0.006	0.083 ± 0.002	0.024 ± 0.002	0.020 ± 0.003	0.043 ± 0.006	0.076 ± 0.017	0.174 ± 0.050	0.448 ± 0.078
Bkg. subtraction	0.650 ± 0.007	0.083 ± 0.002	0.024 ± 0.002	0.021 ± 0.003	0.045 ± 0.007	0.069 ± 0.018	0.159 ± 0.018	0.481 ± 0.088
Jet p_T Reweighting	0.724 ± 0.003	0.094 ± 0.001	0.035 ± 0.001	0.025 ± 0.002	0.022 ± 0.004	0.060 ± 0.015	0.026 ± 0.053	0.044 ± 0.134
	0.648 ± 0.007	0.083 ± 0.002	0.024 ± 0.002	0.019 ± 0.003	0.037 ± 0.007	0.044 ± 0.019	0.096 ± 0.062	0.370 ± 0.082
	0.649 ± 0.007	0.083 ± 0.002	0.025 ± 0.002	0.022 ± 0.003	0.050 ± 0.007	0.090 ± 0.017	0.224 ± 0.052	0.591 ± 0.099
	0.539 ± 0.077	0.093 ± 0.007	0.025 ± 0.004	0.043 ± 0.019	0.063 ± 0.014	0.085 ± 0.025	0.141 ± 0.110	1.962 ± 0.492

(a) Fake-factor values for muons.

fake-factor	$p_T[20, 27]$	$p_T[27, 35]$	$p_T[35, 45]$	$p_T[45, 55]$	$p_T[55, 65]$	$p_T[65, 75]$	$p_T[75, 200]$
nominal	0.491 ± 0.031	0.140 ± 0.020	0.111 ± 0.023	0.256 ± 0.049	0.546 ± 0.091	0.460 ± 0.140	0.939 ± 0.125
MT+MET	0.493 ± 0.030	0.138 ± 0.019	0.115 ± 0.022	0.261 ± 0.045	0.559 ± 0.084	0.656 ± 0.091	0.802 ± 0.016
$\Delta\phi(\ell, j)$	0.488 ± 0.032	0.137 ± 0.020	0.110 ± 0.025	0.283 ± 0.053	0.503 ± 0.097	0.351 ± 0.149	1.117 ± 0.255
Jet p_T	0.489 ± 0.035	0.134 ± 0.021	0.105 ± 0.025	0.224 ± 0.048	0.593 ± 0.093	0.356 ± 0.144	0.928 ± 0.177
$N_{b\text{-jet}} = 0$	0.506 ± 0.029	0.140 ± 0.018	0.111 ± 0.022	0.260 ± 0.046	0.545 ± 0.084	0.546 ± 0.120	0.882 ± 0.103
Jet p_T	0.493 ± 0.032	0.146 ± 0.021	0.115 ± 0.024	0.259 ± 0.049	0.550 ± 0.091	0.460 ± 0.140	0.939 ± 0.125
$N_{b\text{-jet}} = 0$	0.387 ± 0.009	0.130 ± 0.008	0.321 ± 0.012	0.473 ± 0.015	0.716 ± 0.180	0.716 ± 0.180	0.716 ± 0.180
Bkg. subtraction	0.488 ± 0.031	0.138 ± 0.020	0.106 ± 0.023	0.248 ± 0.049	0.529 ± 0.092	0.434 ± 0.143	0.888 ± 0.115
Jet p_T Reweighting	0.493 ± 0.031	0.142 ± 0.020	0.115 ± 0.023	0.264 ± 0.049	0.563 ± 0.090	0.485 ± 0.136	0.989 ± 0.132

(b) Fake-factor values for central electrons ($|\eta| < 1.37$).

fake-factor	$p_T[20, 27]$	$p_T[27, 35]$	$p_T[35, 45]$	$p_T[45, 55]$	$p_T[55, 65]$	$p_T[65, 75]$	$p_T[75, 200]$
nominal	0.487 ± 0.046	0.148 ± 0.031	0.253 ± 0.046	0.412 ± 0.071	0.556 ± 0.117	0.691 ± 0.117	1.340 ± 0.340
MT+MET	0.483 ± 0.045	0.152 ± 0.031	0.241 ± 0.043	0.443 ± 0.070	0.565 ± 0.106	0.668 ± 0.117	1.075 ± 0.189
$\Delta\phi(\ell, j)$	0.495 ± 0.047	0.156 ± 0.033	0.271 ± 0.052	0.364 ± 0.074	0.664 ± 0.107	0.749 ± 0.056	0.885 ± 0.084
Jet p_T	0.471 ± 0.051	0.158 ± 0.035	0.247 ± 0.051	0.474 ± 0.085	0.283 ± 0.107	0.546 ± 0.149	1.189 ± 0.266
$N_{b\text{-jet}} = 0$	0.478 ± 0.042	0.170 ± 0.031	0.274 ± 0.046	0.389 ± 0.066	0.645 ± 0.104	0.757 ± 0.102	1.319 ± 0.326
Jet p_T	0.523 ± 0.048	0.149 ± 0.033	0.235 ± 0.045	0.429 ± 0.073	0.555 ± 0.117	0.691 ± 0.117	1.340 ± 0.340
$N_{b\text{-jet}} = 0$	0.525 ± 0.011	0.234 ± 0.013	0.644 ± 0.016	0.710 ± 0.014	0.274 ± 0.316	0.274 ± 0.316	0.274 ± 0.316
Bkg. subtraction	0.484 ± 0.046	0.146 ± 0.031	0.248 ± 0.046	0.406 ± 0.071	0.545 ± 0.118	0.676 ± 0.118	1.317 ± 0.337
Jet p_T Reweighting	0.489 ± 0.046	0.151 ± 0.031	0.257 ± 0.046	0.419 ± 0.071	0.568 ± 0.117	0.705 ± 0.115	1.363 ± 0.342

(c) Fake-factor values for forward electrons ($1.37 < |\eta|$).Table 5.14: Values of the fake-factor in each p_T bin and for each individual systematic source.

	estimated yield	f_e stat. up	f_e stat. dn	f_e syst. up	f_e syst. dn	f_μ stat. up	f_μ stat. dn	f_μ syst. up	f_μ syst. dn
$e^\pm e^\pm$	11.42 ± 3.13	—	—	—	—	—	—	—	—
$\mu^\pm \mu^\pm$	4.82 ± 0.77	—	—	—	—	0.65	-0.65	3.64	-0.61
$\mu^\pm e^\pm$	37.08 ± 5.16	4.90	-4.90	5.59	-14.34	1.39	-1.39	16.10	-1.98

Table 5.15: Estimated yields for the fake lepton background. The estimated yield is shown in the first column together with the statistical uncertainty followed by the systematic uncertainties from variations of the the fake-factors within their statistical (stat.) and systematic (syst.) uncertainties. The labels f_e and f_μ indicate the fake-factors for electrons and muons, respectively.

5.3.4.6 Validation of the fake-factor

The accuracy of the fake-factor method is tested in several validation regions, the most sensitive of which is the same-sign top fakes VR (SS top VR), defined in Table 5.16. This region inverts the signal region’s b -jet veto to accept events with exactly one b -jet. Due to this requirement, the dominant source of events comes from the $t\bar{t}$ process where a b -jet fakes an isolated lepton. The distribution of the subleading lepton p_T in this VR is shown in Figure 5.21 for all lepton flavor combinations. There is good agreement between the data and the prediction, even when only taking into account the statistical uncertainty and not the large systematic uncertainties assigned to the fake estimation.

Same-sign top fakes VR
Exactly 2 same-sign signal leptons
$p_T > 27$ GeV for both leptons
$m_{ll} > 20$ GeV
$ m_{ee} - m_Z > 15$ GeV ($e^\pm e^\pm$ -channel only)
$N_{b\text{-jet}} = 1$
$N_{\text{jet}} \geq 2$
Leading jet $p_T > 65$ GeV
Subleading jet $p_T > 35$ GeV

Table 5.16: Selection criteria for the same-sign top fakes validation region.

5.3.5 Reduction of WZ background using custom overlap removal

The dominant source of prompt background in this analysis comes from WZ events where both bosons decay leptonically. Traditionally, the background is dealt with by imposing a veto on any event with a third lepton passing some loose identification criteria (the so-called *trilepton veto*). In the case of this analysis, if one or more leptons in addition to the two signal leptons pass the preselection criteria, the event is rejected. However, WZ events can still enter the signal region if one of the leptons fails the preselection or falls outside of the detector’s acceptance.

In order to understand the sources of WZ events that are not removed by the trilepton veto, a study was performed on truth-level leptons in $W^\pm W^\pm jj$ and WZ MC samples. Events with three truth leptons are selected, and each is matched to its reconstruction-level partner by finding the closest match in $\Delta R(\text{truth}, \text{reco})$ and $\Delta p_T(\text{truth}, \text{reco})$. For events surviving the trilepton veto, the two signal leptons are removed, and the remaining leptons represent real leptons that fail to be selected for the veto. Between 40-50% of these leptons fall outside of the eta acceptance of the

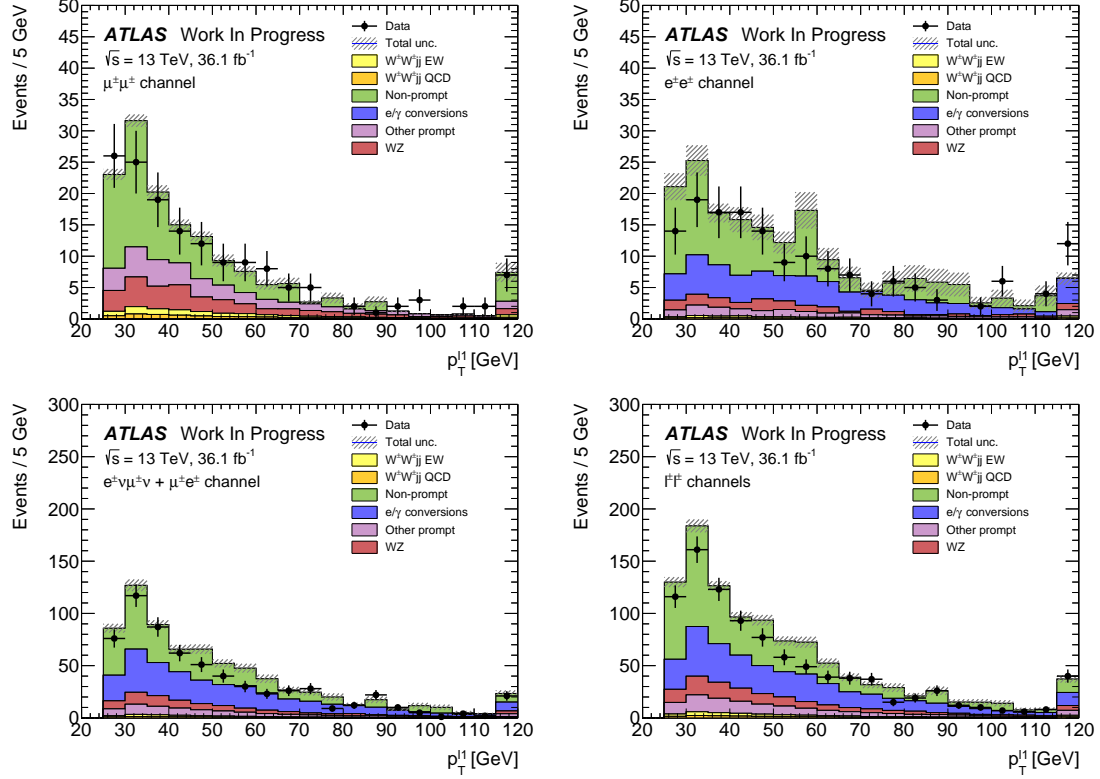


Figure 5.21: Distributions of the subleading lepton p_T in the same-sign top fakes VR for $\mu^\pm\mu^\pm$ events (top right), $e^\pm e^\pm$ events (top left), $\mu^\pm e^\pm$ events (bottom left), and all events combined (bottom right). All errors are statistical only.

analysis (see Figure 5.22) and are unrecoverable. The second largest source of leptons failing the preselection is the OR, defined in Section 5.2.1.4. The standard OR procedure appears to be too aggressive in removing leptons in favor of jets, causing many three lepton events to “lose” their third lepton and pass the trilepton veto. Therefore a *custom OR* is investigated which would replace the standard OR in the preselection and allow for better WZ rejection by removing fewer third leptons.

In order to construct this custom OR, a new quantity is defined between a lepton (l) and a nearby jet (j):

$$p_{T,\text{ratio}}(l, j) = \frac{p_{Tl}}{p_{Tj}}, \quad (5.13)$$

which, along with $\Delta R(l, j)$, will make up the custom OR criteria. The idea behind including $p_{T,\text{ratio}}$ is to be able to preferentially remove background leptons originating from jets (those that carry a low percentage of the total jet momentum) instead of removing *any* lepton near a jet. The distributions of $p_{T,\text{ratio}}$ and the associated efficiency curves for muons and electrons can be found in Figures 5.23

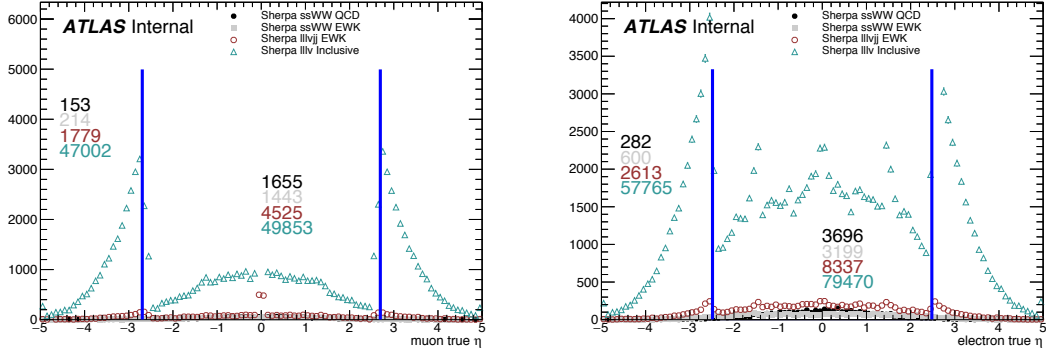


Figure 5.22: Pseudorapidity (η) distributions of truth muons (top) and electrons (bottom) for Sherpa $W^\pm W^\pm jj$ and WZ MC samples. The blue vertical lines represent the allowed η range for each lepton flavor. The numbers correspond to the number of raw MC events that fall within and outside of the allowed η range for each MC sample.

and 5.25, respectively, and the distributions for $\Delta R(\mu, j)$ for muons can be found in Figure 5.24. Since all electrons have an associated jet in the calorimeters, the $\Delta R(e, j)$ variable is not a good quantity to use for this custom OR.

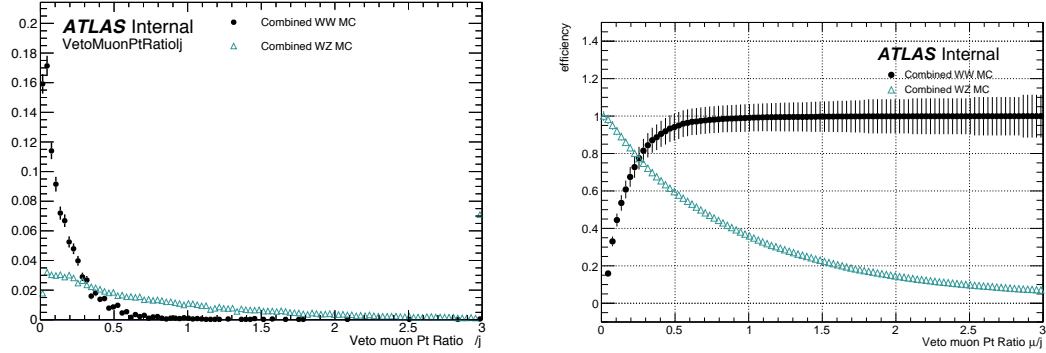


Figure 5.23: Distributions of $p_{T,\text{ratio}}(\mu, j)$ for EWK and QCD $W^\pm W^\pm jj$ signal (black) and WZ background (teal) for truth-matched third muons in events that pass the trilepton veto. Both distributions are normalized to unit area. The associated efficiency curves are on the right where efficiency is defined as the percentage of total events that would pass a cut on $p_{T,\text{ratio}}(\mu, j)$ at a given value on the x -axis.

A working point for the Custom OR was chosen by requiring 90% signal retention for muons and 90% background rejection for electrons. The cut on electrons was allowed to be much tighter because the number of signal events with a third electron is considerably smaller than for muons. It should be emphasized that the signal events present in Figures 5.23–5.25 do not represent the full

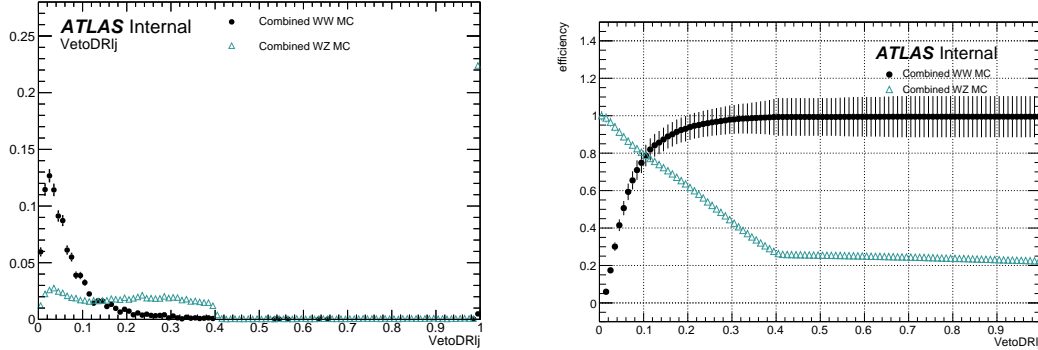


Figure 5.24: Distributions of $\Delta R(\mu, j)$ for EWK and QCD $W^\pm W^\pm jj$ signal (black) and WZ background (teal) for truth-matched third muons in events that pass the trilepton veto. Both distributions are normalized to unit area. The associated efficiency curves are on the right where efficiency is defined as the percentage of total events that would pass a cut on $\Delta R(\mu, j)$ at a given value on the x -axis.

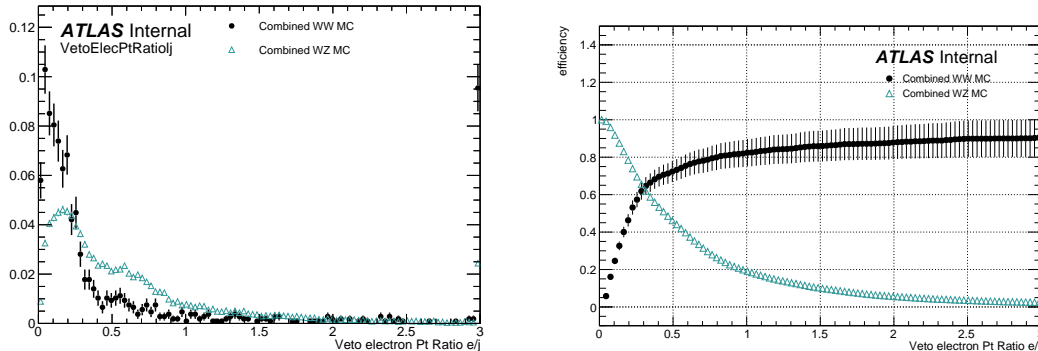


Figure 5.25: Distributions of $p_{T,\text{ratio}}(e, j)$ for EWK and QCD $W^\pm W^\pm jj$ signal (black) and WZ background (teal) for truth-matched third electrons in events that pass the trilepton veto. Both distributions are normalized to unit area. The associated efficiency curves are on the right where efficiency is defined as the percentage of total events that would pass a cut on $p_{T,\text{ratio}}(e, j)$ at a given value on the x -axis.

set of signal events, but only those with a real third lepton (which must come from some source other than the signal $W^\pm W^\pm jj$ process). For muons, a logical ‘or’ of $p_{T,\text{ratio}}(\mu, j)$ and $\Delta R(\mu, j)$ is used to maximize the third lepton acceptance due to correlations between the quantities, as shown in Figure 5.26; for electrons, only a cut on $p_{T,\text{ratio}}(e, j)$ is used. The Custom OR working point is defined in Table 5.17.

Custom OR Definition	
Muons	$p_{T,\text{ratio}}(\mu, j) > 0.40$ or $\Delta R(\mu, j) > 0.15$
Electrons	$p_{T,\text{ratio}}(e, j) > 0.18$

Table 5.17: Custom OR definition. Leptons must pass this selection in order to be counted for the trilepton veto.

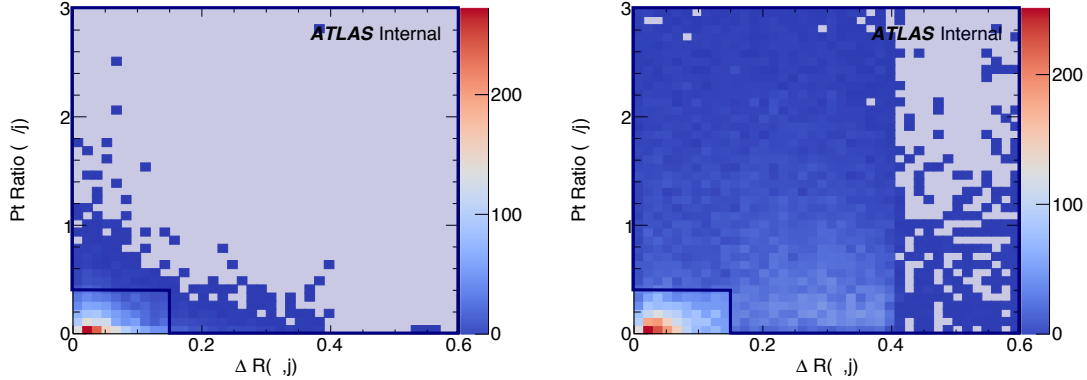


Figure 5.26: Two-dimensional plots of $p_{T,\text{ratio}}(\mu, j)$ vs $\Delta R(\mu, j)$ for truth-matched third muons in events that pass the trilepton veto for EWK and QCD $W^\pm W^\pm jj$ signal (left) and WZ background (right). The blue overlay indicates the area in which the third leptons will pass the custom OR and result in the event failing the trilepton veto.

Initial tests of the performance of the Custom OR yielded promising results, with approximately 20% reduction in WZ background compared to less than 2% signal loss in the signal region. Unfortunately, due to differences between the primary analysis framework and the one used for testing, in practice the gains in WZ rejection were not nearly as substantial, and ultimately the Custom OR was not included in the final analysis. However, it is still a potentially useful tool for improving background rejection based on lepton counting in analyses with overly aggressive OR procedures.

5.4 Cross section measurement

The $W^\pm W^\pm jj$ EWK cross section is extracted from the signal region using a maximum-likelihood fit applied simultaneously to four m_{jj} bins in the signal region as well as to the low- m_{jj} and WZ control regions. For the fit and cross section extraction, the signal region is defined as in Table 5.8 with the dijet invariant mass requirement raised to $m_{jj} > 500$ GeV. The low- m_{jj} region is defined to mirror the signal region exactly with the dijet invariant mass inverted to $200 < m_{jj} < 500$ GeV, and the WZ control region is as defined previously in Section 5.3.1.

The signal and low- m_{jj} regions are split into six channels based on the flavor and charge of the dilepton pair: $\mu^+\mu^+$, $\mu^-\mu^-$, μ^+e^+ , μ^-e^- , e^+e^+ , and e^-e^- . This split by charge increases the sensitivity of the measurement due to the W^+/W^- charge asymmetry favoring the production of W^+ bosons [115]. Since the signal events contain two W bosons, the signal strength compared to charge-symmetric backgrounds is much greater in the $++$ channels than for both charges combined. The WZ control region is included in the fit as a single bin ($l^\pm l^\mp l^\pm$).

The maximum likelihood fit and cross section extractions are outlined in Sections 5.4.1 and 5.4.3, respectively. The results of the cross section measurement and of the analysis as a whole are presented in Section 5.6.

5.4.1 Maximum likelihood fit

The number of predicted signal events in each channel c and m_{jj} bin b can be calculated from the SM predicted total production cross section $\sigma_{\text{theo}}^{\text{tot}}$ scaled by the total integrated luminosity \mathcal{L} , the signal acceptance \mathcal{A} , and the efficiency corrections $\mathcal{C}(\theta)$:

$$N_{cb}^{\text{sig}}(\theta) = \sigma_{\text{theo}}^{\text{tot}} \mathcal{A}_b \mathcal{C}_b(\theta) \mathcal{L}. \quad (5.14)$$

Here, θ represents the set of nuisance parameters that parameterize the effects of each systematic uncertainty on the signal and background expectations. The acceptance and efficiency corrections will be covered in more detail in Section 5.4.2. A signal strength parameter μ is defined as the ratio of the measured cross section to the SM predicted cross section. The expected number of events in a given channel and bin can then be expressed as the sum of the estimated background ($N_{cb}^{\text{bkg}}(\theta)$) and the number of predicted signal events scaled by μ :

$$\begin{aligned} N_{cb}^{\text{exp}}(\theta) &= \mu N_{cb}^{\text{sig}}(\theta) + N_{cb}^{\text{bkg}}(\theta) \\ &= \mu \sigma_{\text{theo}}^{\text{tot}} \mathcal{A}_b \mathcal{C}_b(\theta) \mathcal{L} + N_{cb}^{\text{bkg}}(\theta). \end{aligned} \quad (5.15)$$

The nuisance parameters are constrained by Gaussian probability distribution functions, and the normalization of the WZ background mentioned in Section 5.3.1 is included in the fit as a free parameter. The expected yields for signal and background processes are adjusted by the set of nuisance parameters within the constraints of the systematic uncertainties. The yields after the fit correspond to the value that best matches the observed data.

The number of events per channel and bin after the fit can be written as a sum of the predicted event yields for each sample s :

$$\nu_{cb}(\phi, \theta, \gamma_{cb}) = \gamma_{cb} \sum_s [\eta_{cs}(\theta) \phi_{cs}(\theta) \lambda] h_{cbs}(\theta). \quad (5.16)$$

In this equation, the fitted number of events in a given channel and bin is obtained by weighting the histogram of predicted yields h_{cbs} by the product of a given luminosity λ and any normalization factors ϕ_{cs} that may be given for each channel and sample. The input histogram and the normalization factors may depend on the nuisance parameters θ taking into account sources of systematic uncertainty. Uncertainties on the normalization factors $\eta_{cs}(\theta)$ are also included. Finally, bin-by-bin scale factors γ_{cb} are included to parameterize the statistical uncertainties of the MC predictions.

The binned likelihood function is given by a product of Gaussian functions for the luminosity and for the background uncertainties and a product of Poisson functions for the number of observed events in each bin and channel:

$$L(\mu|\theta) = \mathcal{G}(\mathcal{L}|\theta_{\mathcal{L}}, \sigma_{\mathcal{L}}) \cdot \prod_c \prod_b \mathcal{P}(N_{cb}^{\text{meas.}}|\nu_{cb}(\mu)) \prod_p \mathcal{G}(\theta_p^0|\theta_p), \quad (5.17)$$

where \mathcal{G} and \mathcal{P} are the Gaussian and Poisson functions, respectively. As before, \mathcal{L} represents the integrated luminosity with uncertainty $\sigma_{\mathcal{L}}$ and associated nuisance parameter $\theta_{\mathcal{L}}$. The number of measured events in a given bin and channel is represented by $N_{cb}^{\text{meas.}}$, and $\nu_{cb}(\mu)$ is the predicted number of events defined in Equation 5.16 expressed as a function of the signal strength μ . Finally, the set of nuisance parameters θ and any auxiliary measurements used to constrain them (θ^0) are multiplied for each parameter p .

The profile likelihood ratio is defined as

$$q_{\mu} = -2 \ln \frac{L(\mu, \hat{\theta}_{\mu})}{L(\hat{\mu}, \hat{\theta})}, \quad (5.18)$$

where $\hat{\mu}$ and $\hat{\theta}$ are the unconditional maximum likelihood estimates, and $\hat{\theta}$ is the conditional maximum likelihood estimate for a given value of μ . The fitted signal strength $\hat{\mu}$ is obtained by maximizing the likelihood function with respect to all parameters. The compatibility of the observed data

with the background-only hypothesis can then be calculated by setting $\mu = 0$. Observation of the $W^\pm W^\pm jj$ EWK process is claimed if the data is found to be inconsistent with the background-only hypothesis by more than 5σ .

5.4.2 Definition of the fiducial volume

Before extracting the cross section, it is necessary to define the fiducial volume, or the phase space of measurable events. It is a subset of the total phase space defined by selection requirements designed to mirror those applied in the analysis as closely as possible. The selection criteria for the fiducial volume are listed in Table 5.18.

Fiducial region selection	
Lepton selection	Two prompt leptons (e, μ) $p_T > 27$ GeV and $ \eta < 2.5$ for both leptons Both leptons with the same electric charge Dilepton invariant mass $m_{ll} > 20$ GeV Dilepton separation $\Delta R(ll) > 0.3$
Missing transverse energy	Two neutrino system with $p_T^{\nu\nu} > 30$ GeV
Jet selection	At least two jets Leading jet $p_T > 65$ GeV Subleading jet $p_T > 35$ GeV Leading and subleading jet $ \eta < 4.5$ Jet-lepton separation $\Delta R(l, j) > 0.3$ Dijet invariant mass $m_{jj} > 500$ GeV Dijet separation $\Delta y_{jj} > 2.0$

Table 5.18: Definition of the fiducial volume.

The full phase space is generated in MC simulations, providing the total theoretical cross section $\sigma_{\text{theo}}^{\text{tot}}$ and the total number of signal events $\mathcal{N}_{\text{sig}}^{\text{tot}}$ ²⁰. After applying the fiducial selection at truth level, the total number of signal events in the fiducial region $\mathcal{N}_{\text{sig}}^{\text{fid}}$ is obtained. An acceptance factor \mathcal{A} is used to represent the efficiency of events falling inside the fiducial region at truth level:

$$\mathcal{A} = \frac{\mathcal{N}_{\text{sig}}^{\text{fid}}}{\mathcal{N}_{\text{sig}}^{\text{tot}}} . \quad (5.19)$$

A correction factor \mathcal{C} is also necessary to translate from the truth level fiducial volume to the reconstruction level signal region and is defined in terms of the number of reconstruction level MC events in the signal region $N_{\text{sig},\text{MC}}^{\text{SR}}$:

$$\mathcal{C} = \frac{N_{\text{sig},\text{MC}}^{\text{SR}}}{\mathcal{N}_{\text{sig}}^{\text{fid}}} . \quad (5.20)$$

²⁰For the purpose of clarity, the number of events at truth level is represented by a script \mathcal{N} , and the number of events at reconstruction level uses a regular N .

Since the fit is binned in m_{jj} , the acceptance and efficiency correction factors must be as well. Therefore, \mathcal{A}_i and \mathcal{C}_{ij} are written in terms of truth m_{jj} bins i and reconstruction m_{jj} bins j . A graphical representation of these regions and the use of the acceptance and correction factors can be seen in Figure 5.27.

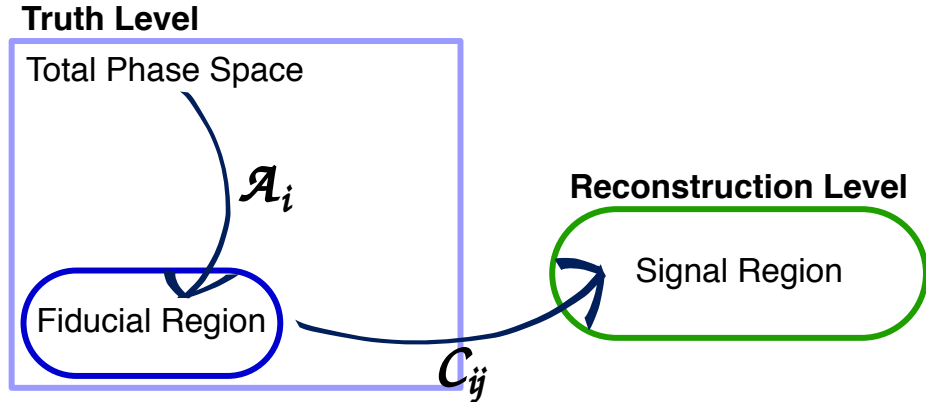


Figure 5.27: Visual representation of the different kinematic regions relevant to the cross section measurement. The acceptance factor \mathcal{A} converts from the truth level total phase space to the truth level fiducial region, and the efficiency correction \mathcal{C} translates the fiducial region in to the reconstruction level signal region.

5.4.3 Cross section extraction

The $W^\pm W^\pm jj$ EWK fiducial cross section is measured using the signal strength parameter μ that is determined by the maximum likelihood fit. This parameter is dependent on the nuisance parameters θ and can be written explicitly in terms of the measured and theoretical cross sections as

$$\mu(\theta) = \frac{\sigma_{\text{meas}}^{\text{SR}}}{\sigma_{\text{theo}}^{\text{SR}}} . \quad (5.21)$$

In the simple case with only one bin, the equation for the total number of expected events in the signal region first introduced in Equation 5.15 can be written as

$$N_{\text{exp}}^{\text{SR}}(\theta) = \mu(\theta) \cdot \sigma_{\text{theo}}^{\text{tot}} \cdot \mathcal{L} \cdot \mathcal{A} \cdot \mathcal{C}(\theta) + N_{\text{bkg}}^{\text{SR}}(\theta) \quad (5.22)$$

with the unbinned versions of \mathcal{A} and \mathcal{C} defined in Equations 5.19 and 5.20, respectively.

If the measured fiducial cross section is written as

$$\sigma_{\text{meas}}^{\text{fid}} = \mu \cdot \mathcal{A} \cdot \sigma_{\text{theo}}^{\text{tot}} , \quad (5.23)$$

then Equation 5.22 can be rearranged to read

$$\sigma_{\text{meas}}^{\text{fid}} = \frac{N_{\text{exp}}^{\text{SR}}(\theta) - N_{\text{bkg}}^{\text{SR}}(\theta)}{\mathcal{L} \cdot \mathcal{C}(\theta)}. \quad (5.24)$$

The measured fiducial cross section can finally be rewritten in terms of $\hat{\mu}$, which is the best estimator of the signal strength as extracted from the fit:

$$\begin{aligned} \sigma_{\text{meas}}^{\text{fid}} &= \hat{\mu}(\theta) \cdot \sigma_{\text{theo}}^{\text{tot}} \cdot \mathcal{A} \\ &= \hat{\mu}(\theta) \cdot \sigma_{\text{theo}}^{\text{fid}}. \end{aligned} \quad (5.25)$$

In practice, however, the cross section is not extracted from a single bin, and Equation 5.22 becomes

$$N_{\text{exp}}^{\text{SR}}(\theta) = \mu(\theta) \cdot \sigma_{\text{theo}}^{\text{tot}} \cdot \mathcal{L} \cdot \sum_i \mathcal{A}_i \sum_j \mathcal{C}_{ij} + \sum_j N_{\text{bkg},j}^{\text{SR}}(\theta) \quad (5.26)$$

for a single channel in truth and reconstruction level m_{jj} bins i and j , respectively, where the binned versions of \mathcal{A}_i and \mathcal{C}_{ij} are used. This equation can be extended to include all the analysis channels by increasing the number of bins i and j . Additionally, it can be shown that Equation 5.25 holds for this more complex case as well [85], provided care is taken to ensure that all the uncertainties are handled properly.

5.5 Summary of uncertainties

Systematic uncertainties enter the final fit as nuisance parameters which can impact the estimated signal and background yields and the shapes of the m_{jj} distributions. These uncertainties can arise from the experimental methods or from the theoretical calculations used in the analysis. This section summarizes the systematic uncertainties; the experimental uncertainties are detailed in Section 5.5.1, and the theoretical uncertainties are covered in Section 5.5.2. The impacts of the systematic uncertainties on the final cross section measurement are summarized in Table 5.19.

5.5.1 Experimental uncertainties

Experimental uncertainties include detector effects as well as uncertainties on the background estimation methods. Sources of systematic uncertainty on the measurement of physics objects are listed in Table 5.20, grouped by the relevant object type. For backgrounds estimated from MC simulations, variations in these sources of uncertainty are propagated through the analysis to obtain the corresponding uncertainties on the event yields. Additional experimental uncertainties include

Source	Impact [%]
Reconstruction	± 4.0
Electrons	± 0.5
Muons	± 1.2
Jets and E_T^{miss}	± 2.8
b -tagging	± 2.0
Pileup	± 1.5
Background	± 5.0
Misid. leptons	± 3.9
Charge misrec.	± 0.3
WZ	± 1.3
$W^\pm W^\pm jj$ QCD	± 2.8
Other	± 0.8
Signal	± 3.6
Interference	± 1.0
EW Corrections	± 1.3
Shower, Scale, PDF & α_s	± 3.2
Total	± 7.4

Table 5.19: Impact of various systematic effects on the fiducial cross section measurement. The impact of a given source of uncertainty is computed by performing the fit with the corresponding nuisance parameter varied up or down by one standard deviation from its nominal value.

the integrated luminosity, the photon conversion rate from Section 5.3.2, and the data driven charge misidentification and fake lepton background estimations from Sections 5.3.3 and 5.3.4.5, respectively.

The largest sources of experimental uncertainty on the MC estimations come from the jet-related uncertainties and the b -tagging efficiency, while the largest uncertainty on the background estimation comes from the fake-factor. The effects of the uncertainties on the $W^\pm W^\pm jj$ EWK signal and the dominant MC estimated background, WZ , are listed in Tables 5.21 and 5.22, respectively. Since the overall contributions from other processes estimated with MC are small, the uncertainties on these backgrounds have a lesser impact on the final measurement; these tables can be found in Appendix A.1.

5.5.2 Theoretical uncertainties

It is also necessary to consider uncertainties on the theoretical predictions in the fiducial region. They include the choice of PDF set, the value of the strong coupling constant α_s , the renormalization scale μ_R , the factorization scale μ_F , and the parton showering. The size of these uncertainties are measured by generating new samples with variations in a chosen parameters and comparing them

Experimental uncertainties	
Electrons	Energy resolution
	Energy scale
	Identification efficiency
	Isolation efficiency
	Reconstruction efficiency
	Trigger efficiency
Muons	Energy scale
	Identification efficiency
	Inner detector track resolution
	Muon spectrometer resolution
	Trigger efficiency
E_T^{miss}	Resolution
	Scale
Jets	Energy resolution
	Energy scale
	JVT cut efficiency
	b -tagging efficiency
	Jets from pileup

Table 5.20: List of sources of experimental uncertainties on the reconstruction of physics objects.

$W^\pm W^\pm jj$ EWK	$e^\pm e^\pm$ % Yield	$\mu^\pm e^\pm$ % Yield	$\mu^\pm \mu^\pm$ % Yield
Jet-related Uncertainties	2.28	2.22	2.28
b -tagging efficiency	1.81	1.76	1.74
Pile-up	0.48	0.97	2.42
Trigger efficiency	0.02	0.08	0.47
Lepton reconstruction/ID	1.45	1.14	1.83
MET reconstruction	0.26	0.17	0.21

Table 5.21: Impact of experimental uncertainties for the $W^\pm W^\pm jj$ EWK processes in all channels.

WZ	$e^\pm e^\pm$ % Yield	$\mu^\pm e^\pm$ % Yield	$\mu^\pm \mu^\pm$ % Yield
Jet-related Uncertainties	9.58	5.03	8.45
b -tagging efficiency	2.49	2.23	2.40
Pile-up	2.99	3.49	3.33
Trigger efficiency	0.03	0.09	0.43
Lepton reconstruction/ID	1.52	1.24	3.07
MET reconstruction	0.93	0.79	1.63

Table 5.22: Impact of experimental uncertainties for the WZ process in all channels.

to samples using the nominal choice of the parameter.

For the signal sample, internal variations on the PDF sets as well as using a different set entirely results in a relative uncertainty of up to 2.25% on the nominal sample. The impact from varying α_s is very small, on the order of < 0.01%. The factorization and renormalization scales are independently varied between 0.5-2.0 from their nominal values of 1.0. This results in relative uncertainties on the prediction of up to 15%. Finally, varying the parameters in the parton showering results in up to 8% uncertainty.

5.5.2.1 Uncertainties from EWK-QCD interference

As mentioned in Section 5.0.1, $W^\pm W^\pm jj$ production consists of both EWK processes. The two production modes cannot be naively separated due to cross terms in the matrix element calculation. These cross terms are referred to as *interference* terms. Since the $W^\pm W^\pm jj$ EWK production is the focus of the analysis, and the signal region is designed to preferentially select those events, it is important to measure the size of the EWK-QCD interference contributions.

The interference effects are estimated using the `MadGraph` MC generator, as it has a feature that allows direct modelling of the interference term. This allows four samples to be generated:

1. Inclusive: All available diagrams are used in the matrix element calculation
2. EWK only: Only EWK diagrams ($\mathcal{O}(\alpha_{\text{EWK}}) = 6$) are used
3. QCD only: Only QCD diagrams ($\mathcal{O}(\alpha_s) = 2 \otimes \mathcal{O}(\alpha_{\text{EWK}}) = 4$) are used
4. Interference: Only the interference terms are used

A minimal set of generator level cuts, listed in Table 5.23, is applied in order to avoid biasing the sample towards either production mode. The cross sections for each of the four channels can be found in Table 5.24. The size of the interference is found to be approximately 6% of the total cross section and is taken as a systematic uncertainty.

Generator level cuts
$\Delta\eta_{jj} < 10$
Jet $p_T > 20$ GeV
$M_{jj} > 10$ GeV

Table 5.23: The set of generator level cuts used for generating the interference samples with `MadGraph`.

Sample	σ (fb)
Inclusive	3.646 ± 0.0012
EWK only	2.132 ± 0.0005
QCD only	1.371 ± 0.0008
Interference	0.227 ± 0.0002

Table 5.24: Cross sections for each different $W^\pm W^\pm jj$ production mode (inclusive, EWK only, QCD only, and interference only) generated using `MadGraph`. The cross sections are calculated using a minimal set of generator level cuts from events where the W decays to a muon.

5.6 Results

After running the full analysis chain, the event yields in the signal region, low- m_{jj} control region, and WZ control region as well as associated nuisance parameters representing the uncertainties are passed to the maximum likelihood fit. From this fit, the normalization factor for the WZ control region μ_{WZ} and the signal strength parameter in the signal region μ_{obs} are determined, and the predicted yields in each input bin have been shifted according to the process detailed in Section 5.4.1.

The WZ normalization factor is measured to be

$$\mu_{WZ} = 0.88^{+0.07}_{-0.07}(\text{stat})^{+0.31}_{-0.21}(\text{model sys})^{+0.22}_{-0.11}(\text{experimental sys}) \quad (5.27)$$

and is constrained primarily by the number of data events in the WZ control region. The observed signal strength of $W^\pm W^\pm jj$ EWK production, defined in Equation 5.21, is extracted from the fit and measured with respect to the prediction of the `SHERPA v2.2.2` MC generator:

$$\mu_{\text{obs}} = 1.45^{+0.25}_{-0.24}(\text{stat})^{+0.27}_{-0.22}(\text{sys}) . \quad (5.28)$$

This corresponds to a rejection of the background-only hypothesis with a significance of 6.9σ .

The observed number of data events are compared to the predicted signal and background yields in the signal region after applying the fit in Table 5.25. The pre-fit event yields can be found in Appendix A.2. 122 candidate events are observed compared to a prediction of 60 signal and 69 background events. The m_{jj} distributions for data and prediction are shown in Figure 5.28 after the fit, and the fitted event yields in the low- m_{jj} and WZ control regions are shown in Figure 5.29.

The last ingredient necessary to measure the $W^\pm W^\pm jj$ EWK cross section is the theory predicted cross section in the fiducial region defined in Table 5.18. `SHERPA v2.2.2` is used for the calculation, and the cross section in the total generator phase space is 40.81 ± 0.05 fb, and the fiducial cross section is 2.01 ± 0.02 fb. This corresponds to an acceptance factor of $\mathcal{A} = 0.0493 \pm 0.0002$. Uncertainties on the simulation are estimated using variations of the scale, parton shower, and PDF set. The final

	e^+e^+	e^-e^-	μ^+e^+	μ^-e^-	$\mu^+\mu^+$	$\mu^-\mu^-$	combined
WZ	1.49 ± 0.30	1.10 ± 0.26	11.7 ± 1.7	8.0 ± 1.3	5.0 ± 0.6	3.5 ± 0.6	31 ± 4
Non-prompt	2.2 ± 1.3	1.2 ± 0.7	5.7 ± 2.8	4.5 ± 1.8	0.57 ± 0.06	0.65 ± 0.14	15 ± 6
e/γ conversions	1.6 ± 0.4	1.6 ± 0.5	6.3 ± 1.6	4.3 ± 1.1	—	—	13.8 ± 2.9
Other prompt	0.16 ± 0.04	0.14 ± 0.04	0.90 ± 0.19	0.63 ± 0.13	0.39 ± 0.09	0.22 ± 0.05	2.4 ± 0.5
$W^\pm W^\pm jj$ QCD	0.35 ± 0.13	0.15 ± 0.05	2.9 ± 1.0	1.2 ± 0.4	1.8 ± 0.6	0.76 ± 0.25	7.2 ± 2.4
Expected background	5.8 ± 1.5	4.1 ± 1.1	27 ± 4	18.7 ± 2.6	7.7 ± 0.8	5.1 ± 0.6	69 ± 7
$W^\pm W^\pm jj$ EWK	5.6 ± 1.0	2.2 ± 0.4	24 ± 5	9.4 ± 1.8	13.5 ± 2.5	5.2 ± 1.0	60 ± 11
Data	10	4	44	28	25	11	122

Table 5.25: Table of the data and prediction event yields in the signal region after the fit. Numbers are shown for the six lepton flavor and charge channels and for all channels combined. The background estimations from the fake-factor are included in the “Non-prompt” category, and backgrounds from $V\gamma$ production and electron charge misidentification are combined in the “ e/γ conversions” category. Finally, ZZ , VVV , and $t\bar{t}V$ backgrounds are combined in the “Other prompt” category.

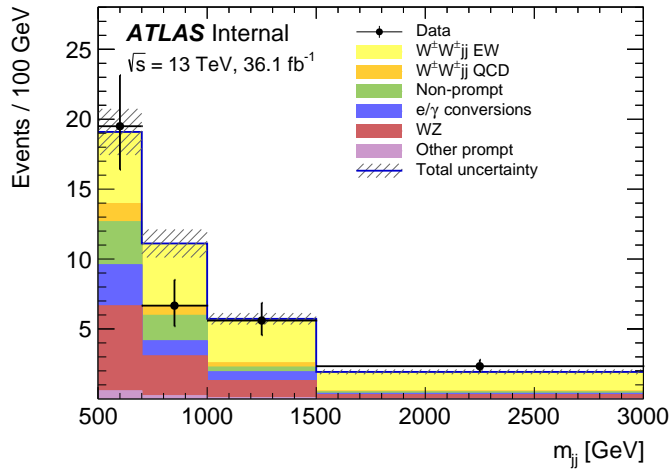


Figure 5.28: The dijet invariant mass m_{jj} distributions for data and predicted signal and background in the signal region after the fit. The shaded band represents the statistical and systematic uncertainties added in quadrature. Note that the bins have been scaled such that they represent the number of events per 100 GeV in m_{jj} . The background estimations from the fake-factor are included in the “Non-prompt” category, and backgrounds from $V\gamma$ production and electron charge misidentification are combined in the “ e/γ conversions” category. Finally, ZZ , VVV , and $t\bar{t} + V$ backgrounds are combined in the “Other prompt” category.

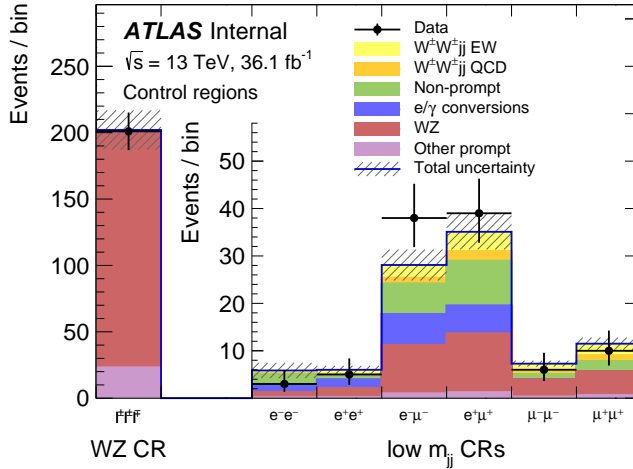


Figure 5.29: The event yields for data and predicted signal and background in the WZ and low- m_{jj} control regions after the fit. The shaded band represents the statistical and systematic uncertainties added in quadrature. The background estimations from the fake-factor are included in the “Non-prompt” category, and backgrounds from $V\gamma$ production and electron charge misidentification are combined in the “ e/γ conversions” category. Finally, ZZ , VVV , and $t\bar{t}V$ backgrounds are combined in the “Other prompt” category.

prediction used in the cross section measurement including uncertainties from Section 5.5.2 is

$$\sigma_{\text{SHERPA}}^{\text{fid}} = 2.01 \pm 0.02(\text{stat}) \pm 0.29(\text{scale}) \pm 0.16(\text{parton shower}) \pm 0.05(\text{PDF}) \text{ fb}. \quad (5.29)$$

Combining this **SHERPA** prediction with the measured signal strength μ_{obs} from Equation 5.28, the measured fiducial cross section $\sigma_{\text{meas}}^{\text{fid}}$ can be calculated using Equation 5.25:

$$\sigma_{\text{meas}}^{\text{fid}} = 2.91^{+0.51}_{-0.47}(\text{stat}) \pm 0.12(\text{model sys}) \pm 0.24(\text{experimental sys}) \pm 0.08(\text{luminosity}) \text{ fb}. \quad (5.30)$$

A plot comparing the measured fiducial cross section to two theoretical calculations is shown in Figure 5.30. The measured value is compared to the **SHERPA v2.2.2** prediction used to calculate μ_{obs} as well as to **POWHEG-BOX v2**. As mentioned in Section 5.1.1, this **POWHEG** sample does not include the resonant triboson diagrams and is only used here for a visual comparison.

5.7 Beyond the Standard Model extensions of $W^\pm W^\pm jj$

Many so-called *Beyond the Standard Model* (BSM) theories exist that incorporate new physics with what has been experimentally observed. BSM theories often manifest as deviations from the expected SM cross sections, either due to additional decay possibilities affecting branching

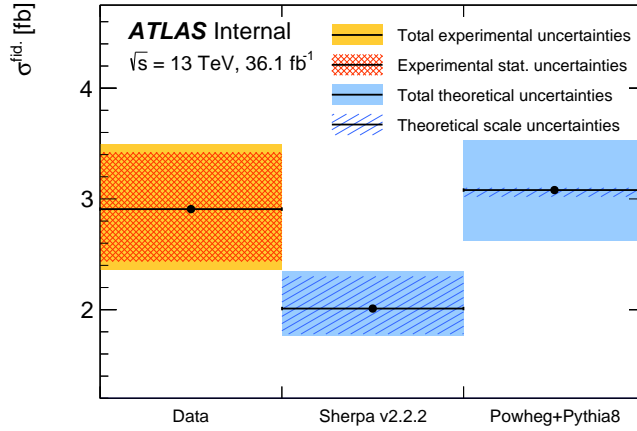


Figure 5.30: Comparison of the measured $W^\pm W^\pm jj$ EWK fiducial cross section with theoretical calculations from **SHERPA** v2.2.2 and **POWHEG-BOX** v2. The light orange band represents the total experimental uncertainty on the measured value, and the dark orange hashed band is the statistical uncertainty. For the simulations, the light blue band represents the total theoretical uncertainty, and the dark blue hashed band are the scale uncertainties. The theory predictions do not include the interference between the EWK and QCD production.

ratios or modifications of the couplings themselves. One of the most well-known avenues for BSM involving new particles is supersymmetry [116]; however, two popular BSM extensions relevant to the $W^\pm W^\pm jj$ process involve a doubly-charged Higgs particle ($H^{\pm\pm}$) and anomalous triple and quartic gauge couplings (aTGC and aQGC, respectively)²¹. These two BSM theories will be touched on in the context of $W^\pm W^\pm jj$ analyses at the LHC.

5.7.1 Doubly charged Higgs bosons

Same-sign $W^\pm W^\pm$ scattering in the SM does not contain the s -channel diagram shown in Figure 5.1, as there is no SM resonance with ± 2 electric charge; however, there are BSM theories that involve expanded Higgs sectors that do include such a particle.

One popular model is the Georgi-Machacek (GM) Higgs-triplet model [117]. The GM model proposes a Higgs triplet field χ in addition to the usual Higgs doublet ϕ . After symmetry breaking, each field obtains its own VEV, v_χ and v_ϕ , and the SM VEV is made up of a combination of the

²¹The aQGC's are the focus in this section since the $WWWW$ QGC vertex is accessible through $W^\pm W^\pm$ scattering, as well as the fact that aTGC's have been studied in far greater detail due to being accessible through a larger number of processes.

two:

$$v_{\text{SM}}^2 = v_\phi^2 + 8v_\chi^2 \approx (246 \text{ GeV})^2. \quad (5.31)$$

As a result, the W^\pm and Z boson masses, which are determined by v_{SM} in the SM, receive contributions from both VEV's here. It is important to note that even though this fixes the value of $v_\phi^2 + 8v_\chi^2$, the ratio v_ϕ/v_χ is not determined. Thus, there is no required hierarchy $v_\chi \ll v_\phi$, and the phenomenology of electroweak bosons can differ from the SM without conflicting with current experimental results [118]. Ultimately, the GM model predicts additional Higgs particles, including a doubly-charged $H^{\pm\pm}$.

The GM model has been tested experimentally by CMS at $\sqrt{s} = 8$ and 13 TeV for the process $H^{\pm\pm} \rightarrow W^\pm W^\pm$ [82, 83]. The coupling depends on the mass of the $H^{\pm\pm}$ as well as s_H , where s_H^2 is the fraction of the W boson mass that is generated by v_χ . The resulting 95% confidence level (CL) limits on the VBS cross section are shown in Figure 5.31. Values of s_H greater than 0.18 and 0.44 are excluded for $m_{H^{\pm\pm}} = 200$ GeV and 1 TeV, respectively.

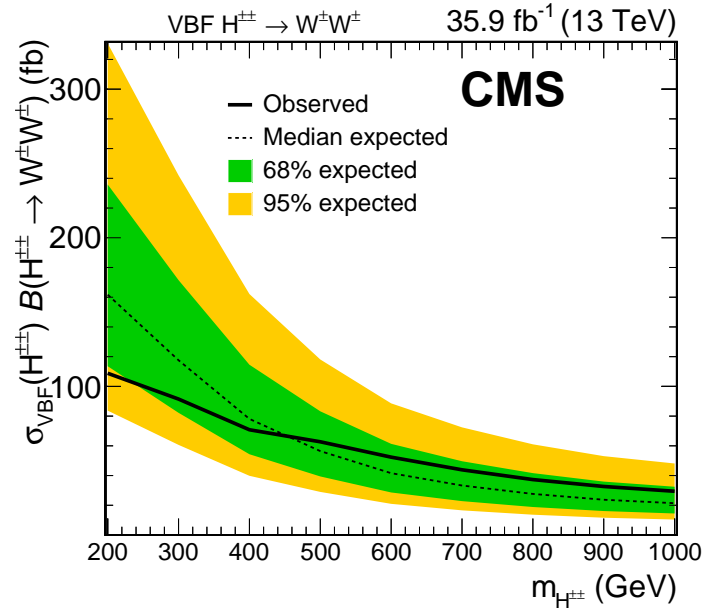


Figure 5.31: CMS observed and expected upper limits for the $H^{\pm\pm} \rightarrow W^\pm W^\pm$ cross section at 95% CL at $\sqrt{s} = 13$ TeV as a function of $H^{\pm\pm}$ mass. The region above the observed limit is excluded by the measurement. Plot taken from [83].

A second model accounts for neutrino masses via a *type II seesaw* mechanism, which involves extending the SM Higgs sector by a complex triplet of scalar fields with hypercharge $Y = 2$ [119].

This results in a similar situation as the GM model, with two VEV's v_d and v_t corresponding to the doublet and triplet fields, respectively, and multiple Higgs bosons, including a doubly-charged $H^{\pm\pm}$. In this model, the relative sizes of the two VEV's is important for the context of the same-sign $W^\pm W^\pm$ process. The observed neutrino masses are proportional to the size of v_t , which motivates a small value of the triplet VEV. However, the $H^{\pm\pm}$ coupling to W^\pm is also proportional to v_t , and for scenarios where $v_t \ll v_d$, the $H^{\pm\pm} \rightarrow W^\pm W^\pm$ decay mode is suppressed [120, 121].

This model has been studied by ATLAS at $\sqrt{s} = 13$ TeV involving pairs of $H^{\pm\pm}$ decaying to four W^\pm bosons [122]. The value of the triplet VEV is set to $v_t = 0.1$ GeV, and the mass region $H^{\pm\pm} > 200$ GeV is considered. No significant excess is seen above the SM predictions, and the 95% CL limits on the $H^{\pm\pm} \rightarrow W^\pm W^\pm$ cross section are reproduced in Figure 5.32.

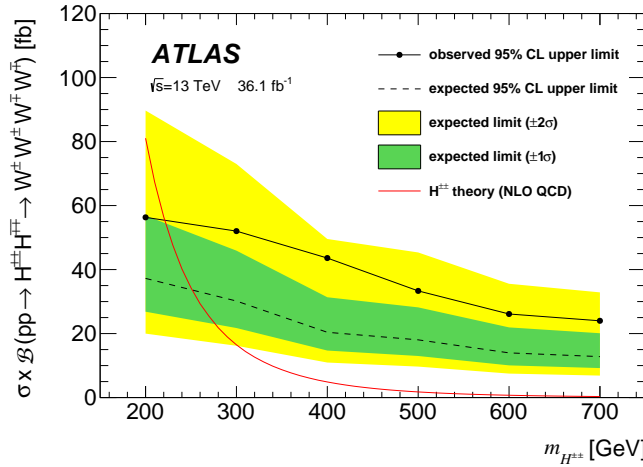


Figure 5.32: ATLAS observed and expected upper limits for the $H^{\pm\pm}H^{\mp\mp} \rightarrow W^\pm W^\pm W^\mp W^\mp$ cross section at 95% CL at $\sqrt{s} = 13$ TeV as a function of $H^{\pm\pm}$ mass. The region above the observed limit is excluded by the measurement. Plot taken from [122].

5.7.2 Anomalous quartic couplings

In the event that new physics exists at an energy scale far above what is currently accessible at the LHC, it cannot be directly observed by the experiment; however, its effects can still appear in the interactions between known particles. In this case, the SM is simply the low-energy behavior of a larger *effective field theory* (EFT), which contains additional, higher-dimensional operators that obey the existing SM symmetries:

$$\mathcal{L}_{EFT} = \mathcal{L}_{SM} + \sum_{d>4} \sum_i \frac{\tilde{c}_i}{\Lambda^{d-4}} \mathcal{O}_i, \quad (5.32)$$

where \mathcal{O}_i are operators of dimension d with coefficients \tilde{c}_i , and Λ is the energy scale of the new physics. Here it can be clearly seen that as the energy scale $\Lambda \rightarrow \infty$, the SM behavior dominates. In the region where $E \ll \Lambda$, operators with high dimensionality contribute less to the total Lagrangian, and the summation may be truncated above a chosen value of d , at which point \mathcal{L}_{EFT} becomes predictive and can parameterize any heavy new physics [123].

Only operators with even dimensionality are allowed in order to conserve baryon and lepton numbers. The largest contributions to \mathcal{L}_{EFT} therefore come from operators with $d = 6$; however, any of these operators which modify the QGC's also modify the TGC's. As a result, these operators are better constrained by existing analyses with greater sensitivity to TGC's. Operators with $d = 8$ are the lowest that modify exclusively the QGC's, of which there are 18, and nine of them modify the $WWWW$ QGC accessible through same-sign $W^\pm W^\pm$ scattering [124, 123]:

$$\begin{aligned}\mathcal{O}_{S,0} &= [(D_\mu \Phi)^\dagger D_\nu \Phi] \times [(D^\mu \Phi)^\dagger D^\nu \Phi], \\ \mathcal{O}_{S,1} &= [(D_\mu \Phi)^\dagger D^\mu \Phi] \times [(D_\nu \Phi)^\dagger D^\nu \Phi], \\ \mathcal{O}_{M,0} &= \text{Tr}[\hat{W}_{\mu\nu} \hat{W}^{\mu\nu}] \times [(D_\beta \Phi)^\dagger D^\beta \Phi], \\ \mathcal{O}_{M,1} &= \text{Tr}[\hat{W}_{\mu\nu} \hat{W}^{\nu\beta}] \times [(D_\beta \Phi)^\dagger D^\mu \Phi], \\ \mathcal{O}_{M,6} &= [(D_\mu \Phi)^\dagger \hat{W}_{\beta\nu} \hat{W}^{\beta\nu} D^\mu \Phi], \\ \mathcal{O}_{M,7} &= [(D_\mu \Phi)^\dagger \hat{W}_{\beta\nu} \hat{W}^{\beta\mu} D^\nu \Phi], \\ \mathcal{O}_{T,0} &= \text{Tr}[\hat{W}_{\mu\nu} \hat{W}^{\mu\nu}] \times \text{Tr}[\hat{W}_{\alpha\beta} \hat{W}^{\alpha\beta}], \\ \mathcal{O}_{T,1} &= \text{Tr}[\hat{W}_{\alpha\nu} \hat{W}^{\mu\beta}] \times \text{Tr}[\hat{W}_{\mu\beta} \hat{W}^{\alpha\nu}], \\ \mathcal{O}_{T,2} &= \text{Tr}[\hat{W}_{\alpha\mu} \hat{W}^{\mu\beta}] \times \text{Tr}[\hat{W}_{\beta\nu} \hat{W}^{\nu\alpha}].\end{aligned}\tag{5.33}$$

Each operator is paired with a coupling in the Lagrangian term: $\mathcal{L}_{S,0} = \frac{f_{S,0}}{\Lambda^4} \mathcal{O}_{S,0}$ and so on. The SM prediction can be compared to simulations generated with chosen values for the anomalous coupling constants, as shown in Figure 5.33.

Limits on the anomalous couplings generated by the $d = 8$ operators of Equation 5.33 have been set by CMS in their $W^\pm W^\pm jj$ analyses at $\sqrt{s} = 8$ and 13 TeV [82, 83]. ATLAS has also set limits at $\sqrt{s} = 8$ TeV [81] using a different parameterization of the anomalous couplings outlined in [125]. The limits set in CMS's 13 TeV analysis are reproduced in Table 5.26. The limits are obtained from fits to the m_{ll} distributions in the signal and WZ control regions, and 95% confidence intervals are calculated by varying each operator individually.

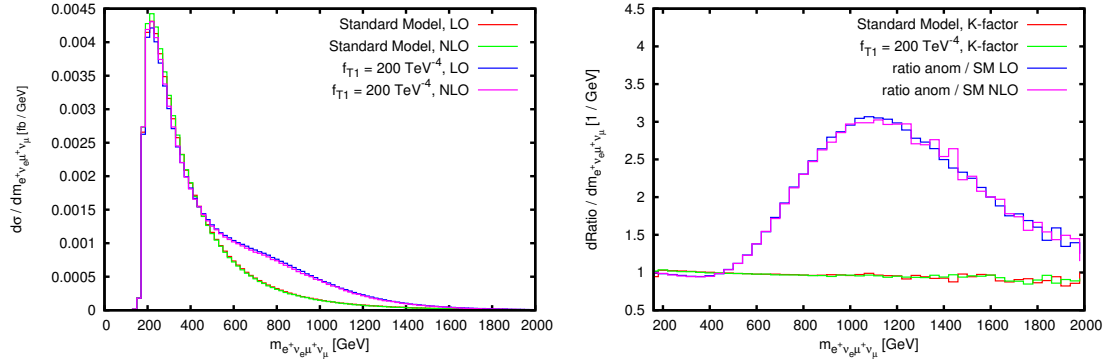


Figure 5.33: Invariant mass distributions of the $2l2\nu$ system in $pp \rightarrow e^+\nu_e\mu^+\nu_\mu jj$ events at LO and NLO with the VBFNLO MC generator. SM predictions are compared to those with the anomalous coupling $\frac{f_{T,1}}{\Lambda^4} = 200 \text{ TeV}^{-4}$. The left plot shows the differential cross section for each prediction, and the right plot shows the K -factors for the SM and anomalous coupling predictions as well as the cross section ratio between the anomalous coupling and SM predictions at LO and NLO. Plots taken from [123].

Coupling	Observed limits [TeV^{-4}]
$f_{S,0}/\Lambda^4$	$[-7.7, 7.7]$
$f_{S,1}/\Lambda^4$	$[-21.6, 21.8]$
$f_{M,0}/\Lambda^4$	$[-6.0, 5.9]$
$f_{M,1}/\Lambda^4$	$[-8.7, 9.1]$
$f_{M,6}/\Lambda^4$	$[-11.9, 11.8]$
$f_{M,7}/\Lambda^4$	$[-13.3, 12.9]$
$f_{T,0}/\Lambda^4$	$[-0.62, 0.65]$
$f_{T,1}/\Lambda^4$	$[-0.28, 0.31]$
$f_{T,2}/\Lambda^4$	$[-0.89, 1.02]$

Table 5.26: Observed 95% confidence limits set by CMS at $\sqrt{s} = 13$ TeV on the nine dimension-eight operators that modify the $WWWW$ QGC listed in Equation 5.33. Table taken from [83].

CHAPTER 6

Prospects for same-sign WW at the High Luminosity LHC

On December 3, 2018, Run 2 of the LHC officially ended, and the collider was shut down to begin the first of two scheduled extended maintenance periods [126]. During these two long shutdowns, the Phase-I and Phase-II upgrades of the LHC and ATLAS will occur in order to prepare for the High-Luminosity LHC (HL-LHC) which is scheduled to begin operation in 2026 [127].

The HL-LHC is planned to run at a center-of-mass energy of $\sqrt{s} = 14$ TeV with an instantaneous luminosity of $\mathcal{L} = 5 \times 10^{34}$ cm $^{-2}$ s $^{-1}$ with up to 200 collisions per beam-crossing. Over the course of operation, the HL-LHC is expected to collect a total integrated luminosity of $\mathcal{L} = 3000$ fb $^{-1}$ by 2035 [128].

These run conditions will be much harsher than what ATLAS has experienced so far, and there are several upgrades planned to adapt the detector to the high luminosity environment. Most notably, the entire ID will be replaced with an all-silicon tracker which will extend the coverage from $|\eta| \leq 2.7$ up to $|\eta| \leq 4.0$. This will allow for forward particle tracks to be reconstructed, which can in turn be matched to clusters in the calorimeters for use in electron identification or forward jet tagging [129].

The upgraded detector, the higher beam energy, and the increased volume of data to be collected provides the opportunity to measure rare processes to a much higher precision than what is possible with the current LHC dataset. Same-sign $W^\pm W^\pm jj$ production is one such process. With greater statistics, the accuracy of the cross section measurement can be improved over the 13 TeV analysis detailed in Chapter 5, and it also will allow for more detailed physics studies, such as measuring the polarization state of the scattered W bosons. A measurement of the cross section

of longitudinally polarized $W^\pm W^\pm jj$ scattering is one of the most enticing extensions of the existing $W^\pm W^\pm jj$ measurements due to its sensitivity to the EWSB mechanism [130], and it is expected to be measurable for the first time at the HL-LHC. The analysis detailed in this chapter is based off of the 2018 ATLAS HL-LHC $W^\pm W^\pm jj$ prospects study [131] which extends upon the results of the previous year’s study [132].

6.0.3 Analysis Overview

The experimental signature of interest is identical to the 13 TeV analysis (see Chapter 5): two prompt leptons (either electrons or muons) with the same electric charge, missing transverse energy, and two high energy forward jets. These jets are again required to have a large angular separation and a high combined invariant mass to preferentially select EWK-produced $W^\pm W^\pm jj$ events.

Background processes are not expected to change with respect to the 13 TeV analysis and are summarized here. The dominant source of prompt background comes from $WZ+jets$ events where both bosons decay leptonically. If the lepton from the Z -decay with opposite charge from the W falls outside of the detector acceptance or is not identified, the remaining two leptons will form a same-sign pair, and the event may pass the signal lepton criteria. To a much lesser extent, $ZZ+jets$ events can enter the signal region this way provided two leptons are “lost”. Other prompt sources include $t\bar{t}+V$ and multiple parton interactions, however both contributions are small. Overall, prompt backgrounds are expected to contribute less in HL-LHC analyses than they do currently due to the forward tracking in the upgraded ATLAS detector reducing the probability of leptons falling outside the detector acceptance. Jets mis-reconstructed as leptons or leptons from hadronic decays (such as $t\bar{t}$ and $W+jets$ production) comprise the non-prompt lepton background. Lastly, events with two prompt, opposite-charge electrons can appear as a same-sign event provided one of the electrons is mis-reconstructed and assigned the wrong charge.

In this analysis, the EWK production of $W^\pm W^\pm jj$ is studied in the context of the planned HL-LHC run conditions and upgraded ATLAS detector. An optimized event selection (referred to as the *optimized selection*) is also explored in an effort to gain increased signal significance over the *default selection*. The cross section of the inclusive EWK production is measured for both the default and optimized selections, and the extraction of the expected longitudinal scattering significance is measured with the optimized selection.

6.1 Theoretical motivation

The motivation for studying the $W^\pm W^\pm jj$ process as well as VBS in general has been established previously in Sections 2.3 and 5.0.1. Since only the longitudinally polarized vector bosons that is sensitive to the EWSB mechanism, a direct measurement of this cross section will be very useful for understanding how the Higgs unitarizes the scattering amplitude [130].

6.1.1 Experimental sensitivity to longitudinal polarization

There are three possible polarization states for a massive vector boson: two transverse (+ or -) and one longitudinal (0). Therefore, in a system with two W bosons, the overall polarization can be purely longitudinal (00), purely transverse (++, --, and +-), or mixed (+0 and -0). The three combinations will be referred to as *LL*, *TT*, and *LT* respectively.

In order extract the longitudinal scattering component, it is necessary to find variables that can help distinguish the LL from the TT and LT events. Several were studied, and those with the best discriminating power between the different polarization states are the leading and subleading lepton transverse momenta as well as the azimuthal separation of the two VBS jets $|\Delta\phi_{jj}|$. Both leptons in LL events tend to be softer than the TT and LT events (see Figure 6.1), which motivates keeping cuts on the lepton p_T as low as possible in the event selection. In the case of the dijet separation, LL events prefer the tag jets to be back-to-back (see Figure 6.2). The $|\Delta\phi_{jj}|$ distribution is chosen to be the discriminating variable between the polarizations, and it is ultimately passed to a binned likelihood fit to extract the longitudinal scattering significance.

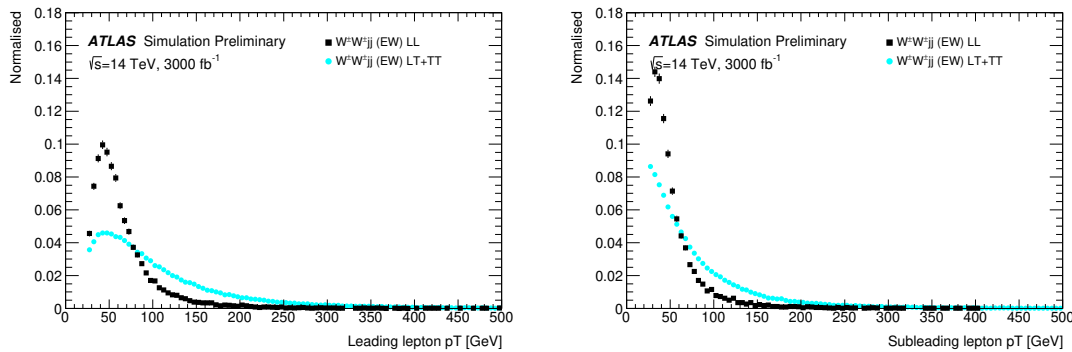


Figure 6.1: Comparison of the leading (left) and subleading (right) lepton p_T distributions for purely longitudinal (LL, black) and mixed polarization (LT+TT, cyan) $W^\pm W^\pm jj$ events.

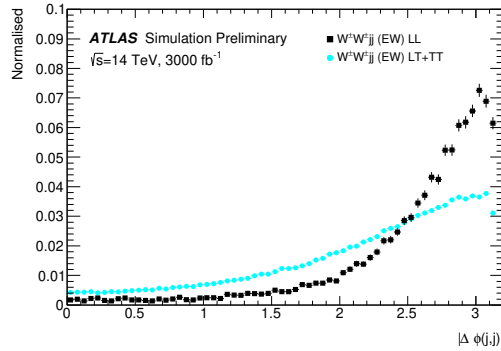


Figure 6.2: Comparison of the azimuthal dijet separation ($|\Delta\phi_{jj}|$) for purely longitudinal (LL, black) and mixed polarization (LT+TT, cyan) $W^\pm W^\pm jj$ events.

6.2 Monte Carlo samples

As this is a prospects study for a future collider, all signal and background processes are modeled using MC simulations. The samples are generated at the expected HL-LHC center of mass energy $\sqrt{s} = 14$ TeV, and the event yields are scaled to the anticipated integrated luminosity of $\mathcal{L} = 3000 \text{ fb}^{-1}$. The MC samples used in the analysis are generated at particle-level and have not been run through the full simulation of the ATLAS detector. Instead, smearing functions derived from a GEANT4 simulation of the upgraded ATLAS detector are used to estimate detector effects such as momentum resolution. In addition, pileup events are fully simulated. The MC samples used in this analysis are summarized in Table 6.1.

The signal sample consists of both VBS and non-VBS electroweak (EWK) $W^\pm W^\pm jj$ production, and it is simulated with the `Madgraph5_aMC@NLO` generator using the `NNPDF3.0` PDF set and interfaced with `PYTHIA v8` [133] for hadronization and parton showering. To study the longitudinal polarization more directly, two additional `Madgraph5_aMC@NLO` $W^\pm W^\pm jj$ samples are used: one containing only the longitudinal contribution (LL) and a second containing the transverse (TT) and mixed (LT) contributions.

There are many other processes that can produce the same final state as the $W^\pm W^\pm jj$ and must also be accounted for using MC simulations. WZ events are generated using `SHERPA v2.2.0`, which includes up to one parton at NLO in the strong coupling constant and up to three additional partons at LO. Both EWK and QCD production are included in these samples. ZZ and triboson VVV ($V = W, Z$) events are generated using `SHERPA v2.2.2` with up to two additional partons in the final state. For the triboson backgrounds, the bosons can decay leptonically or hadronically. $W+jets$

Process	Generator	Comments
$W^\pm W^\pm jj$ (EWK)	<code>Madgraph5_aMC@NLO</code>	Signal sample
$W^\pm W^\pm jj$ (QCD)	<code>Madgraph5_aMC@NLO</code>	
$W^\pm W^\pm jj$ (LL)	<code>Madgraph5_aMC@NLO</code>	Pure longitudinal polarization sample
$W^\pm W^\pm jj$ (TT+LT)	<code>Madgraph5_aMC@NLO</code>	Mixed and transverse polarization sample
Diboson	<code>SHERPA v2.2.0</code>	WZ events
	<code>SHERPA v2.2.2</code>	ZZ events
Triboson	<code>SHERPA v2.2.2</code>	
$W+jets$	<code>Madgraph5_aMC@NLO</code>	
$Z+jets$	<code>POWHEG-BOX v2</code>	
$t\bar{t}$	<code>POWHEG-BOX</code>	
Single top	<code>POWHEG-BOX</code>	

Table 6.1: Summary of MC samples used in the analysis.

backgrounds are generated for electron, muon, and tau final states at LO with `Madgraph5_aMC@NLO` and the NNPDF3.0 PDF set with showering from `PYTHIA v8`. $Z+jets$ events are produced using `POWHEG-BOX v2` and the CT10 PDF set interfaced with `PYTHIA v8`. Finally, $t\bar{t}$ and single-top events are generated using `POWHEG-BOX` with showering from `PYTHIA v6`.

6.3 Background estimations

In this analysis, all background contributions are estimated using MC simulations. Backgrounds from electron charge misidentification and fake electrons from jets, which are traditionally estimated using data-driven techniques, are instead estimated using a set of parameterization functions applied to the MC. These functions calculate the probability that an electron is assigned the wrong charge or a jet is mis-reconstructed as an electron parameterized by the p_T and η of the respective electron or jet. The probabilities are derived from studies on expected electron performance with the upgraded ATLAS detector [134].

Processes involving two W or Z bosons are grouped together as *diboson* backgrounds, with the exception of $W^\pm W^\pm jj$ events produced via QCD interactions, which are kept separate. Similarly, all backgrounds with three vector bosons are combined and labeled as *triboson*. Any $W+jets$ or top events that pass selection and do not contain a fake electron, as well as any $Z+jets$ events without an electron identified as having its charge misidentified are combined as *other non-prompt* backgrounds.

6.3.1 Truth-based isolation

The canonical isolation variables used in ATLAS analyses require detailed information from several detector subsystems including particle tracks and calorimeter responses. Since the MC samples used in this analysis have not been run through a full detector simulation, it is not possible to reproduce the official isolation variables. For truth-level analysis, this is generally not a serious concern, as high- p_T signal leptons tend to be well isolated to begin with. However, isolation is one of the most powerful tools for rejecting leptons from non-prompt sources, such as top events, which are produced in association with additional nearby particles from b and c hadron decays. It was seen in the early stages of this analysis that without any sort of isolation requirement, contributions from top backgrounds (including single top, $t\bar{t}$, and $t\bar{t} + V$) were more than an order of magnitude higher than expected.

As a result, it was necessary to find one or more quantities that are comparable to the isolation information that is available in fully-simulated samples. Analogues to track- and calorimeter-based isolation are constructed by summing the momentum and energy, respectively, of stable truth particles with $p_T > 1$ GeV within a specified radius of each signal lepton. For the track-based isolation, only charged truth particles are used; both charged and neutral particles (excluding neutrinos) are included for the calorimeter-based isolation. Ultimately, a set of isolation cuts are chosen that are similar to the fixed-cut recommendations for ATLAS Run 2 analyses. The truth-based isolation requirements are listed in Table 6.2.

	Electron Isolation	Muon Isolation
Track-based isolation cone size	$\Delta R < 0.2$	$\Delta R < 0.3$
Track-based isolation requirement	$\sum p_T/p_T^e < 0.06$	$\sum p_T/p_T^\mu < 0.04$
Calorimeter-based isolation cone size	$\Delta R < 0.2$	$\Delta R < 0.2$
Calorimeter-based isolation requirement	$\sum E_T/p_T^e < 0.06$	$\sum E_T/p_T^\mu < 0.15$

Table 6.2: Truth-based isolation requirements for electrons and muons.

With no cut on truth-based isolation, 83% of the total background consisted of top events (without including top contributions to the fake electron background). The isolation requirement reduces the top background by over 99%, and the percentage of the total background from top events is reduced to 2%. Additional studies on the truth-based isolation as well as full event yields with and without the isolation requirement can be found in Appendix B.1.

6.4 Object and event selection

The majority of the default object and event selections were determined in the preceding $W^\pm W^\pm jj$ HL-LHC prospects study [132], which focused on the impact of the upgraded detector’s forward tracking capabilities. Several different combinations of lepton and jet η ranges were tested, and the results are used in this study.

6.4.1 Object selection

Electrons and muons are preselected to have $p_T > 7$ and 6 GeV, respectively, and lie within $|\eta| \leq 4.0$. The likelihood of a given lepton to pass the trigger and identification requirements is estimated by calculating an efficiency dependent on the p_T and η of the lepton. The leptons are also required to pass the isolation criteria detailed in Table 6.2. Jets that have been tagged as a fake electron by the functions described in Section 6.3 are treated as electrons for the purpose of the object selection and are subject to the same criteria. In order to be considered a signal lepton, the transverse momentum requirement is raised to $p_T > 25$ GeV. The two highest p_T leptons passing this selection are chosen to be the leading and subleading signal leptons.

Jets are clustered using the anti- k_t algorithm from final-state particles (excluding muons and neutrinos) within a radius of $\Delta R = 0.4$. All jets are required to have $p_T > 30$ GeV and lie within $|\eta| < 4.5$; in order to suppress jets from pileup interactions, jets outside of $|\eta| \geq 3.8$ must pass an higher momentum cut of $p_T > 70$ GeV. Jets overlapping a preselected electron within $\Delta R(e, j) < 0.05$ are removed in order to prevent double counting. The two highest p_T jets are defined as the leading and subleading tag jets.

6.4.2 Event selection

The default event selection is summarized in Table 6.3 and described here. Exactly two signal leptons are required with the same electric charge and separated from each other by $\Delta R(ll) > 0.3$. In order to suppress contributions from Drell-Yan backgrounds, the two signal leptons must have an invariant mass m_{ll} greater than 20 GeV. Additionally, if both signal leptons are electrons, their mass must be at least 10 GeV away from the Z -boson mass in order to reduce background from Z -boson decays²². The event is required to have at least 40 GeV of missing transverse energy (E_T^{miss})

²²The electron charge misidentification rate in the upgraded ATLAS detector is estimated to be high enough that contributions from $Z \rightarrow ee$ backgrounds are non-negligible.

Selection requirement	Selection value
Lepton kinematics	$p_T > 25 \text{ GeV}$ $ \eta \leq 4.0$
Jet kinematics	$p_T > 30 \text{ GeV}$ for $ \eta \leq 4.5$ $p_T > 70 \text{ GeV}$ for $ \eta > 3.8$
Dilepton charge	Exactly two signal leptons with same charge
Dilepton separation	$\Delta R_{l,l} \geq 0.3$
Dilepton mass	$m_{ll} > 20 \text{ GeV}$
Z boson veto	$ m_{ee} - m_Z > 10 \text{ GeV}$ (ee -channel only)
E_T^{miss}	$E_T^{\text{miss}} > 40 \text{ GeV}$
Jet selection	At least two jets with $\Delta R_{l,j} > 0.3$
b jet veto	$N_{\text{b-jet}} = 0$
Dijet separation	$\Delta \eta_{jj} > 2.5$
Trilepton veto	No additional preselected leptons
Dijet mass	$m_{jj} > 500 \text{ GeV}$
Lepton-jet centrality	$\zeta > 0$

Table 6.3: Summary of the signal event selection.

to account for the two final-state neutrinos. Events with additional preselected leptons are vetoed, which greatly reduces WZ and ZZ backgrounds.

Each event must have at least two jets, and both tag jets are required to not overlap with the signal leptons. Events with one or more b -jets are vetoed to suppress backgrounds from heavy-flavor decays. In order to preferentially select EWK production, the tag jets are required to have a large separation between them and a large invariant mass. Finally, a cut on the lepton centrality ζ^{23} , defined in Equation 6.1, further enhances the EWK $W^\pm W^\pm jj$ signal:

$$\zeta = \min[\min(\eta_{\ell 1}, \eta_{\ell 2}) - \min(\eta_{j 1}, \eta_{j 2}), \max(\eta_{j 1}, \eta_{j 2}) - \max(\eta_{\ell 1}, \eta_{\ell 2})]. \quad (6.1)$$

6.5 Selection optimization

The default event selection is optimized in order to improve the strength of the $W^\pm W^\pm jj$ EWK signal. The expectation is that the increased detector acceptance from the forward tracking combined with an increase in center of mass energy and much higher integrated luminosity will allow tighter selection cuts without jeopardizing signal statistics.

²³ ζ is a measurement of whether the two signal leptons lie between the two tagging jets in η , as is preferred by the VBS topology.

6.5.1 Random grid search algorithm

The chosen method for optimizing the event selection is a cut-based algorithm known as the Random Grid Search (RGS) [135]. Consider a simple case of two variables x and y chosen to differentiate signal from background. In order to be considered a signal event, a given event would be required to pass a set of selection criteria, called a *cut point*: $c = \{x > x_c, y > y_c\}$. A simple method to choose the optimal cut point (the “best” values of the cuts x_c and y_c) would be to construct an $n \times m$ rectangular grid in x and y consisting of points $(x_0, y_0), (x_1, y_1), \dots, (x_n, y_m)$, as in Figure 6.3a. One can then choose a cut point $c_k = \{x > x_i, y > y_j\}$ that maximizes the signal significance as given by a chosen metric. This would be considered a *rectangular grid search*.

While effective in principle, a rectangular grid search comes with two major drawbacks:

1. The algorithm scales exponentially as the number of variables to be optimized increases, as this is effectively increasing the dimensionality of the grid. In the simple case of a square grid with N bins per variable v , the number of cut points to be evaluated grows as N^v .
2. Signal and background samples are rarely evenly distributed over the entire grid, resulting in many cut points being sub-optimal, and evaluating them would be a waste of computing resources.

To combat these limitations, the RGS algorithm constructs a grid of cut points directly from the signal sample itself. In the two-dimensional example, this means that the variables x_i and y_j making up the cut point $c_k = \{x > x_i, y > y_j\}$ take their values directly from a given signal event. This creates a *random grid* of cut points that has the benefit of being biased towards regions of high signal concentration by construction. This reduces the need for exponentially increasing numbers of cut points while ensuring that computing resources are not wasted in regions with few to no signal events. An example of a two-dimensional random grid is shown in Figure 6.3b.

Once the random grid of cut points is constructed, the optimal cut point can be chosen using any number of metrics, such as signal to background ratio. For the purpose of the $W^\pm W^\pm jj$ upgrade study, the optimal cut point is chosen to be the one that maximizes the signal significance Z , defined as [136]

$$Z = \sqrt{2 \left[(s + b) \ln \left(\frac{s + b}{b_0} \right) + b_0 - s - b \right] + \frac{(b - b_0)^2}{\sigma_b^2}}, \quad (6.2)$$

where s and b are the number of signal and background events, respectively, σ_b is the total uncertainty

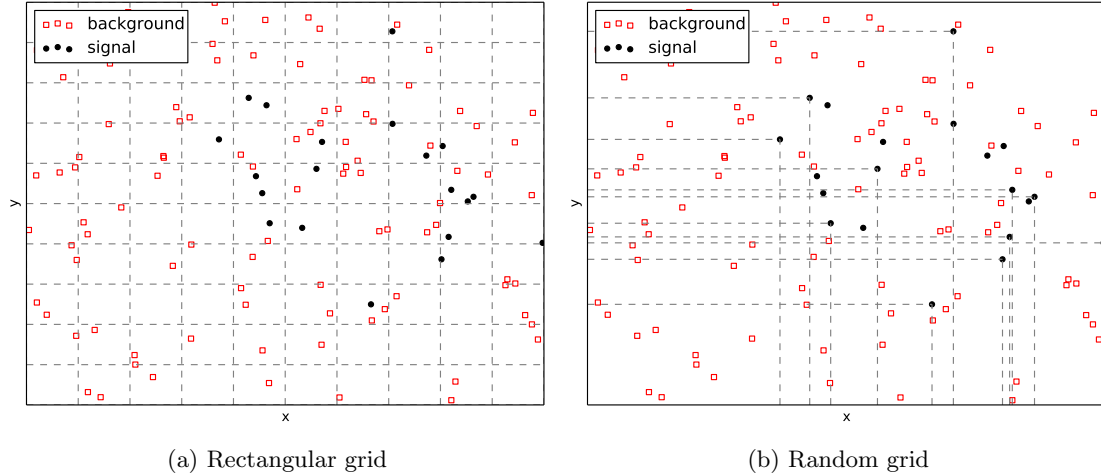


Figure 6.3: A visual representation of a two-dimensional rectangular grid (left) and a random grid (right) in variables x and y . The signal events are the black circles, and the red squares are the background events. Each intersection of gray dashed lines represents a cut point to be evaluated by the optimization.

on the background, and b_0 is defined as

$$b_0 = \frac{1}{2} \left(b - \sigma_b^2 + \sqrt{(b - \sigma_b^2)^2 + 4(s + b)\sigma_b^2} \right). \quad (6.3)$$

In the case where the background is known precisely (i.e. $\sigma_b = 0$), Equation 6.2 simplifies to

$$Z = \sqrt{2 \left(b \left[(1 + s/b) \ln(1 + s/b) - s/b \right] \right)}, \quad (6.4)$$

which further reduces to the familiar $Z = s/\sqrt{b}$ for the case when $s \ll b$.

6.5.2 Inputs to the optimization

In order to train the RGS, signal and background samples are prepared from events passing the event selection outlined in Table 6.3 up through the b -jet veto. The signal sample is chosen to be the longitudinally polarized $W^\pm W^\pm jj$ EWK events, and the transverse and mixed polarizations are treated as background along with $W^\pm W^\pm jj$ events from QCD interactions and the traditional backgrounds listed in Section 6.3. Splitting the inclusive $W^\pm W^\pm jj$ EWK events by polarization allows the optimization to favor the longitudinally polarized events as much as possible, even though they both contribute to the EWK signal.

The following variables are chosen for optimization:

- Leading lepton p_T

- Dilepton invariant mass (m_{ll})
- Leading and subleading jet p_T
- Dijet invariant mass (m_{jj})
- Lepton-jet centrality (ζ)

Subleading lepton p_T is omitted as it is desirable to keep the cut value as low as possible due to its sensitivity to the longitudinal polarization (as discussed in Section 6.1.1); despite this, the leading lepton p_T is still allowed to be optimized as it can have strong background rejection power. Additionally, the dijet separation $\Delta\eta_{jj}$ was included in early studies of the optimization, however it was dropped due to the cut value being motivated by well-studied differences between EWK- and QCD-produced $W^\pm W^\pm jj$ events (as in Figure 5.6b).

Two additional constraints are imposed on the optimal cut point:

1. At least 1000 signal events must survive in order to prevent the optimization from being too aggressive and unnecessarily reducing signal statistics.
2. The dijet invariant mass may only vary within a 50 GeV range of the default value (from 450–550 GeV) due to the cut being physically motivated by the VBS event topology described in Section 5.0.2.

Lastly, the signal significance is calculated without taking into account the uncertainty of the background using Equation 6.4. This is due to the fact that the statistical uncertainties of the fake electron and charge misidentification backgrounds are quite large, owing to poor MC statistics in a few of the samples. If Equation 6.2 were used instead, the optimization would cut unreasonably hard against these backgrounds. Since Monte Carlo statistics is not expected to be a limiting factor when this analysis is performed at the HL-LHC, it is more realistic to simply ignore these large statistical uncertainties for the purpose of the optimization.

6.5.3 Results of the optimization

Ultimately, the random grid is constructed from over 38,000 LL-polarized $W^\pm W^\pm jj$ events in the six variables listed above. After applying the constraints, the optimal cut point reduces the total background from 9900 to 2310 while reducing the signal from 3489 to 2958. This corresponds to an increase in signal significance from $Z = 33.26$ to $Z = 52.63$ as calculated by Equation 6.4. The updates to the event selection are listed in Table 6.4.

The large reduction in the background is primarily a result of increasing the leading and sub-leading jet p_T from 30 GeV to 90 GeV and 45 GeV, respectively. As can be seen in Figure 6.4, this increase removes a significant portion of the backgrounds from jets faking electrons and charge mis-ID. Additionally, the loosening of the lepton-jet centrality cut ζ allows more signal events to survive the event selection (see Figure 6.5). Other changes to the event selection are minor and do not individually have a large impact on the signal or background yields; similar distributions for these variables are shown in Appendix B.2.

The full event yields after optimization as well as the cross section measurement are detailed alongside those using the default selection in Section 6.6.

Selection requirement	Selection value
Lepton kinematics	$p_T > 28$ GeV (leading lepton only)
Jet kinematics	$p_T > 90$ GeV (leading jet) $p_T > 45$ GeV (subleading jet)
Dilepton mass	$m_{ll} > 28$ GeV
Dijet mass	$m_{jj} > 520$ GeV
Lepton-jet centrality	$\zeta > -0.5$

Table 6.4: Updates to the $W^\pm W^\pm jj$ event selection criteria after optimization. Cuts not listed remain unchanged from the default selection in Table 6.3.

6.6 Results

6.6.1 Event yields

After applying the full event selection, the analysis is broken down into four channels based off of the flavor of the signal leptons: $\mu\mu$, ee , μe , and $e\mu$. The full signal and background event yields are shown in Table 6.5 for each channel separately and combined using the default event selection. 3489 EWK $W^\pm W^\pm jj$ events are expected compared to 9900 background events. The dominant sources of background are jets faking electrons followed by charge misidentification and diboson processes. Triboson events, QCD $W^\pm W^\pm jj$, and other non-prompt sources make up approximately 5% of the total background combined.

The event yields for the optimized selection detailed in Section 6.5.3 are listed in Table 6.6. After optimization, 2958 signal events and just 2310 background events are expected. Diboson events are now the primary source of background, as the optimization greatly reduces the fake and charge mis-ID contributions. As discussed earlier, the increase in the leading and subleading jet p_T cuts as well as the loosening of the centrality cut are most responsible for the changes in the signal

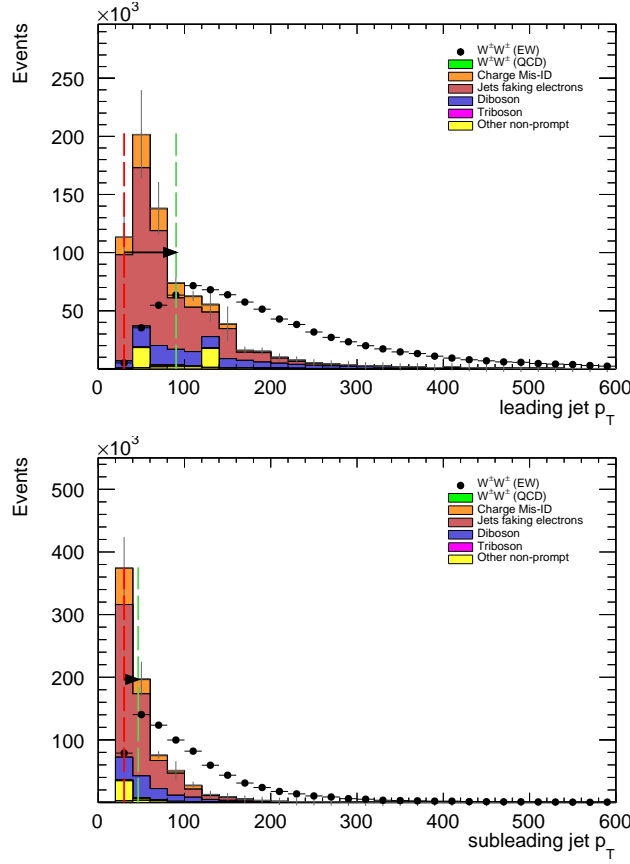


Figure 6.4: Leading (top) and subleading (bottom) jet p_T distributions. The default and optimized cuts are represented by the red and green dashed lines, respectively. The $W^\pm W^\pm jj$ EWK signal (black points) is normalized to the same area as the sum of the backgrounds (colored histogram).

	All channels	$\mu\mu$	ee	μe	$e\mu$
$W^\pm W^\pm jj$ (QCD)	206.4	91.1	22.8	38.4	54.1
Charge Misidentification	2300	0.0	2100	90	160
Jets faking electrons	5000	0.0	3400	1200	340
$WZ + ZZ$	2040	500	438	423	680
Tribosons	115	47	15.4	21.6	31.2
Other non-prompt	210	110	20	60	27
Total Background	9900	750	6000	1900	1290
Signal $W^\pm W^\pm jj$ (EWK)	3489	1435	432	679	944

Table 6.5: Signal and background event yields using the default event selection for an integrated luminosity of $\mathcal{L} = 3000 \text{ fb}^{-1}$. Events containing a fake or charge-flipped electron are removed from their respective sources and combined into a single entry each.

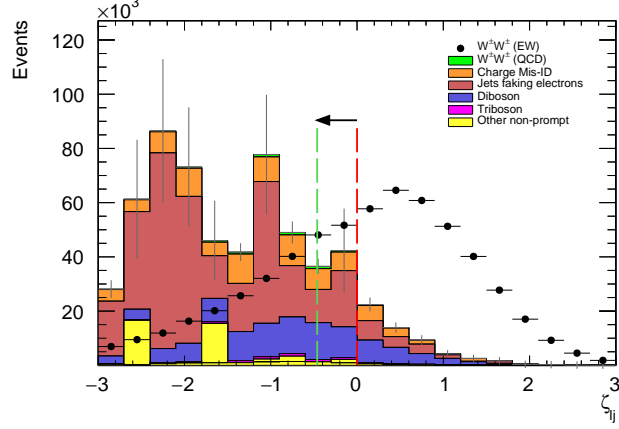


Figure 6.5: Lepton-jet centrality distribution. The default and optimized cuts are represented by the red and green dashed lines, respectively. The $W^\pm W^\pm jj$ EWK signal (black points) is normalized to the same area as the sum of the backgrounds (colored histogram).

and background yields; distributions of these quantities using the default and the optimized event selections can be found in Figures 6.6, 6.7, and 6.8, respectively.

	All channels	$\mu\mu$	ee	μe	$e\mu$
$W^\pm W^\pm jj$ (QCD)	168.7	74.6	19.7	32.2	42.2
Charge Misidentification	200	0.0	11	30	160
Jets faking electrons	460	0.0	130	260	70
$WZ + ZZ$	1286	322	289	271	404
Tribosons	76	30.1	9.6	15.1	21.6
Other non-prompt	120	29	16.6	50	19
Total Background	2310	455	480	660	710
Signal $W^\pm W^\pm jj$ (EWK)	2958	1228	380	589	761

Table 6.6: Signal and background event yields using the optimized event selection for an integrated luminosity of $\mathcal{L} = 3000 \text{ fb}^{-1}$. Events containing a fake or charge-flipped electron are removed from their respective sources and combined into a single entry each.

It is important to note, however, that the MC sample used to estimate $Z+\text{jets}$ events suffers from poor statistics which results in large per-event weights once scaled to $\mathcal{L} = 3000 \text{ fb}^{-1}$. This sample contributes heavily to the fake and charge misidentification backgrounds, and a handful of these events being cut out by the optimization is largely responsible for the dramatic reduction of the corresponding backgrounds. As a result, the optimized results presented here are likely overly optimistic. However, given proper MC statistics, it is still expected that this optimization will outperform the default selection.

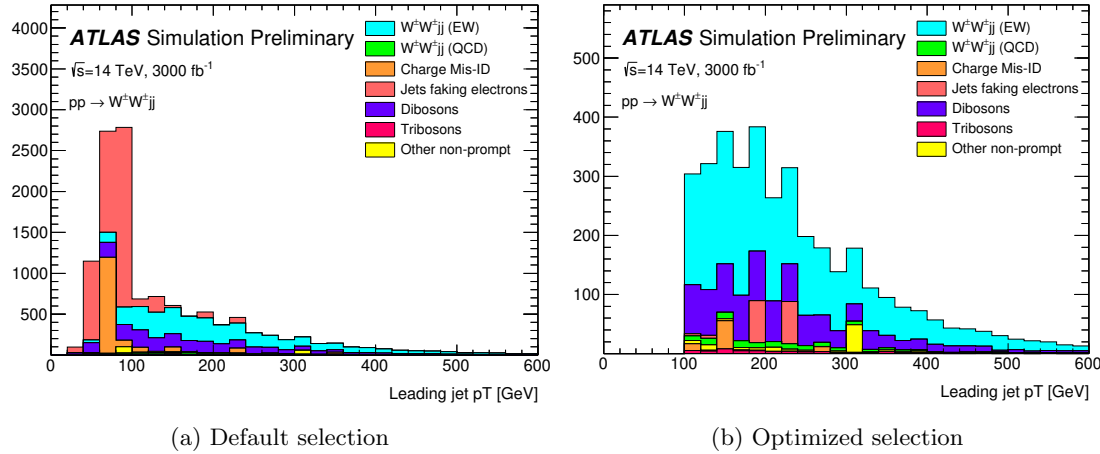


Figure 6.6: p_T distributions for the leading jet using the default (left) and optimized (right) event selections for all channels combined.

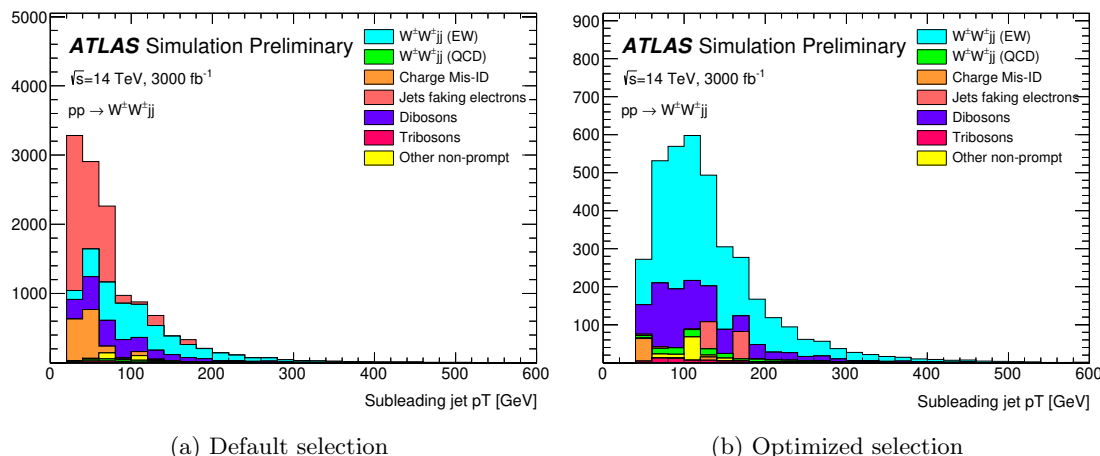


Figure 6.7: p_T distributions for the subleading jet using the default (left) and optimized (right) event selections for all channels combined.

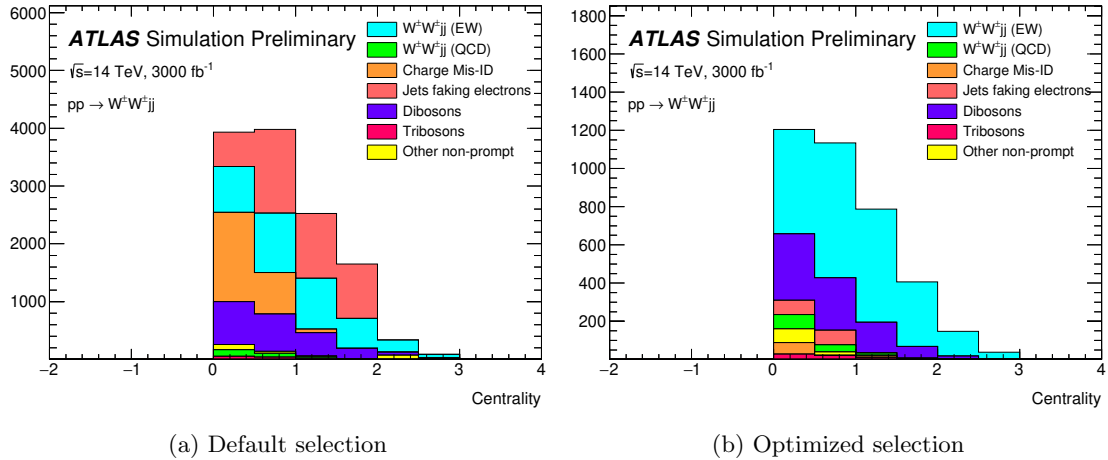


Figure 6.8: p_T distributions for lepton-jet centrality ζ using the default (left) and optimized (right) event selections for all channels combined.

6.6.2 Uncertainties

The uncertainties considered for the analysis are summarized in Table 6.7. Values for experimental systematics on the trigger efficiency, lepton and jet reconstruction, and flavor tagging are taken directly from the 13 TeV analysis [84]. The rate uncertainties for the background processes are halved from the 13 TeV values according to ATLAS recommendations. The uncertainty on the fake electron estimation is also halved from the 13 TeV analysis. Finally, a conservative estimate of the uncertainty on the charge flip background is used as the electron charge mis-ID rate due to material interactions is difficult to predict at this stage.

Source	Uncertainty (%)
$W^\pm W^\pm jj$ (EWK)	3
Luminosity	1
Trigger efficiency	0.5
Lepton reconstruction and identification	1.8
Jets	2.3
Flavor tagging	1.8
Jets faking electrons	20
Charge misidentification	25
$W^\pm W^\pm jj$ (QCD)	20
Top	15
Diboson	10
Triboson	15

Table 6.7: Summary of estimated experimental and rate uncertainties.

6.6.3 Cross section measurement

The cross section is calculated using the same method as in the 13 TeV analysis, detailed in Section 5.4. Unlike the previous analysis, however, eight lepton channels are used here instead of six. The μe and $e\mu$ channels remain separated in addition to the $\mu\mu$ and ee channels, and each lepton flavor channel is further split by charge, as this increases the sensitivity of the analysis. Each channel's m_{jj} distribution is combined in a profile likelihood fit to extract the EWK $W^\pm W^\pm jj$ production cross section. Using the default event selection, the expected cross section calculated to be

$$\sigma_{W^\pm W^\pm jj}^{\text{expected}} = 16.89 \pm 0.36 \text{ (stat)} \pm 0.53 \text{ (theory)} \pm 0.84 \text{ (syst)} \text{ fb}. \quad (6.5)$$

With the optimized event selection, the expected cross section is

$$\sigma_{W^\pm W^\pm jj}^{\text{expected}} = 16.94 \pm 0.36 \text{ (stat)} \pm 0.53 \text{ (theory)} \pm 0.78 \text{ (syst)} \text{ fb}. \quad (6.6)$$

The optimized selection should not change the measured value of the cross section, and indeed both are consistent within uncertainties. The systematic uncertainty is reduced by about 7% with the optimized selection. The total uncertainty on the cross section measurement is approximately 6%, compared to the 20% uncertainty on the measured fiducial cross section of the 13 TeV analysis reported in Equation 5.30.

Projections of each uncertainty type and the total uncertainty on the cross section as a function of integrated luminosity are shown in Figure 6.9. The predictions are made by scaling the event yields by different luminosity values and re-running the fitting procedure. As the integrated luminosity increases past $\mathcal{L} > 3000 \text{ fb}^{-1}$, the statistical uncertainty continues to reduce; however, the total uncertainty will be limited by the systematics. The end result is that after collecting the planned 3000 fb^{-1} , the precision the $W^\pm W^\pm jj$ cross section measurement is expected to be more than a factor of three better than in the 13 TeV analysis, with diminishing returns with additional data.

6.6.4 Longitudinal scattering significance

The longitudinal scattering significance is extracted in much the same way as the cross section, this time using a binned likelihood fit on the $|\Delta\phi_{jj}|$ distribution. In order to increase sensitivity, the $|\Delta\phi_{jj}|$ distribution is split into two bins in m_{jj} , and an additional cut on the pseudorapidity of the subleading lepton is applied ($|\eta| < 2.5$) to reduce background contributions from fake electrons and charge flip. The $|\Delta\phi_{jj}|$ distributions used in the fit are shown in Figure 6.10. Due to limited statistics in the LL events, the four lepton flavor channels are not split by charge. The expected significance

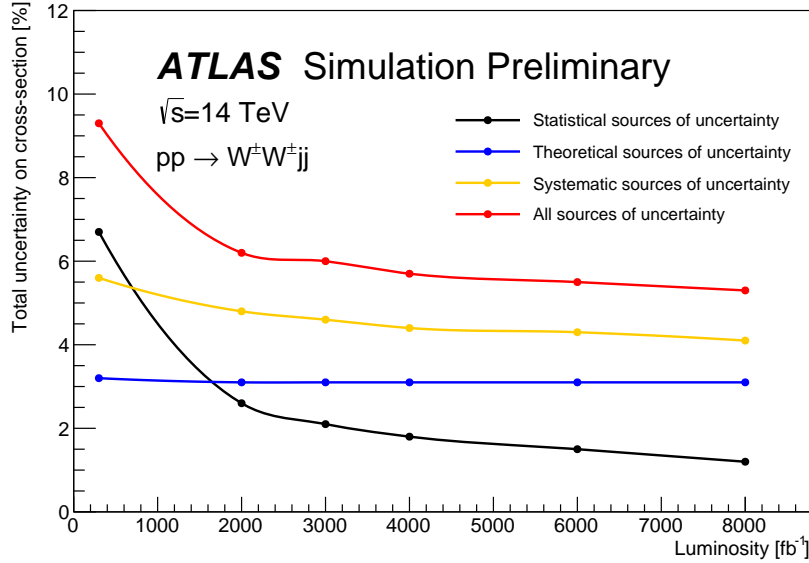


Figure 6.9: Projections of the statistical (black), theoretical (blue), systematic (yellow), and total (red) uncertainties on the measured cross section as a function of integrated luminosity using the optimized event selection.

of the $W_L^\pm W_L^\pm jj$ process is 1.8σ with a precision of 47% on the measurement. Projections of the expected significance as a function of integrated luminosity is shown in Figure 6.11, and once again, the improvement in the precision with additional data becomes small after the initial 3000 fb^{-1} .

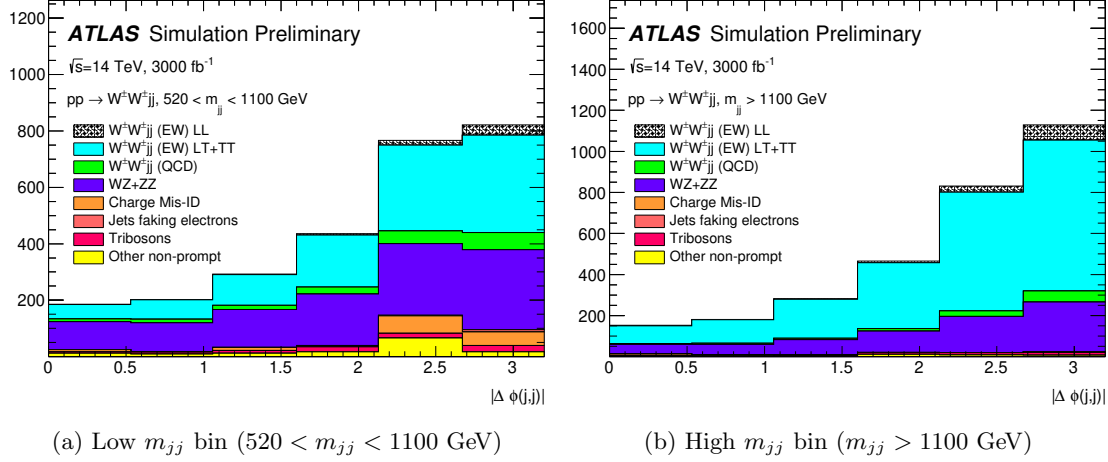


Figure 6.10: Dijet azimuthal separation ($|\Delta\phi_{jj}|$) for the low m_{jj} region ($520 < m_{jj} < 1100$ GeV, top) and the high m_{jj} region ($m_{jj} > 1100$ GeV, bottom). The purely longitudinal (LL, gray) is plotted separately from the mixed and transverse (LT+TT, cyan) polarizations.

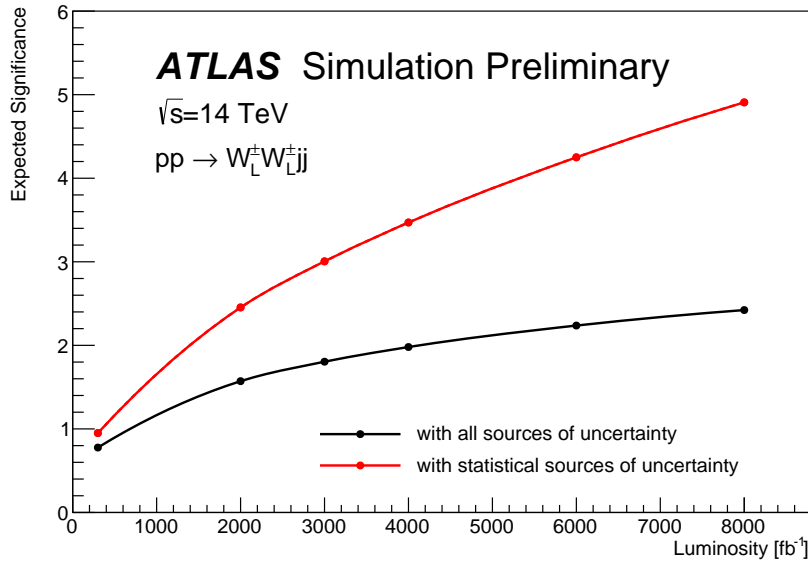


Figure 6.11: Projections of the expected longitudinal scattering significance as a function of integrated luminosity when considering all sources of uncertainties (black) or only statistical uncertainties (red).

CHAPTER 7

Conclusion

This thesis presented a measurement of the fiducial cross section of EWK production of same-sign W boson pairs at $\sqrt{s} = 13$ TeV with the ATLAS experiment as well as prospects for the measurement at the planned High-Luminosity LHC. The $W^\pm W^\pm jj$ EWK process is observed in 36.1 fb^{-1} of proton-proton collision data recorded by ATLAS at 13 TeV with a signal significance of 6.9σ . The fiducial cross section is measured to be $\sigma_{\text{meas}}^{\text{fid}} = 2.91^{+0.51}_{-0.47}(\text{stat})^{+0.12}_{-0.16}(\text{theory})^{+0.24}_{-0.23}(\text{sys})^{+0.08}_{-0.06}(\text{lumi}) \text{ fb}$. The future prospects of the measurement at the HL-LHC at 14 TeV and a planned 3000 fb^{-1} of data is predicted to have a precision of 6%. In addition, the significance of a potential measurement of the purely longitudinally polarized component of $W^\pm W^\pm$ scattering is predicted to be 1.8σ .

In addition, the track-based alignment of the ATLAS Inner Detector is described in detail as well as its applications during Run 2. The alignment campaign using the first $\sqrt{s} = 13$ TeV pp collision data in early 2015 was described in detail, and it provided the baseline alignment used for the remainder of the year. The monitoring of momentum biases using electron $\langle E/p \rangle$ was also presented, including results on sagitta biases in the Inner Detector after the reprocessing of the 2016 data.

APPENDIX A

Additional material on $W^\pm W^\pm jj$ measurement at $\sqrt{s} = 13$ TeV

A.1 Impact of experimental uncertainty on MC background estimations

Tables A.1-A.6 contain the impact of experimental systematic uncertainties for the remaining backgrounds estimated from MC simulation. The $W^\pm W^\pm jj$ EWK signal and WZ background systematics are listed in the main body of the document, in Tables 5.21 and 5.22, respectively. While the percentage of the contributions for some systematics appear large, the size of these backgrounds are quite small compared to the total background.

$W^\pm W^\pm jj$ QCD	ee % Yield	$e\mu$ % Yield	$\mu\mu$ % Yield
Jet-related Uncertainties	3.41	3.04	2.85
b-tagging efficiency	2.56	2.48	2.48
Pile-up	4.99	0.45	0.33
Trigger efficiency	0.02	0.08	0.41
Lepton reconstruction/ID	1.62	1.19	1.89
MET reconstruction	0.41	0.22	0.34

Table A.1: Impact of experimental uncertainties for the $W^\pm W^\pm jj$ QCD processes in all channels.

Triboson	ee % Yield	$e\mu$ % Yield	$\mu\mu$ % Yield
Jet-related Uncertainties	13.09	13.39	16.85
b-tagging efficiency	2.96	3.77	4.95
Pile-up	19.37	24.66	6.87
Trigger efficiency	0.02	0.07	0.47
Lepton reconstruction/ID	1.66	1.27	2.48
MET reconstruction	0.00	0.46	0.00

Table A.2: Impact of experimental uncertainties for triboson process in all channels.

$t\bar{t}V$	ee % Yield	$e\mu$ % Yield	$\mu\mu$ % Yield
Jet-related Uncertainties	17.65	11.97	14.27
b-tagging efficiency	15.02	9.04	13.83
Pile-up	8.73	10.69	4.18
Trigger efficiency	0.03	0.08	0.39
Lepton reconstruction/ID	2.57	3.27	2.66
MET reconstruction	1.75	4.16	1.62

Table A.3: Impact of experimental uncertainties for $t\bar{t}V$ processes in all channels.

$W\gamma$	ee % Yield	$e\mu$ % Yield	$\mu\mu$ % Yield
Jet-related Uncertainties	7.05	33.36	—
b-tagging efficiency	1.97	2.94	—
Pile-up	4.11	14.17	—
Trigger efficiency	0.01	0.14	—
Lepton reconstruction/ID	1.40	1.13	—
MET reconstruction	0.00	0.00	—

Table A.4: Impact of experimental uncertainties for the $W\gamma$ process in all channels.

$Z\gamma$	ee % Yield	$e\mu$ % Yield	$\mu\mu$ % Yield
Jet-related Uncertainties	16.22	370.44	—
b-tagging efficiency	1.08	3.10	—
Pile-up	12.57	11.51	—
Trigger efficiency	0.02	0.07	—
Lepton reconstruction/ID	1.26	22.01	—
MET reconstruction	0.00	0.00	—

Table A.5: Impact of experimental uncertainties for the $Z\gamma$ process in all channels.

ZZ	ee % Yield	$e\mu$ % Yield	$\mu\mu$ % Yield
Jet-related Uncertainties	15.71	15.76	35.18
b-tagging efficiency	2.23	2.35	2.89
Pile-up	1.22	3.20	4.58
Trigger efficiency	0.03	0.10	0.36
Lepton reconstruction/ID	3.59	3.10	5.70
MET reconstruction	4.84	3.26	3.24

Table A.6: Impact of experimental uncertainties for the ZZ process in all channels.

A.2 Pre-fit event yields

Table A.7 contains the event yields for each source and channel before the fit.

	e^+e^+	e^-e^-	μ^+e^+	μ^-e^-	$\mu^+\mu^+$	$\mu^-\mu^-$	combined
WZ	1.9 ± 0.6	1.3 ± 0.4	14 ± 4	8.9 ± 2.6	5.5 ± 1.6	3.6 ± 1.1	35 ± 10
Non-prompt	4.1 ± 2.3	2.3 ± 1.7	9 ± 5	6 ± 4	0.57 ± 0.15	0.67 ± 0.25	23 ± 10
e/γ conversions	1.74 ± 0.29	1.8 ± 0.4	6.1 ± 1.6	3.7 ± 0.8	—	—	13.4 ± 2.5
Other prompt	0.17 ± 0.05	0.14 ± 0.04	0.90 ± 0.19	0.60 ± 0.14	0.36 ± 0.10	0.19 ± 0.05	2.4 ± 0.5
$W^\pm W^\pm jj$ QCD	0.38 ± 0.13	0.16 ± 0.05	3.0 ± 1.0	1.2 ± 0.4	1.8 ± 0.6	0.76 ± 0.25	7.3 ± 2.5
Expected background	8.2 ± 2.4	5.7 ± 1.8	33 ± 7	21 ± 5	8.2 ± 1.8	5.3 ± 1.2	81 ± 14
$W^\pm W^\pm jj$ EWK	3.8 ± 0.6	1.49 ± 0.22	16.5 ± 2.5	6.5 ± 1.0	9.1 ± 1.4	3.5 ± 0.5	41 ± 6
Data	10	4	44	28	25	11	122

Table A.7: Table of the data and prediction event yields in the signal region before the fit. Numbers are shown for the six lepton flavor and charge channels and for all channels combined. Here the WZ background yields are normalized to the data in the WZ control region. The background estimations from the fake-factor are included in the “Non-prompt” category, and backgrounds from $V\gamma$ production and electron charge misidentification are combined in the “ e/γ conversions” category. Finally, ZZ , VVV , and $t\bar{t} + V$ backgrounds are combined in the “Other prompt” category.

APPENDIX B

Additional material on $W^\pm W^\pm jj$ prospects at the HL-LHC

B.1 Truth isolation

As mentioned in Section 6.3.1, the size of the background contribution from top processes are much larger than expected when no isolation is applied. The event yields using an earlier version of the event selection with no truth-based isolation requirement are listed in Table B.1. Here, top events make up nearly 90% of the total background, and the contributions from fake and charge-flipped electrons are also large. The event yields using the same event selection with the truth-based isolation included are shown in Figure B.2. When comparing the two tables, the considerable reduction in the top background can be clearly seen.

yields by type	all channels	$\mu\mu$	ee	μe	$e\mu$
signal	4011	1583.2	531.7	793.1	1103.1
ww qcd	252.6	105.8	30.4	48	68.4
charge flip	2528.4	0.0	2075.4	255.1	197.8
fakes	7135.4	0.0	4675.1	1904.3	555.9
diboson	2370.4	581.2	491.8	517.9	779.6
triboson	125.5	49.1	17.8	24.6	34.1
top	90150.5	26618	15301.6	25277.9	22953.1
z+jets	241.2	0.0	0.0	0.0	241.2
w+jets	31.4	3.9	7.6	13.2	6.7
total bkg	102803.9	27354	22592	28027.8	24830.1
signal	4011	1583.2	531.7	793.1	1103.1

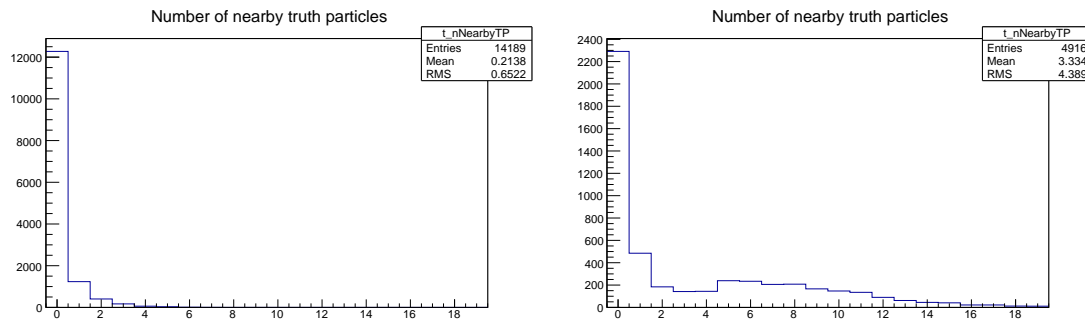
Table B.1: Event yields prior to applying any form of truth-based isolation criteria.

yields by type	all channels	$\mu\mu$	ee	μe	$e\mu$
signal	3470.5	1427.3	428.8	675.8	938.7
ww qcd	205.8	90.8	22.7	38.3	54
charge flip	2398.3	0.0	2104.6	95.8	197.9
fakes	4309.7	0.0	3390.6	750.8	168.3
diboson	1552.4	311.3	355.6	346.8	538.7
triboson	115	46.8	15.4	21.6	31.2
top	156.9	42.3	14.8	76.6	23.3
$z+jets$	0.0	0.0	0.0	0.0	0.0
$w+jets$	0.3	0.0	0.0	0.3	0.0
total bkg	8738.1	491.3	5903.7	1329.8	1013.4
signal	3470.5	1427.3	428.8	675.8	938.7

Table B.2: Event yields after applying a test version of the truth-based isolation.

B.1.1 TRUTH1++ derivations

The ATLAS standard TRUTH1 derivations used for this analysis contain a slimmed truth particle container in order to reduce the file size. As a result, many of the truth particles that would be included in the isolation variables are missing, and the truth-based isolation will not accurately model the reconstruction-level isolation variables. In order to recover the performance of the truth-based isolation in the top MC samples (where it is most needed), a custom derivation was produced privately that duplicated the default TRUTH1 data structure but includes the full truth particle record. The reduced size of the truth particle information in the TRUTH1 derivation compared to the TRUTH1++ derivation is shown in Figure B.1.



B.1.2 Check of truth-based isolation

Since the isolation variables are constructed from truth particles, there is an expectation that the efficiency of the isolation selection will be higher than what would be seen in the full simulation. In order to test this, a truth-level 13 TeV $t\bar{t}$ MC sample was run through a selection altered to mimic the 13 TeV $W^\pm W^\pm jj$ measurement as closely as possible. The results were compared to the $t\bar{t}$ background in the 13 TeV analysis extrapolated to 14 TeV and 3000 fb^{-1} , and the truth-based isolation reduces the expected events by a factor of approximately 4. However, the statistics in the 13 TeV truth-level sample are low, and it is therefore difficult to measure precisely how much the truth-based isolation overperforms.

B.1.3 Loose isolation working point

As another check on the truth-based isolation, a second isolation working point was constructed to match the official ATLAS Fixed Cut Loose isolation working point. The definition of this loose isolation are found in Table B.3.

The primary impact of loosening the isolation is a substantial increase in the non-prompt background from top processes, and a moderate increase in the charge mis-ID and fake backgrounds. Backgrounds from prompt leptons only did not see major changes. As a result, the tight working point is chosen for the analysis. The event yields by sample and by background type using the loose working point are in Table B.4, and Table B.5 has the numbers using the tight working point (defined in Table 6.2) for comparison.

	Electron Isolation	Muon Isolation
Track-based isolation cone size	$\Delta R < 0.2$	$\Delta R < 0.3$
Track-based isolation requirement	$\sum p_T/p_T^e < 0.15$	$\sum p_T/p_T^\mu < 0.15$
Calorimeter-based isolation cone size	$\Delta R < 0.2$	$\Delta R < 0.2$
Calorimeter-based isolation requirement	$\sum E_T/p_T^e < 0.2$	$\sum E_T/p_T^\mu < 0.3$

Table B.3: Electron and muon isolation requirements for the loose working point.

run number	all channels			mm			ee			me			em		
	events	stat	sys	events	stat	sys	events	stat	sys	events	stat	sys	events	stat	sys
signal	3783.21	22.08	0.00	1524.99	15.00	0.00	484.74	7.01	0.00	740.76	9.01	0.00	1032.72	11.50	0.00
ww qcd	223.95	3.54	44.79	97.17	2.51	19.43	25.51	1.03	5.10	42.23	1.40	8.45	59.04	1.80	11.81
charge flip	3025.40	1276.74	0.00	0.00	0.00	0.00	2615.30	1267.89	0.00	197.20	87.94	0.00	212.90	121.63	0.00
fakes	5315.55	1775.87	0.00	0.00	0.00	0.00	3524.24	1694.39	0.00	1356.74	450.60	0.00	434.57	282.33	0.00
diboson	2195.61	38.10	219.58	548.72	18.54	54.87	451.27	18.29	45.14	470.61	15.71	47.07	725.01	22.95	72.50
triboson	117.43	5.90	17.62	47.55	4.32	7.13	15.83	1.94	2.37	22.11	2.18	3.32	31.94	2.76	4.80
top	554.63	218.75	83.21	229.26	135.53	34.40	61.15	38.23	9.18	232.30	167.28	34.85	31.92	6.43	4.78
z+jets	0.00	0.00	0.00	0.00	0.00	0.00	0.00	0.00	0.00	0.00	0.00	0.00	0.00	0.00	0.00
w+jets	1.21	0.87	0.00	0.00	0.00	0.00	0.00	0.00	0.00	0.00	0.00	0.00	0.02	0.00	0.00
total bkg	11433.78	2198.44	239.70	922.70	136.88	67.99	6693.30	2116.67	46.41	2322.38	488.89	59.27	1495.40	308.36	73.77
signal	3783.21	22.08	0.00	1524.99	15.00	0.00	484.74	7.01	0.00	740.76	9.01	0.00	1032.72	11.50	0.00

Table B.4: Event yields broken down by sample and by background type using the loose isolation working point. Events containing a fake or charge-flipped electron are removed from their respective sample and added to the ‘fakes’ and ‘charge flip’ rows, respectively. Errors include statistical uncertainty and estimated systematic rate uncertainty based on the background process.

run number	all channels			mm			ee			me			em		
	events	stat	sys	events	stat	sys	events	stat	sys	events	stat	sys	events	stat	sys
signal	3489.49	21.23	0.00	1434.85	14.55	0.00	431.75	6.61	0.00	679.09	8.63	0.00	943.8	11.00	0.00
ww qcd	206.42	3.41	41.28	91.12	2.43	18.22	22.84	0.98	4.57	38.37	1.34	7.67	54.09	1.72	10.82
charge flip	2335.73	1163.47	0.00	0.00	0.00	0.00	2087.78	1159.5	0.00	90.37	33.32	0.00	157.58	90.02	0.00
fakes	4979.27	1756.47	0.00	0.00	0.00	0.00	3406.20	1705.03	0.00	1230.80	362.15	0.00	342.27	216.54	0.00
diboson	2039.94	36.93	204.00	499.69	18.04	49.97	437.60	14.12	43.76	422.90	14.18	42.29	679.75	25.25	67.98
triboson	115.03	5.87	17.29	46.84	4.31	7.03	15.40	1.94	2.32	21.55	2.17	3.24	31.24	2.74	4.70
top	211.74	84.14	31.76	107.96	71.12	16.20	19.58	3.76	2.93	57.21	44.47	8.58	26.99	5.40	4.05
z+jets	0.00	0.00	0.00	0.00	0.00	0.00	0.00	0.00	0.00	0.00	0.00	0.00	0.00	0.00	0.00
w+jets	0.30	0.28	0.00	0.00	0.00	0.00	0.00	0.00	0.00	0.28	0.28	0.00	0.02	0.02	0.00
total bkg	9888.43	2108.87	211.25	745.61	73.54	56.04	5898.40	2061.99	44.16	1861.48	366.67	43.95	1291.94	235.95	69.11
signal	3489.49	21.23	0.00	1434.85	14.55	0.00	431.75	6.61	0.00	679.09	8.63	0.00	943.80	11.00	0.00

Table B.5: Event yields broken down by background type using the tight isolation working point. Events containing a fake or charge-flipped electron are removed from their respective sample and added to the “fakes” and “charge flip” rows, respectively. Errors include statistical uncertainty and estimated systematic rate uncertainty based on the background process.

B.2 Plots of other optimization variables

Plots of the remaining optimization variables not shown in Section 6.5.3 are presented here for reference. Figures B.2, B.3, and B.4 compare signal and background distributions for the default and optimized cuts. None of these cuts change by much in the optimized selection and their impacts on the overall event selection is minimal.

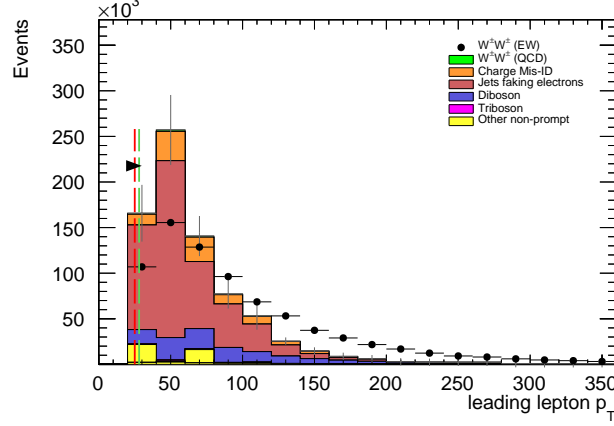


Figure B.2: Leading lepton p_T distribution. The default and optimized cuts are represented by the red and green dashed lines, respectively. The $W^\pm W^\pm jj$ EWK signal (black points) is normalized to the same area as the sum of the backgrounds (colored histogram).

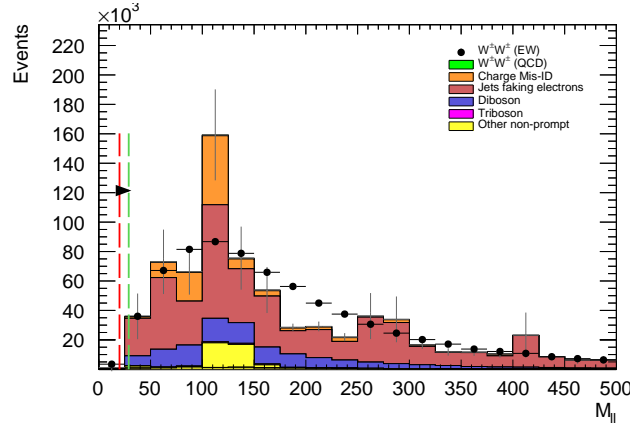


Figure B.3: Dilepton invariant mass distribution. The default and optimized cuts are represented by the red and green dashed lines, respectively. The $W^\pm W^\pm jj$ EWK signal (black points) is normalized to the same area as the sum of the backgrounds (colored histogram).

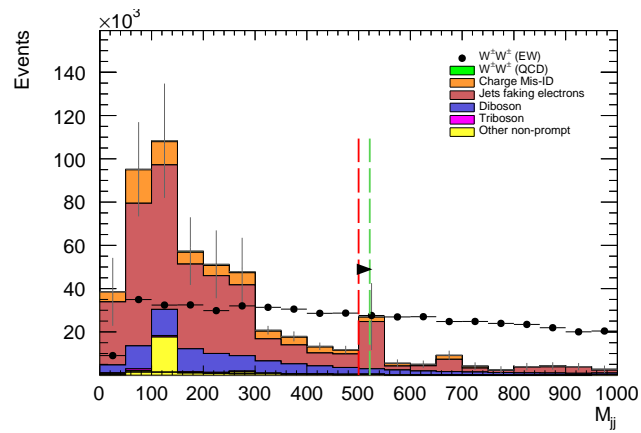


Figure B.4: Dijet invariant mass distribution. The default and optimized cuts are represented by the red and green dashed lines, respectively. The $W^\pm W^\pm jj$ EW signal (black points) is normalized to the same area as the sum of the backgrounds (colored histogram).

Bibliography

- [1] ATLAS Collaboration, M. Aaboud et al., *Measurement of the $W^\pm Z$ boson pair-production cross section in pp collisions at $\sqrt{s} = 13$ TeV with the ATLAS Detector*, Phys. Lett. **B762** (2016) 1–22, arXiv:1606.04017 [hep-ex]. Cited on page xxi.
- [2] ATLAS Collaboration, *Observation of electroweak production of a same-sign W boson pair in association with two jets in pp collisions at $\sqrt{s} = 13$ TeV with the ATLAS detector*, Tech. Rep. ATLAS-CONF-2018-030, CERN, Geneva, Jul, 2018.
<https://cds.cern.ch/record/2629411>. Cited on pages xxi and 58.
- [3] ATLAS, CMS Collaboration, *Report on the Physics at the HL-LHC and Perspectives for the HE-LHC*, in *HL/HE-LHC Physics Workshop: final jamboree Geneva, CERN, March 1, 2019*. 2019. arXiv:1902.10229 [hep-ex]. Cited on page xxi.
- [4] ATLAS Collaboration, *Summary plots from the ATLAS Standard Model physics group*, February, 2019.
<https://atlas.web.cern.ch/Atlas/GROUPS/PHYSICS/CombinedSummaryPlots/SM/>. Cited on page 4.
- [5] S. Weinberg, *The Quantum Theory of Fields, Volume 1: Foundations*. Cambridge University Press, 1995. Cited on page 3.
- [6] M. E. Peskin and D. V. Schroeder, *An Introduction to Quantum Field Theory*. Addison-Wesley, 1995. Cited on page 3.
- [7] R. P. Feynman, *Mathematical formulation of the quantum theory of electromagnetic interaction*, Phys. Rev. **80** (1950) 440–457. Cited on page 3.
- [8] M. Y. Han and Y. Nambu, *Three-triplet model with double SU(3) symmetry*, Phys. Rev. **139** (1965) B1006–B1010. Cited on page 4.
- [9] D. J. Gross and F. Wilczek, *Asymptotically Free Gauge Theories - I*, Phys. Rev. **D8** (1973) 3633–3652. Cited on page 5.
- [10] D. J. Gross and F. Wilczek, *ASYMPTOTICALLY FREE GAUGE THEORIES. 2.*, Phys. Rev. **D9** (1974) 980–993. Cited on page 5.

- [11] H. D. Politzer, *Reliable Perturbative Results for Strong Interactions?*, Phys. Rev. Lett. **30** (1973) 1346–1349. [,274(1973)]. Cited on page 5.
- [12] A. Salam and J. C. Ward, *Weak and Electromagnetic Interactions*, Nuovo Cimento **11** (1959) 568–577. Cited on page 5.
- [13] S. L. Glashow, *The Renormalizability of Vector Meson Interactions*, Nucl. Phys. **10** (1959) 107–117. Cited on page 5.
- [14] ALEPH, DELPHI, L3, OPAL, SLD, LEP Electroweak Working Group, SLD Electroweak Group, SLD Heavy Flavour Group Collaboration, S. Schael et al., *Precision electroweak measurements on the Z resonance*, Phys. Rept. **427** (2006) 257–454, arXiv:hep-ex/0509008 [hep-ex]. Cited on page 5.
- [15] F. Englert and R. Brout, *Broken symmetry and the mass of gauge vector mesons*, Phys. Rev. Lett. **13** (1964) 321–323. Cited on page 5.
- [16] P. W. Higgs, *Broken symmetries, massless particles and gauge fields*, Physics Letters **12** (1964) 132–133. Cited on page 5.
- [17] P. W. Higgs, *Broken symmetries and the masses of gauge bosons*, Phys. Rev. Lett. **13** (1964) 508–509. Cited on page 5.
- [18] ATLAS Collaboration, *Observation of a new particle in the search for the Standard Model Higgs boson with the ATLAS detector at the LHC*, Phys. Lett. B **716** (2012) 1, arXiv:1207.7214 [hep-ex]. Cited on pages 6 and 59.
- [19] CMS Collaboration, *Observation of a new boson at a mass of 125 GeV with the CMS experiment at the LHC*, Phys. Lett. B **716** (2012) 30, arXiv:1207.7235 [hep-ex]. Cited on pages 6 and 59.
- [20] UA1 Collaboration, G. Arnison et al., *Experimental Observation of Isolated Large Transverse Energy Electrons with Associated Missing Energy at $s^{**}(1/2) = 540\text{-GeV}$* , Phys. Lett. **B122** (1983) 103–116. [,611(1983)]. Cited on page 6.
- [21] UA1 Collaboration, G. Arnison et al., *Experimental Observation of Lepton Pairs of Invariant Mass Around $95\text{-GeV}/c^{**2}$ at the CERN SPS Collider*, Phys. Lett. **B126** (1983) 398–410. [,755(1983)]. Cited on page 6.
- [22] Particle Data Group Collaboration, K. A. Olive et al., *Review of Particle Physics*, Chin. Phys. **C38** (2014) 090001. Cited on pages 6 and 8.
- [23] F. Halzen and A. D. Martin, *Quarks and Leptons: An Introductory Course in Modern Particle Physics*. John Wiley & Sons, 1984. Cited on page 7.
- [24] D. R. Green, P. Meade, and M.-A. Pleier, *Multiboson interactions at the LHC*, Rev. Mod. Phys. **89** (2017) no. 3, 035008, arXiv:1610.07572 [hep-ex]. Cited on page 9.
- [25] H.-J. He and W. B. Kilgore, *The Equivalence theorem and its radiative correction - free formulation for all $R(xi)$ gauges*, Phys. Rev. **D55** (1997) 1515–1532, arXiv:hep-ph/9609326 [hep-ph]. Cited on page 10.
- [26] B. W. Lee, C. Quigg, and H. B. Thacker, *The Strength of Weak Interactions at Very High-Energies and the Higgs Boson Mass*, Phys. Rev. Lett. **38** (1977) 883–885. Cited on page 11.

- [27] S. D. Rindani, *Strong gauge boson scattering at the LHC*, in *Physics at the Large Hadron Collider*, A. Datta, B. Mukhopadhyaya, A. Raychaudhuri, A. K. Gupta, C. L. Khetrapal, T. Padmanabhan, and M. Vijayan, eds., pp. 145–155. 2009. arXiv:0910.5068 [hep-ph]. Cited on page 11.
- [28] V. D. Barger, K.-m. Cheung, T. Han, and R. J. N. Phillips, *Strong W^+W^+ scattering signals at pp supercolliders*, Phys. Rev. **D42** (1990) 3052–3077. Cited on page 11.
- [29] G. van den Oord, *Recursion, Monte Carlo and Vector Boson Scattering at Hadron Colliders*. PhD thesis, Nijmegen U., 2012.
http://www.nikhef.nl/pub/services/biblio/theses_pdf/thesis_G_v_d_Oord.pdf. Cited on page 11.
- [30] A. Alboteanu, W. Kilian, and J. Reuter, *Resonances and Unitarity in Weak Boson Scattering at the LHC*, JHEP **11** (2008) 010, arXiv:0806.4145 [hep-ph]. Cited on page 12.
- [31] L. R. Evans and P. Bryant, *LHC Machine*, JINST **3** (2008) S08001.
<https://cds.cern.ch/record/1129806>. This report is an abridged version of the LHC Design Report (CERN-2004-003). Cited on page 13.
- [32] ATLAS Collaboration, *The ATLAS Experiment at the CERN Large Hadron Collider*, JINST **3** (2008) S08003. Cited on pages 13 and 17.
- [33] ALICE Collaboration, K. Aamodt et al., *The ALICE experiment at the CERN LHC*, JINST **3** (2008) S08002. Cited on page 13.
- [34] CMS Collaboration, S. Chatrchyan et al., *The CMS Experiment at the CERN LHC*, JINST **3** (2008) S08004. Cited on page 13.
- [35] LHCb Collaboration, A. A. Alves, Jr. et al., *The LHCb Detector at the LHC*, JINST **3** (2008) S08005. Cited on page 13.
- [36] CERN, *The accelerator complex*, February, 2019.
<https://home.cern/science/accelerators/accelerator-complex>. Cited on page 13.
- [37] E. Mobs, *The CERN accelerator complex. Complexe des accrateurs du CERN*, .
<https://cds.cern.ch/record/2197559>. General Photo. Cited on page 14.
- [38] W. Herr and B. Muratori, *Concept of luminosity*, . <https://cds.cern.ch/record/941318>. Cited on page 14.
- [39] ATLAS Collaboration, *ATLAS Experiment – Public Results: Luminosity Public Results Run 2*, February, 2019.
<https://twiki.cern.ch/twiki/bin/view/AtlasPublic/LuminosityPublicResultsRun2>. Cited on pages 14, 15, and 16.
- [40] ATLAS Collaboration, *ATLAS inner detector: Technical Design Report, 1*. Technical Design Report ATLAS. CERN, Geneva, 1997. <https://cds.cern.ch/record/331063>. Cited on pages 17 and 32.
- [41] ATLAS Collaboration, *ATLAS inner detector: Technical Design Report, 2*. Technical Design Report ATLAS. CERN, Geneva, 1997. <https://cds.cern.ch/record/331064>. Cited on page 17.

- [42] ATLAS Collaboration, *Track Reconstruction Performance of the ATLAS Inner Detector at $\sqrt{s} = 13 \text{ TeV}$* , Tech. Rep. ATL-PHYS-PUB-2015-018, CERN, Geneva, Jul, 2015. <http://cds.cern.ch/record/2037683>. Cited on page 18.
- [43] ATLAS Collaboration, *ATLAS Insertable B-Layer Technical Design Report*, Tech. Rep. CERN-LHCC-2010-013. ATLAS-TDR-19, Sep, 2010. <https://cds.cern.ch/record/1291633>. Cited on page 18.
- [44] ATLAS Collaboration, G. Darbo, *Experience on 3D Silicon Sensors for ATLAS IBL*, JINST **10** (2015) no. 05, C05001, arXiv:1411.6937 [physics.ins-det]. Cited on page 19.
- [45] E. Stanecka, *ATLAS Inner Tracker Performance at the Beginning of the LHC Run 2*, Tech. Rep. ATL-INDET-PROC-2016-002, CERN, Geneva, Apr, 2016. <https://cds.cern.ch/record/2147407>. Cited on page 19.
- [46] ATLAS TRT Collaboration, E. Abat et al., *The ATLAS Transition Radiation Tracker (TRT) proportional drift tube: Design and performance*, JINST **3** (2008) P02013. Cited on page 19.
- [47] ATLAS TRT Collaboration, E. Abat et al., *The ATLAS TRT barrel detector*, JINST **3** (2008) P02014. Cited on page 19.
- [48] E. Abat et al., *The ATLAS TRT end-cap detectors*, JINST **3** (2008) P10003. Cited on page 19.
- [49] ATLAS Collaboration, *ATLAS liquid-argon calorimeter: Technical Design Report*. Technical Design Report ATLAS. CERN, Geneva, 1996. <https://cds.cern.ch/record/331061>. Cited on pages 20 and 22.
- [50] ATLAS Collaboration, *ATLAS tile calorimeter: Technical Design Report*. Technical Design Report ATLAS. CERN, Geneva, 1996. <https://cds.cern.ch/record/331062>. Cited on page 20.
- [51] ATLAS Collaboration, M. Marjanovic, *ATLAS Tile calorimeter calibration and monitoring systems*, Tech. Rep. arXiv:1806.09156, Jun, 2018. <http://cds.cern.ch/record/2629424>. 8 pages, 21 figures, IEEE Real Time 2018 proceedings. Cited on page 20.
- [52] ATLAS Collaboration, *ATLAS muon spectrometer: Technical Design Report*. Technical Design Report ATLAS. CERN, Geneva, 1997. <https://cds.cern.ch/record/331068>. Cited on page 23.
- [53] ATLAS Collaboration, M. Aaboud et al., *Performance of the ATLAS Track Reconstruction Algorithms in Dense Environments in LHC Run 2*, Eur. Phys. J. **C77** (2017) no. 10, 673, arXiv:1704.07983 [hep-ex]. Cited on page 24.
- [54] R. Fruhwirth, *Application of Kalman filtering to track and vertex fitting*, Nucl. Instrum. Meth. **A262** (1987) 444–450. Cited on page 24.
- [55] T. Cornelissen, M. Elsing, I. Gavrilenko, W. Liebig, E. Moyse, and A. Salzburger, *The new ATLAS track reconstruction (NEWT)*, J. Phys.: Conf. Ser. **119** (2008) 032014. <http://cds.cern.ch/record/1176900>. Cited on page 25.
- [56] ATLAS Collaboration, *Electron reconstruction and identification in the ATLAS experiment using the 2015 and 2016 LHC proton-proton collision data at $\sqrt{s} = 13 \text{ TeV}$* , Submitted to: Eur. Phys. J. (2019) , arXiv:1902.04655 [physics.ins-det]. Cited on pages 25, 26, and 28.

- [57] W. Lampl, S. Laplace, D. Lelas, P. Loch, H. Ma, S. Menke, S. Rajagopalan, D. Rousseau, S. Snyder, and G. Unal, *Calorimeter Clustering Algorithms: Description and Performance*, Tech. Rep. ATL-LARG-PUB-2008-002. ATL-COM-LARG-2008-003, CERN, Geneva, Apr, 2008. <https://cds.cern.ch/record/1099735>. Cited on page 25.
- [58] R. Frhwirth, *A Gaussian-mixture approximation of the BetheHeitler model of electron energy loss by bremsstrahlung*, Computer Physics Communications **154** (2003) no. 2, 131 – 142. <http://www.sciencedirect.com/science/article/pii/S0010465503002923>. Cited on page 25.
- [59] ATLAS Collaboration, G. Aad et al., *Electron and photon energy calibration with the ATLAS detector using LHC Run 1 data*, Eur. Phys. J. **C74** (2014) no. 10, 3071, arXiv:1407.5063 [hep-ex]. Cited on page 26.
- [60] ATLAS Collaboration, M. Aaboud et al., *Electron and photon energy calibration with the ATLAS detector using 2015-2016 LHC proton-proton collision data*, Submitted to: JINST (2018) , arXiv:1812.03848 [hep-ex]. Cited on page 26.
- [61] ATLAS Collaboration, *Electron efficiency measurements with the ATLAS detector using the 2015 LHC proton-proton collision data*, Tech. Rep. ATLAS-CONF-2016-024, CERN, Geneva, Jun, 2016. <https://cds.cern.ch/record/2157687>. Cited on page 26.
- [62] ATLAS Collaboration, G. Aad et al., *Topological cell clustering in the ATLAS calorimeters and its performance in LHC Run 1*, Eur. Phys. J. **C77** (2017) 490, arXiv:1603.02934 [hep-ex]. Cited on page 27.
- [63] ATLAS Collaboration, G. Aad et al., *Measurement of the muon reconstruction performance of the ATLAS detector using 2011 and 2012 LHC protonproton collision data*, Eur. Phys. J. **C74** (2014) no. 11, 3130, arXiv:1407.3935 [hep-ex]. Cited on page 28.
- [64] ATLAS Collaboration, G. Aad et al., *Muon reconstruction performance of the ATLAS detector in protonproton collision data at $\sqrt{s} = 13$ TeV*, Eur. Phys. J. **C76** (2016) no. 5, 292, arXiv:1603.05598 [hep-ex]. Cited on pages 28, 31, and 66.
- [65] ATLAS Collaboration, *ATLAS Muon Combined Performance with the full 2016 dataset*, March, 2017. <https://atlas.web.cern.ch/Atlas/GROUPS/PHYSICS/PLOTS/MUON-2017-001/index.html>. Cited on page 30.
- [66] ATLAS Collaboration, *Alignment of the ATLAS Inner Detector Tracking System with 2010 LHC proton-proton collisions at $\sqrt{s} = 7$ TeV*, Tech. Rep. ATLAS-CONF-2011-012, CERN, Geneva, Mar, 2011. <https://cds.cern.ch/record/1334582>. Cited on pages 32, 35, 48, and 51.
- [67] P. F. Åkesson, T. Atkinson, et al., *ATLAS Tracking Event Data Model*, Tech. Rep. ATL-SOFT-PUB-2006-004. ATL-COM-SOFT-2006-005. CERN-ATL-COM-SOFT-2006-005, CERN, Geneva, Jul, 2006. <https://cds.cern.ch/record/973401>. Cited on page 33.
- [68] P. Brückman, A. Hicheur, and S. J. Haywood, *Global chi2 approach to the Alignment of the ATLAS Silicon Tracking Detectors*, Tech. Rep. ATL-INDET-PUB-2005-002. ATL-COM-INDET-2005-004. CERN-ATL-INDET-PUB-2005-002, CERN, Geneva, 2005. <https://cds.cern.ch/record/835270>. Cited on pages 33 and 35.

- [69] R. Härtel and S. Bethke, *Iterative local Chi2 alignment approach for the ATLAS SCT detector*. PhD thesis, Nov, 2005. <http://cds.cern.ch/record/1511044>. Presented 28 Nov 2005. Cited on page 35.
- [70] ATLAS Collaboration, P. Brückman de Renstrom, *Alignment strategy for the Inner Detector of ATLAS*, . <https://cds.cern.ch/record/1047114>. Cited on page 35.
- [71] ATLAS Collaboration, *Alignment of the ATLAS Inner Detector and its Performance in 2012*, Tech. Rep. ATLAS-CONF-2014-047, CERN, Geneva, Jul, 2014. <https://cds.cern.ch/record/1741021>. Cited on pages 36, 41, and 51.
- [72] J. J. Peña, *Alignment of the ATLAS Inner Detector Upgraded for the LHC Run II*, J. Phys. Conf. Ser. **664** (2015) no. 7, 072025. Cited on page 37.
- [73] J. Alison and I. J. Kroll, *The Road to Discovery: Detector Alignment, Electron Identification, Particle Misidentification, WW Physics, and the Discovery of the Higgs Boson*. PhD thesis, University of Pennsylvania, Dec, 2015. <https://cds.cern.ch/record/1536507>. Presented 08 Nov 2012. Cited on page 38.
- [74] ATLAS Collaboration, *ATLAS Inner Detector Alignment Performance with February 2015 Cosmic Rays Data*, Tech. Rep. ATL-PHYS-PUB-2015-009, CERN, Geneva, Apr, 2015. <https://cds.cern.ch/record/2008724>. Cited on pages 39 and 40.
- [75] ATLAS Collaboration, *Alignment of the ATLAS Inner Detector with the initial LHC data at $\sqrt{s} = 13$ TeV*, Tech. Rep. ATL-PHYS-PUB-2015-031, CERN, Geneva, Jul, 2015. <https://cds.cern.ch/record/2038139>. Cited on page 40.
- [76] ATLAS Collaboration, *Study of the mechanical stability of the ATLAS Insertable B-Layer*, Tech. Rep. ATL-INDET-PUB-2015-001, CERN, Geneva, Jun, 2015. <https://cds.cern.ch/record/2022587>. Cited on page 40.
- [77] ATLAS Collaboration, *Common Framework Implementation for the Track-Based Alignment of the ATLAS Detector*, Tech. Rep. ATL-SOFT-PUB-2014-003, CERN, Geneva, Mar, 2014. <https://cds.cern.ch/record/1670354>. Cited on page 41.
- [78] ATLAS Collaboration, *Study of alignment-related systematic effects on the ATLAS Inner Detector track reconstruction*, Tech. Rep. ATLAS-CONF-2012-141, CERN, Geneva, Oct, 2012. <https://cds.cern.ch/record/1483518>. Cited on pages 51, 52, and 55.
- [79] S. Martí-García, S. Camarda, et al., *Studies of radial distortions of the ATLAS Inner Detector*, Tech. Rep. ATL-COM-INDET-2018-010, CERN, Geneva, Mar, 2018. <https://cds.cern.ch/record/2306724>. Cited on page 52.
- [80] ATLAS Collaboration, *Electron and photon energy calibration with the ATLAS detector using data collected in 2015 at $\sqrt{s} = 13$ TeV*, Tech. Rep. ATL-PHYS-PUB-2016-015, CERN, Geneva, Aug, 2016. <https://cds.cern.ch/record/2203514>. Cited on page 53.
- [81] ATLAS Collaboration, *Evidence for Electroweak Production of $W^\pm W^\pm jj$ in pp Collisions at $\sqrt{s} = 8$ TeV with the ATLAS Detector*, Phys. Rev. Lett. **113** (2014) no. 14, 141803, arXiv:1405.6241 [hep-ex]. Cited on pages 58 and 109.
- [82] CMS Collaboration, V. Khachatryan et al., *Study of vector boson scattering and search for new physics in events with two same-sign leptons and two jets*, Phys. Rev. Lett. **114** (2015) no. 5, 051801, arXiv:1410.6315 [hep-ex]. Cited on pages 58, 107, and 109.

- [83] CMS Collaboration, CMS Collaboration, *Observation of electroweak production of same-sign W boson pairs in the two jet and two same-sign lepton final state in proton-proton collisions at $\sqrt{s} = 13$ TeV*, arXiv:1709.05822 [hep-ex]. Cited on pages 58, 107, 109, and 110.
- [84] C. Bittrich, W. K. Di Clemente, et al., *Observation of electroweak production of a same-sign W boson pair in association with two jets in pp collisions at $\sqrt{s} = 13$ TeV with the ATLAS detector*, Tech. Rep. ATL-COM-PHYS-2018-745, CERN, Geneva, Jun, 2018. <https://cds.cern.ch/record/2621617>. Cited on pages 58, 64, and 126.
- [85] C. Bittrich, W. K. Di Clemente, et al., *Support note for measurement of electroweak $W^\pm W^\pm jj$ production at $\sqrt{s} = 13$ TeV*, Tech. Rep. ATL-COM-PHYS-2018-252, CERN, Geneva, Mar, 2018. <https://cds.cern.ch/record/2309552>. Cited on pages 58, 75, 86, 87, and 99.
- [86] J. M. Campbell and R. K. Ellis, *Higgs Constraints from Vector Boson Fusion and Scattering*, JHEP **04** (2015) 030, arXiv:1502.02990 [hep-ph]. Cited on page 59.
- [87] M. Szleper, *The Higgs boson and the physics of WW scattering before and after Higgs discovery*, arXiv:1412.8367 [hep-ph]. Cited on page 59.
- [88] E. Accomando, A. Ballestrero, A. Belhouari, and E. Maina, *Isolating Vector Boson Scattering at the LHC: Gauge cancellations and the Equivalent Vector Boson Approximation vs complete calculations*, Phys. Rev. **D74** (2006) 073010, arXiv:hep-ph/0608019 [hep-ph]. Cited on page 59.
- [89] C. Gumpert, M. Kobel, B. Heinemann, and U. Klein, *Measurement of Electroweak Gauge Boson Scattering in the Channel $pp \rightarrow W^\pm W^\pm jj$ with the ATLAS Detector at the Large Hadron Collider*. PhD thesis, Dec, 2014. <https://cds.cern.ch/record/2003240>. Presented 27 Feb 2015. Cited on page 61.
- [90] P. Anger, B. Axen, et al., *Same Sign $W^\pm W^\pm$ Production and Limits on Anomalous Quartic Gauge Couplings*, Tech. Rep. ATL-COM-PHYS-2013-990, CERN, Geneva, Jul, 2013. <https://cds.cern.ch/record/1561731>. Internal note for approved paper STDM-2013-06. Cited on page 62.
- [91] B. Jager, L. Salfelder, M. Worek, and D. Zeppenfeld, *Physics opportunities for vector-boson scattering at a future 100 TeV hadron collider*, Phys. Rev. **D96** (2017) no. 7, 073008, arXiv:1704.04911 [hep-ph]. Cited on page 63.
- [92] J. Almond, L. Bianchini, et al., *Search for heavy neutrino, W_R and Z_R gauge bosons in events with two high- P_T leptons and jets with the ATLAS detector in pp collisions at $\sqrt{s} = 8$ TeV*, Tech. Rep. ATL-COM-PHYS-2013-810, CERN, Geneva, Jun, 2013. <https://cds.cern.ch/record/1555805>. Supporting note for EXOT-2012-24, published as JHEP07 (2015) 162. Cited on page 63.
- [93] ATLAS Collaboration, M. Aaboud et al., *Luminosity determination in pp collisions at $\sqrt{s} = 8$ TeV using the ATLAS detector at the LHC*, Eur. Phys. J. **C76** (2016) no. 12, 653, arXiv:1608.03953 [hep-ex]. Cited on page 63.
- [94] G. Avoni et al., *The new LUCID-2 detector for luminosity measurement and monitoring in ATLAS*, JINST **13** (2018) no. 07, P07017. Cited on page 64.

- [95] ATLAS Collaboration, G. Aad et al., *The ATLAS Simulation Infrastructure*, Eur. Phys. J. **C70** (2010) 823–874, arXiv:1005.4568 [physics.ins-det]. Cited on page 64.
- [96] S. Agostinelli et al., *GEANT4 - a simulation toolkit*, Nucl. Instrum. Meth. **A506** (2003) 250–303. Cited on page 64.
- [97] T. Sjostrand, S. Mrenna, and P. Skands, *A Brief Introduction to PYTHIA 8.1*, Comput. Phys. Commun. **178** (2008) 852–867, arXiv:0710.3820 [hep-ph]. Cited on page 64.
- [98] T. Gleisberg et al., *Event generation with SHERPA 1.1*, JHEP **02** (2009) 007, arXiv:0811.4622 [hep-ph]. Cited on page 65.
- [99] S. Schumann and F. Krauss, *A parton shower algorithm based on Catani-Seymour dipole factorization*, JHEP **03** (2008) 038, arXiv:0709.1027 [hep-ph]. Cited on page 65.
- [100] S. Höche, F. Krauss, S. Schumann, and F. Siegert, *QCD matrix elements and truncated showers*, JHEP **05** (2009) 053, arXiv:0903.1219 [hep-ph]. Cited on page 65.
- [101] R. D. Ball et al., *Parton distributions for the LHC Run II*, JHEP **04** (2015) 040, arXiv:1410.8849 [hep-ph]. Cited on page 65.
- [102] S. Alioli, P. Nason, C. Oleari, and E. Re, *A general framework for implementing NLO calculations in shower Monte Carlo programs: the POWHEG BOX*, JHEP **06** (2010) 043, arXiv:1002.2581 [hep-ph]. Cited on page 65.
- [103] A. Ballestrero et al., *Precise predictions for same-sign W-boson scattering at the LHC*, Eur. Phys. J. **C78** (2018) no. 8, 671, arXiv:1803.07943 [hep-ph]. Cited on page 65.
- [104] J. Alwall, R. Frederix, S. Frixione, V. Hirschi, F. Maltoni, O. Mattelaer, H. S. Shao, T. Stelzer, P. Torrielli, and M. Zaro, *The automated computation of tree-level and next-to-leading order differential cross sections, and their matching to parton shower simulations*, JHEP **07** (2014) 079, arXiv:1405.0301 [hep-ph]. Cited on page 65.
- [105] H.-L. Lai, M. Guzzi, J. Huston, Z. Li, P. M. Nadolsky, J. Pumplin, and C. P. Yuan, *New parton distributions for collider physics*, Phys. Rev. D **82** (2010) 074024, arXiv:1007.2241 [hep-ph]. Cited on page 65.
- [106] T. Sjostrand, S. Mrenna, and P. Skands, *PYTHIA 6.4 physics and manual*, JHEP **05** (2006) 026, arXiv:0603175 [hep-ph]. Cited on page 65.
- [107] M. Cacciari, G. P. Salam, G. Soyez, *The anti- k_t jet clustering algorithm*, JHEP **04** (2008) 063, arXiv:0802.1189 [hep-ph]. Cited on page 69.
- [108] ATLAS Collaboration, M. Aaboud et al., *Jet energy scale measurements and their systematic uncertainties in proton-proton collisions at $\sqrt{s} = 13$ TeV with the ATLAS detector*, Phys. Rev. **D96** (2017) no. 7, 072002, arXiv:1703.09665 [hep-ex]. Cited on page 69.
- [109] *Tagging and suppression of pileup jets with the ATLAS detector*, Tech. Rep. ATLAS-CONF-2014-018, CERN, Geneva, May, 2014.
<http://cds.cern.ch/record/1700870>. Cited on page 69.
- [110] D. Adams, C. Anastopoulos, et al., *Recommendations of the Physics Objects and Analysis Harmonisation Study Groups 2014*, Tech. Rep. ATL-PHYS-INT-2014-018, CERN, Geneva, Jul, 2014. <https://cds.cern.ch/record/1743654>. Cited on page 69.

- [111] ATLAS Collaboration, M. Aaboud et al., *Measurement of the cross-section for producing a W boson in association with a single top quark in pp collisions at $\sqrt{s} = 13$ TeV with ATLAS*, JHEP **01** (2018) 063, arXiv:1612.07231 [hep-ex]. Cited on page 69.
- [112] ATLAS Collaboration, M. Aaboud et al., *Performance of missing transverse momentum reconstruction with the ATLAS detector using proton-proton collisions at $\sqrt{s} = 13$ TeV*, Eur. Phys. J. **C78** (2018) no. 11, 903, arXiv:1802.08168 [hep-ex]. Cited on page 71.
- [113] ATLAS Collaboration, M. Aaboud et al., *Measurements of b-jet tagging efficiency with the ATLAS detector using $t\bar{t}$ events at $\sqrt{s} = 13$ TeV*, JHEP **08** (2018) 089, arXiv:1805.01845 [hep-ex]. Cited on page 71.
- [114] J.-F. Arguin, J. Claude, G. Gonella, B. P. Kersevan, K. Koneke, K. Lohwasser, K. Mochizuki, M. Muskinja, C. Piaulet, and P. Sommer, *Support Note for Electron ID: charge mis-identification*, Tech. Rep. ATL-COM-PHYS-2017-1014, CERN, Geneva, Jul, 2017. <https://cds.cern.ch/record/2273365>. Cited on page 75.
- [115] C.-H. Kom and W. J. Stirling, *Charge asymmetry in $W + \text{jets}$ production at the LHC*, Eur. Phys. J. **C69** (2010) 67–73, arXiv:1004.3404 [hep-ph]. Cited on page 95.
- [116] S. P. Martin, *A Supersymmetry primer*, arXiv:hep-ph/9709356 [hep-ph]. [Adv. Ser. Direct. High Energy Phys.18,1(1998)]. Cited on page 106.
- [117] H. Georgi and M. Machacek, *Doubly charged Higgs bosons*, Nuclear Physics B **262** (1985) no. 3, 463 – 477.
<http://www.sciencedirect.com/science/article/pii/0550321385903256>. Cited on page 106.
- [118] C. Englert, E. Re, and M. Spannowsky, *Triplet Higgs boson collider phenomenology after the LHC*, Phys. Rev. **D87** (2013) no. 9, 095014, arXiv:1302.6505 [hep-ph]. Cited on page 107.
- [119] J. Schechter and J. W. F. Valle, *Neutrino Masses in $SU(2) \times U(1)$ Theories*, Phys. Rev. **D22** (1980) 2227. Cited on page 107.
- [120] P. Fileviez Perez, T. Han, G.-y. Huang, T. Li, and K. Wang, *Neutrino Masses and the CERN LHC: Testing Type II Seesaw*, Phys. Rev. **D78** (2008) 015018, arXiv:0805.3536 [hep-ph]. Cited on page 108.
- [121] A. Arhrib, R. Benbrik, M. Chabab, G. Moultaka, M. C. Peyranere, L. Rahili, and J. Ramadan, *The Higgs Potential in the Type II Seesaw Model*, Phys. Rev. **D84** (2011) 095005, arXiv:1105.1925 [hep-ph]. Cited on page 108.
- [122] ATLAS Collaboration, M. Aaboud et al., *Search for doubly charged scalar bosons decaying into same-sign W boson pairs with the ATLAS detector*, Eur. Phys. J. **C79** (2019) no. 1, 58, arXiv:1808.01899 [hep-ex]. Cited on page 108.
- [123] C. Degrande, O. Éboli, et al., *Monte Carlo tools for studies of non-standard electroweak gauge boson interactions in multi-boson processes: A Snowmass White Paper*, in *Proceedings, 2013 Community Summer Study on the Future of U.S. Particle Physics: Snowmass on the Mississippi (CSS2013): Minneapolis, MN, USA, July 29-August 6, 2013*. 2013. arXiv:1309.7890 [hep-ph]. Cited on pages 109 and 110.

- [124] O. J. P. Éboli, M. C. Gonzalez-Garcia, and J. K. Mizukoshi, *$pp \rightarrow jj e^\pm \mu^\pm \nu\nu$ and $jje^\pm \mu^\pm \nu\nu$ at $\mathcal{O}(\alpha_{em}^6)$ and $\mathcal{O}(\alpha_{em}^4 \alpha_s^2)$ for the study of the quartic electroweak gauge boson vertex at CERN LHC*, Phys. Rev. **D74** (2006) 073005, arXiv:hep-ph/0606118 [hep-ph]. Cited on page 109.
- [125] J. Reuter, W. Kilian, and M. Sekulla, *Simplified Models for New Physics in Vector Boson Scattering - Input for Snowmass 2013*, arXiv:1307.8170 [hep-ph]. Cited on page 109.
- [126] R. Steerenberg, *LHC Report: Another run is over and LS2 has just begun...*, <https://home.cern/news/news/accelerators/lhc-report-another-run-over-and-ls2-has-just-begun>, 2018. Accessed: 2018-12-14. Cited on page 111.
- [127] *Letter of Intent for the Phase-I Upgrade of the ATLAS Experiment*, Tech. Rep. CERN-LHCC-2011-012. LHCC-I-020, CERN, Geneva, Nov, 2011. <http://cds.cern.ch/record/1402470>. Cited on page 111.
- [128] G. Apollinari, I. Bjar Alonso, O. Brning, M. Lamont, and L. Rossi, *High-Luminosity Large Hadron Collider (HL-LHC): Preliminary Design Report*. CERN Yellow Reports: Monographs. CERN, Geneva, 2015. <https://cds.cern.ch/record/2116337>. Cited on page 111.
- [129] ATLAS Collaboration, ATLAS Collaboration, *ATLAS Phase-II Upgrade Scoping Document*, Cern-lhcc-2015-020, Geneva, Sep, 2015. <http://cds.cern.ch/record/2055248>. Cited on page 111.
- [130] D. Espriu and B. Yencho, *Longitudinal WW scattering in light of the “Higgs boson” discovery*, Phys. Rev. D **87** (2013) 055017, arXiv:1212.4158 [hep-ph]. Cited on pages 112 and 113.
- [131] ATLAS Collaboration, *Prospects for the measurement of the $W^\pm W^\pm$ scattering cross section and extraction of the longitudinal scattering component in pp collisions at the High-Luminosity LHC with the ATLAS experiment*, Tech. Rep. ATL-PHYS-PUB-2018-052, CERN, Geneva, Dec, 2018. <http://cds.cern.ch/record/2652447>. Cited on page 112.
- [132] ATLAS Collaboration, *Studies on the impact of an extended Inner Detector tracker and a forward muon tagger on $W^\pm W^\pm$ scattering in pp collisions at the High-Luminosity LHC with the ATLAS experiment*, Tech. Rep. ATL-PHYS-PUB-2017-023, CERN, Geneva, Dec, 2017. <https://cds.cern.ch/record/2298958>. Cited on pages 112 and 117.
- [133] T. Sjöstrand, S. Ask, J. R. Christiansen, R. Corke, N. Desai, P. Ilten, S. Mrenna, S. Prestel, C. O. Rasmussen, and P. Z. Skands, *An Introduction to PYTHIA 8.2*, Comput. Phys. Commun. **191** (2015) 159–177, arXiv:1410.3012 [hep-ph]. Cited on page 114.
- [134] ATLAS Collaboration, *Expected performance for an upgraded ATLAS detector at High-Luminosity LHC*, Tech. Rep. ATL-PHYS-PUB-2016-026, CERN, Geneva, Oct, 2016. <http://cds.cern.ch/record/2223839>. Cited on page 115.
- [135] P. C. Bhat, H. B. Prosper, S. Sekmen, and C. Stewart, *Optimizing Event Selection with the Random Grid Search*, Comput. Phys. Commun. **228** (2018) 245–257, arXiv:1706.09907 [hep-ph]. Cited on page 119.

- [136] G. Cowan, K. Cranmer, E. Gross, and O. Vitells, *Asymptotic formulae for likelihood-based tests of new physics*, Eur. Phys. J. **C71** (2011) 1554, arXiv:1007.1727 [physics.data-an]. [Erratum: Eur. Phys. J.C73,2501(2013)]. Cited on page 119.